

Teleconnections for precipitation

Dissertation
zur Erlangung des Doktorgrades der Naturwissenschaften
im Department Geowissenschaften
der Universität Hamburg

vorgelegt von

Oliver Bothe

aus

Kassel

Hamburg

2010

Als Dissertation angenommen vom Department Geowissenschaften der Universität Hamburg

auf Grund der Gutachten von Professor Dr. Klaus Fraedrich
und Professor Dr. Thomas Frisius

Hamburg, den 18. Januar 2010

Professor Dr. Jürgen Oßenbrügge
(Leiter des Departments Geowissenschaften)

Man kann als Wissenschaftler
nur durch den endlosen
finsternen, die meiste Zeit fast
zur Gänze luftleeren Gang
seiner Wissenschaft durch das
Leben gehen.

*Thomas Bernhard, 1967,
Verstörung*

Abstract

The following basic assumption is studied regarding Asian mountain regions and catchments of Asian rivers: Precipitation as spatially and temporally small-scale, relatively poorly observed and insufficiently predictable phenomenon is on larger spatial and longer temporal scales to some extent determined by large-scale influences. The focus is on impacts of the atmospheric variability in the Atlantic-Europe region on a monthly time scale in boreal summer. The identification and evaluation of remote interactions, that is to say teleconnections, is carried out in a study of the temporal and spatial covariability of standardised, spatially averaged precipitation time series, the systematic examination of the zonal wind variability in central Asia and the detection of dynamical influences in composite studies of single climate variables.

The temporal covariability of different regions in south-east and central Asia and known northern hemispheric atmospheric and oceanic teleconnection indices is studied based on regional time series and northern hemispheric fields of precipitation. Data spans the second half of the 20th century. Temporal trends in mean and variance of the standardised indices match for precipitation and single pattern-indices for certain periods, but differ completely for other time-ranges. This hampers efforts to identify predictors for precipitation patterns.

For the Tibetan Plateau and further regions in central Asia it is found, that the structure of the zonal wind upstream of the Asian mountain range explains a noteworthy part of the variability of the standardised spatially averaged precipitation. The zonal inflow is following the calendar subject to temporally and spatially varying influences of tropical heating and extratropical atmospheric variability patterns. Considering Tibetan Plateau precipitation, wave trains are found in model-data and in observational and re-analysis data. Originating in the north Atlantic, these wave trains impact months of severe and extreme dryness or severe and extreme wetness. In months of wetness the wave patterns assume a zonal orientation across the Mediterranean. In dry months their origin is an anomalous high over Scandinavia, and they subsequently build an atmospheric bridge that stretches south-eastward to east Asia.

The displayed bridges between the north Atlantic and east Asia as well as their variability allow a better estimation of the relative importance of regional and large-scale influences on the summertime Asian (monsoon) circulation. This is of importance for an assessment of present and future monthly and seasonal precipitation in their economic, social and ecological meaning for Asian states and their human populations.

Zusammenfassung

Die Grundannahme, dass großskalige Einflussfaktoren ein solch räumlich und zeitlich kleinskaliges, verhältnismäßig schlecht beobachtetes und unzureichend vorhersagbares Phänomen wie Niederschlag auf größeren räumlichen und längeren zeitlichen Skalen partiell bestimmen, wird untersucht anhand asiatischer Gebirgsregionen und Einzugsgebieten asiatischer Flüsse. Im Fokus stehen Auswirkungen der sommerlichen atmosphärischen Variabilität im atlantisch-europäischen Raum auf einer monatlichen Zeitskala. Die Identifikation und Bewertung der Fernwirkungen, sogenannter Telekonnectionen, erfolgt mittels der Betrachtung der zeitlichen und räumlichen Kovariabilität standardisierter, räumlich gemittelter Niederschlagszeitreihen, der systematischen Untersuchung der Variabilität des Zonalwindes in Zentralasien und der Lokalisierung dynamischer Einflussfaktoren in zusammenschauenden Studien einzelner Klimafaktoren.

Basierend auf regionalen Zeitreihen und nord-hemisphärischen Feldern des Niederschlags wird die zeitliche Kovariabilität zwischen verschiedenen Regionen in Südost- und Zentralasien und bekannten nord-hemisphärischen atmosphärischen wie ozeanischen Indizes studiert. Dies erfolgt für die zweite Hälfte des 20. Jahrhunderts. Zeitliche Trends in Mittel und Varianz der standardisierten Zeitreihen stimmen in bestimmten Perioden für Niederschlag und einzelne Muster-Indizes überein, während sie in anderen Perioden keine Gemeinsamkeit zeigen. Dies erschwert Bemühungen, Prediktoren für Niederschlagsmuster zu bestimmen.

Für das tibetanische Plateau und weitere zentralasiatische Regionen lässt sich ein nennenswerter Anteil der Variabilität des standardisierten, räumlich gemittelten Niederschlags erklären durch die Struktur des die zentralasiatischen Gebirge anströmenden zonalen Winds. Diese zonale Anströmung unterliegt im Laufe des Jahres unterschiedlichen zeitlich und räumlich variierenden Einflüssen sowohl tropischer Wärmequellen wie außertropischer atmosphärischer Variabilitätsmuster. Für das tibetanische Plateau werden in Modelldaten sowie mit Beobachtungs- und Re-Analyse-Daten Wellenzüge beobachtet, die, ausgehend vom Nordatlantik, Monate schwerer und extremer Trockenheit oder schwer und extrem erhöhter Niederschläge beeinflussen. Diese Wellenzüge nehmen besonders in feuchten Monaten eine zonale Zugbahn durch die Mittelmeer-Region ein, während sie in trockenen Monaten ihren Ursprung in einem anomalen Hoch über Skandinavien haben und von dort eine süd-östlich gerichtete atmosphärische Brücke nach Ostasien bilden.

Die aufgezeigten Brücken zwischen Nordatlantik und Ostasien sowie ihre Variabilität ermöglichen eine klarere Abschätzung der relativen Bedeutung regionaler und großskaliger Einflüsse auf die sommerliche asiatische (Monsun-)Zirkulation. Dies ist relevant für die Abschätzung gegenwärtiger und zukünftiger monatlicher und saisonaler Niederschläge in ihrer ökonomischen, sozialen und ökologischen Bedeutung für die Staaten und Bevölkerungen Asiens.

Contents

| | | |
|----------|--|-----------|
| 1 | Introduction | 7 |
| 1.1 | Teleconnections and precipitation | 8 |
| 1.1.1 | Teleconnections — a general description | 8 |
| 1.1.2 | Precipitation and the Standardised Precipitation Index (SPI) | 12 |
| 1.1.3 | Teleconnectivity and precipitation teleconnections | 21 |
| 1.1.4 | General notes on data and methods | 24 |
| 1.2 | Scope, objective and outline | 27 |
| 2 | Teleconnections of the northern hemisphere SPI field in boreal summer | 29 |
| 2.1 | Introduction | 29 |
| 2.2 | Data and methods | 31 |
| 2.2.1 | Regional setting | 32 |
| 2.2.2 | Methods | 35 |
| 2.3 | Teleconnectivity and teleconnection patterns | 36 |
| 2.4 | Asian precipitation and teleconnections: 1951-2000 | 41 |
| 2.4.1 | Summer time series | 41 |
| 2.4.2 | SPI covariability in Asia along 30°N: Moving window correlations | 45 |
| 2.5 | Summary | 51 |
| 3 | Central Asian precipitation – the upstream zonal wind structure | 55 |
| 3.1 | Introduction | 55 |
| 3.2 | Data and methods | 58 |
| 3.3 | Climatology | 62 |
| 3.4 | Upstream influence on precipitation | 66 |
| 3.4.1 | Principal component analysis | 67 |
| 3.4.2 | Correlation analysis | 69 |
| 3.4.3 | Composite analysis | 73 |
| 3.4.4 | Teleconnections | 85 |
| 3.5 | Summary and discussion | 90 |
| 4 | Eurasian bridges | 93 |
| 4.1 | Introduction | 93 |
| 4.2 | Data and methods | 96 |

Contents

| | | |
|----------|--|------------|
| 4.3 | Tibetan Plateau | 98 |
| 4.3.1 | Climatological setting | 98 |
| 4.3.2 | Observations and ERA-40 re-analysis | 103 |
| 4.3.3 | ECHAM5/MPI-OM simulations for the IPCC AR4 | 111 |
| 4.4 | Summary | 118 |
| 5 | Synopsis and outlook | 123 |
| 5.1 | Synopsis | 124 |
| 5.2 | Discussion | 125 |
| 5.3 | Outlook | 128 |
| A | Methods and third party software | 131 |
| A.1 | Significances of moving window analyses | 131 |
| A.2 | Calculation of vertically integrated moisture fluxes | 132 |
| A.3 | Empirical Orthogonal Functions or Principal Component Analysis | 133 |
| A.4 | Third party software | 135 |
| B | Supplement to chapter 2 | 137 |
| C | Supplement to chapter 3 | 143 |
| D | Revisiting the structures of 500hPa geopotential anomalies | 147 |
| | Bibliography | 149 |
| | List of Figures | 165 |
| | List of Tables | 167 |

1 Introduction

Every winter, in Greenland, is severe; but they are not all equally so. The Danes have observed, that, if the winter in Denmark has been severe, that in Greenland was, in its kind, more mild an vice versa.

*Hans Egede Saabye, 1818, Greenland:
Being Extracts From A Journal Kept In
That Country In The Years 1770 to 1778*

The human curiosity related to weather and climate extends beyond the concern to know the weather next Sunday 18 PM. Upcoming seasonal climate-states in terms of average temperature and precipitation are as much of personal interest as they are of political, sociological, economic and ecological importance. Projected scenarios of future evolutions of major climate variables are first and foremost designed to be regarded by the “policymakers”. Irrespective of the personal trust in future projections, understanding the variability of climate variables and their interactions in observations and in numerical frameworks with multiply varied forcings and boundary conditions results, in a first step, in more detailed descriptions of possible scenarios to serve the requirements of these decision-makers, and, subsequently, will also improve the elaborateness of the projections and simulations with respect to possible future climate-states on various spatial and temporal scales.

Studies of so called low frequency atmospheric variability serve the purpose of understanding and subsequently predicting the atmospheric behaviour on a time scale beyond the daily weather but shorter than the simulation of future climates. Nevertheless they also help to improve latter projections. Finding factors influential for the upcoming seasonal, e.g., storminess, temperature and precipitation gives means to politics and economics for improved intra- to inter-annual management in such various fields as hydrology and agriculture, insurances and energy, health and environment. Knowledge of decadal climate variability related to atmospheric and oceanic features improves long term future projections and, thus, helps the same anthropospheric sectors in planning.

The identification of potential seasonal predictors is of particular importance for regions of the globe with pronounced annual cycles in precipitation or regular persistent episodes in extreme high or low temperatures. Reliable knowledge of potential flood

1 Introduction

and drought risks helps to reduce the economic and sociological vulnerability of these areas. While the study of such potentially remote predictors is pursued for many years, the failure in predicting the cold Chinese winter of 2005 is a notable example of insufficient certainty in predictions (Lu and Chang, 2009). Similarly the works of Rajeevan et al. (2007) and Peings et al. (2009) try to improve the operational forecasts for the Indian summer monsoon rainfall in view of the failed drought predictions in 2002 and 2004. The 2009 forecasts from the India Meteorological Department (IMD) for the Indian south-west monsoon predicted “Near Normal” conditions for the period from June to September on the long range forecast stage in April (<http://www.imd.gov.in/>). On the second stage update in June 2009 the quantitative prediction read, that India was thought to receive about 93% of the normal long period average precipitation amount with the error being about $\pm 4\%$. The ultimate evaluation lists an average deficit in rainfall for all India of 23% and of 36% for the north-west country, where the second stage forecast predicted a deficit of 19% with an error-bar of $\pm 8\%$. Thus, as the monsoons of 2002 and 2004, the deficit in the 2009 south-west monsoon has not been predicted by the operational model forecasts (compare <http://www.tropmet.res.in/~kolli/MOL/Monsoon/frameindex.html>). Understanding large-scale atmospheric dynamics relevant for precipitation climates is a prerequisite in the assessment of future small scale environmental changes. A detailed understanding is inter alia of particular relevance with respect to the water resources in “High Asia” (Böhner and Lehmkuhl, 2005) on which about 40% of the global population rely (Xu et al., 2008).

Identifying regional and remote impact factors for precipitation on a monthly, seasonal or extended seasonal time scale is an aid for explaining regional climatological mean and variance characteristics and trends. Such an approach serves political and scientific strategies to reduce drought and flood related losses. Therein, it has to consider possible long term climate variability on time scales from years to decades.

1.1 Teleconnections and precipitation

1.1.1 Teleconnections — a general description

The Glossary of Meteorology (Glickman, 2000) defines a teleconnection as

1. *A linkage between weather changes occurring in widely separated regions of the globe.*
2. *A significant positive or negative correlation in the fluctuations of a field at widely separated points.*

Most commonly applied to variability on monthly and longer time scales, the name refers to the fact that such correlations suggest that information is propagating between the distant points through the atmosphere.

1.1 Teleconnections and precipitation

According to Liu and Alexander (2007) such interdependencies were first noted by Swedish meteorologist Hugo Hildebrand Hildebrandsson in the year 1897, while a short note in *Science* in April 1884 (U., 1884) hints to similar observations by French meteorologist Léon Philippe Teisserenc de Bort for the cold winter of 1879/80. Indeed van Loon and Rogers (1978) detail references to an inverse relation between relative intensity of winter climate in Greenland and Denmark dating back to the early 18th century. Further studies find similar long range linkages. Among these, Lockyer and Lockyer (1902) describe an inverse relation between the pressure in Bombay and Cordoba, and Wiese (1924) presents results concerning the atmospheric circulation in the north Atlantic sector and its relation to the sea-ice extent in the Barents Sea and the Greenland Sea. Defant (1924) publishes results capturing the typical patterns of the two phases of the North Atlantic Oscillation. The most prominent example is certainly Sir Gilbert Thomas Walker who first coined the expression “Southern Oscillation”, and who referred to locations connected by correlation analysis as “centres of action” (e.g. Walker, 1925).

The concept of “teleconnections” with reference to simultaneous variations in distant regions was possibly first used by Swedish geologist Gerard de Geer (e.g. De Geer, 1926), who, in his studies of varves, proposed linkages between varves in remote areas of the planet (e.g. Sweden and north America) and referred, forejudging, to them as proxies for past changes in solar radiation. Ångström (1935) first employed the term “teleconnection” in an original climatological context discussing primarily teleconnections in variations of temperature in the north Atlantic region. Teleconnections of weather were classified as (among others) changes in a parameter that is not necessarily part of “weather” but affects the weather in different locations (Ångström, 1935).

Suchlike defined, a “teleconnection” mainly links weather (e.g. precipitation and temperature) in one location and circulation changes in non-adjacent locations. However, the definition incorporates relations between dynamical circulation changes in one location with those in remote areas. The latter view validly depicts the “Southern Oscillation”, its combination with the El Niño phenomenon and “seesaws” like the North Atlantic Oscillation, whose basic description reaches back to the early 18th century (compare van Loon and Rogers, 1978). Thus the terminology mingles (i) features, where a reaction in one location is related to an action in a remote region, and (ii) patterns, which interact coequal or where, at least, action and reaction are not easily assigned.

The most prominent works on “teleconnections” focus on the latter patterns and try to identify major “modes” of variability. These works are motivated by the hope to achieve progress in the prediction not only of weather but also of climate, if such modes of variability are known. Its popularity owes the term “teleconnection” the works of Wallace and Gutzler (1981) and Barnston and Livezey (1987), who utilise the, in their time, newly available computing facilities. Wallace and Gutzler (1981) directly succeed the studies of Ångström (1935) and Bjercknes (1969) in the use of the terminology and

1 Introduction

Defant (1924), Kutzbach (1970) and van Loon and Rogers (1978) in the employment of variations in pressure to find large-scale features and “centres of action”. They take teleconnections to be significant simultaneous correlations in the variability of meteorological parameters at distant locations. For each available spatial data point, a map is constructed consisting of the correlations of this point with all other available spatial data points (stations, grid points). These oodles of maps can be summarised by assigning to each point the value of its largest anti-correlation. This is the first of two, now classical, approaches to compute and to analyse remote interactions or teleconnections. Indeed already Wiese (1924) uses similar maps to describe the influence of the Arctic sea-ice on summer-temperatures in central Europe. Walkers “Correlation in Seasonal Variations of Weather” serve the same purpose (e.g. Walker, 1925, in continuation of earlier work) without visualising the correlation coefficients and centres of action in the form of maps.

The work of Barnston and Livezey (1987) constitutes the other seminal manuscript on the computation and evaluation of teleconnection patterns. It follows earlier research by Lorenz (1956) on the application of Empirical Orthogonal Functions or Principal Components in the prediction of weather. Employing a rotated principal component analysis on one monthly mean geopotential heights, Barnston and Livezey (1987) identify patterns or modes of inter-annual variability. The common definition and nomenclature of atmospheric northern hemispheric teleconnection patterns is based on their study.

Both studies (Wallace and Gutzler, 1981; Barnston and Livezey, 1987) concentrate on dominant or major modes of variability. In recent years, a vast number of studies based on principal component analyses or one point correlation maps propose even more teleconnection patterns or modes of variability in various regional and hemispheric domains. These patterns are either assumed to be the prevailing patterns of the considered region of the globe or defined as the predominant influence on a single phenomenon in the domain of interest. Liu and Alexander (2007) review oceanic and atmospheric teleconnections and their role in the coupled climate system. They section the modes into atmospheric bridges and oceanic tunnels. This terminology meets the fact, that many or most of the regional teleconnections described succeeding Wallace and Gutzler (1981) and Barnston and Livezey (1987) serve primarily as connections or links between a particular occurrence of a parameter like temperature or precipitation at one location and a claimed distant dynamical cause. Thus, in contrast to its antecessors, this “newer” research follows the first interpretation of the definition of Ångström (1935). Quadrelli and Wallace (2004a,b) try to connect these localised teleconnections with major modes of variability by presenting prove, that identified atmospheric teleconnections can be interpreted as interactions or juxtapositions of only two dominant patterns of variability.

This is summarised by Faulwetter (2007) in the sense, that the multitude of patterns in the literature is in a substantial proportion redundant. Differences in results for pos-

sibly the same linkage may arise from differences in data sets, such as their length, their spatial and temporal resolution, slight differences in regional domains, or even just from different means that are subtracted in preparing the data. An inherent problem, further, is the seasonal cycle. A pattern defined in December or for the winter season can be possibly traced in July or summer, but as likely may be obscured by different solar and surface boundary conditions. Thus, in an extreme view, a particular dynamical mode defined in one month may look quite different in another season and similar patterns may arise from different processes in subsequent seasons. Faulwetter (2007) presents a pattern matching algorithm to identify the development of rotated principal components throughout the year following Barnston and Livezey (1987). The algorithm allows to identify periods where found patterns are mixed with others. The results establish new applications to trace the development of teleconnection patterns under possible climate changes on longer time scales. Faulwetter further finds some teleconnections to be more likely part of a continuum of patterns than spatially localised multi-poles.

Kushnir and Wallace (1989) study shorter time scale variations partitioned by frequency bands and propose a continuum of perturbations for fluctuations from 10 to 60 days based on a “lack of uniqueness” of found patterns. The continuum view is supported by Franzke and Feldstein (2005). They describe northern hemispheric teleconnection patterns in terms of nonorthogonal base functions, so called empirical teleconnection patterns. These functions are derived by identifying the one-point regression pattern with maximum variance, subtracting this pattern from the field and repeating the procedure to obtain the successive pattern. The space spanned by these base functions is interpreted as a continuum (Franzke and Feldstein, 2005). This assumption is based on the finding, that similar probabilities of occurrence are displayed for flow patterns, which project simultaneously on two base functions, as for the base functions themselves. The continuum perspective results in two advanced interpretations. The first follows from the construction of the empirical patterns and states the possibility of all members of the continuum just being combinations of few physical modes. The second view interprets the continuum as consisting of a very large number of real physical patterns with specific temporal and spatial properties. This even stronger contrasts the traditional assumption of the existence of a number of dominant modes and the rest of the variability being indistinguishable from some colored noise.

The more regional view in recent research on teleconnections is closely related to the question of “Grosswetterlagen” or weather types and regimes (e.g. Gerstengarbe et al., 1999; James, 2007). While these weather regimes are subject to the influence of remote connections like El Niño/Southern Oscillation (Fraedrich, 1990; Werner et al., 2000), they, by definition, also describe interactions between steering in regions at least as large as Europe (e.g. Gerstengarbe et al., 1999; James, 2007) and the impact of these remote controls on local weather. For example, research on extreme precipitation

1 Introduction

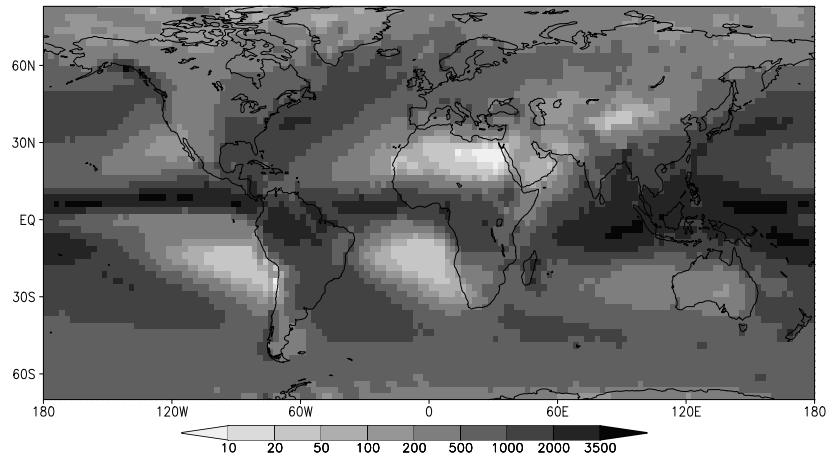


Figure 1.1. Annual sum of precipitation in mm per year for the CMAP (enhanced version) precipitation climatology.

episodes in central Asia identifies persistent anomalies, which are remote connections but also easily classified as being dominant weather regimes or Grosswetterlagen for central Asia (compare the results of Yatagai and Yasunari, 1995, 1998; Barlow and Tippet, 2008). More obvious are overlaps between so called teleconnections and subjective Grosswetterlagen for the recently described North Sea–Caspian Pattern and the Eastern Mediterranean Pattern (e.g. Hatzaki et al., 2007). Comparing Figures of Hatzaki et al. (2007) with those of Gerstengarbe et al. (1999) or James (2007), it is obvious, that both patterns merge different weather regimes together to a “mode” of variability in the north Atlantic/European sector.

1.1.2 Precipitation and the Standardised Precipitation Index (SPI)

Precipitation, temperature and wind affect most intensely the subjective and the public perception of weather and climate. Precipitation, in turn, is the one factor, that most easily can sway the public opinion. The impression of the weather of a day and the climate of a month, a season or a year is dominated by amount, intensity and duration of precipitation-events in the respective period of time. Collective and personal satisfaction with the “weather” depend on precipitation, especially rainfall, or its absence, on the intensity of periodic patterns like the monsoon-circulations or short-time irregular events, on temporally and spatially exceeding or insufficient amounts of precipitation. If only the weather of September and early October 2009 is considered, one finds rainfall causing human, economic and ecological losses throughout the Mediterranean region from Spain through Sicily to Turkey. At the same time in southern Asia two typhoons passed the Philippines and the Indochinese Peninsula flooding vast areas. In southern India, according to CNN and the India Meteorological Department, a revival of the south-west

monsoon resulted in more than 450 000 people to be accommodated in relief camps.

The “Elbehochwasser” of 2002 is still remembered as one of the largest environmental catastrophes in northern central Europe, while similar events occurred in south-eastern Europe quite frequently in the last ten years. The “Elbeflut” was caused by two days of perpetual precipitation in the Giant Mountains and the Ore Mountains. The year 2007 stood out in basically the whole of the Asian monsoon region with floods in Bangladesh, India, Nepal and various parts of China. The Murray-Darling basin is an example for the other pluvial extreme. There, drought conditions are diagnosed since 2002. So while too much precipitation can result in catastrophes in as short a time scale as minutes, droughts happen on time scales of weeks to years. The National Drought Mitigation Centre at the University of Nebraska in Lincoln (<http://www.drought.unl.edu/>) classifies drought with increasing duration as follows (compare Dracup et al., 1980):

- *Meteorological Drought* is based on dryness relative to a normal situation for a specific region on a specific time scale. Thereby the dry condition depends on a deficit in precipitation and increases in evaporation and evapotranspiration (due to higher than normal temperatures, winds or greater sunshine).
- *Agricultural Drought* may be diagnosed as soon as a deficit in soil water arises, that leads to larger stress for plants and reductions in agricultural production. Its diagnosis has to attribute for specific crops and soil structures.
- *Hydrological Drought* summarises the effects of precipitation on pre-defined longer time scales and evaluates the surface and subsurface water. It accounts for reduced streamflow or groundwater flow and reductions in wetlands on a larger regional basis (e.g. river basins and catchments). The state of the components of the hydrological cycle (Brutsaert, 2005) also depend on their consumption by the anthroposphere. Irrigation and growth of populations are impacts possibly leading to conditions of hydrological drought.
- *Socio-Economic Drought* denotes, that, due to a deficit water supply, the demand for an economic good exceeds the supply.

A prominent example for the interaction of anthroposphere and hydrological cycle is the recent drop in groundwater in northern India (Rodell et al., 2009; Tiwari et al., 2009). Rodell et al. (2009) state, that the depletion is probably mostly due to unsustainable consumption of the resource water (e.g. for irrigation). However, just irregularities in the frequency of rainfall events can lead to a depletion of water storages, when high short time scale precipitation amounts drain off. The impact of changes in precipitation in a changing climate are as likely to result from changes in integrated precipitation sums as from changes in the frequencies of precipitation events.

The interaction of the hydrological cycle and the (dry) atmospheric circulation is of great importance for the understanding of weather and climate not only in monsoon

1 Introduction

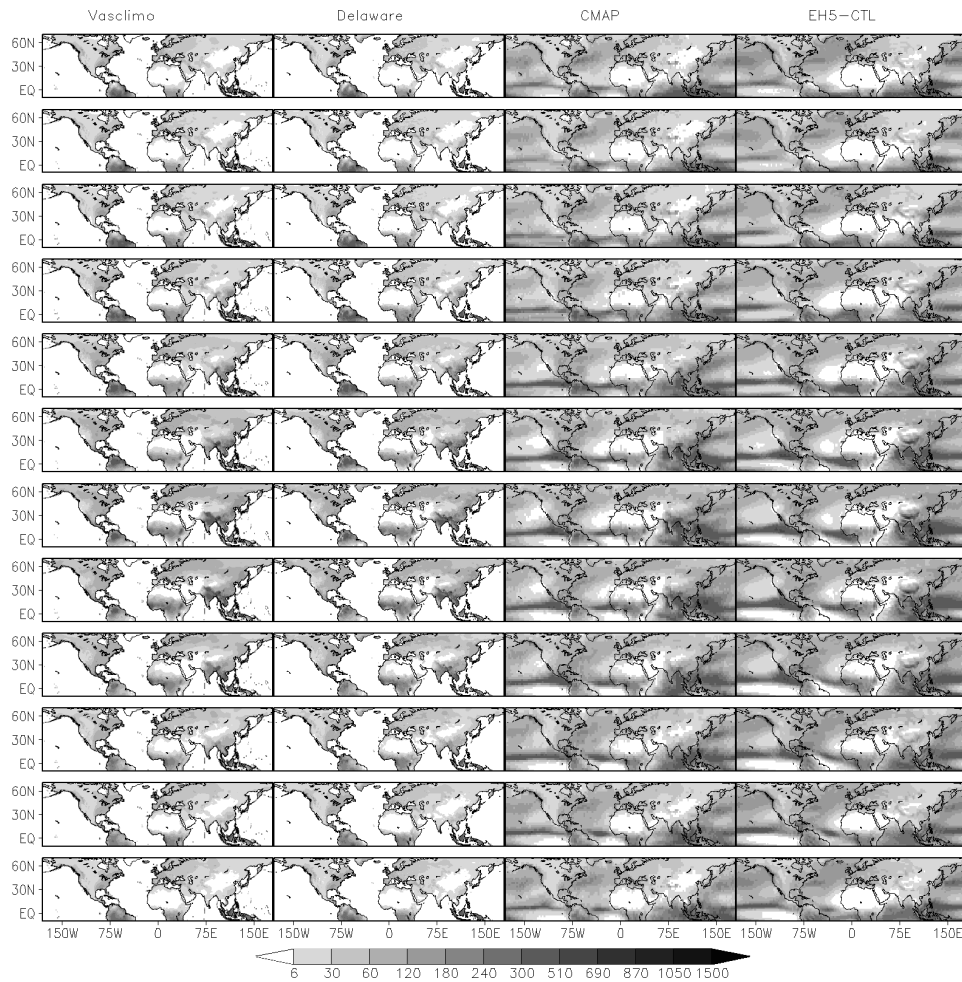


Figure 1.2. Annual cycles of precipitation in mm per month for the Vasclimo, University of Delaware and CMAP (standard version) precipitation climatologies and an ECHAM5/MPI-OM pre-industrial control-run simulation. Top to bottom: January to December.

regions. While the formation of precipitation is partially controlled by the atmospheric dynamics on various spatial and temporal scales, the release of latent heat due to the formation of precipitation drives the general circulation to a large extent. Hydrological surface conditions are found to have a large impact on the onset of the monsoon seasons and its development (Li and Yanai, 1996), while societies depend not only in their agriculture on the storage of water in groundwater and glaciers.

Pronounced differences exist between tropical and extratropical precipitation (Figure 1.1), especially in terms of the zonal mean of annual sums. Outside the tropical regions, precipitation is mainly associated with the fronts of cyclones and troughs. Nevertheless, the extratropical rainfall over the oceans is connected to the large moisture sources in the tropics. This is readily seen in plots of atmospheric moisture content and in the moisture

1.1 Teleconnections and precipitation

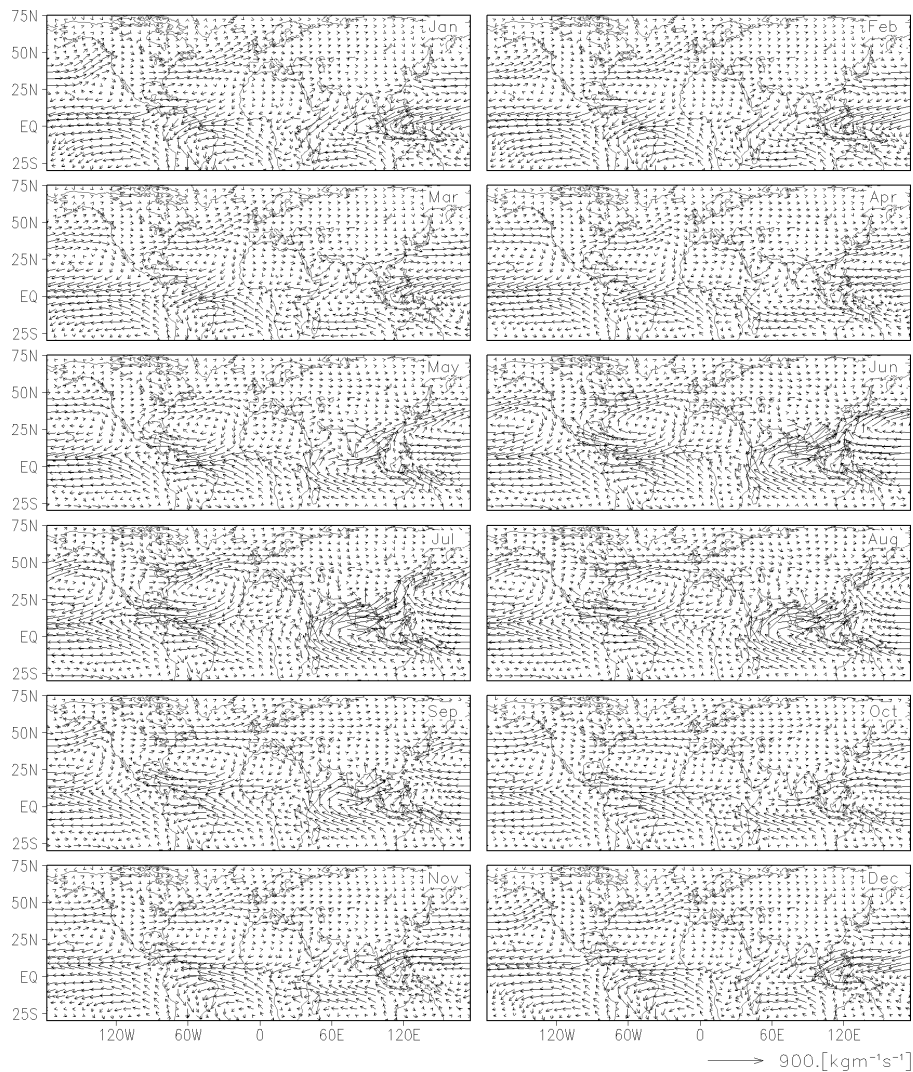


Figure 1.3. Annual cycle of vertically integrated moisture fluxes from the ERA-40 re-analysis

fluxes (e.g. Figure 1.3). While convection dominates in the tropical domain, large-scale (stratiform) precipitation accounts for the largest fraction of rain in the extratropics. Cyclones and corresponding frontal zones are the expression of the storm tracks, whose visualisation can be seen as an integration of the synoptic systems over climatological time scales. This integral view illustrates the difficulties, which arise in the attempt to find connections between a temporally and spatially small scale phenomenon like extratropical precipitation and the atmospheric circulation on time scales of months and seasons. Another substantial fraction of extratropical precipitation arises in orographically pronounced landscapes.

Monsoon circulations by definition consist of changes in the mean wind direction of more than 120° between two seasons. The classical definition validly describes the

1 Introduction

African and Asian-Australian monsoons, while the wind reversals are not fully established for the so called American monsoon and the more loosely named European monsoon. Subsystems of the large-scale monsoons exist, such as the Indian monsoon and the east Asian (or western north Pacific) monsoon. The latter even reaches the mid-latitudes of the north Pacific western coast. The seasonal changes in circulation are directly related to the changes in temperature gradients between continents and adjacent oceans, which, in turn, result from the seasonal cycle in solar radiation. Nowadays, “monsoon” refers more generally to reversals in circulation associated with precipitation in the tropics and subtropics and describes rather the precipitation extremes of wet and dry seasons than the classical climatic changes between winter and summer. The large-scale monsoons are viewed as parts of a global-scale monsoon. Trenberth et al. (2000) use the term of a global monsoon to reference the global extent of an overturning of the atmosphere in the tropical domain and its variations throughout the year. The most notable characteristic of tropical precipitation is the migration of the wet season from one hemisphere to the other following the solar insolation.

Precipitation in Asia The Köppen-Geiger climate classification describes Asia north of 50° as snow climates and most regions south of 20° as monsoonal or winter dry climates (compare Kottke et al., 2006). Warm temperate and fully humid climates are found along the east Asian coast from southern China to central Japan. Central western and northern China and the southern flanks of the Himalaya Range are found to be of warm temperate climate with dry winters. The north coast of the Arabian Sea is primarily arid steppe or to the west even desert. The larger Tibetan Plateau is classified as polar tundra.

Most areas between 60° and 110°E and between 35° and 50°N are cold arid steppe or desert. Only the region upstream of the Tian Shan and the Altai Shan are partially described as fully humid snow climate with warm to hot summers.

Precipitation and moisture flux climatologies (e.g. Figures 1.2 and 1.3) display how, with the seasonal cycle, rainfall first intrudes south-eastern China. With the south-west monsoon the rainy season starts in India, while south-east and south-west monsoon bring rain over the Indochinese Peninsula. The seasonal migration of the jet (for more see chapter 3 and, e.g., Schiemann et al., 2008) brings moisture to western central Asia in spring and autumn (Figure 1.5), while the leeward side of the Tian Shan and the Tibetan Plateau receive rain when the jet resides over this area in summer.

The climatological annual cycles of precipitation present the large variations for regions considered in this thesis (Figures 1.4 and 1.5). Note, the regional annual cycles (Figure 1.4) base on area averaged time series and, thus, may blur features. The Tarim basin has a notable precipitation maximum in summer, while the extreme rainfall is largest in early and late summer. The north-western Tian Shan has two maxima in late spring/early summer and late autumn, while the north-eastern Tian Shan has only small

1.1 Teleconnections and precipitation

variations with the largest precipitation amount occurring in summer. The Indus river catchment is influenced by the south-west monsoon in summer and basically dry the rest of the year. The Tibetan Plateau and the upper Yangtze have annual cycles similar to one another. Both regions overlap in the source region of the Yangtze. The Yangtze is influenced by the east Asian monsoon and the Meiyu frontal zone (e.g. Simmonds et al., 1999; Ding, 2007; Ding et al., 2008). The upper catchment further is influenced by the monsoon flow from the Bay of Bengal. The recreation of the monsoonal rains is seen especially in the upper basin time series when the east Asian monsoon retreats.

Elbe and Amur river catchments are displayed for comparison. The latter has a large maximum in summer, when the western north Pacific monsoon transports moisture as far north as Sakhalin island. The annual precipitation cycle for the Elbe basin is relatively flat with two maxima in summer and winter.

Standardised Precipitation Index A variety of indices are used to assess drought or to capture, in a broader sense, abnormal wetness. Most prominent and still a major

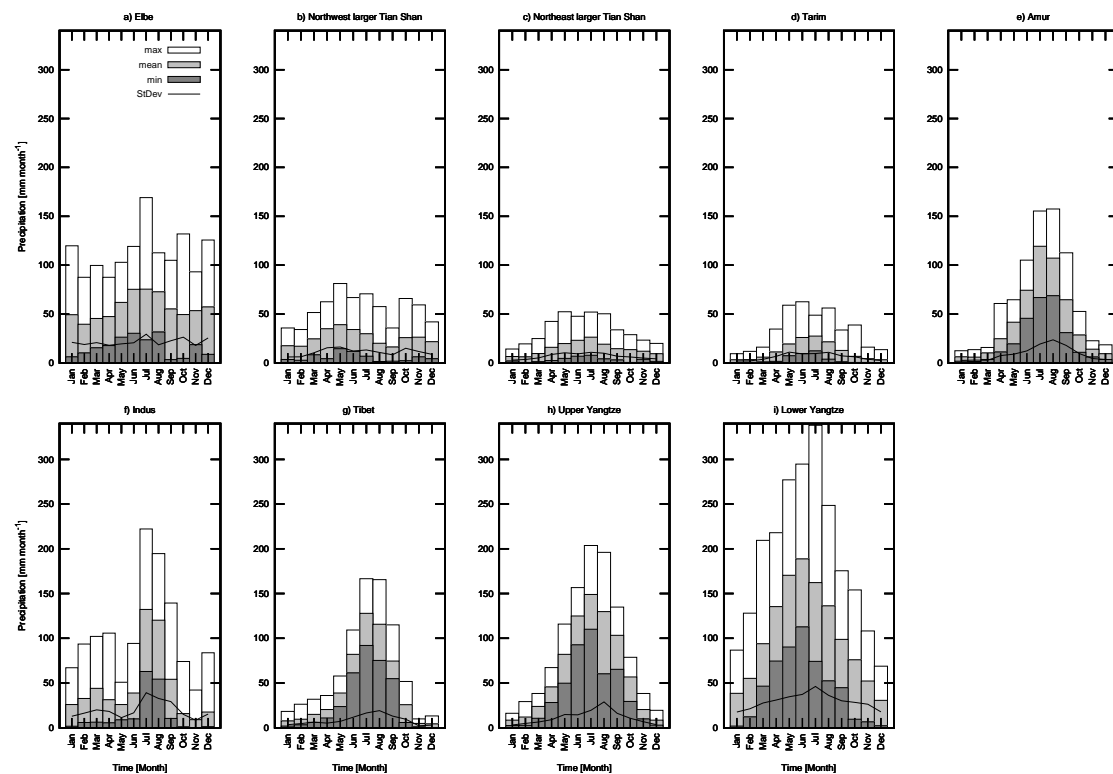


Figure 1.4. Annual mean cycles of area averaged precipitation (Vasclimo) in mm per month: a) Elbe river catchment, b) North-west of the Tian-Shan, c) North-east of the Tian-Shan, d) drainage area from the Tian Shan to the Tarim river, e) Amur river basin, f) Indus river basin, g) Tibetan Plateau, h) Upper Yangtze river reaches, i) Lower Yangtze.

1 Introduction

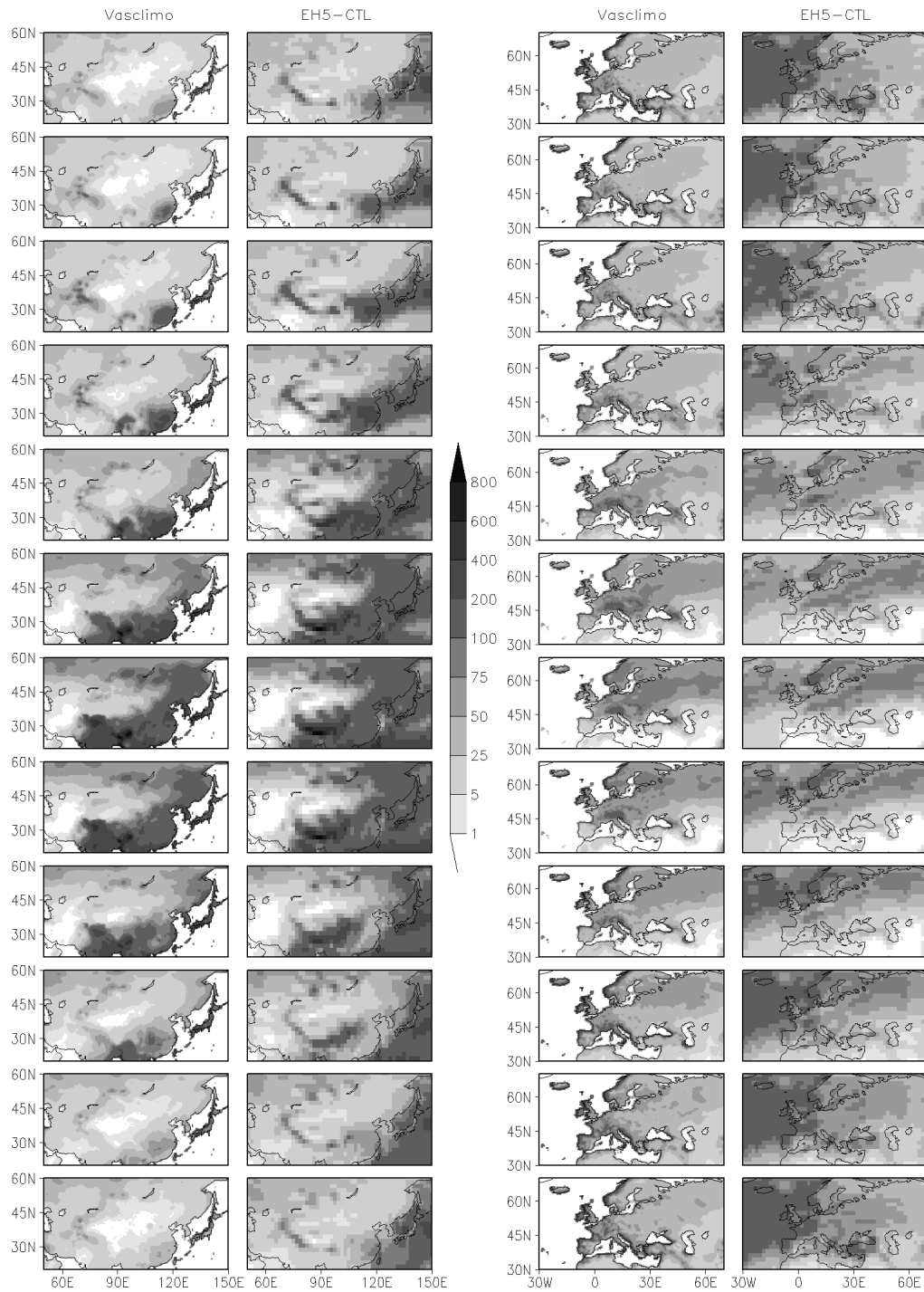


Figure 1.5. Asian and European annual cycles of precipitation in mm per month for the Vasclimo precipitation climatology and an ECHAM5/MPI-OM pre-industrial control-run simulation of 506 years. January to December from top to bottom.

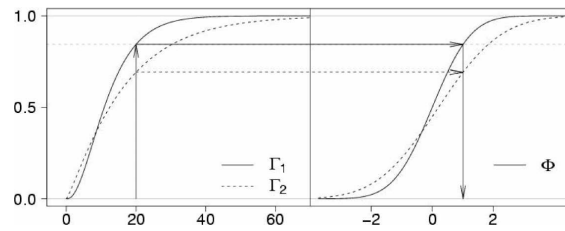


Figure 1.6. Illustration of the transformation of precipitation (adopted from Sienz et al., 2007): The gamma distribution Γ_1 on the left is transformed to the standard normal distribution Φ on the right. Change in the distribution is visualised by the second gamma distribution Γ_2 on the left. The latter is transformed using the probability differences of the first transformation. Then the second distribution on the right is not necessarily normal distributed.

resource in drought monitoring are the Palmer Drought Severity Index (PDSI, Palmer, 1965) and its variations (Guttman, 1998), which in principle evaluate abnormal wetness and dryness based on the water balance (Guttman, 1998). The varied implications of the various time scales of drought require a detailed description of drought for a time-range that may not be achieved by a single index, but rather by a potentially subjective drought monitoring network as is installed in the USA (Svoboda et al., 2002, compare <http://drought.unl.edu/monitor/monitor.htm> and <http://drought.unl.edu/dm/>, where various indices are discussed in detail). In addition, assessments of meteorological, hydrological and agricultural drought can be provided by single indices. For example, the Climate Prediction Center of the National Weather Service in the USA utilises monthly mean soil moisture anomaly percentiles for classifying agricultural drought and a Standardised Runoff Index (SRI) to describe hydrological drought conditions. The SRI bases on the Standardised Precipitation Index (SPI), first proposed by McKee et al. (1993), which is employed to monitor meteorological drought.

Table 1.1. Standardised Precipitation Index (SPI) classification and event-probability (P in %) following McKee et al. (1993).

| SPI-Intervals | SPI-Classes | P-Values |
|----------------------|----------------|----------|
| $SPI \geq 2$ | extremely wet | 2.3 |
| $2 > SPI \geq 1.5$ | severely wet | 4.4 |
| $1.5 > SPI \geq 1$ | moderately wet | 9.2 |
| $1 > SPI > -1$ | normal | 68.2 |
| $-1 \geq SPI > -1.5$ | moderately dry | 9.2 |
| $-1.5 \geq SPI > -2$ | severely dry | 4.4 |
| $SPI \leq -2$ | extremely dry | 2.3 |

1 Introduction

McKee et al. (1993) develop the SPI as a measure to evaluate water resources from a *climate perspective beginning with precipitation*. Therefore an index is needed, that gives a comprehensible measure for pluvial conditions. This is furthered by the standardisation of precipitation anomalies for a fixed time period with reference to known past mean and standard deviation for this period. Thus in the simplest version, a standardised index for precipitation is the deviation of precipitation from the climatology divided by the climatological standard deviation. However, precipitation usually is not normal distributed for most accumulation periods.

McKee et al. (1993) handle this complication by introducing a transformation process prior to the index calculation. The “equal probability transformation” results in a linearly proportional index respective to measured precipitation. The calculation procedure can be applied to sums of precipitation (and other water cycle variables) for various periods of time from half months to, for example, four years. Therein the data is used as a running sum or average, that is at the end of each full or half month a value can be computed from the previous period of interest. The achieved drought and wetness classification directly relates to probabilities of events and does so in an at once comparable manner for different climates and time periods.

Prerequisite for the calculation is the fit of a probability distribution to each data set for a time period of interest. Here data set refers to the time series of the running sum or average of precipitation with respect to its point in the annual cycle. McKee et al. (1993) suggest to fit precipitation data to a Gamma function to identify the coherence between probability and precipitation amount. A successful fit allows to directly compute the probability for any observed precipitation amount and to define the standardised precipitation value with respect to a normal probability density distribution with zero mean and unit standard deviation (compare Table 1.1). McKee et al. (1993) conclude that at least 30 values, that is 30 years of data, are necessary to successfully compute the SPI. The impact of the sample size is revisited by Wu et al. (2005). The computation process is thoroughly discussed in the appendix of Bordi and Sutera (2001).

Already Guttman (1999) notices shortcomings of fits with a Gamma distribution. Non-normality in the SPI can especially arise in arid climates and dry seasons (Wu et al., 2007). Sienz et al. (2007) report further improved results for Iceland precipitation with a Weibull or a Generalised Gamma Distribution. Contrastingly, Husak et al. (2007) test the ability of the Gamma distribution to describe African rainfall series and are not able to reject the assumption, that the Gamma distribution reasonably captures observed precipitation distributions. However, Sienz (2009) describes notable deviations from normality for Gamma distribution fits especially for precipitation time series from coupled atmosphere ocean general circulation model (AOGCM) simulation output. Improper distribution fits result in systematic errors. These are most pronounced in the tails of the distributions (the extreme cases for wetness and dryness). Sienz et al. recommend the

use of the Generalised Gamma Distribution, if one unifying distribution type is wanted, and to test the normality of the SPI distribution (for details, see Sienz et al., 2007).

Here, precipitation is considered in terms of SPI-values in most instances. This includes, again following Sienz et al. (2007), the assessment of changing precipitation climates. Therefore two data sets of precipitation (e.g. from an AOGCM control run and a future climate scenario) are transformed with respect to the distribution fitted to one of these data sets or a third reference data set. Then, the same monthly precipitation amounts in reference and “new” data set result in the same SPI-values, but the “equal probabilities” represent the probabilities of the potentially different distribution. Deviations from the standard normal distribution now can be interpreted in terms of precipitation changes between the two data sets (compare Figure 1.6 adopted from Sienz et al., 2007). In a similar context it is noted, that the mean interval between crossings of a certain “severity” level and the mean residence time above or below this level can easily be computed (compare Wunsch, 1999; VanMarcke, 1983), if fit and transformation are correctly calculated and, thus, the SPI is normal distributed and if furthermore the time series is assumed to be stationary.

1.1.3 Teleconnectivity and precipitation teleconnections

The introductory considerations on the topics of teleconnections and precipitation are completed by simple analyses of remote coherence in the northern hemispheric summer. First, Figure 1.7 displays the teleconnectivity map following Wallace and Gutzler (1981) for the anomalies of the mean summer season (June, July, August) geopotential on the $500hPa$ level. The field is shown for a box from 20° to $85^{\circ}N$. Grid points with an absolute value of maximum anti-correlation larger 0.5 are shaded and contours signify intervals of 0.05 for anti-correlation coefficients from 0.45 to 0.7. The straight lines link complementary centres of correlation. The left panel shows all major centres, where “major” means maximal anti-correlations larger 0.55 for at least one centre, while secondary teleconnections are highlighted in the panel on the right.

The primary teleconnection in the Pacific region can easily be identified as the Pacific/North America pattern (PNA), while the secondary one is similar to the autumn map of the East Pacific/North Pacific pattern (EPNP, maps presented by the Climate Prediction Center, CPC, of the U.S. National Weather Service, NOAA, 2005–2008; Barnston and Livezey, 1987). This latter correlation dipole can further be an expression of the western north Pacific monsoon and its relation to sea surface temperatures in the tropical to subtropical Pacific sector. North American patterns also relate to the major atmospheric Pacific teleconnections, the PNA, the EPNP, the West Pacific Pattern (WP) and the Pacific Transition (PT). The origin of the polar signature is ambiguous.

In the Atlantic sector, a tripole between the Greenland Sea, central northern Europe and the Mediterranean is an expression of the North Atlantic Oscillation (NAO), while

1 Introduction

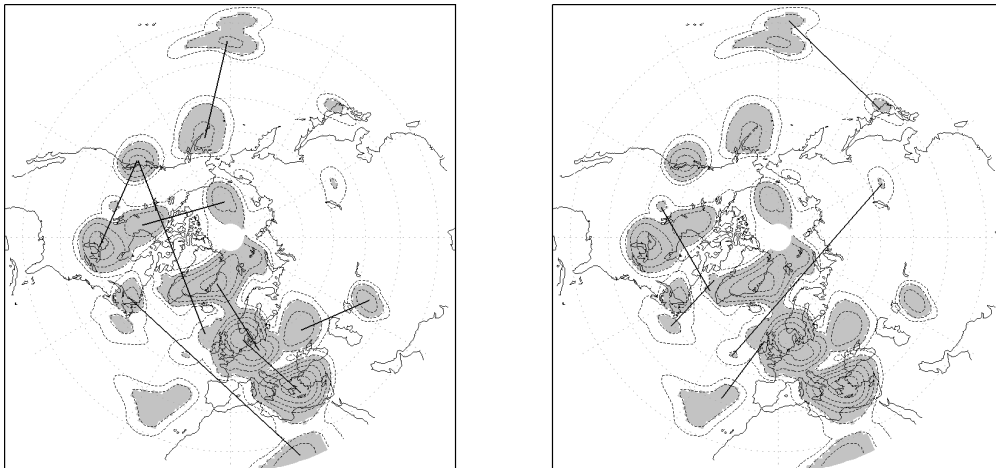


Figure 1.7. Teleconnectivity map following Wallace and Gutzler (1981) for anomalies of northern hemisphere summer mean geopotential at 500hPa. Subsection 1.1.3 describes details.

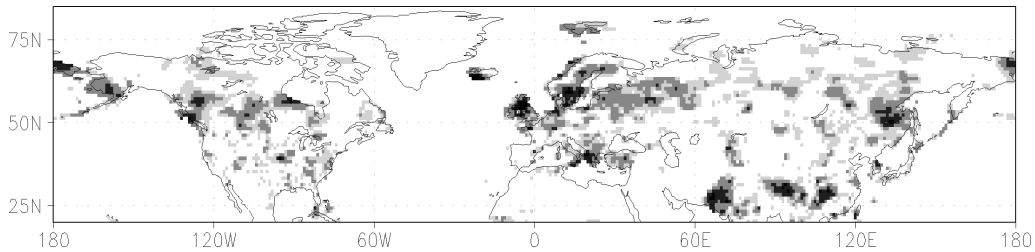


Figure 1.8. Teleconnectivity map following Wallace and Gutzler (1981) for northern hemispheric summer precipitation in terms of the SPI. Shading is for anti-correlations ≥ 0.5 , 0.55, 0.625 and 0.675. No color is assigned to values below 0.5 and missing values (due to failed SPI-fits, especially in dry summer climates).

the dipole west and east of the Caspian Sea shows the signature of the Scandinavia pattern (SCA), even if it deviates from the map of the CPC. The Polar Eurasian pattern (POL) explains the long range correlation from the Atlantic to Eurasia. The NAO is also seen in the weak pattern at the eastern American coast and the New Foundland/Africa coherence is possibly connected with the NAO as well.

Teleconnections for precipitation Already early in the 20th century, Walker (1925) presents teleconnections or correlative action centres for precipitation. Later, Schütte (1967) and Doberitz (1968) try to deepen the understanding of El Niño by identifying teleconnections in and for precipitation. However, the direct application of the method of teleconnectivity maps to precipitation data may be questioned because of the localised character of the data. Figure 1.8 displays such a map for the northern hemispheric summer (June, July, August) SPI-3, that is for the standardised precipitation sum following McKee et al. (1993) for the summer season. Section 2.3 gives more details on the patterns,

1.1 Teleconnections and precipitation

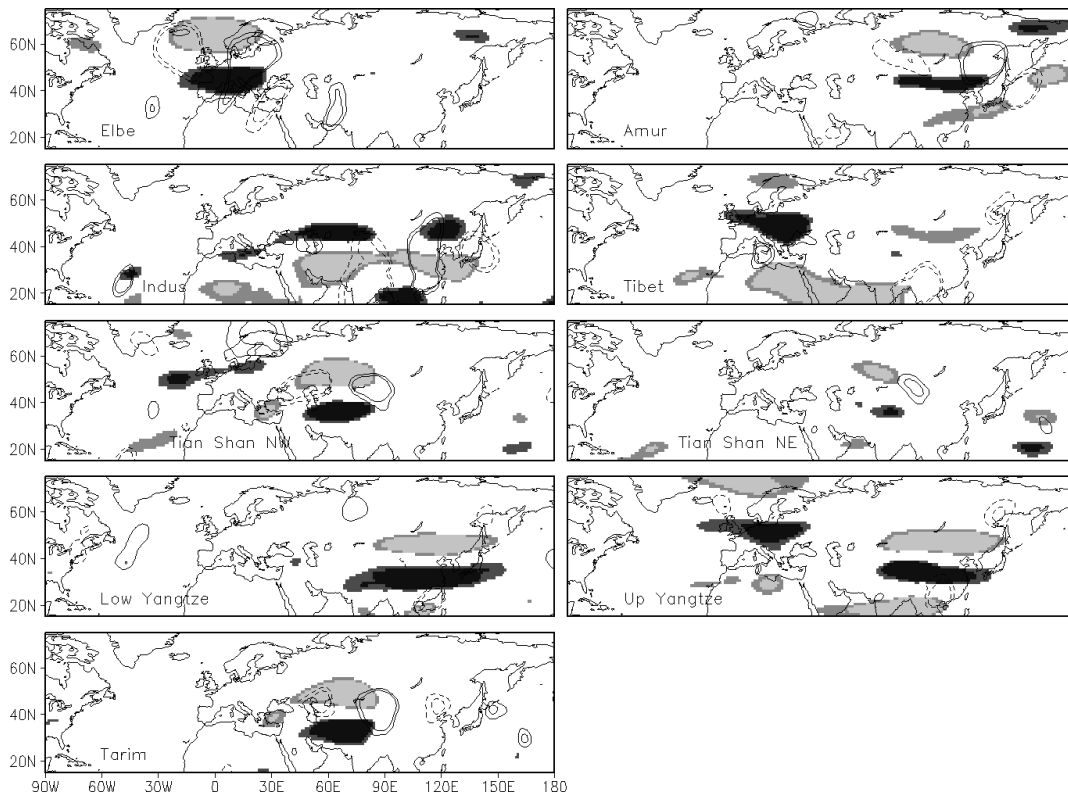


Figure 1.9. Correlations for area averaged summer precipitation time series in terms of the SPI with zonal (shaded) and meridional (contours) wind fields on the $200hPa$ level for selected regions. On the left from top to bottom: Elbe basin, Indus basin, north-western flank of the larger Tian Shan, lower Yangtze basin, Tarim basin. On the right: Amur basin, Tibetan Plateau, north-eastern flank of the larger Tian Shan and upper Yangtze basin. Dark (light) shades and solid (stippled) contours are correlations larger (smaller) 0.25 and 0.3 (-0.25 and -0.3).

which build up this map. Comparison with teleconnectivity maps for the geopotential (Figure 1.7) exhibit notable similarities. Noteworthy are the strongly anti-correlated European centres in central northern Europe, the eastern central Mediterranean and Iceland. The main Asian centres are the Indus basin region, the Tibetan Plateau, the upper Yangtze river basin, the Amur basin and the Chukchi Peninsula. Southern Alaska and Canada from the Pacific to the Hudson Bay are the strongest features in north America. Possible similarities in precipitation correlations and atmospheric flow field teleconnections are easily explained by the link between precipitation and atmospheric variability in terms of upper-level troughs and surface cyclones and their associated frontal systems (e.g. Garreaud, 2007). Chapter 2.3 comments on the remote connections in the northern hemispheric SPI field.

Supplementary, Figure 1.9 shows correlations of regional SPI time series with the components of the horizontal wind field. The Elbe basin SPI series is regionally corre-

1 Introduction

lated, associated with the north Atlantic storm track exit. Some notable extensions are found in the meridional wind in the Mediterranean and in southern central Asia. Correlations are local as well for the summer SPI of the Amur river catchment. Connections are deducible to the polar front jet and the east Asian summer monsoon. The monsoon link is strongest for the Indus basin, where the correlations are found from the south-west monsoon region in the Indian ocean to the western north Pacific monsoon. Further notable correlations are found with the zonal wind upstream. The Tibetan Plateau shows strong correlation patterns in the Indian ocean sector with further features in the region of the south-east monsoon; most conspicuous is the connection to Europe. The two parts of the larger Tian Shan area and the part of the Tarim basin considered here display localised patterns in central Asia with only few extensions. The summer SPI correlations for the two parts of the Yangtze highlight the influence of the east Asian monsoon circulation, but the upper Yangtze is further correlated with the European sector; the pattern resembles the one for the Tibetan Plateau. The similarities may be partially due to the overlap of the Plateau and the basin, as the Yangtze rises from the Plateau.

The Amur and Elbe basins are only presented as comparison, but the preliminary diagnoses are extended with respect to Indus and Yangtze basins and the Tibetan Plateau in chapter 2.4. The role of the upstream zonal wind structure is detailed in chapter 3 considering the central Asian regions of the larger Tian Shan, part of the Tarim river basin and the Tibetan Plateau. Impacts on pluvial conditions on the Plateau are further discussed in chapter 4.

1.1.4 General notes on data and methods

The ERA-40 re-analysis (Uppala et al., 2005) data is taken to be one of the closest possible approximations of the real observed atmospheric flow in the late 20th century. Daily and monthly data on pressure levels is employed in a resolution of approximately $1^\circ \times 1^\circ$. In addition, the skin temperature and surface flux computations are taken from the re-analysis. The representation of found features and possible future changes with respect to the present climate are studied in output of the coupled atmosphere ocean general circulation model ECHAM5/MPI-OM (Roeckner et al., 2003; Marsland et al., 2003) for the fourth IPCC Assessment Report (IPCC AR4, <http://www.ipcc.ch/>) according to the relevant emission scenarios (Nakicenovic and Swart, 2001). The resolution of the ECHAM5/MPI-OM data is approximately $2^\circ \times 2^\circ$ with 31 vertical levels. Hagemann et al. (2005, 2006) evaluate the hydrological cycle in the re-analysis and the AOGCM. Various atmospheric and oceanic indices are obtained from NOAA (2006, 2008, 2005–2008), Ogi et al. (2004), the International Pacific Research Center (Wang and Fan, 1999; Webster and Yang, 1992) and the Frontier Research Center for Global Change (FRCGCC, the Indian Ocean Dipole Mode Index, DMI, Saji et al., 1999).

Precipitation Meteorological observations and station data are scarce in numerous regions of the globe. In addition, single station data has to undergo a thorough quality control before it may be employed in research. A number of climatologic precipitation data sets are available, which are meant to serve as basis for the analysis of the spatial and temporal variability of precipitation. They further help to evaluate the quality of model and re-analysis data of precipitation. All such climatologies over land suffer from the mentioned sparseness of data in some areas. While these products on the global scale are mostly quite similar, differences arise in the study of specified regions. It is not easy to decide, which product represents best the true precipitation climate, if station data is limited. Gruber and Levizzani (2008) evaluate the quality of precipitation climatologies with special focus on the Global Precipitation Climatology Project (GPCP) product. The most commonly utilised precipitation data sets are

- University of Delaware Air Temperature & Precipitation data (1950 to 1999 over land, 0.5° resolution global grid, available from NOAA / OAR / ESRL PSD, Boulder, Colorado, USA, <http://www.cdc.noaa.gov>, Legates and Willmott, 1990),
- CPC Merged Analysis of Precipitation (CMAP, 1979 to delayed present, 2.5° global grid, available at <http://www.cdc.noaa.gov>, Xie and Arkin, 1997),
- Global Precipitation Climatology Project Version 2 (GPCP, 1979 to delayed present, 2.5° global grid, available at NASA Goddard Space Flight Center (GSFC) <http://precip.gsfc.nasa.gov>, Adler et al., 2003),
- the precipitation over land reconstruction (PREC/L, 1948 to delayed present, 2.5° global grid, <http://www.cpc.ncep.noaa.gov>, Chen et al., 2002),
- Variability Analysis of Surface Climate Observations (Vasclimo, 1951 to 2000, 0.5°, 1.° and 2.5° resolution global grids over land, available at the Global Precipitation Climatology Centre <http://gpcc.dwd.de>, Beck et al., 2005) and
- Climatic Research Unit data for precipitation (here: CRU version 2.10, 1901 to 2002 over land, 0.5° global grid, available from <http://www.cru.uea.ac.uk/~timm>, Mitchell and Jones, 2005).

The CRU 2.10 data allows to evaluate precipitation data in relation to the number of available stations. The data set is interpolated over missing data points in space and time and is best employed in areas where at least one station per grid point is available over the whole time period of interest. Which data is best considered in a study on teleconnections for precipitation, is answered by various compromises. Spatial and temporal resolution and the time period covered are the most important factors. Such research will benefit from daily or pentad data (for example available for GPCP), but a spatial resolution of 2.5° degrees is possibly too coarse. Further, if the standardised precipitation index (SPI, see above) is utilised, McKee et al. (1993) recommend at least 30 years of available data. In addition, the precipitation data should have enough overlap

1 Introduction

with atmospheric data (here the ERA-40 re-analysis from 1957 to 2002). Thus, this thesis uses the Vasclimo precipitation data of Beck et al. (2005). Dinku et al. (2008) declare the Vasclimo data to perform rather bad in a study region in Ethiopia, while Schiemann et al. (2008) find the Vasclimo data to be well feasible to validate precipitation climate simulations for central Asia.

The daily gridded precipitation data for the period 1961 to 2004 by Yatagai et al. (2009) is available since May 2009 from <http://www.chikyu.ac.jp/precip>. It is presented in 0.5° and 0.25° resolutions based on Asian rain gauge observations for monsoon Asia, Russia and the Middle East.

Overview of methods Vertically integrated moisture fluxes are computed for the ERA-40 re-analysis and ECHAM5/MPI-OM output following the outline given by Simmonds et al. (1999). Thereby, as the data is used on pressure levels, residuals are possibly neglected for the mass balance (compare Trenberth, 1991). The procedure of Simmonds et al. (1999) is detailed in appendix A.

Stationary wave activity is approximated following Plumb (1985) with a utility programmed by Sielmann (2007). The program takes stream-function and temperature data on two pressure levels and calculates the three spatial components of the stationary wave activity flux of Plumb (1985) in-between. Variances and covariances for the eddy components are computed for re-analysis data of temperature and zonal and meridional wind components on selected pressure levels ($300hPa$, $500hPa$ and $850hPa$, program Fluxes, available from <http://www.mi.uni-hamburg.de/283.0.html>). Input data is interpolated to a T21-grid (approximately $5.6^\circ \times 5.6^\circ$).

Results of chapters 2.3 and 3 are in parts obtained with simple Principal Component analyses (PCA), otherwise called Empirical Orthogonal Function (EOF) analyses (e.g. von Storch and Zwiers, 1999). A short discussion of the method is given in appendix A. Particular reference is made to recent “caveat” publications by (among others) Hannachi et al. (2007), Dommenges (2007) and Monahan et al. (2009).

Composites of variables respective to “extremes” of time series are presented in chapters 3 and 4. Anomaly composites are achieved by subtracting the mean of all cases not complying to a specific criterion from the mean of all cases complying.

With reference to statistical properties in most instances the “R” software environment is employed (R Development Core Team, 2005). Where significance levels and properties are discussed, these in principle refer to the simple t-test significances with no further discussion of the true or effective number of degrees of freedom. The presented correlation coefficients are generally Pearson’s product moment correlation coefficient (e.g. R Development Core Team, 2005; von Storch and Zwiers, 1999). Only in chapters 3 and 4 effective degrees of freedom Φ_{eff} are computed for monthly time series and daily summer fields respectively. The calculation is simplified by using the largest overall co-

efficients of lagged auto-correlations of various time series or in the spatial field. The computation follows the equation

$$\Phi_{eff} = \Phi \cdot \frac{1 - r_{Max_1} \cdot r_{Max_2}}{1 + r_{Max_1} \cdot r_{Max_2}}$$

Φ is the length of the respective time series diminished by two, Φ_{eff} are the effective degrees of freedom, and r_{Max_i} are the maximum lagged auto-correlation coefficients.

Chapter 2.4 presents moving window correlations (Krishnamurthy and Goswami, 2000; Gershunov et al., 2001; Rimbu et al., 2005) and further considers moving averages and variance calculations. That study proceeds along the recommendations of Gershunov et al. (2001) by backing up the results with bootstrap estimates (Efron and Tibshirani, 1993) of the theoretical variability and covariability of the time series considered. The approach is detailed in chapter 2.4 and appendix A. In addition, multiple regressions are computed in chapter 3 to assess the amount of variance attributable to certain indices. The calculation is based on a Fortran program by Sielmann (2008). The routine uses the Gauss-Jordan method (code partially from Press et al., 1992).

1.2 Scope, objective and outline

The present thesis tries to identify persistent impacts on monthly to seasonal regional precipitation, to describe their variability and non-stationarity and to understand their dynamics. This is attended to by studying the observed, re-analysed and simulated data stated above. The simulation data allows to assess the extent to which the model is able to capture observed dynamics and to re-evaluate the findings from the observations in a larger sample size. The regional focus is (i) on the Asian summer monsoon variability and associated regular droughts and floodings and (ii) on semi-arid to arid central Asia, which is particularly vulnerable to predicted climate changes and related effects on glacier mass and precipitation characteristics. The adopted rationale is:

Notwithstanding its spatially and temporally localised character, precipitation is partially determined by large-scale and low frequent factors.

Pursuing this general objective, three subjects are closer looked into:

- I *The inter-annual and interdecadal variability of the Asian monsoons and its connection to the large-scale circulation:* The annual mean monsoon in Asia and its related precipitation exhibit large variations on inter-annual to decadal time scales (Chang et al., 2000b; Wang et al., 2001, 2008b; Ding et al., 2008). Notable variability is also found in the coherence between the subsystems of the Asian monsoon and large-scale climatic features (Chang et al., 2000a,b; Wang et al., 2008c; Kumar et al., 1999; Krishnamurthy and Goswami, 2000). However, Wunsch (1999) and Gershunov et al. (2001) stress the stochastic uncertainties in the assessment of such connections due to the shortness of observational records.

1 Introduction

Therefore, chapter 2 systematically studies the temporal variations in relations between selected regional precipitation time series in Asia and climatic large-scale features and considers their possible randomness. Prior to that, the covariability of the northern hemisphere summer precipitation is described in terms of teleconnectivity maps.

- II** *The zonal wind upstream of the central Asian orography:* The atmospheric westerly wind maximum undergoes a strong seasonal cycle in intensity and position over the Asian continent (Academica Sinica, 1957). Schiemann et al. (2009) depict its evolution in the Tibetan Plateau region, and Schiemann et al. (2008) refer to the role of the westerly wind in discussing the central Asian precipitation climate.

Chapter 3 systematically approaches the seasonal variations in the relationship between regionally averaged precipitation for subdivisions of mountainous central Asia and the upstream zonal wind. Furthermore, the chapter discusses large-scale influences on the zonal wind structure in summer.

- III** *Pluvial conditions on the Tibetan Plateau:* Particular importance is assigned to the Tibetan Plateau and how its heating and moisture properties influence onset and evolution of the Asian monsoon circulations (e.g. Academica Sinica, 1958; Flohn, 1968; Li and Yanai, 1996; Yanai and Li, 1994; Ueda et al., 2003; Hahn and Manabe, 1975). The atmospheric response to anomalies on the Plateau is promoted downstream via wave trains (Wang et al., 2008a) while, on the other hand, upstream variability patterns are linked to precipitation on the eastern portion of the Plateau (Liu and Yin, 2001).

Pluvial severe and extreme conditions are considered for the Tibetan Plateau area averaged monthly summer precipitation in chapter 4 to evaluate the dynamical large-scale influences.

In all chapters the north Atlantic arises as a major influence on the climate of central and eastern Asia. These are accentuated in the synopsis of chapter 5 where also a outlook is presented.

Sections of chapter 4 have been published (Bothe et al., 2009) or are accepted for publication (Bothe et al., 2010) as separate journal publications. This results in a stand-alone structure of chapter 4. This structure is applied to the other chapters as well to make them basically independently readable. However, such an approach further involves minor repetitions among the chapters.

2 Teleconnections of the northern hemisphere SPI field in boreal summer

Abstract

Remote correlations for precipitation are studied using the three monthly standardised precipitation index for the boreal summer season. Influences of common teleconnection patterns on precipitation are displayed. Centers of extratropical teleconnectivity are found on all northern continents linked with all other continents. Strongest relationships arise spatially within single continental land masses. The largest influence on summer teleconnectivity of the standardised precipitation index (SPI) is assigned to the North Atlantic Oscillation affecting north America and Eurasian continental areas.

The standardised precipitation index is employed for summer season in the Indus and Yangtze river basins as well as on the Tibetan Plateau. Correlations among these areas are analysed and remote influences localised. The decadal variability of precipitation in the east Asian monsoon domain is of particular interest. Based on the established relations of the standardised precipitation series to northern hemispheric teleconnections, the covariability of the SPI series with the teleconnection indices is analysed with respect to its temporal variations. The stationarity of the relationships is assessed.

2.1 Introduction

Precipitation varies on a multitude of spatial and temporal scales. The impact of abundant or below normal rainfall is huge on most of these. Viewed globally the large tropical and subtropical monsoon systems dominate intra-seasonal to inter-annual time scales. Excluding seasonal variations, the strong monsoon circulations appear as global linkage of precipitation (compare Rasmusson and Arkin, 1993; Trenberth et al., 2000; Wang and Ding, 2006). The south, east and south-east of Asia are part of the Asian summer monsoon circulation. Standardised precipitation allows direct comparison of precipitation conditions (e.g. extreme wetness and dryness) between different climates (e.g. deserts and monsoon regions). Here, precipitation is characterised in terms of the Standardised Precipitation Index (SPI, McKee et al., 1993).

Teleconnections are, in a first step, assumed as simultaneous correlations in temporal

2 Teleconnections of the northern hemisphere SPI field in boreal summer

fluctuating parameters between spatially distinct locations (Wallace and Gutzler, 1981). Generally such statistical analyses are conducted using parameters of atmospheric circulation intensity like geopotential height or sea level pressure. However, the application to precipitation or the SPI seems legitimate due to the standardisation and if further proves for remote relationships are presented.

Low-frequency modes of precipitation exhibit regularities as reported for the tropical atmosphere by Rasmusson and Arkin (1993), while reports on remote connectivity of precipitation in the extratropics are scarce. Lau and Weng (2002) describe relationships between summer rainfall in the Midwestern US and east Asia. Garreaud (2007) reports local correlations between anomalies of precipitation and parameters of local flow on a monthly basis to be largest over the oceans of the mid-latitudes for upper level zonal flow and upstream of the large mountain ranges for low level flow. Correlations between precipitation in spatially distinct locations can be explained as impact of large-scale circulation patterns (e.g. the North Atlantic Oscillation, the Pacific/North American pattern) or as effect of climate anomalies known to influence the large-scale circulation (e.g. El Niño/Southern Oscillation). The Climate Prediction Center (CPC) of the US National Weather Service (NOAA, 2005–2008) explicitly publishes correlation maps of seasonal precipitation anomalies with monthly teleconnection indices for the central month of respective seasons. These maps show, for summer and the North Atlantic Oscillation as an example, notable negative anomalies in northern Europe, southern Canada and weaker positive anomalies in the southern USA, the Mediterranean and south-west Asia.

Subsequent to the discussion of the remote connections of the SPI in boreal summer, the covariability of established teleconnection indices and regionally averaged precipitation is analysed for the catchments of Indus and Yangtze and the Tibetan Plateau (Figure 2.1). These regions arise as highly anti-correlated centres in southern and eastern Asia. Due to the longitudinal extent of its catchment, the Yangtze basin is subdivided into lower and upper reaches. The upper reaches partially overlap with the Tibetan Plateau.

The Asian monsoon precipitation exhibits, especially in the east Asian monsoon domain, a strong decadal variability (e.g. Jiang et al., 1997; Qian et al., 2003, 2007; Ding et al., 2008, 2009). In addition, a change in covariability is widely reported between the Asian monsoon precipitation and the various indices for El Niño (compare the critical review of Gershunov et al., 2001).

This chapter describes variability and covariability of the standardised precipitation index for the northern hemisphere land masses excluding the tropics from 0 to 20°N and for selected regions in the Asian monsoon domain for the boreal summer season. Data and analysis methods are presented in section 2.2 before, in section 2.3 the teleconnectivity of the boreal summer SPI field is displayed. Section 2.4 describes and discusses changes in covariability between regional summer SPI time series and teleconnection indices. The regional setting is motivated in section 2.2.

2.2 Data and methods

Precipitation data utilised in this chapter stems from the Vasclimo project (Variability Analysis of Surface Climate Observations, Beck et al., 2005). The $1^\circ \times 1^\circ$ resolution is chosen and the data spans the period 1951–2000. The influence of the tropical atmosphere and precipitation variability is excluded by limiting the research area to the latitudinal range of 20° to 90°N . Indices of common teleconnection or circulation patterns are obtained from the Climate Prediction Center (NOAA, 2005–2008, 2006, 2008): Arctic Oscillation (AO), North Atlantic Oscillation (NAO), Pacific/North America pattern (PNA), East Atlantic (EA), East Atlantic/West Russia (EAWR), Scandinavia (SCA), Polar/Eurasia (POL), West Pacific (WP), East Pacific/North Pacific (EPNP), Tropical/Northern Hemisphere (TNH), Pacific Transition (PT) and various regional indices for El Niño/Southern Oscillation (NINO12, NINO3, NINO4, NINO34). Ogi et al. (2004) describe the Seasonally Varying Northern Hemisphere Annular Mode (SV-NAM) and provide the index data. The Indian Ocean Dipole Mode index (Saji et al., 1999) of the Frontier Research Center for Global Change (FRCGCC) is based on the SST data of Kaplan et al. (1998). Monsoon indices are available at the International Pacific Research Center (Indian summer monsoon index, ISM, Western North Pacific monsoon index, WNP, and Webster and Yang monsoon index, WYM, Wang and Fan, 1999; Webster and Yang, 1992).

The precipitation data is studied in terms of the standardised precipitation index (SPI, McKee et al., 1993; Bordi and Sutera, 2001; Sienz et al., 2007) at each grid point. Originally constructed to assess droughts in the USA, it measures the temporally accumulated amount of precipitation as deficit or excess relative to the chosen time scale. Here, the three monthly SPI is used and only the values for August are considered characterising the summer season (June, July, August). Due to the scarcity of precipitation even on seasonal time scales in some regions during the dry summer, areas like California, North Africa, the Arab and Middle East states and inner Asia from the Caspian Sea to the Arabian Sea as well as parts of the Taklamakan and Mongolia are represented by missing values; see Wu et al. (2007) for a discussion of the application of the SPI in arid areas

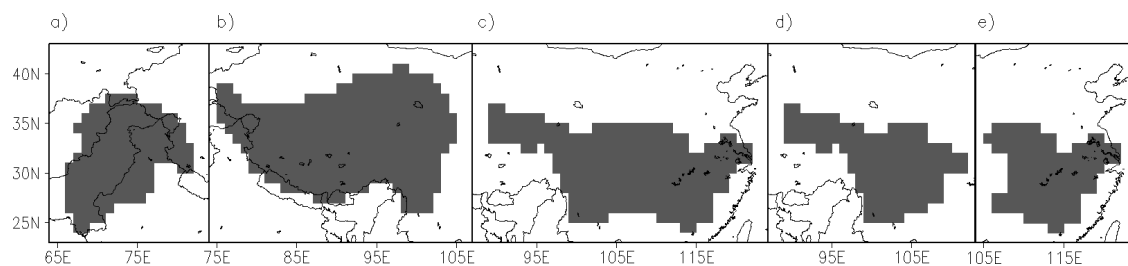


Figure 2.1. Illustration of considered regions: a) Indus river basin, b) Tibetan Plateau, c) whole Yangtze river basin, d) upper reaches of the Yangtze, e) lower reaches of the Yangtze.

2 Teleconnections of the northern hemisphere SPI field in boreal summer

and dry seasons. In section 2.4 area averaged precipitation is employed for the Indus and Yangtze river catchments and for the Tibetan Plateau. Precipitation data and other indices are not detrended, as the interest is to some extent on the decadal covariability of precipitation and teleconnections.

2.2.1 Regional setting

In the course of the present chapter notable linkages are displayed between standardised precipitation in the catchments of the Amur, the Indus and the Yangtze rivers and the Tibetan Plateau. The covariability of the standardised (regionally averaged) summer precipitation is analysed in section 2.4 with respect to those regions, which are reliably affected by sub-systems of the Asian summer monsoon (the Indus river by the Indian summer monsoon, the Yangtze by the east Asian summer monsoon) or described as a major influence on the Asian monsoon (the Tibetan Plateau). Figure 2.1 depicts these regions, whose setting is specified as follows:

Indus river basin The Indus river is of outstanding relevance for society and industry of Pakistan (Ali and De Boer, 2007) and one of the worlds largest rivers in terms of discharge and area drained (Fekete et al., 1999, 2000). As the Yangtze river, the Indus springs from the Tibetan Plateau. Studies on the western Himalaya and the Indus river basin are rather sparse. Yadav et al. (2004) report a notable deviation of the response of the western Himalaya region to the global mean temperature increase with increasing daily temperature ranges and a decrease in mean temperature in some seasons. Singh and Bengtsson (2005) study the effect of global change on Himalayan river basins fed by the glaciers and snowfields of the region. The water resource in the glaciers in the upper Indus basin relies on the winter precipitation (Ali and De Boer, 2007).

The Indus basin can be described in its upper ranges as a boundary region between tropical and continental mid-latitude influences, and the climate is substantially different from other regions of the Himalaya. It is found to be arid to semi-arid in the northern domain affected by potential rain-shadow effects of the Nanga Parbat and subtropical to tropical dry in its further course (Kottek et al., 2006; Young and Hewitt, 1990; Ali and De Boer, 2007). While precipitation in the upper catchment is predominantly due to westerlies from the Mediterranean and Caspian Sea during boreal winter and spring seasons, the Indian monsoon brings large amounts of rain to the southern tip of the upper basin in summer. The monsoon moisture flux from the Arabian Sea is even stronger and results in most intense precipitation in the lower Indus basin (Fowler and Archer, 2006; Ali and De Boer, 2007). The short summer monsoon spells of heavy precipitation contribute to snow accumulation in the elevated areas and result in potential flood risks in the lower parts of the catchment.

With the Asian rivers rising in the Himalayas the principle truth, that the source of

a river ultimately depends on the precipitation amount, is alleviated due to the great potential of modifications by the storage in snowpack and glaciers in the upper basins. Hydrological research in the water resources is relevant with respect to the economical and agricultural security and to hydrological planning in relationship to the risk of flooding. Archer and Fowler (2004) and Fowler and Archer (2005) report correlations between summer rainfall at some upper Indus basin stations and the North Atlantic Oscillation and El Niño/Southern Oscillation but further remark, that the low level of coherence discourage the application for the management of water resources.

Tibetan Plateau The Tibetan Plateau covers an area of more than two million square kilometers. With its average elevation of about four kilometers, it is of primary importance for the northern hemispheric climate and the Asian monsoon circulation. It serves as an elevated heat source and its extent (including the Himalaya Range) presents a mechanical barrier (for example Flohn, 1968; Raghavan, 1973; Hahn and Manabe, 1975; Tang and Reiter, 1984; He et al., 1987; Li and Yanai, 1996; Wu and Zhang, 1998; Held et al., 2002; Hsu and Liu, 2003; Zhang et al., 2004; Sato and Kimura, 2007; Wang et al., 2008a). Hydrology and agriculture of the downstream river basins depend on precipitation on the Plateau. This includes the catchments of Ganges, Indus, Mekong, Huang He, and Yangtze (Fekete et al., 1999, 2000). Some authors regard the Plateau as Asia's or the world's 'water tower', because Tibetan Plateau hydrological variability and the factors influencing it affect the lives of about 40% of the world's population (Xu et al., 2008).

Simmonds et al. (1999) describe three routes of moisture supply to the Tibetan Plateau (e.g. Figure 4.1): (i) from the south (Arabian Sea and Bay of Bengal), (ii) from the south-east (the South China Sea), and (iii) the mid-latitude westerlies. The massif of the Himalaya shadows the Tibetan Plateau partially against the south and east Asian monsoon circulations. However, the monsoon moisture fluxes may reach the Plateau under certain favourable meteorological and climatological conditions. In addition, the monsoonal circulation itself depends on the heating conditions on the Plateau (e.g. He et al., 1987; Yanai and Li, 1994; Li and Yanai, 1996; Ye and Wu, 1998). In summer, the westerly jet resides over or just north of the Tibetan Plateau. Thus, the Plateau is directly situated below the westerly wave guide (Hoskins and Ambrizzi, 1993) and is subject to the influence of incoming wave trains from the upstream north Atlantic/European sector (compare chapters 3 and 4 and discussions therein). Fujinami and Yasunari (2009) describe the effect of waves passing the Plateau on downstream precipitation in the east Asian summer monsoon domain. Additionally sea surface temperature conditions in the adjacent oceans impact the moisture fluxes to the Plateau. Hong et al. (2008) present the influence of the Indian Ocean Dipole Mode (IOD, Saji et al., 1999) and El Niño/Southern Oscillation (ENSO, Webster and Yang, 1992) on the moisture fluxes in the domain between 60° and 150°E.

Yangtze river basin A thorough review of the hydrology of the Yangtze river catchment with particular regard to the influence of the east Asian monsoon circulation would make up a book of its own. While such a review is of imperatively necessity, the interested reader may refer to the respective chapters of Wang (2006) and the summaries of He et al. (2007) and Ding and Chan (2005). Lau and Li (1984) and Lau et al. (1988) present introductory considerations on the east Asian monsoon and its effect on precipitation in the domain to which the Yangtze catchment belongs.

The Yangtze river transects China roughly along the latitude circle of 30°N. Its climate varies from polar tundra at the spring on the Tibetan Plateau to a subtropical monsoon climate in the delta at the East China Sea (Kottke et al., 2006). With a length of more than 6300km it is the largest river of China and with an area of about 1.8 million km² the thirteenth largest river basin in the world (Fekete et al., 1999, 2000). The basin is, seen in its entirety, of huge economic and agricultural importance for the People's Republic of China with more than 400 million people living in its catchment (Xu et al., 2007).

Regular floodings occur throughout the summer monsoon season due to short intensive local rain spells. Wu et al. (2006) succeed in classifying flood and drought in the Yangtze under "normal" conditions. Excessive rain on longer time scales can result in superposition of flood waves along the river. Flood frequency increased in the 1990s. Besides the monsoonal influences, the lower basin is subject to heavy precipitation related to typhoons in the adjacent western north Pacific. Moisture is transported to the main part of the catchment from the Bay of Bengal and from the western north Pacific in summer (on average; compare chapter 1 and Simmonds et al., 1999; Chow et al., 2008), but due to the longitudinal extent and the altitudinal differences, the spatial distribution of rainfall is quite irregular (Zhang et al., 2005; Orlowsky et al., 2009). Simplified, precipitation amount decreases with altitude and from east to west.

Summer monsoon rainfall in the Yangtze basin is primarily related to the so called "Plum rains", the Meiyu. Located at approximately 30°N, the Yangtze resides in the transition of tropical to moderate extratropical climates. The east Asian summer monsoon and the Meiyu front are subject to the intrusion of cooler continental air masses from the north. The Meiyu, so to speak, demarcates both domains and focusses moisture in the Yangtze (see, for the dynamics of the Meiyu front, Zhou et al., 2004; Ninomiya and Shibagaki, 2007; Sampe and Xie, 2009). The confluence of warm southerly and cold northerly flow is fundamental to the formation of the Meiyu.

The east Asian summer monsoon precipitation distribution basically consists of a tripole (Hsu and Lin, 2007). Its structure is expression of the mean asymmetry between rainfall in the Yangtze basin and the regions north and south of it. A wet year in the Yangtze basin is accompanied by dry conditions to its north and to its south, while more precipitation in the north results in relative dryness in the Yangtze area. Climatologically, heavy rainfall reaches the Yangtze basin in mid-June, when the Meiyu frontal zone

is fully established, and subsequently migrates to the north until the end of July. A revival of rainfall is experienced in eastern Asia in August, which is occasionally described as the southward retreat of the frontal zone. Chen et al. (2004) relate it to additional northward intrusions of monsoon rainfall in connection with the northward progression of the intertropical convergence zone (ITCZ). The described evolution is subject to large inter-annual variability. Floods may be caused by larger than average rain in the Meiyu season as well as by heavy rain episodes outside the normal monsoon season (Chang et al., 2000a; Mao and Wu, 2006). On longer time scales, Gong and Ho (2002) describe a shift in summer rainfall in the Yangtze area in the late 1970s with reduced summer rain in the northern regions of China and increased precipitation in the south.

Research on the east Asian monsoon variability, and thus on variability of precipitation in the Yangtze river basin, identifies a number of impact factors. The works of Chang et al. (2000a,b) give an overview of the regional sea surface temperature influences, and Yun et al. (2008) detail a mechanism, how ENSO affects the east Asian summer monsoon. Direct connections further exist to the dynamics of the western north Pacific subtropical high (compare Rodwell and Hoskins, 2001; Chang et al., 2000b). Gong and Ho (2003) link the variability of the monsoonal circulation to the Arctic Oscillation, while, among others, Sun et al. (2009a), Nan and Li (2003) and Xue et al. (2003) establish relations to the southern hemisphere annular mode. Furthermore, Eurasian blocking intensity is found to influence the intensity of rainfall in the Yangtze catchment (compare Wang, 1992; Li et al., 2001b,a).

2.2.2 Methods

Fields and area averaged time series of precipitation are considered in the standardised form of the SPI (compare, section 1.1.2 and McKee et al., 1993). As an initial point, the SPI field is subjected to a teleconnectivity analysis following Wallace and Gutzler (1981). The map and patterns building it up are discussed in section 2.3. Additionally, the correlations of the summer SPI with common teleconnection indices are considered. Passing by, results of a principal component analysis (PCA, compare appendix A and, e.g., von Storch and Zwiers, 1999) are mentioned. Fields of correlation coefficients are primarily presented with respect to their similarity with SPI-teleconnectivity features.

A more detailed analysis of the covariability of regional SPI series and the coherence of time series follows in section 2.4. Assigned significances in general neglect possible stochastic dependencies. An assessment of the temporal evolution of coherence between SPI and popular as well as public data for teleconnections is attempted by applying moving window correlation analyses to the data. Thirty overlapping windows of 21 years are employed for 50 years of available data for each time series. Supplementary material is presented in appendix B.

Significances of moving window analyses Following the comments of Wunsch (1999) on the interpretation of short climate records, Gershunov et al. (2001) systematically discuss the claimed weakening in the relationship between the Indian monsoon and El Niño/Southern Oscillation (e.g. Krishnamurthy and Goswami, 2000; Kumar et al., 1999) and are not able to describe the variability in the relationship as exceeding the variance of purely stochastic processes. Therefore, they recommend to use a bootstrap approach (Efron and Tibshirani, 1993) in any research on decadal variability in the linkage between time series, particularly in any utilisation of running window correlations.

Using the R-software package, the “best” autoregressive model is established to fit the data. For all indices, except the one for the West Pacific pattern, this results in a zero order assumption. Visual inspection and subsequently presented results suggest no necessity to consider the West Pacific pattern separately. All indices are assumed to be expressions of independent random variables.

The natural variability of the coherence of two time series is easily evaluated by simulating pairs of correlated white noise time series: Is $x_1(t)$ a time series equalling ε_1 , then a series correlated with a correlation coefficient c can be constructed by $x_2(t) = cx_1(t) + \varepsilon_2$, with ε_i being random normal distributed variables with zero mean and unit variance (σ_1^2) for ε_1 and $\sigma_2^2 = 1 - c^2$ for ε_2 because x_1 , due to the correlation, explains c^2 of the variance of x_2 . The correlation coefficient c refers to the full length time series, which in this case consists of 50 years or 50 data points. The simulation is done for correlation coefficients from 0.05 to 0.9 in 0.01 intervals. Afterwards moving window correlations, means and variances are computed for a window length of 21 data points. Standard deviations are computed over the running measures for each correlation coefficient c . If this simulation is repeated M times in an bootstrap approach, the 95% and 5% percentiles of the standard deviations of moving window correlations (and means and variances) serve as 95% significance levels for one-tailed tests. The tested hypothesis is: The variations of running measures are of purely stochastic origin. Variability exceeding the 95% percentile is significantly enlarged relative to a pure random white noise process, and it is significantly smaller than in a pure random white noise process, if it is below the 5% percentile. The 95% percentile is included in the respective figures relative to the correlation over the full period (see also Figure A.1). $M = 5000$ is utilised. As an example, a window correlation coefficient of 0.69 is possible due to pure stochastic variability for windows of 21 data points and a correlation coefficient of $c = 0.5$ (that is an explained variance of 25%) between two base time series with 50 data points.

2.3 Teleconnectivity and teleconnection patterns

The teleconnectivity of the JJA SPI-3 is analysed in terms of temporal correlations between all grid points following Wallace and Gutzler (1981). They raise the question of

2.3 Teleconnectivity and teleconnection patterns

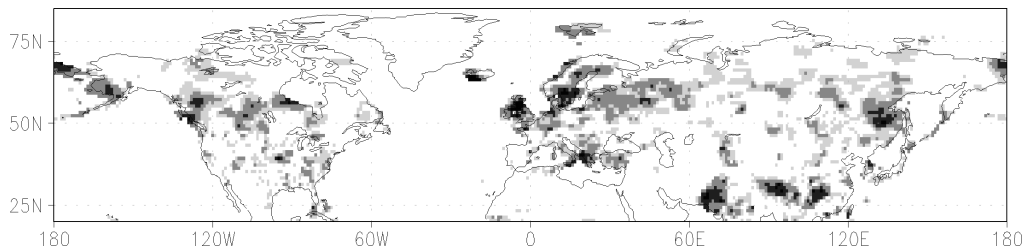


Figure 2.2. Teleconnectivity map following Wallace and Gutzler (1981) for northern hemispheric precipitation in terms of the SPI. Shading is for anti-correlations ≥ 0.5 , 0.55, 0.625 and 0.675. No color is assigned to values below 0.5 and missing values (due to failed SPI-fits, especially in dry summer climates).

the reliability of significant remote correlations and conclude, that features with a correlation larger or equal to 0.75 are usually consistent. Here, the reproducibility is tested by comparing the teleconnections for the whole 50 year period with the correlations for thirty overlapping 21 year windows (not shown). Patterns remain obtainable for nearly all periods. Nevertheless no anti-correlations larger than 0.675 are found, while 0.625 is exceeded regularly. The teleconnectivity map is already displayed in chapter 1 and repeated in Figure 2.2 as largest anti-correlations found per grid point.

Main centers of teleconnectivity in Europe are Iceland, the British Isles, Scandinavia and the central Mediterranean. Svalbard and a tongue from the east European plain through the west Siberian plain occur as secondary centres. In north America, centres exist in Alaska, west of the Canadian Rocky Mountains, west of the Hudson Bay and in the Midwestern United States. On the Asian landmass, the vicinity of the Amur river basin overlapping with the region of the Okhotsk High and the Chukchi Peninsula appear as teleconnectivity centres. In addition, the belt between 25° and 32°N occurs as special area of interest including the Tibetan Plateau and the catchments of the Indus and Yangtze rivers. In Asia, further notable coherence is seen of the Korean peninsula and Japan with the island of Taiwan. The latter feature is not well displayed in the hemispheric map due to the small number of land grid points per each of these marine bounded countries. The about 20 locations contribute to about five major SPI teleconnection patterns for the 50 year period.

Teleconnection patterns Figure 2.3 depicts the most notable correlation patterns. As the maps are computed for every grid point over land with data, the patterns for adjacent grid points are similar to one another. Panels a) to c) show the exemplary patterns for Europe. In principle a tripole arises between north Atlantic high latitudes, central northern Europe and the central northern Mediterranean overlapping with the Balkans. Further covariance is seen between central Europe and the western coast of Norway.

A number of covariability patterns involve the far north-west of north America. The

2 Teleconnections of the northern hemisphere SPI field in boreal summer

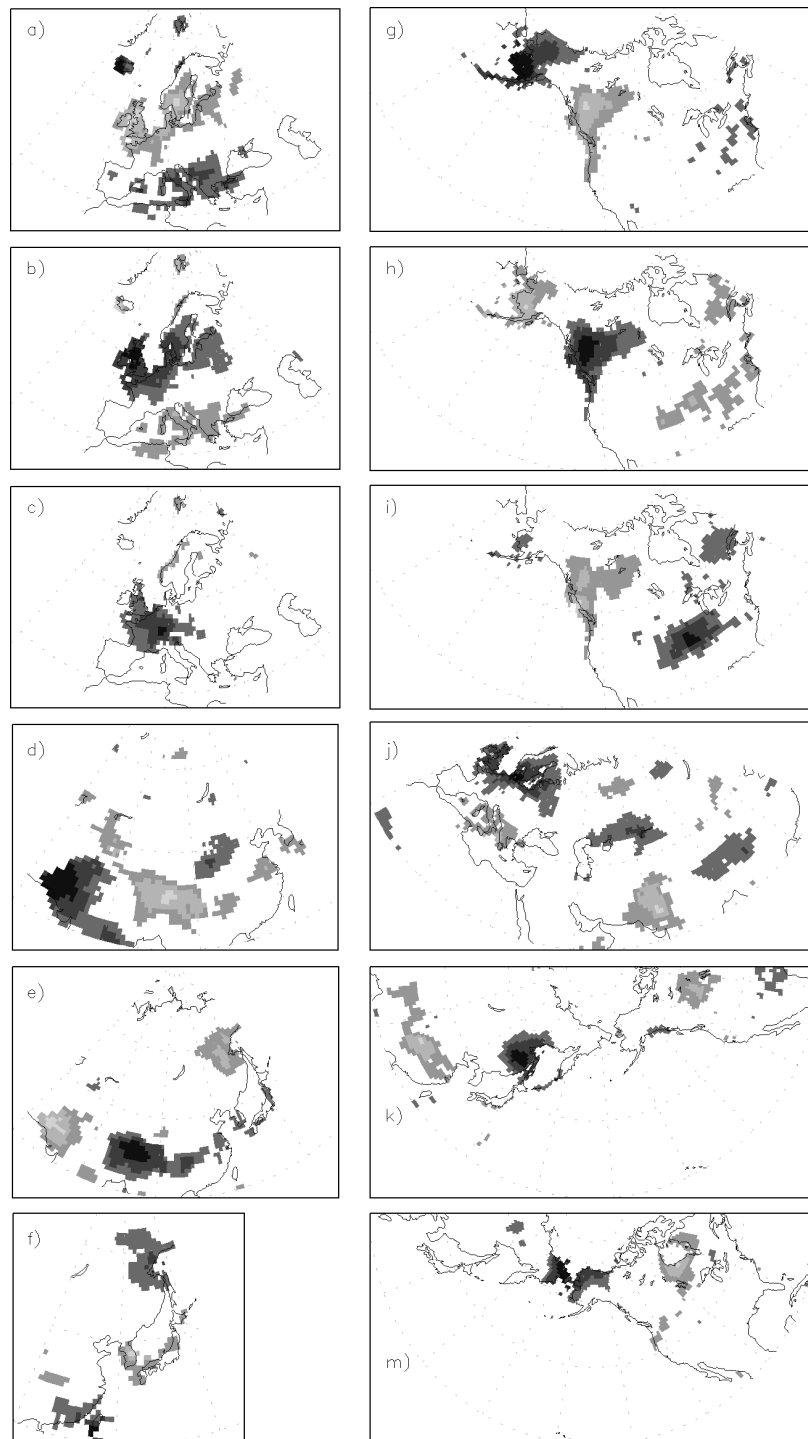


Figure 2.3. Regional SPI correlation maps. Shading is for -0.65 , -0.5 and -0.3 (light), 0.3 , 0.5 and 0.8 (dark). No color is further assigned to missing values (due to failed SPI-fits, especially in dry summer climates). The negative correlations in panel c) stretch along the north-west coast of Norway. In panel f) the primary centre is at the southern tip of Taiwan. For details see section 2.3.

2.3 Teleconnectivity and teleconnection patterns

last panel of Figure 2.3 shows the relationship of the larger Hudson Bay area with northern Alaska and the Chukchi Peninsula. In addition, the Aleutian Islands, the larger Alaska Range and weaker the Brooks Range are correlated with southern Canada from the Pacific coast across the Rocky Mountains and inland to Saskatchewan (Figure 2.3g,h). This region in turn correlates negatively with the larger Midwest of the US, which subsequently is co-varying with approximately the Canadian province of Quebec.

A multitude of correlated areas exist over the Asian continent from 20°N northwards. First, Figure 2.3j displays the downstream relation from central Europe to the Indus river basin and the western flank of the Himalaya Range and in turn to the Tibetan Plateau. The dipole between Indus basin and eastern Tibetan Plateau is more detailed visible in Figure 2.3d. Centred on the Plateau (Figure 2.3e) the upper Yangtze basin is additionally positive correlated, and roughly the eastern part of the Amur basin appears anti-correlated. The middle and lower reaches of the Yangtze display coherence with the Amur and Okhotsk High region. A secondary pole is found over central Canada (Figure 2.3k) and even down to the coast of the Gulf of Mexico.

These patterns also arise in the first loadings of a PC-analysis for the northern hemispheric SPI field (not shown), where the first loading includes nearly all mentioned centres, and the Hudson Bay/Chukchi Peninsula feature is found as part of the fourth loading. The third PC pattern shows inter alia the Alaska/Canada/Midwest US link.

Correlations Next, correlations are presented of the extratropical northern hemispheric summer SPI-3 field with large-scale oceanic and atmospheric circulation pattern indices. Prior to that, correlations are mentioned of principal components with these indices (not shown). The first PC simultaneously correlates negatively with the AO, the EAWR and the SCA pattern indices. The greatest relationship is found with the NAO with the correlation coefficient exceeding an absolute value of 0.7. None of the other PCs reach a similar level. PC2 shows simultaneous correlations with the AO, the Polar Eurasian pattern index (POL) and all considered NINO indices (all values ~ 0.4). The third PC shows absolute correlation values from 0.3 to 0.4 with EA, SCA, POL and the NINO4 index, but correlates strongest at 0.57 with the EPNP series. PC4 correlates further with the EA-pattern index (~ 0.4). Variances attributed to the PC loadings put the correlation coefficients into perspective, as the first four principal components account only for about 23 percent of variance (7.15%, 5.95%, 5.48% and 5.00%, respectively).

The indications given by the loading correlations are substantiated by correlations between the summer SPI-3 field and 'teleconnection' indices (Figure 2.4). Especially the relationship of the NAO time series and the field corresponds well with the teleconnectivity patterns described above. All European centres are resolved, and strong covariance is found in the Indus basin (compare Fowler and Archer, 2005), on the eastern Tibetan Plateau (compare Liu and Yin, 2001) and in the region around the Sea of

2 Teleconnections of the northern hemisphere SPI field in boreal summer

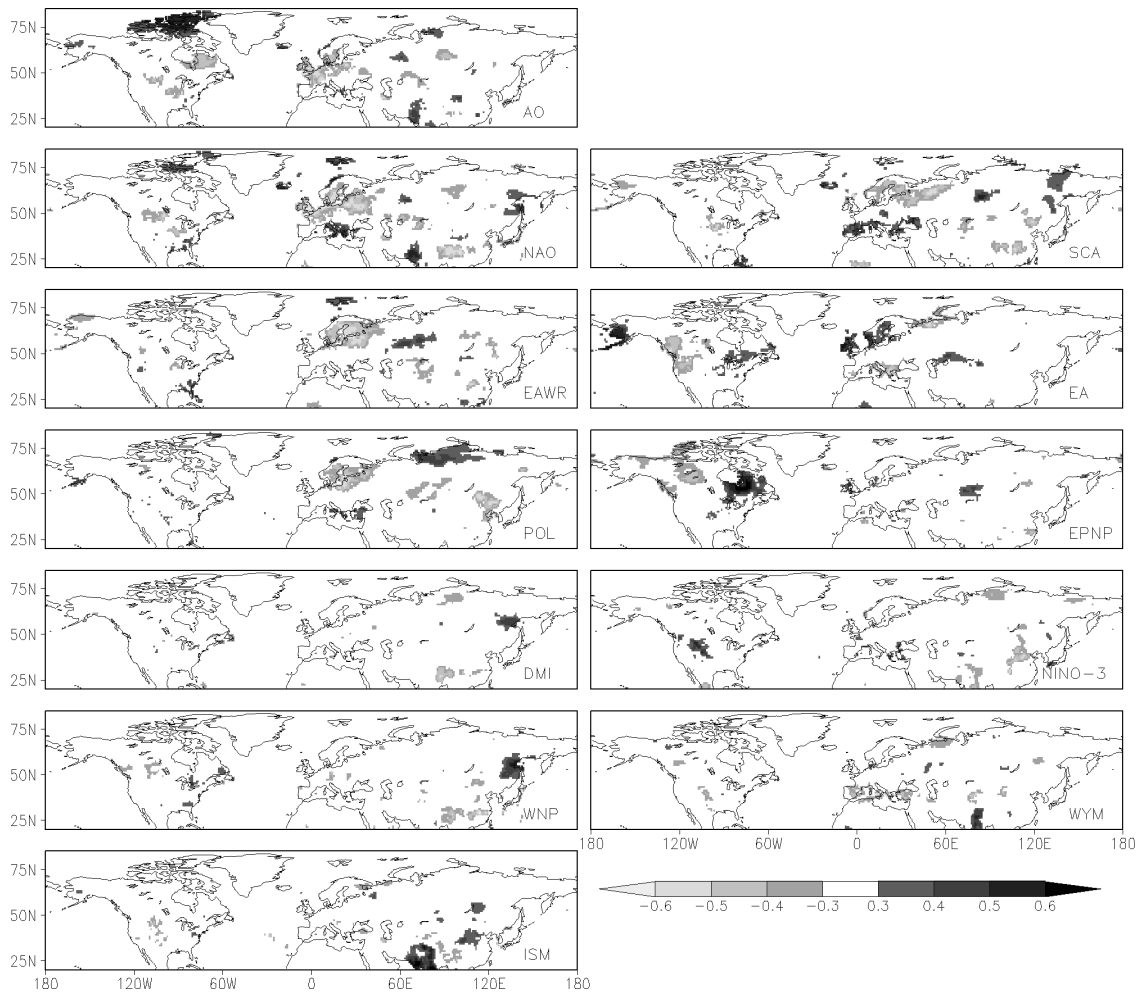


Figure 2.4. Correlation maps of teleconnection and monsoon indices with the northern hemispheric summer SPI field.

Okhotsk. The AO correlations, and weaker those with the seasonally varying northern hemisphere annular mode (not shown, Ogi et al., 2004), capture the teleconnectivity map between central Europe and the west coast of Norway (Figure 2.3c). Additional positive signatures are found in the Canadian Arctic and Pakistan. The indices for SCA, EAWR, EA and POL all correlate to some extent with northern Europe and the Mediterranean with further features east (EA) and north-east (EAWR) of the Caspian Sea, in northern Eurasia (POL) and in the Yangtze basin (SCA). The EA index further correlates with southern Alaska and the north American east coast. Notable opposite correlations in eastern Canada and central Canada arise with the EPNP index. Not displayed are the correlations for the PNA index with central Eurasia and the WP index with northern Canada and the Kamchatka Peninsula. Considering the sea surface temperature indices, the El Niño region 3 (similar for the other NINO regions) correlates negatively

2.4 Asian precipitation and teleconnections: 1951-2000

with northern China and parts of the north-east coast of the Arabian Sea. The Indian Ocean Dipole Mode index (IOD DMI) displays coherence with the Okhotsk Sea coast and the south-eastern ranges of the Tibetan Plateau and the Himalaya Range.

The monsoon circulations have to be considered in the Asian regions. The Indian summer monsoon index correlates highly positive with the Indus region but displays also coherence with northern China. Furthermore, the western north Pacific monsoon (WNP) index shows correlations with the Okhotsk area and the Yangtze river basin from the Tibetan Plateau to the delta. The Webster and Yang monsoon index (compare for all indices Wang and Fan, 1999; Wang et al., 2001) co-varies with the north-west coast of the Bay of Bengal up to the Himalayas, and some significant correlations arise in southern Europe as well (possibly related to the monsoon-desert-mechanism, Rodwell and Hoskins, 1996).

2.4 Asian precipitation and teleconnections: 1951-2000

Asian precipitation, from the Arabian Sea to the East China Sea, is found to be correlated to various common atmospheric and oceanic teleconnection indices. The following specifies, with respect to certain regions, the covariability of standardised summer precipitation and the indices. Three regions are included, which emerge as highly interdependent in the previous section: the Indus river basin, the Tibetan Plateau and the Yangtze river basin. The latter is considered as a whole, but also subdivided in upper and lower reaches (compare Figure 2.1). Area averaged precipitation is employed in the standardised form of the SPI. While, obviously, not always the simultaneous correlations are most significant, the window correlation analyses concentrate on the concurrent summer to identify the coexistent influences on precipitation. Lagged correlations remain for future discussion. Appendix B presents supplementary information on running window means and window variances and the index and SPI time series.

2.4.1 Summer time series

Before the moving window correlations are discussed, the SPI (Figures 2.5, B.1, B.2 and B.4) and index time series (Figures 2.6 to 2.8, and B.1, B.2 and B.5) are shortly referred to.

Regional summer SPI-3 The Indus SPI series displays a reduction in dry and an increase in severe wet summers in the last 25 years (e.g. Figure 2.5). A weak trend is visible in its mean. It is significantly reduced in the beginning and increased at the end. The variance of the Tibetan Plateau summer SPI is significantly enlarged in the last windows due to increased wetness from 1998 to 2000. Overall a reduction of “normal” conditions is found between the 1961-window and the 1990-window. The summer

2 Teleconnections of the northern hemisphere SPI field in boreal summer

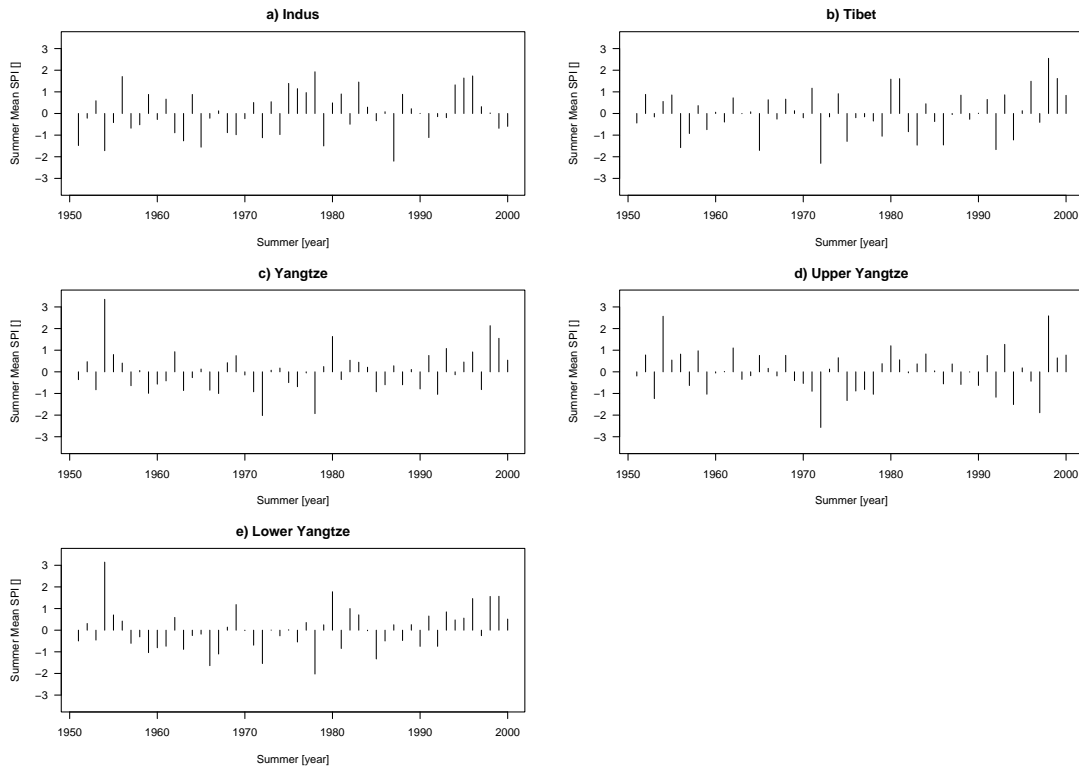


Figure 2.5. Summer SPI-3 time series for area averaged precipitation: a) Indus, b) Tibetan Plateau, c) whole Yangtze basin, d) upper Yangtze reaches, e) lower Yangtze reaches.

SPI-3 time series averaged over the whole domain of the Yangtze catchment displays a number of distinct shifts, or even an oscillating behaviour. The time series exhibits a reduction of normal conditions with slightly more wetness in the later years, while the basin experiences drier conditions in the middle of the second half of the last century. The variance is most notably reduced in the late 1960s. For the upper Yangtze reaches, normal conditions are reduced in later windows. A few more severe and extreme events are found for dryness and wetness. The lower reaches SPI series indicates a drier period in the middle of the second half of the 20th century and slightly wetter conditions in the 1990s (compare Ding et al., 2008). The mean is reduced significantly in the late 1960s and displays a sharp increase in the late 20th century windows.

Monsoon indices For the Indian Summer monsoon index, a SPI-like classification in normal, severe and extreme conditions displays, that the early and late decades are “normal”, while more extreme values occur in-between (e.g. Figure 2.6). ISM variance is enhanced in the 1960s and 1970s. Early and late decades, for the Western North Pacific monsoon index, experience more negative index-summers, while the number of large positive episodes is nearly constant considering the decades from 1951 to 2000.

2.4 Asian precipitation and teleconnections: 1951-2000

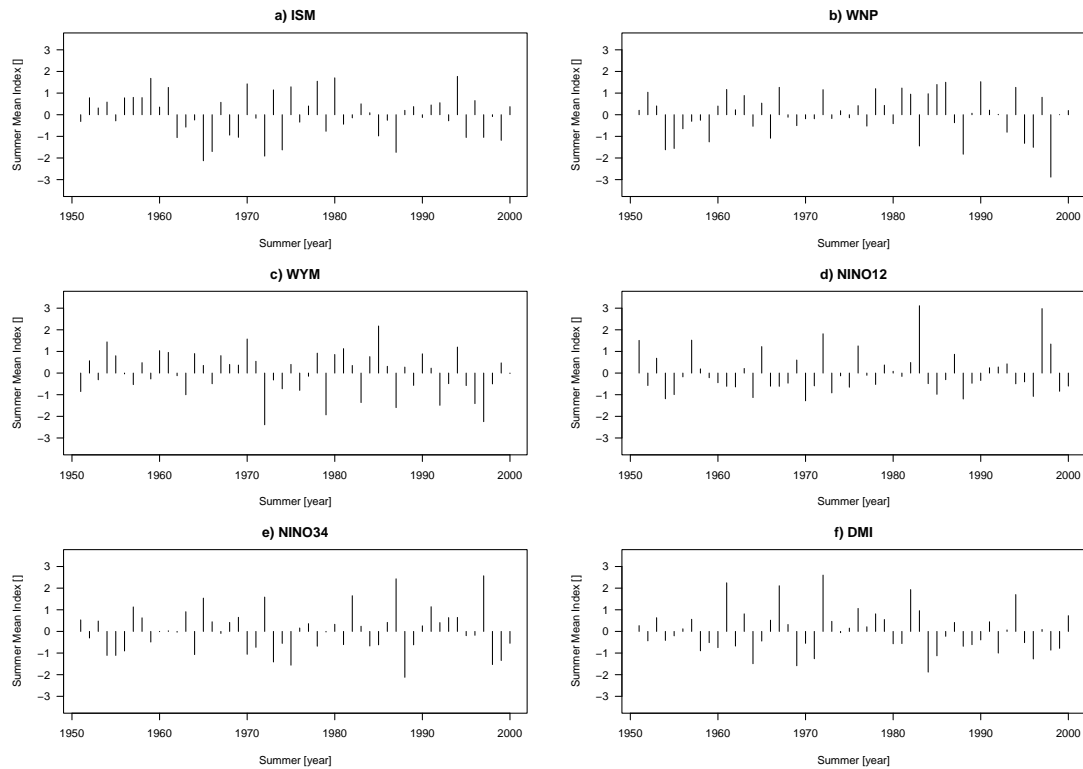


Figure 2.6. Summer mean monsoon and SST-index time series: a) Indian summer monsoon, b) Western North Pacific monsoon, c) Webster and Yang monsoon index, d) NINO12 index, e) NINO34 index, f) Indian Ocean Dipole Mode index.

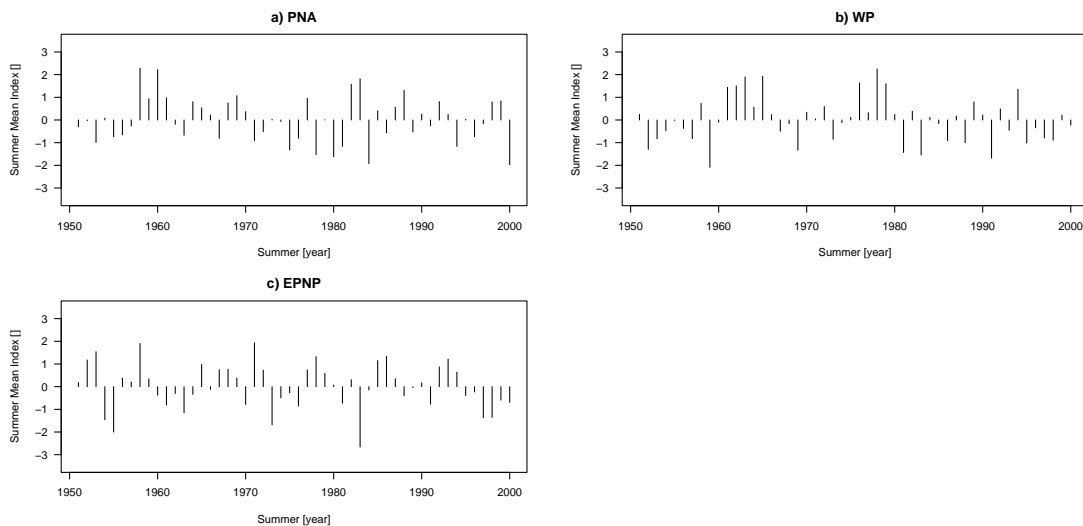


Figure 2.7. Summer mean atmospheric indices: a) Pacific/North American pattern, b) West Pacific pattern, c) East Pacific/North Pacific pattern.

2 Teleconnections of the northern hemisphere SPI field in boreal summer

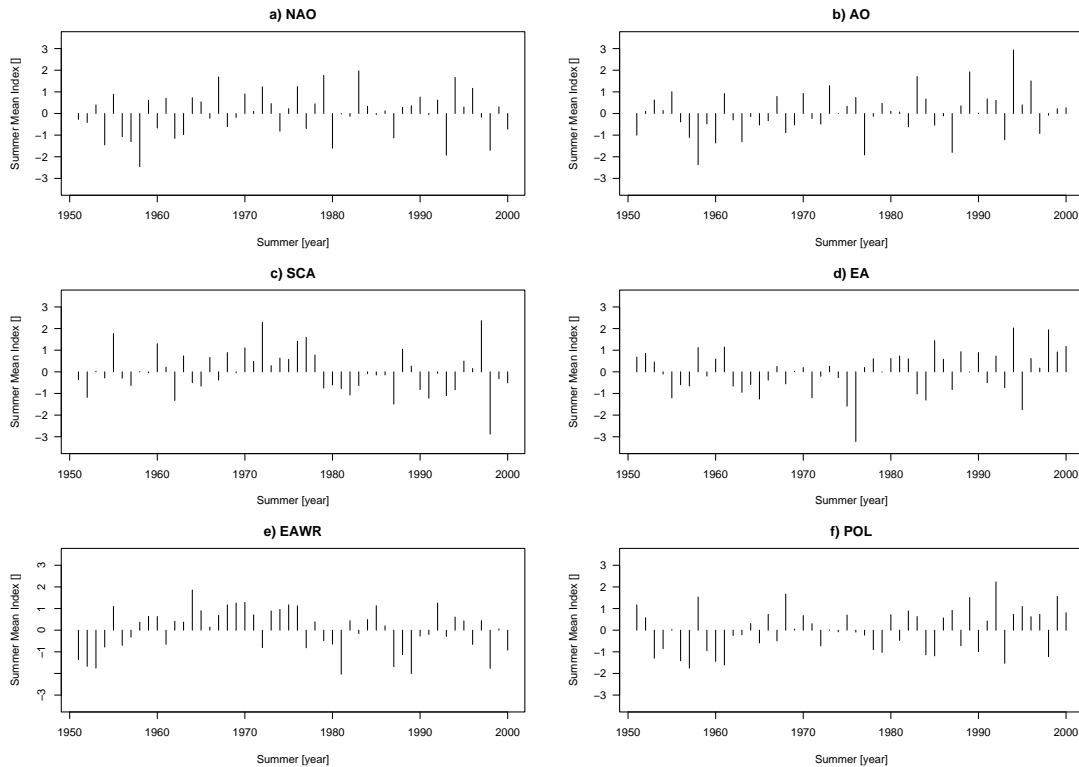


Figure 2.8. Summer mean atmospheric indices: a) North Atlantic Oscillation, b) Arctic Oscillation, c) Scandinavia pattern, d) East Atlantic pattern, e) East Atlantic/Western Russia pattern, f) Polar/Eurasia pattern.

“Normal” conditions are reduced in the last twenty years. WNP-variance shows a steep increase and its mean is slightly enhanced in the 1970s and 1980s. In the Webster and Yang index larger absolute values and more negative WYM-episodes occur in the later decades. Its variance increases continuously but not as steep as for the WNP.

Teleconnection pattern indices An increase of the NINO12-index mean can be easily attributed to the strong El Niño events of 1982/1983 and 1997/1998 (e.g. Figure 2.6). A decrease reflects the period with lower temperatures in-between. Distributions are nearly unchanged considering a SPI-like classification. A bias may be imprinted to the IOD DMI variance by the three large positive episodes in 1961, 1967 and 1972.

For the PNA, “normal” conditions are reduced in the late 20th century, when the WP displays more “normal” conditions (e.g. Figure 2.7). The WP mean is strongly enhanced in the 1960s to 1970s. The NAO mean is higher since approximately 1970 (e.g. Figure 2.8). Late decades higher AO-variance is due to an “extreme” summer value in 1994 and further positive events in 1995 and 1996. The window means increase for the AO. For the SCA, slightly fewer “normal” conditions are found in the late 20th century. A jump in

variance is related to a strong positive SCA episode in 1997 and a strong negative one in 1998. The mean is enhanced in the early windows and strongly reduced in the late windows. The EA-variance development represents an “extreme” negative summer in 1976 and generally enhanced variability in the 1990s. Then, its mean is strongly increased. EAWR mean and variance reflect different periods in the EAWR in the 20th century: (i) the early 1950s (strongly negative), (ii) late 1950s to late 1970s (mostly positive), (iii) the 1980s (at first negative, then “normal”, then again strongly negative), (iv) the 1990s with alternating positive and negative summers. More negative summer episodes are seen at the end of the century. The POL-variance is notably reduced in the mid of the second half of the 20th century, and a trend is seen in the mean.

2.4.2 SPI covariability in Asia along 30°N: Moving window correlations

Indus river catchment The Indus river catchment partially overlaps with the regions used to compute the Indian summer monsoon index (Wang and Fan, 1999) and the All-India rainfall series (AIR, Parthasarathy et al., 1994). While the summer monsoon moisture transport through and from the Arabian Sea is a major influence on the basin, it is not necessarily a part of the Asian summer monsoon region (see Wang and Ho, 2002).

In Figure 2.9 persistent significant positive correlations are displayed between the area averaged precipitation time series for the Indus catchment in terms of the three-monthly summer SPI and the Indian summer monsoon index (ISM). Slightly higher coefficients are found between 1966 and 1984 (where dates refer to the year the correlation-window is centred). Similar large but negative correlations are found for the NINO34-index. The largest correlation occurs for the window centred about 1965. The correlation becomes insignificant in the last windows. NINO12-index, Webster and Yang monsoon index (WYM) and the Pacific/North America pattern index (PNA) show only sporadic correlations as do the North Atlantic Oscillation index (NAO) and the Arctic Oscillation index (AO). The latter gains significance in the last windows; the AO correlation coefficient increases continually from the early 1980s. In the mid-1980s additionally the Scandinavia pattern index (SCA) becomes significantly positive correlated with the Indus catchment summer SPI-3. Coefficients decrease approaching 1990.

If the full 50 year period from 1951 to 2000 is considered, the Indus basin summer SPI is significantly correlated with ISM, NAO, AO (positive) and NINO34 (negative). Correlations are largest with the ISM, NINO34 and the AO. Only the transitions of the correlations with the SCA seem conspicuous.

Changes in correlation coefficients may be related to differing changes in mean or variance of the correlated time series. A contrary development of the variance is seen for ISM and Indus basin SPI-3 in the last third of the studied period. This coincides with a reduction in the correlation. Tendencies of the means resemble each other. Similarly the short correlated periods with the WYM are found in periods with coherent variance

2 Teleconnections of the northern hemisphere SPI field in boreal summer

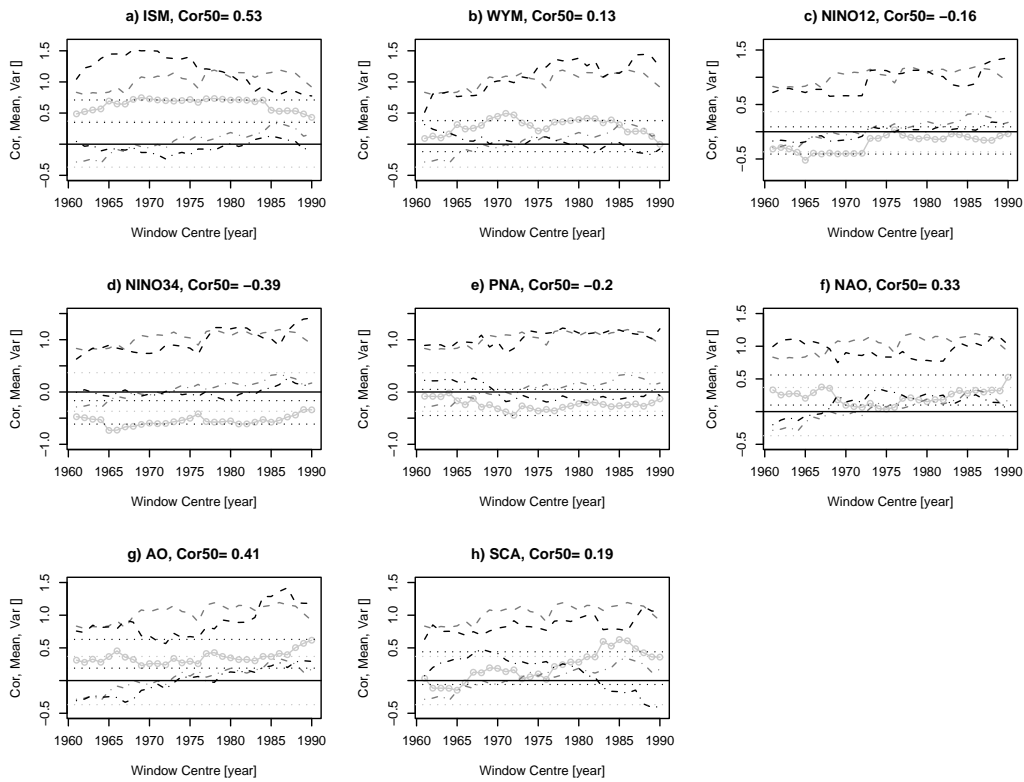


Figure 2.9. Indus basin summer SPI covariability 1951 to 2000: a) ISM, b) WYM, c) NINO12, d) NINO34, e) PNA, f) NAO, g) AO, h) SCA. Plotted are moving window correlations (line-points), moving variances (dashed lines), moving means (dash dotted, SPI-means and variances, grey, index means and variances, black). Horizontal lines are t-test significances (90% level, grey dotted) and bootstrap estimates of correlation variability (95%, black dotted). Indices are considered, for which a significant (t-test) correlation is found in at least one window.

behaviour. The NINO12-relation is mostly affected by a notable change in variance and mean of the NINO12-index in the early 1970s, which, however, is not significant. A similar shift occurs in the variance of the SPI-3 some years earlier. The NINO34-series shifts even later concurrent with a second change in SPI-3-variance. The correlation becomes insignificant as the time series develop oppositely in the last windows of the 20th century. While AO and Indus-SPI-3 means are more or less parallel from the window centred about 1970 onwards, they greatly differ in the evolution of their variances. A notable shift is visible in the SCA-variance in the early 1980s concurrent with a period of significant correlations between the SCA and Indus-SPI-3.

Tibetan Plateau Although the Tibetan Plateau resides in the Asian monsoon region, common monsoon indices show only little coherence with the Plateau summer SPI-3 (Figure 2.10). ISM and Plateau SPI-3 are uncorrelated. However, the sliding correlation

2.4 Asian precipitation and teleconnections: 1951-2000

time series follow the index series of WNP and WYM. The WNP is for some windows negatively correlated, the WYM occasionally positive. The WYM correlation is seen from 1971 to 1981, when the WNP correlation is not significant, while from 1988 to 1990 the situation is converse with the WNP correlating significantly and the WYM uncorrelated. The relation between NINO12 and Plateau precipitation is almost continuously weakening, and the NINO34 shows coherence only in the early 1960s and from 1988 to 1990. The Plateau SPI-3 is significantly negative correlated with the Indian Ocean Dipole Mode index (IOD DMI, DMI in the following, Saji et al., 1999) for most 21 year windows. A maximum negative correlation arises about 1980. Correlations with atmospheric teleconnection pattern time series in the Pacific display almost no coherence. Contrastingly, the SPI-3 series displays strong negative coherence with the NAO after the mid-1960s. The correlations with the East Atlantic/West Russia pattern index (EAWR) and the Polar Transition pattern index (POL) show a change from slight positive correlations to weak negative ones from the 1960s to the late 1980s.

50-year-correlations for the Tibetan Plateau SPI-3 are significant with WNP, NINO12, NINO34, DMI, NAO, EAWR (negative) and WYM (positive). Largest absolute coefficients are found with DMI and NAO. The window-correlations with POL and EAWR vary too much when compared to the bootstrap estimates.

Mean and variance of Tibetan Plateau SPI-3 and the WNP are relatively parallel for most of the studied period. The largest correlation in the late 20th century is related to a large shift in both variances. The relationship to the WYM is characterised by periodical near parallelism of means and variances. The shift in the variance of the NINO12-series in the early 1970s (centre of window) has no larger impact on the correlation with the Plateau SPI-3. The correlation becomes insignificant with further shifts in variance in the early and mid 1980s windows. The link of NINO12 and Tibetan Plateau SPI-3 is dominated by the cooccurrence of dryness relative to the years before and after an El Niño (compare Figure 2.5 and 2.6). In the 1990s a shift in NINO12-variance precedes a similar one in the SPI-3 series, while in the 1970s the NINO12-variance seems to lag the SPI-3. The large changes in the relationship of SPI-3 on the Plateau and the DMI can both be referred to changes in DMI variance. The NAO-Tibet-relation becomes significantly negative with a change of variance and mean in the NAO series in the late 1960s (window centre). Both series develop approximately as mirror images of one another from then onwards. EAWR and Tibetan SPI-3 show significant covariability after large changes in mean and variance of the EAWR-series from 1976 to 1981 (window centre). The evolution from significant positive to negative correlations between the Plateau and POL are visible not only in both time series (Figures 2.5 and 2.8) but also in the changes of mean and variance. Parallelism in mean and variance for the first ten windows is replaced by mirror-wise behavior changing back to near parallelism.

2 Teleconnections of the northern hemisphere SPI field in boreal summer

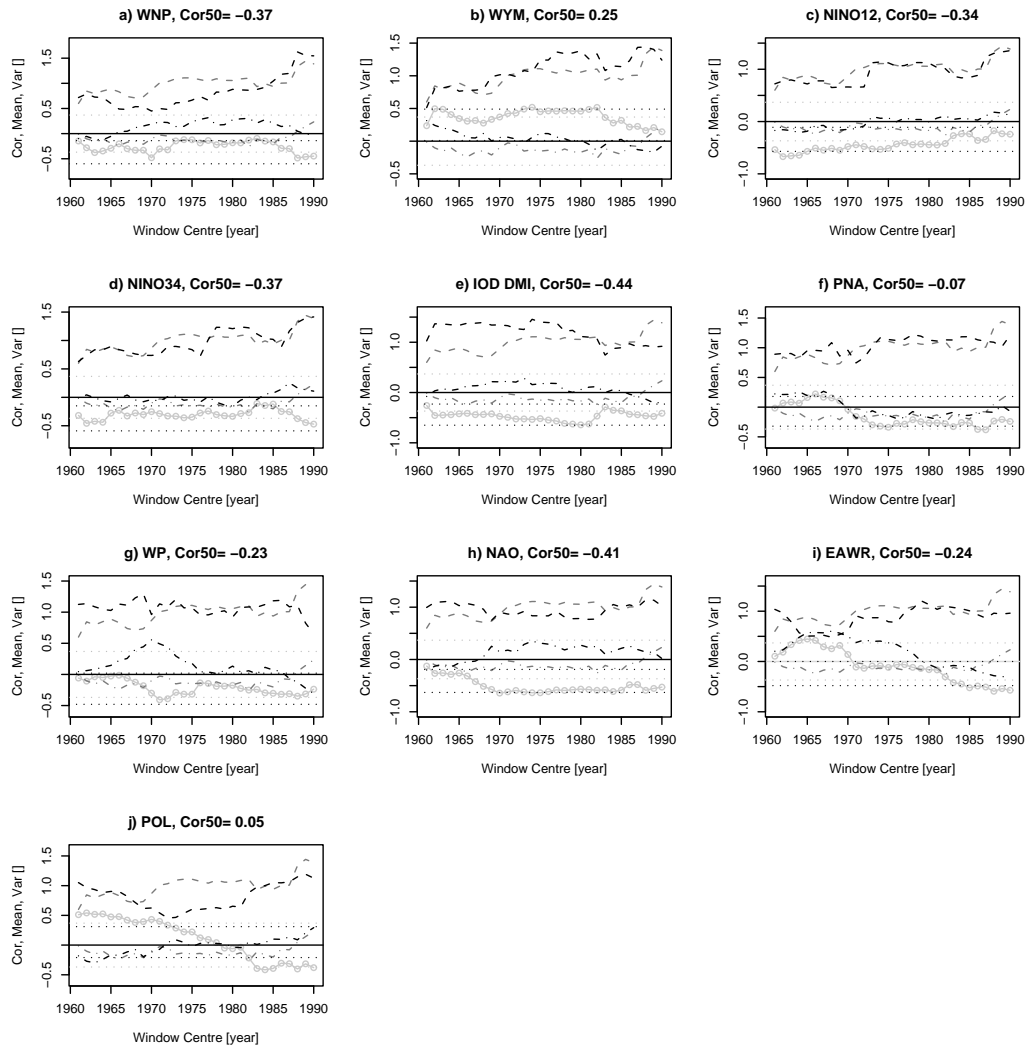


Figure 2.10. Tibetan Plateau summer SPI covariability 1951 to 2000: a) WNP, b) WYM, c) NINO12, d) NINO34, e) DMI, f) PNA, g) WP, h) NAO, i) EAWR, j) POL. Moving window correlations (line-points), variances (dashed), means (dash-dotted, SPI-means and variances, grey, index means and variances, black). Horizontal lines: t-test significances (90% level, grey dotted), bootstrap estimates of correlation variability (95%, black dotted).

The upper Yangtze catchment The upper Yangtze catchment overlaps in its source region with the Tibetan Plateau. The further course of the river down to Wuhan can be seen as part of the east Asian summer monsoon region. However, it is described more accurately as a transitional region from pure non-monsoon to pure monsoonal. This view is confirmed by weak correlations with the monsoon indices. Noteworthy are negative coherence with the WNP in the late 20th century and positive coherence in the early sixties (centre of window) with the WYM. This corresponds to negative correlations in the early sixties with NINO12. The DMI displays negative correlations for a period in the 1970s and 1980s. Again only a faint Pacific atmospheric influence is found. The correlation with the West Pacific pattern index (WP) in the mid-1980s is the most significant. Correlations with the NAO undergo obvious changes. They are significantly negative in the early and late periods of the studied era and become insignificant in-between. The SCA has an correlative influence nearly throughout the second half of the 20th century but with fluctuations. Weak correlations with EAWR and POL exist in the late 20th century.

Over the full second half of the 20th century the upper Yangtze SPI-3 series is significantly correlated with WNP, NINO34, DMI, EPNP, NAO, SCA (negative) and WYM (weak positive). Largest correlations are found for NAO and SCA. Conspicuous is again the development of the correlation with the EAWR. Changes in WYM, NINO12 and POL relations are not easily explained.

Negative upper Yangtze SPI-3 coherence with the ISM in the window from 1973 to 1993 may be attributed to mirror image development from 1991 to 1994. Late 20th century negative correlations with the WNP are linked with concurrent shifts in variance and mirrored shifts in the respective means. The shift in variance of the WNP is larger than that of the SPI-3. Changes in the WYM variance affect upper Yangtze precipitation early in the second half of the 20th century. Significant coherency vanishes with strong changes in the WYM about 1970. Correlations with the NINO12 index are significant only for a short period centred in the 1960s, when variances and means are slightly coherent. While upper Yangtze SPI-3 and DMI variances and means show similar development, their correlations are significant only from the early 1970s to the early 1980s (window centre). The correlation becomes insignificant with a coherent change in both variances and, following that, a change in the development of the SPI-3 series. NAO and SPI-3 are significantly negative correlated in the beginning and at the end of the studied period with substantial changes throughout. In-between the means develop parallel, thus the negative coherence is broken. The EAWR displays strong variations in variance throughout the second half of the 20th century, while its mean decreases nearly continuously with subsequent significantly negative correlations.

2 Teleconnections of the northern hemisphere SPI field in boreal summer

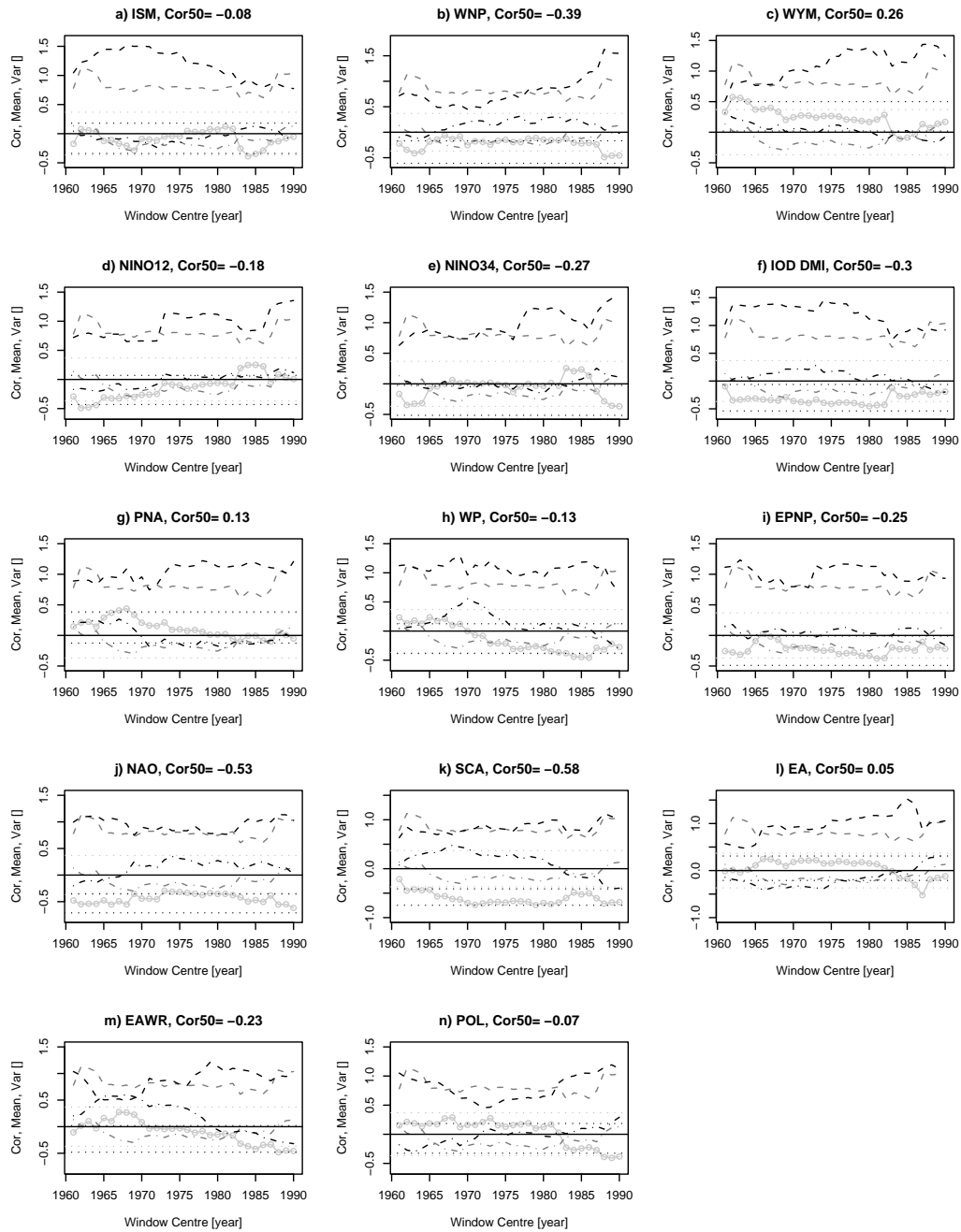


Figure 2.11. Upper Yangtze reaches summer SPI covariability 1951 to 2000: a) ISM, b) WNP, c) WYM, d) NINO12, e) NINO34, f) DMI, g) PNA, h) WP, i) EPNP, j) NAO, k) SCA, l) EA, m) EAWR, n) POL. Plotted are moving window correlations (line-points), moving variances (dashed), moving means (dash dotted, SPI-means and variances, grey, index means and variances, black). Horizontal lines are t-test significances (90% level, grey dotted) and bootstrap estimates of correlation variability (95%, black dotted).

The lower Yangtze catchment Due to the employed 1° resolution of the precipitation data and differences between its grid and the river-streamflow-mask, a clear differentiation is not possible between upper and lower Yangtze river catchments at their interface. Thus, single interface grid points may be simultaneously referred to as upper and lower Yangtze. A weak positive correlation with the WYM is found for the early 1960s for the summer SPI-3 in the lower catchment of the Yangtze. Correlations with the WNP are slightly significant and negative for nearly all windows of the 50 year period. All three SST-indices show a progressive change from negative to positive correlations. The NINO34-index coherence changes from negative and weakly significant to slightly significant positive correlations and subsequently nearly reverses. The DMI is significantly negative correlated up to the early 1970s. Afterwards coherence is diminished. The SCA is slightly coherent in most of the windows. In addition, positive correlations are noteworthy with the POL in the 1970s and early 1980s.

Lower Yangtze reaches correlations are significantly negative for WNP, DMI, EPNP, NAO and SCA using all 50 years. Coherence is unsurprisingly largest with the WNP. Variations in EAWR, POL, WYM and the SST indices are conspicuous. Especially the EAWR variance and the lower Yangtze SPI show dependence on a common impact for windows centred in the late 1960s. Note that correlations with EPNP and WNP calculated for the whole Yangtze (see Figure B.3) are larger than for the both sub-catchments.

The nearly continuous negative correlation of the lower Yangtze SPI-3 and the WNP becomes insignificant in the late 1960s after a drop in SPI-3 variance. Later the variance gains previous levels. Differently, the relation to the WYM does not recover after a decreasing period in the WYM-mean. The NINO34 correlation strongly varies because of large shifts in both variances and a continuous wetting of the lower Yangtze catchment, that also contributes to the reduction in the coherence with the DMI. A weak relationship exists with the SCA from the 1970s after the change in SPI-3-variance. This is disturbed in the late 1980s (window centre) by a sudden increase in SCA-variance. The SCA-mean decreases from the late 1960s onwards. Positive correlations exist with the POL index from the early 1970s to the early 1980s, when both time series develop parallel.

2.5 Summary

The northern hemispheric summer SPI is studied over land with respect to its covariability with its field and with common teleconnection indices. A number of covariability patterns arise on all northern hemispheric landmasses. The most prominent feature is an obvious mutual interdependence of standardised precipitation in the Indus, Yangtze and Amur river basins and on the Tibetan Plateau. Links are further identified downstream to north America and upstream to Europe and the north Atlantic.

The analysis of coherence of the summer SPI field with teleconnection indices ex-

2 Teleconnections of the northern hemisphere SPI field in boreal summer

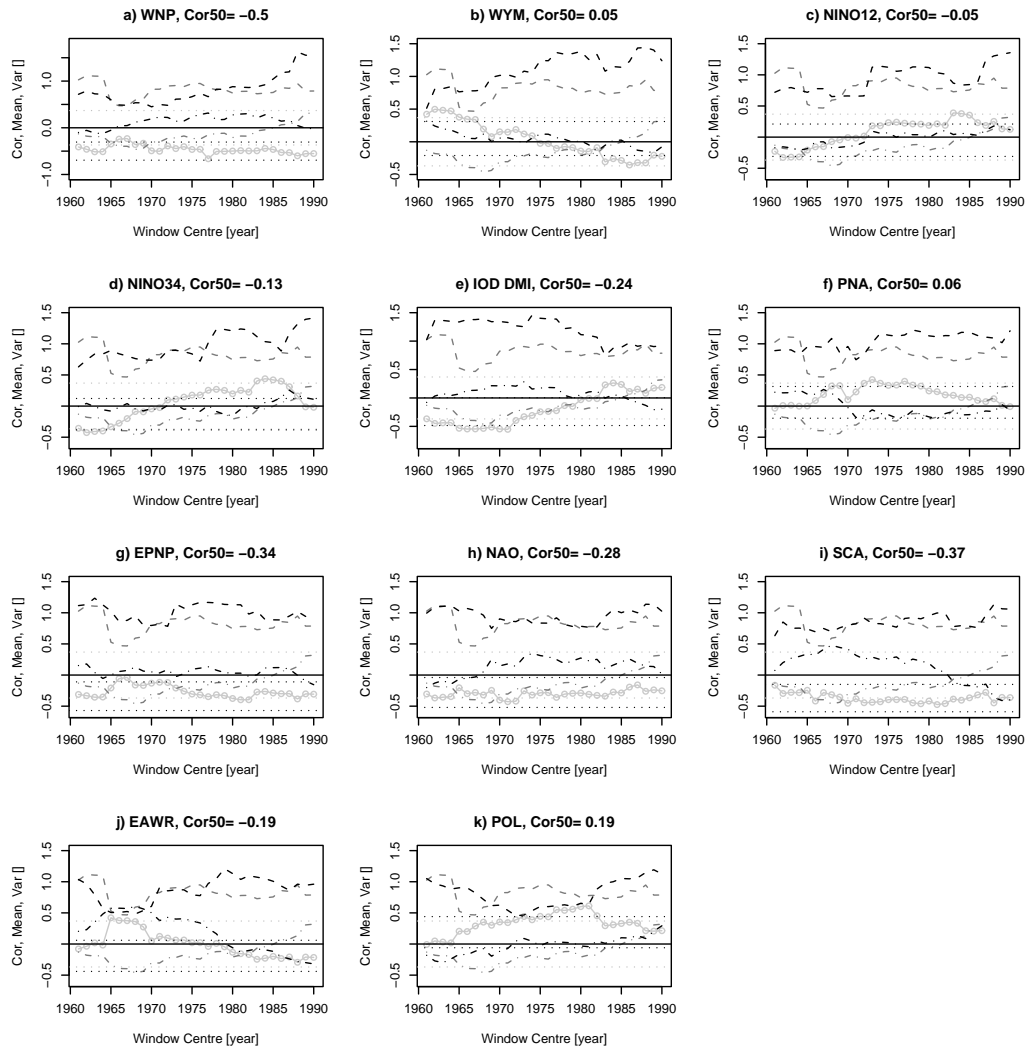


Figure 2.12. Lower Yangtze reaches summer SPI covariability 1951 to 2000: a) WNP, b) WYM, c) NINO12, d) NINO34, e) DMI, f) PNA, g) EPNP, h) NAO, i) SCA, j) EAWR, k) POL. Plotted are moving window correlations (line-points), moving variances (dashed), moving means (dash dotted), SPI-means and variances, grey, index means and variances, black). Horizontal lines are t-test significances (90% level, grey dotted) and bootstrap estimates of correlation variability (95%, black dotted).

hibits strong covariability with the North Atlantic Oscillation, the Arctic Oscillation and the Scandinavia pattern for the Tibetan Plateau, the Yangtze basin and the Indus catchment. The SCA primarily correlates with the larger Yangtze region. El Niño is found to influence parts of India and Pakistan, while the Indian Ocean Dipole Mode index is coherent with parts of the Tibetan Plateau. Considering monsoon indices, the unsurprising results are, that the western north Pacific monsoon influences east China and the Indian monsoon India and Pakistan and weakly the Tibetan Plateau. The Webster and Yang index co-varies with the area to the north-west of the Bay of Bengal up to the Yangtze basin and the Tibetan Plateau.

Moving window correlations of standardised area averaged precipitation are utilised to resolve possible changes in covariability of the regional precipitation and their teleconnections. For single regions the following is noteworthy:

In the Indus catchment the primary influence is the Indian summer monsoon, but variances develop contrary in the late 20th century. Large negative correlations are seen with the NINO34-index. Only in the last years of the 20th century, the coherence becomes insignificant. The influence, in terms of correlations, of the AO increases from the early 1980s. Then the variances of Indus-SPI and AO change similar to one another.

On the Tibetan Plateau, only weak coherence is found with the monsoon indices. While no definite signal is visible for the NINO-indices, the IOD DMI is mostly significant negative correlated with the Plateau precipitation. NAO and the Plateau are strongly coherent from about 1970. Variability of the DMI-Plateau-link is due to changes in DMI-variance. The onset of NAO-coherence relates to changes in variance and mean of the NAO.

The upper Yangtze reaches are only weakly coherent with the monsoon indices as well. Over all, due to the decadal variability of precipitation in eastern Asia, correlations to all indices show strong changes. Most notable is the coherence with the NAO in early and late decades, in-between no correlations are significant when the means vary parallel. The Scandinavia pattern is the sole index significantly co-varying nearly throughout the period from 1951 to 2000. The western north Pacific monsoon impacts the lower Yangtze reaches nearly continuously. The link to the SST-indices is strongly changing. A weak influence is further identified for the SCA.

This assessment of change in the relation of precipitation in Asia and atmospheric and oceanic modes and patterns fails to identify possible act and response relationships. However, results systematically detail the change of variance and mean in the considered teleconnection indices and the regional summer SPI series and in the covariance of both. The possible stochastic variability is considered as well. The principle conclusion can possibly follow Archer and Fowler (2004) who state, that the amount of covariability is not enough to be applicable in water resources management, which is further hampered by the strong variability of relationships between precipitation and indices.

3 Central Asian precipitation – the upstream zonal wind structure

Abstract

Precipitation in central Asia is subject to the annual cycle of the westerly jet. The annual cycle of precipitation in large areas can be directly attributed to the transition of the jet northwards and its retreat relative to the solar insolation. The importance of calendar monthly variability of the zonal wind structure on downstream regional precipitation is studied for a zonally averaged section between 50° and 65°E. The considered region is a rectangular box around the Tian Shan, which is subdivided into drainage areas to the south into the Tarim river basin, the north-west and the north-east. In addition, the Tibetan Plateau is included to evaluate the dependence of Plateau precipitation on the upstream zonal wind. While detected remote relations warrant the assumption that the precipitation variability partially is explained by the westerly inflow to the larger Himalaya region, it is not feasible to base a predictability study on the results.

3.1 Introduction

Atmospheric flow climatologies for Asia show the prominent seasonal cycle of the zonal wind fields (e.g. Academia Sinica, 1957; Schiemann et al., 2009; Hahn and Manabe, 1975; Lau and Li, 1984). The shifts of the westerly wind maximum to the north from winter to summer and back in autumn follow the seasonal cycle of insolation and surface and tropospheric temperatures. In particular the elevated heat source of the Tibetan Plateau alters the meridional gradient of tropospheric temperatures (e.g. Duan and Wu, 2005; Hsu and Liu, 2003). The Iranian Plateau affects the atmosphere in a similar manner further to the west (Zhang et al., 2002). Thus, an elementary explanation of the seasonal cycle of the westerlies can be achieved via the thermal wind relation. The Tibetan Plateau also functions as a mechanical barrier (e.g. Academia Sinica, 1958; Hahn and Manabe, 1975). Kuang and Zhang (2005) describe the dependence of the seasonal variation of the westerly flow over east Asia on the heating structure, and members of the Academia Sinica (1957) depict the zonal wind structure in east Asia based on aerological data from the 1950s.

The shift of the jet is an important factor in the development of the Asian monsoon

3 Central Asian precipitation – the upstream zonal wind structure

systems. Especially the development of the east Asian monsoon's Meiyu-Baiu frontal system is influenced by the changed circumflow around the Asian orography (Academia Sinica, 1957, 1958; Zhou et al., 2004; Liu et al., 2007; Frisius et al., 2009). Sampe and Xie (2009) describe the influence of temperature advection from the Tibetan Plateau on the development of the Meiyu-Baiu rainband of central China and Japan.

Furthermore the seasonal cycles of central Asian precipitation are dominated by the seasonal cycle of the jet, as the moisture fluxes to specific central Asian domains are enhanced or weakened following the circumflow and overflow of the Asian orography. However, precipitation events in the mountainous regions of Tian Shan and Altai Shan result primarily from local processes (Schiemann et al., 2008; Small et al., 1999). Regional and large-scale phenomena are only relevant in terms of moisture transport. The main climatological moisture transport for central Asia follows the westerly flow (Figures 1.3 and 3.6). The south-easterly and south-westerly flows of the Asian monsoon subsystems are important on average only for the Tibetan Plateau. The mean flow for the Taklamakan desert is presented as northwesterly flow for the early 1980s, while southerly flow over the Tibetan Plateau leads to extreme precipitation episodes (Yatagai and Yasunari, 1998). The variability of the Tibetan anticyclone and the upstream mid-latitude westerlies explains to some extent daily and monthly extreme wet events. The zonal wind structure over the Tibetan Plateau in late spring may help to improve the forecast of anomalous rainfall in India (Dugam et al., 2009). An up-to-date evaluation of the general climatic setting of central Asia may be achieved from Böhner (2006). Sato et al. (2007) trace a notable portion of the moisture inflow to Mongolia back to central Asia and western Siberia, and Sato (2005) doubts the rain-shadow effect of the Tian Shan for the aridity of the climate of the Taklamakan desert and the Mongolian Plateau. The importance of inflow from the north-west and west, especially from the Caspian Sea, is deducible from studies on water recycling (e.g. Dirmeyer and Brubaker, 2007).

The existence of zonal westerly flow in the atmosphere is owed to mainly two mechanisms (Holton, 1992; Vallis, 2006; Vallis and Gerber, 2008), which are distinct for the two, locally labeled, subtropical and polar front jets. The former is related to the aforementioned thermal wind balance. Thus, the equator–pole temperature gradient and the accompanying shear in the zonal wind lead to an eastward flow aloft due to a limiting drag of the wind at the surface. Largest meridional temperature gradients are found in the subtropics related to the Hadley cell. There the baroclinic subtropical jet arises. Polar front jets are due to the momentum convergence in regions of baroclinic instability (Vallis and Gerber, 2008): Excitation of meridionally propagating Rossby-waves generates an eastward zonal flow, where eastward zonal momentum converges. Vallis and Gerber (2008) detail the possible ways of variability of mid-latitude westerly winds as 'wobbling', 'pulsing' or 'bulging', where the latter refers to variations in the meridional extent, pulsing means local variations in strength of the zonal flow, and a jet wobbles,

if it changes its meridional position. The interaction of subtropical and polar front or so called eddy-driven jets is studied by Lee and Kim (2003), who conclude that subtropical and eddy-driven jet locations are close to one another in regions with a strong subtropical jet, while a distinct polar front jet is found in the mid-latitude baroclinic zone, when the subtropical jet is weak. A climatology of northern hemisphere tropospheric jets in July shows three types of multiple jet occurrences (Bordi et al., 2008): a single jet with a weak bulge of the main jet at mid-high latitudes, a distinct secondary jet at mid-high latitudes and a distinct secondary jet at high latitudes. The typology is based on monthly values. Latitude-time diagrams of daily data resolve representative developments. Seasonally or monthly averaging of zonal winds may conceal features of transient behaviour in meridional sections or horizontal fields of zonal winds.

Koch et al. (2006) develop a daily event-based jet climatology subject to various constraints (e.g. a jet event is assumed to occur, if a wind velocity threshold of 30 m s^{-1} is exceeded). The approach reduces the smoothing of other jet-characterisations and displays the spiralling character of the zonal wind maximum throughout the seasons. Nevertheless the necessity of the threshold and the specific choice of 30 m s^{-1} simplify the structure of the northern hemispheric tropospheric wind in summer. The climatology is utilised by Koch et al. (2006) to classify jet streams in two categories, so called shallow and deep jet events. Here, shallow refers to jets confined to the upper troposphere, while deep jets penetrate lower atmospheric levels as well. In boreal summer, the shallow events have the highest frequency over the Eurasian continent and in the entrance of the north Atlantic storm track, while deep jets stretch across the northern oceans along the storm tracks. If this characterisation is adopted with regard to the polar front and the subtropical jet, the latter is confined to the upper troposphere and the former overlays deeper baroclinic zones (Koch et al., 2006). The seasonal cycle and inter-annual behavior of the westerly jet in the larger region of the Tibetan Plateau is studied by Schiemann et al. (2009) with a similar climatology. Thus a detailed representation of the variability of the seasonal cycle of the jet is achieved for central Asia. Schiemann et al. (2009) further show the dependencies of the jet transition on the vertical temperature structure and of the regional precipitation on the jet.

The importance of the jet as a wave guide (Hoskins and Ambrizzi, 1993) is stressed by various studies in the context of the dynamics of atmospheric teleconnection patterns (e.g. Ding and Wang, 2005; Enomoto et al., 2003; Terao, 1998, see also chapter 4). Ambrizzi et al. (1995) note the extent of the north African-Asian jet as a waveguide in boreal summer. Ambrizzi and Hoskins (1997) further emphasise the importance of a connection from the Mediterranean to Asia in summer, while in winter two waveguides are found over southern Asia and northern Europe. These may connect from north-west to south-east similar to the circumglobal teleconnection (Ding and Wang, 2005), which impacts central Asia (compare also Figure 16 of Ambrizzi et al., 1995). Terao (1998) de-

3 Central Asian precipitation – the upstream zonal wind structure

scribes two wave guide effects over Eurasia (connected and separated cases) in detail for a set of temporal bandwidths. His results are extended to study the effect of the wave trains on the east Asian summer monsoon in the basins of Yangtze and Huaihe (Fuji-nami and Yasunari, 2009). This directly relates to the summer Europe-Japan patterns of Wakabayashi and Kawamura (2004) and the early spring extension of the North Atlantic Oscillation described by Watanabe (2004). Northern hemispheric teleconnection patterns as defined by Barnston and Livezey (1987) integrate the structure of the zonal wind over the Eurasian landmass and the related wave guide effects on longer time scales. Especially the Scandinavia (SCA), East Atlantic (EA) and East Atlantic/Western Russia (EAWR) patterns give indications of a connection to the wave guide effect in the north and in the south of Eurasia (compare NOAA, 2005–2008). In addition, the North Atlantic Oscillation in July exhibits a weak wave-like pattern over the Mediterranean.

In the present chapter, the westerly wind is characterised by its zonal mean between 50°E and 65°E . Its vertical and meridional structure is studied to identify its impacts on precipitation in central Asia. Section 3.2 gives a short overview over data used and methods applied. The division of the larger Tian Shan region into three subregions is also motivated in section 3.2. The Tibetan Plateau is considered as a fourth region; for its definition refer to chapters 2 and 4. Section 3.2 further details, why the considered ECHAM5/MPI-OM simulation data is unfeasible for studies on precipitation in the larger Tian Shan region. A climatology is given in section 3.3, results follow in section 3.4 and a discussion closes this chapter.

3.2 Data and methods

Data Pressure level data and surface parameters are obtained from the ERA-40 re-analysis (Uppala et al., 2005). Vertically integrated moisture fluxes are computed according to the procedure of Simmonds et al. (1999), which is detailed in appendix A. Precipitation data stems from the Vasclimo project (Variability Analysis of Surface Climate Observations, Beck et al., 2005). Both datasets are considered for the overlapping period 1958 to 2000. Precipitation data is utilised in terms of the standardised precipitation index (SPI, McKee et al., 1993, see also section 1.1.2). Teleconnection indices are obtained from NOAA (2005–2008, 2008, 2006) and the Frontier Research Center for Global Change (FRCGCC, the Indian Ocean Dipole Mode Index, DMI, Saji et al., 1999).

Methods This chapter specifies the impact of the zonal wind structure upstream of the Tian Shan and the Himalaya Range on precipitation. In doing so the zonal wind is surveyed in a zonally averaged meridional and vertical section between 50°E and 65°E north of the equator. The section is selected to avoid regions where the climatological zonal mean jet is subject to a strong meridional curvature in summer. The

seasonal evolution of the zonal wind over Asia is described in terms of the monthly climatological means for each calendar month and an analysis of Empirical Orthogonal Functions (EOFs) or Principal Components (PCs, PC analysis, PCA, e.g. von Storch and Zwiers, 1999) applied to the vertical fields of monthly anomalies from the climatological monthly mean for each calendar month. While this approach is similar to the study of July zonal mean winds via PCA by Bordi et al. (2008), here the zonal winds are considered from equator to pole and on pressure levels from 1000hPa to 100hPa. A minimal discussion of the principal component or EOF analysis can be found in appendix A.3.

Principal components are correlated with SPI-time series, spatial fields and the time series of the rotated EOF-analysis-loadings presented by NOAA (2005–2008) for the northern hemispheric teleconnection patterns. Significances are assigned to these correlation coefficients according to a t -distribution with $N - 2$ degrees of freedom (Φ , $N = 43$). The underlying assumption of normal distributed data is probably valid and stationarity of the time series is supposed following chapter 2.4. Results obtained in the course of the study of chapter 2.4 (not shown) also allow to expect auto-correlations of nearly all monthly separated time series to be insignificant. Nevertheless, effective degrees of freedom are computed, corresponding to the overall largest coefficients of auto-correlations (r_{Max}) for SPI series and principal component time series

$$\Phi_{eff} = \Phi \cdot \frac{1 - r_{MaxSPI} \cdot r_{MaxPC}}{1 + r_{MaxSPI} \cdot r_{MaxPC}}.$$

This results in estimated effective degrees of freedom $\Phi_{eff} \approx 26$ with $\Phi = length\ of\ record = 43 - 2$, $r_{MaxSPI} = abs(-0.53)$ and $r_{MaxPC} = 0.41$. Similar values are obtained if teleconnection indices are considered. In addition, multiple regressions are computed to assess how much variability of the regional monthly SPI time series is attributable to the upstream zonal wind principal components. The calculation is based on Fortran program code by Sielmann (2008).

ERA-40 data of temperature and zonal and meridional wind components are utilised to compute variances and covariances for the eddy components (program Fluxes, available from <http://www.mi.uni-hamburg.de/283.0.html>). The input data for the flux calculation is interpolated to a T21-grid (approximately $5.6^\circ \times 5.6^\circ$).

Definition of central Asian regions The section of the zonal wind is defined as described above. West of the meridional line in Figure 3.1 the zonal wind is averaged zonally. Thus, the southern Eurasian flow is distinguished in the flow passing over and around (a) the Turkish Plateau upstream, which is not included, (b) the orography of the Himalayas and the Tian Shan, on which the influence of the upstream flow is to be studied, and (c) the Iranian Plateau from the coasts of the Arabian Sea and the Persian Gulf in the south to the Caspian Sea in the north. In the east, the section stops just short of the Hindu Kush as the westernmost sub-range of the Himalayas.

3 Central Asian precipitation – the upstream zonal wind structure

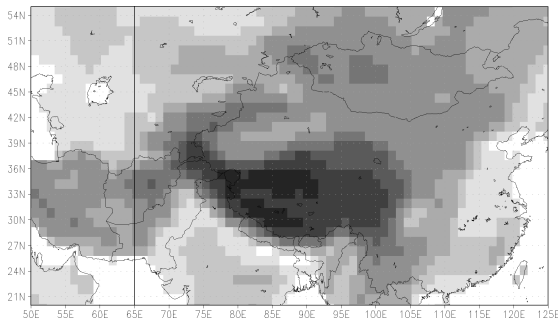


Figure 3.1. Depiction of the larger study area. The orography (ERA-40) is shaded, with darker shades for higher altitudes. The region west of the black vertical line is used for the zonal average of the zonal wind.

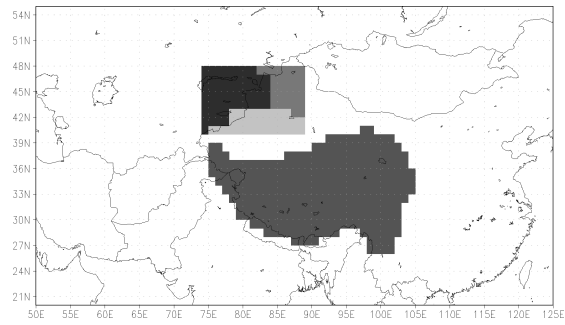


Figure 3.2. Regions utilised: the Tibetan Plateau and a box around the Tian Shan: region with drainage to the Tarim basin (light grey), drainage to the North-West (dark), drainage to the North-East (medium).

Obvious is the large extent of the Tibetan Plateau (compare section 4 and Figure 3.2). North of the Himalaya Range the Tian Shan spreads in a south-west to north-east direction from the Pamir mountains in the south-west to the Altai Shan in the north-east. The main region of interest is defined by a box, whose diagonal is partially given by the Tian Shan. The box is divided into three sub-regions using the flow direction grid of the UNH / GRDC (Fekete et al., 1999, 2000). The central southern part captures the catchment of the Tarim river as it is fed by the Tian Shan glaciers and precipitation there. Cells with mainly westward flow directions are attributed to the so called north-western (NW) subregion, those with primarily eastward flow to the north-east (NE). The flow directions are available on a 0.5° grid. The Vasclimo data is used on a 1° grid. Membership to one of the three subregions is assigned visually and subjectively.

This tripartition receives additional support from the annual cycle of precipitation for the grid points considered. The pronounced annual cycle of precipitation results in a strong agricultural and hydrological dependence on months of maximum precipitation in the semi-arid to arid areas of central Asia (e.g. Domrös and Peng, 1988). In north-west China, that is north of the Tibetan Plateau, more than 50% of the annual precipitation occurs in the summer season (Figures 1.4, 1.5 and 3.3, and Yatagai and Yasunari, 1995). An exception is the region north of the Tian Shan mountains. Figure 3.3 shows a time-longitude diagram of the annual precipitation cycles divided by the maximum at each grid point. The annual maximum of precipitation displays a strong dependence on latitude and longitude. The region of the Tarim river (compare Figure 3.2) is, simplified, the area from 78°E to 87°E and 40°N to 43°N . There, the annual maximum precipitation occurs in June and July (Figure 3.3). In these lower latitudes of the studied region an early summer (April to May) maximum appears further west, while in the east a single June/July peak is found. A secondary maximum in fall is seen in the west of the box accompanying the one in spring. Two maxima of nearly equal size emerge in winter and

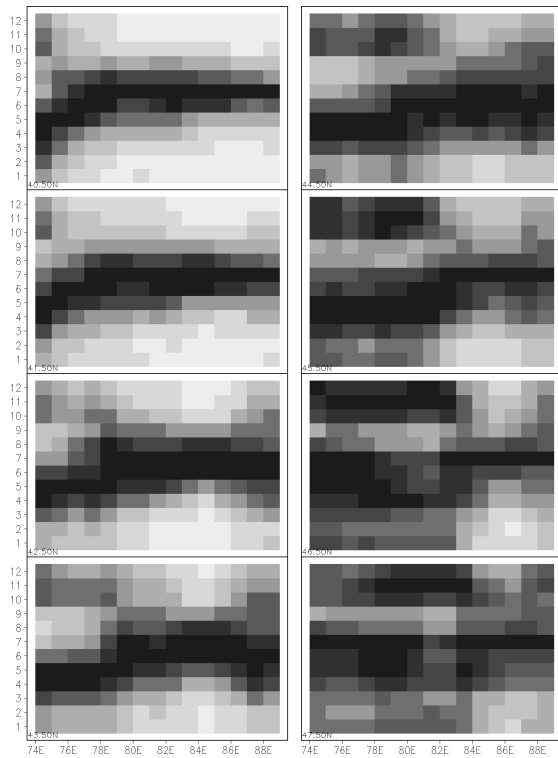


Figure 3.3. Longitude sections of annual cycles for monthly precipitation (Vasclimo data) for each grid point divided by the annual maximum. Shadings from smaller 10% (light) to larger 90% (darkest grey) of the maximum. Latitude of each panel in the lower left corner.

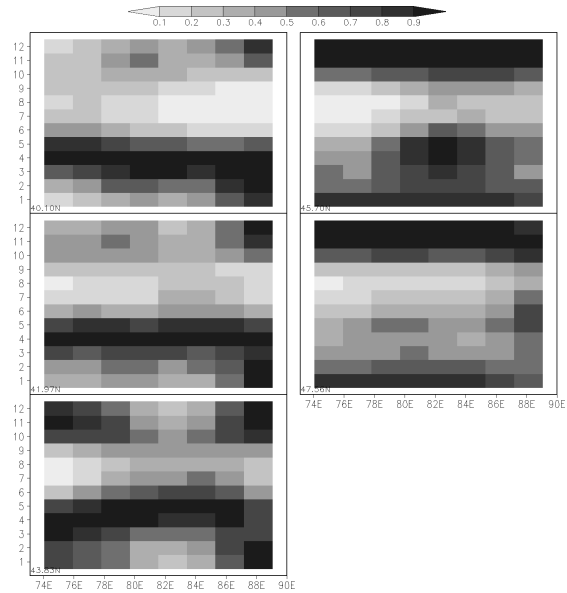


Figure 3.4. Longitude sections of annual cycles for monthly precipitation (ECHAM5 control-run, 506 years) for each grid point divided by the annual maximum. Shades from smaller 10% (light) to larger 90% (darkest grey) of the maximum. Latitude of each panel in the lower left corner.

summer in the north. Thus, from west to east the maximum of precipitation shifts from spring to summer, while from south to north a single maximum is replaced by two maxima. These are in late spring and late fall in the south-west and in summer and winter in the central- and north-west (Figure 3.3). Therefore the trisection defines a section with single summer maximum (Tarim), a region with two maxima (north-west) and a section that shows a rather small annual cycle (north-east).

The pronounced regional differences in annual precipitation distributions or rather the non-existence of them in the ECHAM5 pre-industrial IPCC AR4 control-run (Jungclaus et al., 2006; Roeckner et al., 2003) hinders the utilisation of the respective data for a comparison with the present chapter. Figure 3.4 reveals a singular spring maximum in the south, a singular winter maximum in the north, a slight bimodality in the central west and a broad winter maximum in the central east of the region. Simplified, a weak bimodality can be addressed to most locations. This insufficiency of the model is easily

3 Central Asian precipitation – the upstream zonal wind structure

explained, if the close connection between the annual cycles of the jet and precipitation is considered in, for example, the southern Asian mountains or the region between the Caspian Sea and the Tian Shan (Schiemann et al., 2008), where precipitation is related to cyclonic activities in the jet. This is equivalent to the observed annual cycle in the west of the region studied here. Resolution and subsequently implemented orography lead to notable errors in the representation of the zonal wind in the ECHAM5 atmospheric model (compared to ERA-40 data, Roeckner et al., 2006). The bimodality can be explained by a too strong moisture transport along the jet over the too low orography into the studied region. This is supported by the tendency of ECHAM5 in some resolutions to model a bimodal precipitation distribution even for the Yangtze river basin in central China (Hagemann et al., 2006).

3.3 Climatology

Precipitation In discussed central Asian regions, precipitation is basically represented by two distinct types of annual cycle. The first is found with a single maximum in summer from the south following the barrier of the Tian Shan to the north-east. This single maximum distribution is varied by the maximum becoming broadened from early summer to late autumn and even winter the further to the east. The second type reaches from the west up to the orographic barrier of the Tian Shan and shows two distinct maxima in the first and second half of the year. Again the distribution becomes more uniform farther to the north. The summer maximum can be attributed to the enhanced westerly mean moisture inflow in summer and to increased southerly eddy moisture inflow around the western and eastern slopes of the Himalayas. The bi-maxima-cycle is explained by Schiemann et al. (2008) with the larger cyclonic activity along the intermediate jet position in spring and autumn. The relative minimum in summer is caused by the formation of heat lows and subsequent clear conditions, while the Siberian High reduces precipitation in winter (Schiemann et al., 2008). Precipitation is studied in terms of the SPI based on area averaged time series for the three regions and the Tibetan Plateau for each calendar month.

Zonal wind The maximum westerly wind resides at $200hPa$ and just south of $30^{\circ}N$ in the calendar-monthly mean zonal wind climatology for the zonal mean between 50° and $65^{\circ}E$ from November to April (Figure 3.5). Thus, the seasonal cycle of the jet position lags relative to the one of insolation, due to the lag of air and surface temperatures against the received solar radiation (e.g. Prescott and Collins, 1951; Trenberth, 1983).

Largest zonal wind speeds are found in January and February, decreasing until the maximum shifts north of $30^{\circ}N$ in May and further north until July. It is weakest in July and August with only 15 to $20m s^{-1}$. The jet moves southward from September to

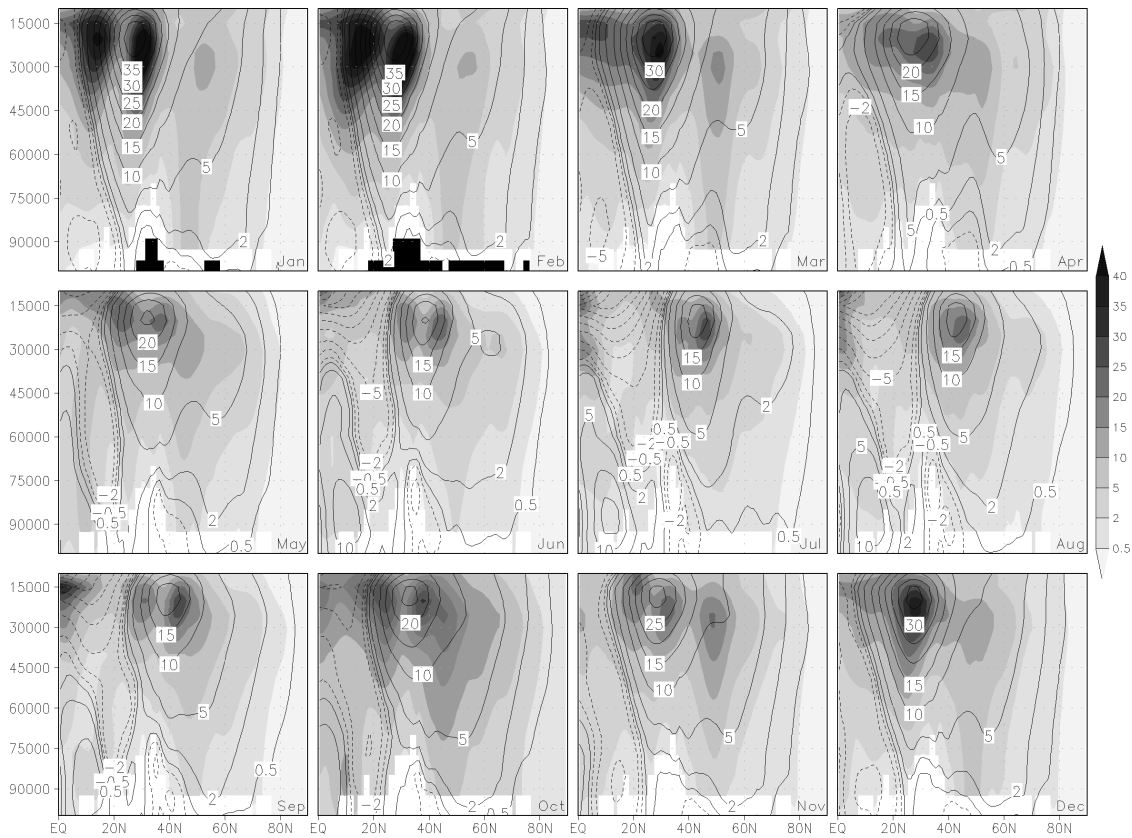


Figure 3.5. Annual cycle for the zonally averaged monthly mean zonal wind in $m s^{-1}$ in the section 50° and $65^{\circ}E$: mean (contours) and variance (shades). Regional horizontal fields of variance and mean for each calendar month are supplemented in Figure C.1 in appendix C. Orography is displayed masked-out. Each panel shows the maximum orography in the section for ERA-40. Minimum height is added to the January panel and the average in February.

November, when it reaches its winter latitude at about $30^{\circ}N$. Note the bifurcation of the westerly flow in lower levels due to the onstream orography, which is also already an expression of the downstream central Asian mountains. Easterlies prevail throughout the troposphere south of $30^{\circ}N$ from November to March. From May to September they are lifted from the surface and westerlies are found below and south of this easterly flow as part of the monsoon circulation. In October and November the easterlies again are found throughout the troposphere except in the lower levels just north of the equator.

The inter-annual variance of the zonal wind (Figure 3.5) emphasises the flanks of the monthly jet as an expression of a ‘bulging’ and ‘wobbling’ of the jet. The jet core shows the strongest variance in December, when thus ‘pulsing’ seems to dominate (for a definition of the three modes of variability see section 3.1 and Vallis and Gerber, 2008). Complementary variance maxima indicate secondary jets in the mid to high latitudes (e.g. Bordi et al., 2008).

3 Central Asian precipitation – the upstream zonal wind structure

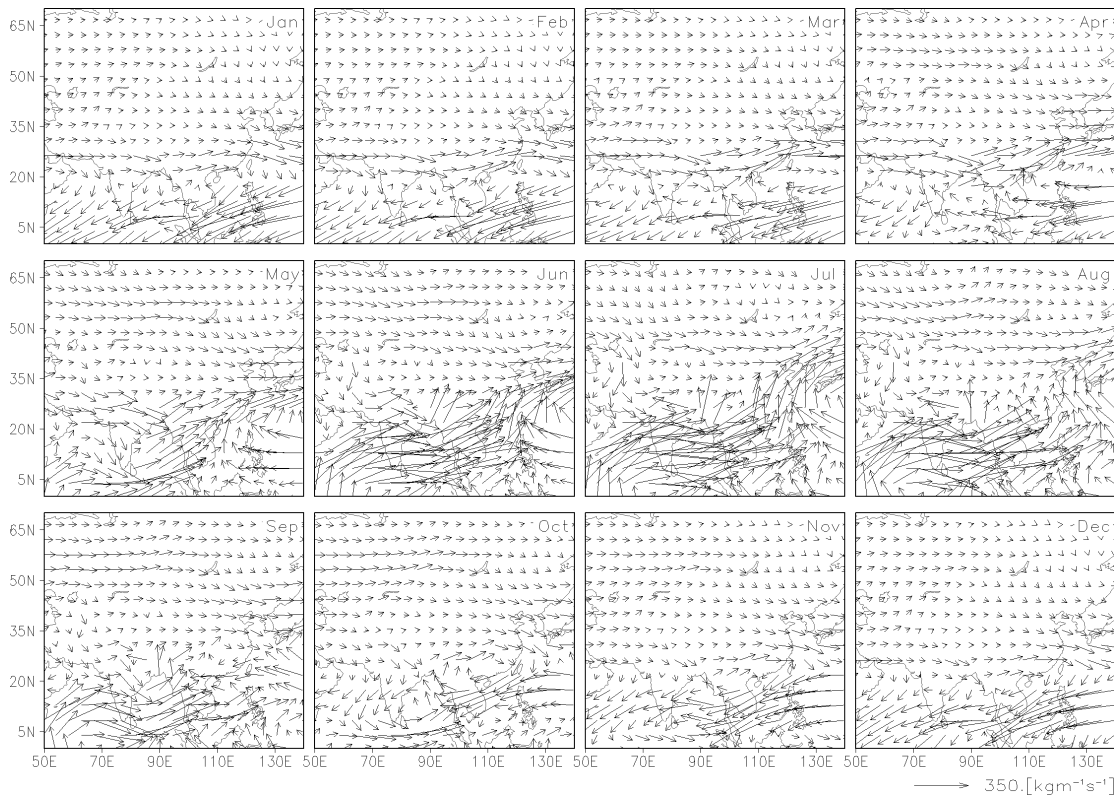


Figure 3.6. Annual cycle of monthly mean vertically integrated moisture fluxes from the ERA-40 re-analysis for the larger Asian region.

Moisture and moisture flux The climatology of monthly mean moisture fluxes is dominated by easterlies in the tropics and weaker flow along the westerly jet north of them in winter and spring (Figure 3.6). Besides the southern summer monsoon moisture fluxes, westerly flow is enhanced over continental Eurasia in summer and at least partially deflected by the central Asian mountains. Southward deflection dominates in an extended summer season from May to September. Closer inspection detects a deflection north of the jet core in spring and winter and to its south in summer.

The monthly mean eddy moisture flux (shown in appendix C, Figure C.2) consists of mostly northerly flow. It is prominent over the Pacific ocean and in northern Eurasia. The orography of the Himalayas constitutes a barrier for the eddy fluxes from the Indian ocean. The flow around the massif converges to the north-east and north-west of the studied geographical box. This convergence partially seems to overlap with the northern subregions. The fluxes only serve as a measure of atmospheric moisture transport at a re-analysis grid point. They give neither indication of the origin of the moisture nor whether the moisture is available to precipitate at a remote or adjacent grid point.

The availability of moisture can be deduced from the climatology of the ERA-40 total column water vapour in figure 3.7. Water vapour content of central Asian air columns

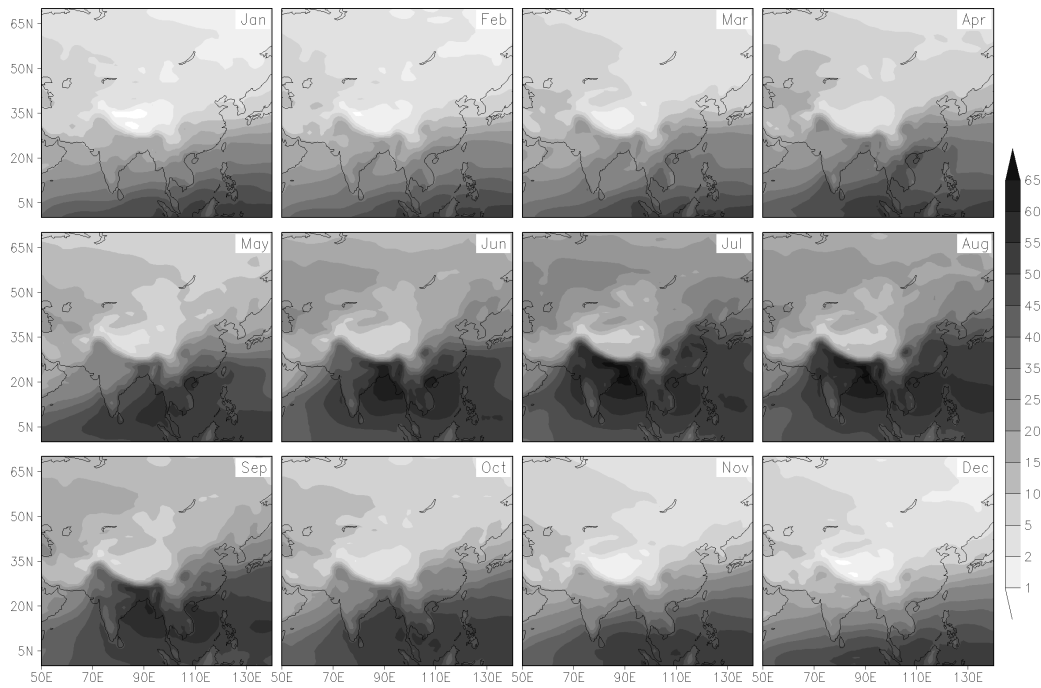


Figure 3.7. Annual cycle of the vertically integrated water vapor content (in kg m^{-2} , ERA-40 re-analysis) for the larger Asian sector.

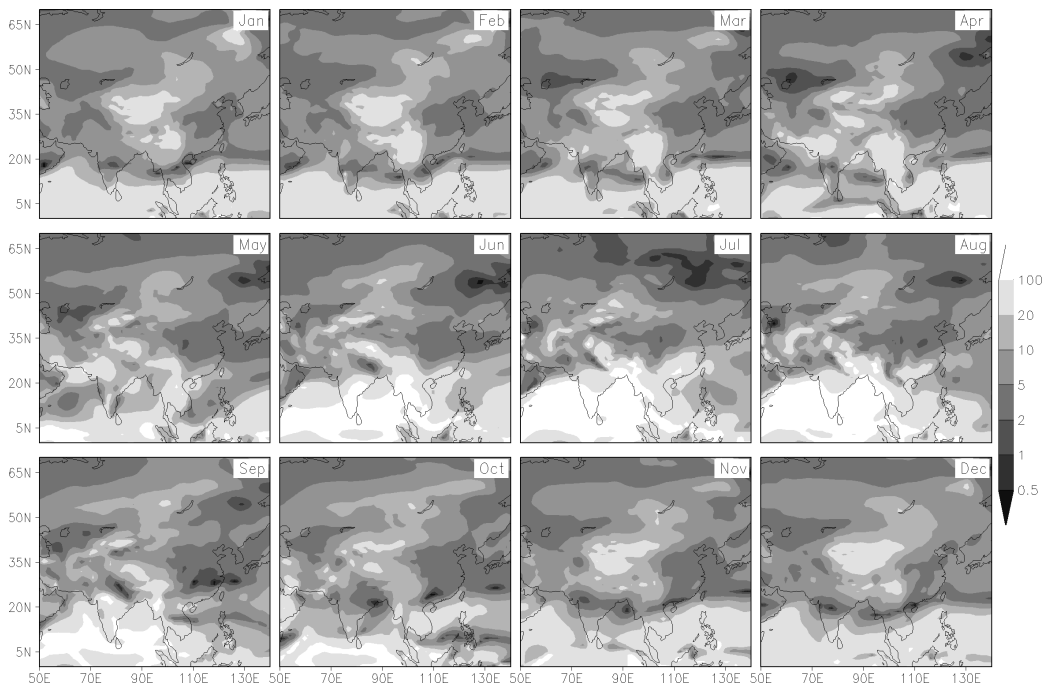


Figure 3.8. Annual cycle of the ratio of the magnitude of monthly mean moisture fluxes to the magnitude of the eddy monthly mean moisture fluxes.

3 Central Asian precipitation – the upstream zonal wind structure

increases with the northward movement of the westerly jet. The contours span around the central Asian orography. Relative maxima are seen in the lee of the Caspian Sea. In view of the zonal and meridional components of the moisture fluxes, both monthly mean components are of about the same size directly upstream of the Tian Shan (not shown). This holds for the eddy components relative to one another (not shown, deducible from Figure C.2 in appendix C). Notable easterly components arise in the zonal eddy fluxes downstream of the studied region. The magnitude of the mean fluxes relative to the eddy fluxes is displayed in Figure 3.8. Considering central Asia, eddy fluxes only prevail slightly north of the Aral Sea in April and south-east of the Caspian Sea in August. However, the mean fluxes do not overly outbalance the eddy fluxes upstream of the Tian Shan. There, the meridional component of the monthly mean fluxes is approximately of the same size as the zonal component of the monthly mean fluxes (not shown) or, regionally in summer, even outweighs the latter. In view of the eddy fluxes, meridional and zonal fluxes are basically of the same size upstream of the Tian Shan (not shown), with the zonal component dominating directly to the south-east of the Caspian Sea and further east in late summer. The zonal eddy flux also prevails from Lake Balkash eastwards from fall to spring.

3.4 Influence of the upstream zonal inflow on precipitation

The relation of precipitation in the considered regions and the zonal wind upstream is studied under the following rationale:

The zonal wind structure upstream of the central Asian mountains regulates the variability of precipitation in central Asia to a notable extent. Thus, general circulation model simulations and re-analysis data are adequate to describe a relevant fraction of the central Asian precipitation variability on monthly time scales.

Three regions are defined as seen in Figure 3.1 inside a rectangular box: (i) the northern portion of the Tarim catchment, (ii) the north-eastern portion of the larger Tian Shan region up to the Altai Shan and (iii) the upstream region around the Lake Balkash. The separation is primarily achieved by streamflow directions (Fekete et al., 1999) and the precipitation regimes (Figure 3.3). The Tibetan Plateau is considered as a fourth region in the south with a pronounced summer maximum in precipitation.

First, results of principal component analyses are presented for the zonally averaged fields in the latitude-height-plane for all calendar months. Afterwards correlations and composites are considered for summer and late spring only.

Even though the individual PCs are discussed independent of each other in the following, it is always remembered that individual principal component loadings can generally not be interpreted as individual dynamical modes and are usually not statistically independent of the other loadings (Monahan et al., 2009). Thus, even though the PCs

are described in a self-contained manner, they are not interpreted as independent in a dynamical or statistical way. If a physical interpretation is given, it is meant to give a statement, first, where the corresponding loading represents most variance and, second, to help in the assessment whether any physical processes can explain the PC-features.

3.4.1 Principal component analysis

The climatology of the monthly mean zonally averaged vertical zonal wind section between 50° and 65°E is complemented by PC analyses of the monthly zonal means for each calendar month. Principal component loadings (or eigenfunctions) are not displayed here, but rather the zonal wind sections are composited relative to the principal component time series exceeding plus and minus one standard deviation. As the signs of the PCs are arbitrary, all related parameters are defined such that the maximum mean westerly flow is enhanced by the pattern. However, this procedure replaces one arbitrariness by another for higher order PCs. The PC-loadings are supplemented in appendix C (Figures C.3 to C.6).

Not all eigenvalues are visually well separated as described by the relative variance they account for (Figure 3.9, see also table C.1 in appendix C). The selection of the first four PCs for further examination seems justified for most months. Only April and October eigenvalues hint to the necessity to use the fifth PC as well. As the focus is on summer and late spring, the first four PCs are further inspected.

The first loading represents between 31% and 52% of the variance depending on the

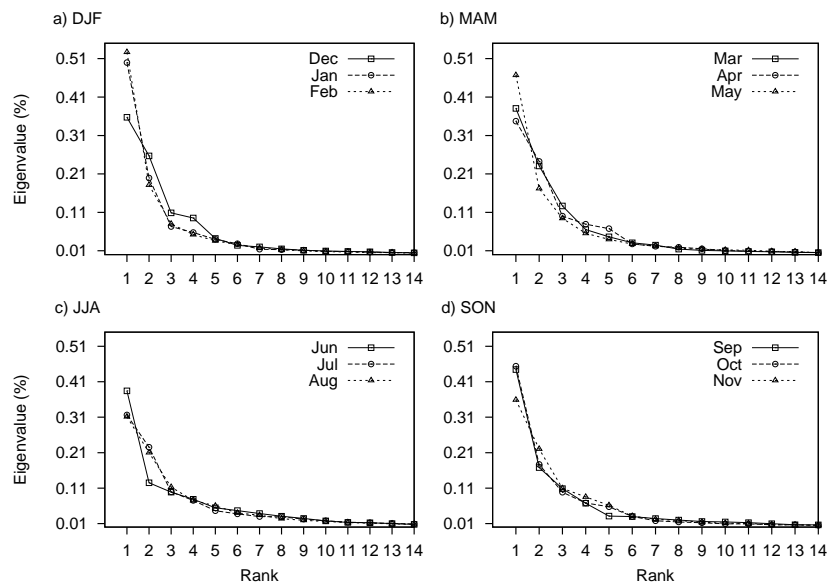


Figure 3.9. Variance explained by the first fourteen PC loadings in each month.

3 Central Asian precipitation – the upstream zonal wind structure

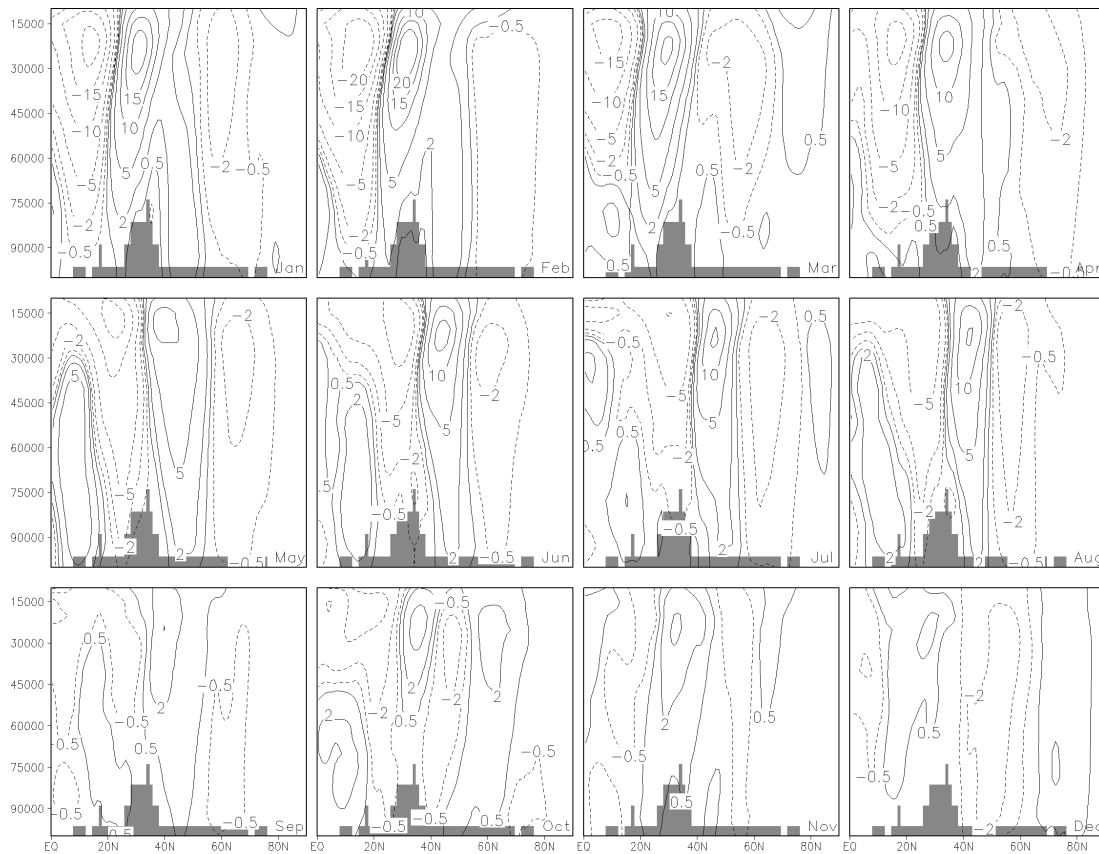


Figure 3.10. Calendar monthly composite differences for the zonal wind section between 50° and 65°E relative to the PC1 time series exceeding plus/minus one standard deviation.

calendar month (compare table C.1). Its patterns and the relative composite differences (compare Figure 3.10) describe, in most months, the interfaces between the easterly and westerly flow regions and between the strong westerly flow region and subsequent weaker flow. Thus, the loading can be associated with meridional and vertical variations in the jet position, that is the ‘wobbling’ of the jet as coined by Vallis and Gerber (2008). Variations in jet ‘thickness’ (‘pulsing’) also contribute to the first loadings. Additional features are found in the mid-latitudes, where secondary jets can be found (Bordi et al., 2008). The weakness of composites is noteworthy from September to December.

The variability of the mean intensity is primarily seen in the composites for the second loadings (Figure 3.11), which represent 12% to 25% of the variability. A weakening (strengthening) of the westerly flow centre is accompanied by a decrease (increase) of the easterly flow to its south and enhanced (weakened) westerly flow to its north.

Third loadings represent 7% to 12% of the variability. The composites (Figure 3.12) are built up by five meridional poles. Composites for loading four appear similar, but are less organised (Figure 3.13). The circulation north of the Iranian mountains is most notable in both loadings. 5% to 9% of variance are attributable to the fourth loadings.

3.4 Upstream influence on precipitation

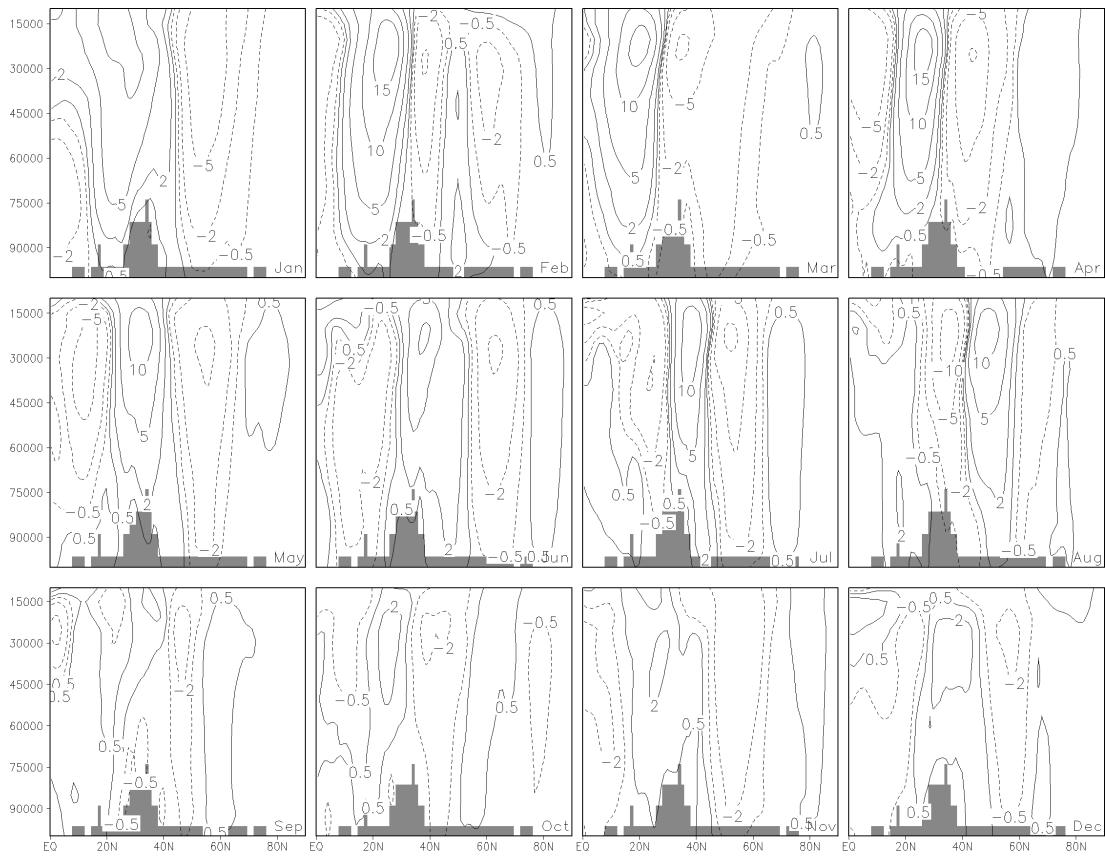


Figure 3.11. Calendar monthly composite differences for the zonal wind section between 50° and 65°E relative to the PC2 time series exceeding plus/minus one standard deviation.

3.4.2 Correlation analysis

If the principal assumption stated above is correct, significant concurrent correlations exist between the precipitation in the four regions and the PCs of the mean zonal wind throughout the year. This holds for all months except September, but the correlations are relatively weak (compare table 3.1), especially so from October to March.

October to March: In October, significant correlations are found only for the Tibetan Plateau (with PC2, PC3). The northern regions correlate significantly with the fourth PC for November, and they do so with the second PC in December. The December-Tarim-SPI is significantly correlated with the November-PC4 (preceding months correlations are detailed in table 3.2). January-correlations with the PC2 time series are found for the Tarim and, weakly, the north-east region. The January SPI series of the northern regions display significant correlations with the December-PCs. Significance is seen in correlations of the northern regional SPI series with PC4 and of the Tibetan Plateau series with PC2 in February. In March, correlations are found for all regions, largest for Tibet

3 Central Asian precipitation – the upstream zonal wind structure

Table 3.1. Correlations of monthly PC time series with concurrent regional SPI time series for October to March (left) and April to September (right). * and boxes denote, respectively, 90% significance levels relative to 41 degrees of freedom and calculated minimal effective degrees of freedom.

| | | PC | | | | Regional SPI | | | | | |
|-----|---|-------|--------|--------|--------|--------------|---|-------|--------|--------|--------|
| | | Tar | NW | NE | Tib | | | Tar | NW | NE | Tib |
| Oct | 1 | 0.20 | -0.17 | 0.05 | 0.07 | Apr | 1 | 0.35 | 0.39 | 0.23 | -0.07 |
| | 2 | 0.13 | 0.04 | 0.09 | -0.40 | | 2 | -0.23 | -0.48 | -0.45 | 0.15 |
| | 3 | 0.08 | 0.09 | 0.09 | -0.28* | | 3 | -0.11 | -0.28* | -0.26 | -0.21 |
| | 4 | 0.02 | -0.05 | -0.11 | -0.17 | | 4 | 0.13 | 0.12 | 0.07 | -0.05 |
| Nov | 1 | -0.16 | -0.08 | -0.03 | 0.15 | May | 1 | 0.09 | 0.08 | 0.07 | 0.65 |
| | 2 | 0.11 | 0.01 | -0.18 | -0.02 | | 2 | 0.30* | 0.20 | 0.03 | 0.10 |
| | 3 | 0.21 | 0.06 | 0.15 | 0.12 | | 3 | -0.22 | -0.30* | -0.34 | -0.02 |
| | 4 | -0.08 | -0.31* | -0.38 | 0.15 | | 4 | 0.46 | 0.45 | 0.41 | 0.12 |
| Dec | 1 | 0.07 | -0.07 | 0.09 | 0.18 | Jun | 1 | -0.52 | -0.28* | -0.08 | 0.40 |
| | 2 | 0.24 | 0.39 | 0.31* | 0.03 | | 2 | 0.10 | 0.17 | 0.13 | -0.08 |
| | 3 | 0.07 | -0.03 | -0.12 | 0.03 | | 3 | 0.08 | 0.12 | -0.08 | 0.08 |
| | 4 | 0.04 | -0.24 | -0.21 | 0.07 | | 4 | 0.09 | -0.02 | -0.06 | 0.04 |
| Jan | 1 | -0.09 | 0.05 | -0.03 | -0.02 | Jul | 1 | -0.34 | -0.17 | 0.03 | -0.24 |
| | 2 | 0.31* | 0.09 | -0.27* | 0.13 | | 2 | 0.22 | 0.55 | 0.34 | -0.08 |
| | 3 | -0.02 | -0.18 | -0.07 | 0.06 | | 3 | -0.36 | -0.31* | -0.23 | -0.12 |
| | 4 | -0.18 | -0.12 | -0.13 | -0.06 | | 4 | -0.06 | -0.13 | -0.21 | -0.31* |
| Feb | 1 | -0.02 | 0.24 | 0.11 | 0.09 | Aug | 1 | 0.06 | 0.18 | 0.35 | 0.23 |
| | 2 | 0.01 | -0.20 | -0.16 | 0.47 | | 2 | -0.46 | -0.55 | -0.30* | -0.17 |
| | 3 | 0.25 | -0.11 | -0.16 | -0.03 | | 3 | 0.35 | 0.31* | 0.45 | 0.56 |
| | 4 | -0.15 | -0.40 | -0.34* | -0.00 | | 4 | -0.13 | -0.14 | -0.08 | -0.27* |
| Mar | 1 | 0.21 | 0.08 | 0.01 | 0.43 | Sep | 1 | 0.11 | 0.02 | 0.01 | 0.24 |
| | 2 | -0.11 | -0.37 | -0.37 | 0.24 | | 2 | 0.05 | 0.00 | 0.14 | 0.13 |
| | 3 | 0.29* | -0.18 | -0.22 | 0.16 | | 3 | -0.04 | -0.07 | -0.04 | -0.18 |
| | 4 | 0.14 | 0.18 | 0.04 | 0.18 | | 4 | 0.17 | 0.06 | 0.10 | 0.20 |

3.4 Upstream influence on precipitation

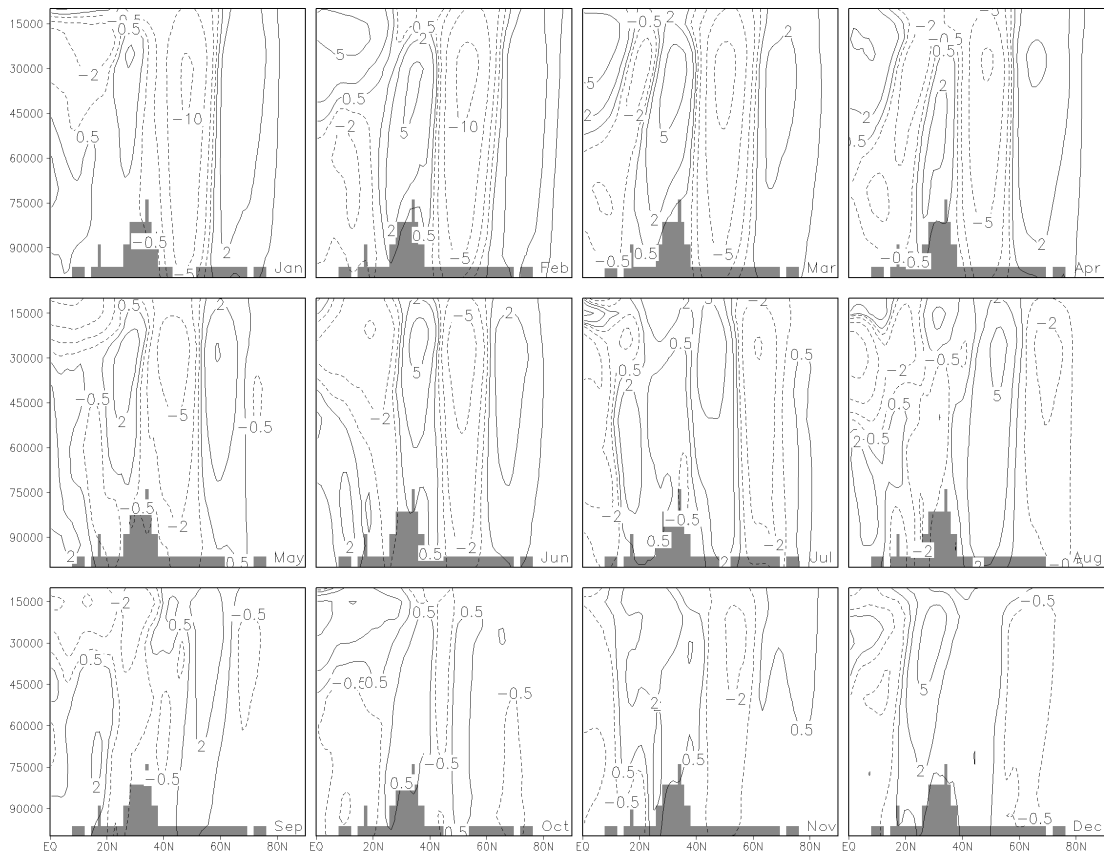


Figure 3.12. Calendar monthly composite differences for the zonal wind section between 50° and 65°E relative to the PC3 time series exceeding plus/minus one standard deviation.

with PC1. The northern regions are correlated with PC2.

The weak, mostly zonal moisture flux in the mid-latitudes explains the influence of the second loading in winter on the northern regions, while both, PC1 and PC2, well capture the primary fluxes to the Tibetan Plateau in the early calendar months.

Extended summer, April to August: The coherence is enlarged in an extended summer season from April to August. In April, correlations exist between Tarim and the PC1 time series, for the north-east (with PC2) and the north-west (with PC1, PC2 and PC3). The latter correlations justify a multiple regression, yielding 45% of explained variance.

The picture becomes slightly more complicated in May. The Tarim correlates significantly with the time series of PC4, and each of the northern regions with those of PC3 and PC4. Large correlations are found with the time series of the simultaneous PC1, the PC1 for the previous April and the PC2 for the previous March for the Tibetan Plateau SPI. Indeed, the May-PC1 shows significant coherence with both previous PCs. For the Plateau, the May-PC1 accounts for about 40% of the simultaneous SPI variance. Multiple

3 Central Asian precipitation – the upstream zonal wind structure

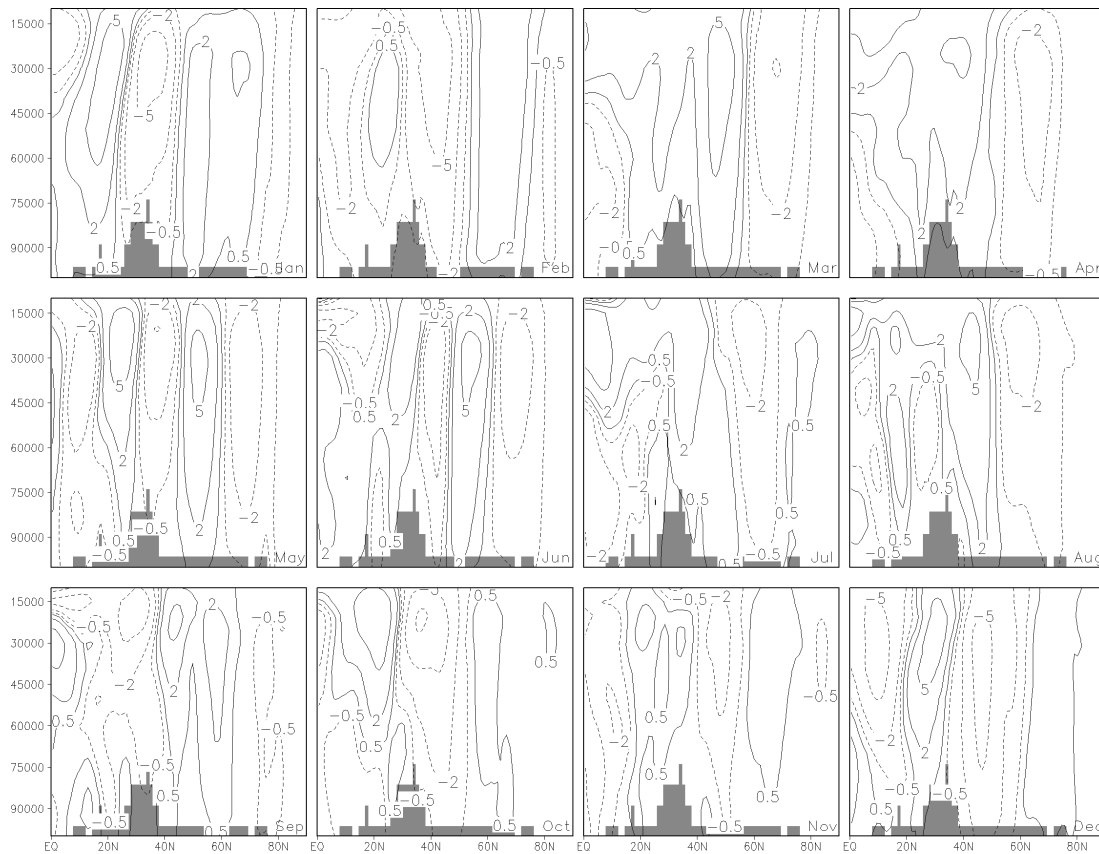


Figure 3.13. Calendar monthly composite differences for the zonal wind section between 50° and 65°E relative to the PC4 time series exceeding plus/minus one standard deviation.

regressions with PC3 and PC4 yield explained variances of nearly 30% with respect to the May-SPI time series of the northern regions. The coherence of the wind upstream of mountainous central Asia with the wind structure of previous months can be explained by the relative persistence of the main jet in March and April. While the jet weakens, its position is basically unchanged due to the lag between temperature (or heating) and insolation (Prescott and Collins, 1951).

The relations are diminished in June. The PC1 time series is significantly correlated with the SPI series for the north-west region, Tibet and the Tarim, but only the latter correlation is notably large. The Tarim also shows large correlations with the PC3 for the previous May and smaller ones with the May-PC1 and May-PC2. Due to the common strong maximum north of the Iranian Plateau, the PC1 for June is significantly correlated with May-PC1 and May-PC3. A multiple regression of the Tarim June-SPI against the three May-PCs explains nearly 50% of the Tarim June-SPI variance.

All regions show significant correlations in July. Tibet correlates with the PC4 time series, the north-east with the one for PC2, the Tarim with those for PC1 and PC3 and the north-west with those for PC2 and PC3. A multiple regression results in nearly 40%

3.4 Upstream influence on precipitation

of explained SPI-variance in July for the north-west.

The most detected correlative relations exist in August. The correlations are for Tibet with the August PC3 and PC4 and, additionally, with PC2 and PC4 of July, while the Tarim basin, the north-west and the north-east correlate significantly with simultaneous PC2 and PC3 and the July PC2. Furthermore, the north-east SPI time series is significantly coherent with the concurrent PC1 time series.

However, August PC2 and PC4 are not independent of July PC2. Further found dependencies are weak between August PC1 and July PC1, August PC2 and July PC3, and stronger between August PC3 and the PC1 and PC4 for July. Again, the strong lagged connections can be attributed to the persistence of the summer jet (compare Figure 3.5). Using July-PC2 in a multiple regression yields only better results for the north-east region. This multiple regression against the August PC1, the August PC3 and July PC2 explains about 48% of the variance of the August-SPI series in the north-east region.

3.4.3 Composite analysis

The foregoing considerations of coherent behaviour justify, to some extent, the rationale of this chapter. However the (four) leading PCs do not suffice to explain reasonably well

Table 3.2. Additional significant correlations of regional SPI time series with preceding monthly PC time series (left), and for PC time series with PCs for preceding months (right).

| Month | Additional correlations | Month | Additional correlations |
|----------|------------------------------|--------|------------------------------------|
| December | $R_{P4_{-1}, Tarim} = -0.40$ | May | $R_{P1_{-1}, P1_{May}} = -0.34$ |
| January | $R_{P1_{-1}, NE} = 0.36$ | May | $R_{P2_{-2}, P1_{May}} = 0.33$ |
| January | $R_{P4_{-1}, NE} = -0.34$ | June | $R_{P1_{-1}, P1_{June}} = -0.38$ |
| January | $R_{P3_{-1}, NW} = -0.33$ | June | $R_{P3_{-1}, P1_{June}} = -0.37$ |
| May | $R_{P1_{-1}, Tibet} = 0.45$ | August | $R_{P2_{-1}, P2_{August}} = -0.36$ |
| May | $R_{P2_{-2}, Tibet} = 0.43$ | August | $R_{P2_{-1}, P4_{August}} = -0.28$ |
| June | $R_{P3_{-1}, Tarim} = -0.54$ | August | $R_{P1_{-1}, P1_{August}} = -0.27$ |
| June | $R_{P1_{-1}, Tarim} = -0.34$ | August | $R_{P3_{-1}, P2_{August}} = 0.28$ |
| June | $R_{P2_{-1}, Tarim} = 0.29$ | August | $R_{P1_{-1}, P3_{August}} = 0.30$ |
| August | $R_{P2_{-1}, Tibet} = 0.39$ | August | $R_{P4_{-1}, P3_{August}} = 0.48$ |
| August | $R_{P4_{-1}, Tibet} = -0.35$ | | |
| August | $R_{P2_{-1}, Tarim} = 0.41$ | | |
| August | $R_{P2_{-2}, NWest} = 0.58$ | | |
| August | $R_{P2_{-2}, NEast} = 0.53$ | | |

3 Central Asian precipitation – the upstream zonal wind structure

the SPI-variations in the studied areas from September to March. Nevertheless the basic assumption seems to be valid from April to August. In the following, composites for these months are discussed especially relative to the significantly coherent PCs.

The zonal mean wind climatology (Figure 3.5) displays the annual cycle of the jet position from its winter position south of 30°N (November to April) to a summer position north of 40°N (July) and back. Zonal wind speeds are largest in January and February with up to 40 m s^{-1} and weakest in July and August with 15 to 20 m s^{-1} . Again the influence of the orography is stressed by noting the deflection and splitting of the zonal wind in lower levels.

Vertical structure of the zonal wind and moisture transport

April The mean zonal wind maximum between 50° and 65°E is reduced and broadens to the north in April. Composite differences of the zonal wind section in the latitude-height-plane are computed relative to the PC time series exceeding one standard deviation (Figures 3.10 to 3.13). For the first April-PC, these composites display, in the chosen nomenclature, a decrease of southern and lower tropospheric easterlies and a strengthening of the overlying easterlies concurrent with a northward displacement or weakening of the westerlies compared to the climatology (Figure 3.5). The latter are strengthened in turn north of the Iranian Plateau and not as pronounced in the mid- to high-latitudes. Such cases would result in stronger flow up to the Pamir and possibly into the Tarim basin. Composites relative to April-PC2, equatorward easterlies are enhanced in the upper troposphere and lessened in the lower troposphere up to the orography. The westerlies are more pronounced in the south and diminished in the north of the Iranian mountains. Slightly stronger westerlies are found in the higher latitudes. With respect to PC3 upper tropospheric easterlies are reduced at the equator but strengthened in the lower troposphere. Just north of the easterlies similar anomalies are seen for the westerlies. The southern part of the jet is weaker in the upper and enhanced in the lower troposphere just south of the Iranian orography. Largest negative deviations are found in mid-latitudes.

Monthly mean moisture flux composite differences (Figure 3.14) relative to PC1 show an enhanced westerly moisture flow from the Caspian Sea into the boxed Tian Shan region. This is associated with a strong cyclonic anomaly over northern Eurasia. Additional westerly flow is visible south of the Caspian Sea, which is deflected by the orography of the Himalayas. The westerly flow between 40° and 50°N is sustained further to the east. Relative to PC2 the westerly flow in the mid-latitudes is diminished as is the easterly flux further to the south. Moisture reaches the studied region from the east. Southerly flow is seen up to the Tibetan Plateau. PC3-composites of moisture flux show a strong anticyclonic anomaly to the north of central Asia, thus, the westerly flux is reduced. In the south, enhanced moisture flux is seen from the Persian Gulf to the Indus

3.4 Upstream influence on precipitation

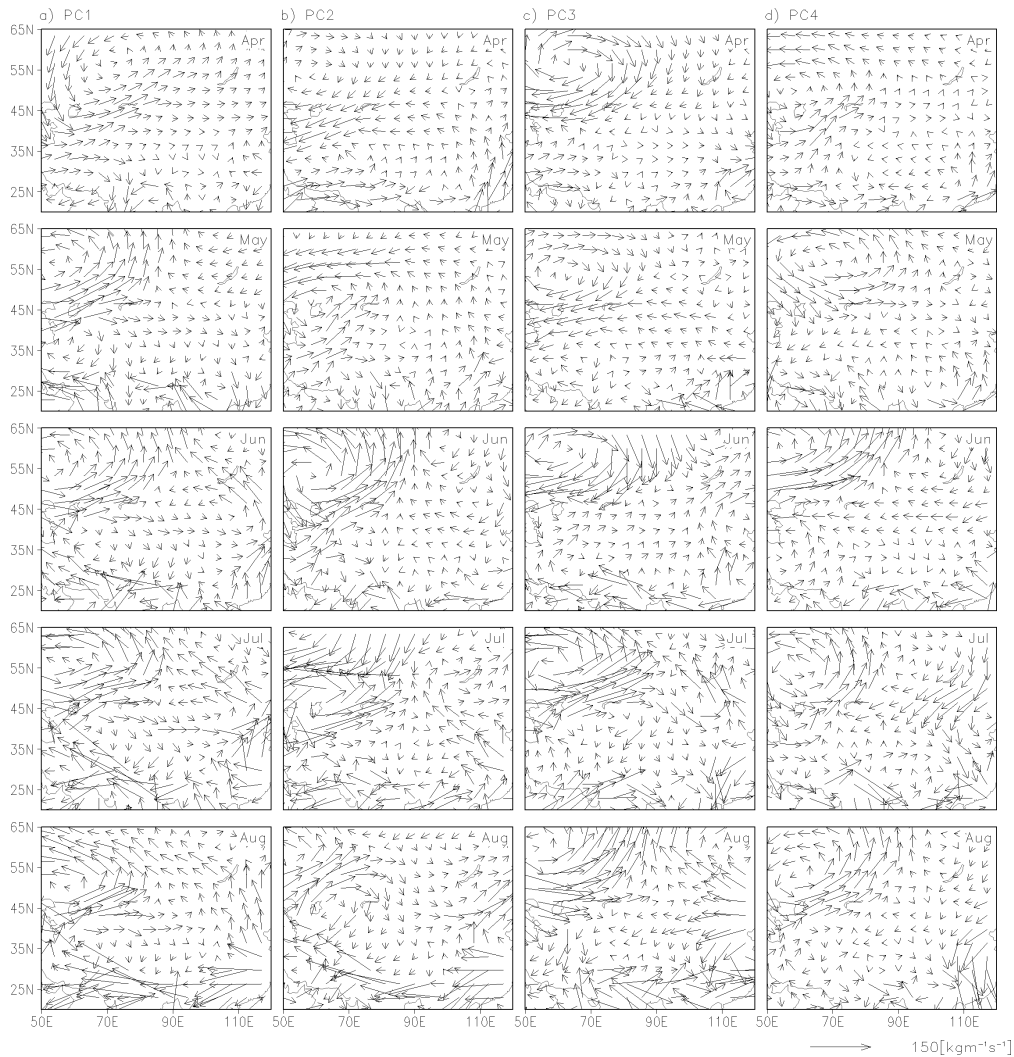


Figure 3.14. Calendar monthly composite differences for the monthly mean moisture fluxes from April to August (top to bottom) for a) PC1, b) PC2, c) PC3, d) PC4.

basin. South-westerlies from the Persian Gulf and the Arabian Sea are visible in composites relative to PC4. The north-eastward component is due to a large cyclonic anomaly over central Asia.

Composites of the eddy moisture fluxes are about an order of magnitude smaller (Figure 3.15) and reveal, relative to PC1, fluxes from the Bay of Bengal onto the Tibetan Plateau and from the west into the Tarim basin. Strong fluxes from the south-west are seen relative to PC2, with weak unstructured fluxes further to the north. An area of convergence relative to PC3 is seen at about 45°N between the Caspian Sea and Lake Balkash. Eddies appear to transport moisture around the Tian Shan in composite differences for PC4.

3 Central Asian precipitation – the upstream zonal wind structure

May The transition of the jet centre to the north fully commences in May. Southern upper level easterlies also shift north and westerlies appear in lower levels at the equator. PC1-composites display a strengthening of the southern westerlies, the southern easterlies and the main jet. For the second PC, the composite difference reminds of a belated transition process with the easterlies enhanced and more to the south. The zonal wind maximum is shifted less far to the north, relative to climatology. The third PC shows diminished flow directly north of the Iranian orography. South of the Iranian Plateau, the anomaly patterns are unorganised. The upper tropospheric easterlies at the equator are strengthened. As shown above, the PC4 time series correlates with the SPI-series for all three subdivisions of the Tian Shan. Composites relative to PC4 consist of stronger easterlies throughout the troposphere in the south with reduced underlying westerlies. The westerlies are also weakened over the topography but enhanced over central Asia and south of the mountainous plateau. Thus, precipitation in the northern regions and over Tibet is to some extent attributable to the westerly flow anomalies related to PC4 plus PC3 and PC1, respectively. Indeed, the Tarim is also affected by this flow.

Figure 3.14 reveals vertically integrated monthly mean moisture fluxes north of 40°N relative to PC1 similar to the ones found in April. Easterly anomalies are seen further to the south. Southerly and northerly moisture fluxes converge over the southern Tibetan Plateau. Strong easterlies arise in composites relative to PC2 north of central Asia. Westerlies and south-westerlies bring more moisture onto the Tibetan Plateau and into the Tian Shan. A northern anticyclonic anomaly is found in the composite differences for PC3, which reduces westerly flow. Moisture reaches the Tian Shan from the east. Considering composites for PC4, a cyclonic anomaly in the moisture flux is seen north of central Asia. This leads to enhanced north-westerly flow into central Asia and the Tian Shan. In the south, more moisture reaches the Tibetan Plateau from the Bay of Bengal.

In terms of eddy fluxes, westerly inflow into the northern Tian Shan is displayed relative to PC1. A zone of convergence in northern Eurasia and an easterly anomaly in central Asia are the most prominent features arising for PC2. In the eddy moisture flux composite differences for PC3 more moisture is transported into the region between the Caspian Sea and the Tian Shan, and fluxes are enhanced from the Bay of Bengal onto the Tibetan Plateau. Pronounced easterly and north-easterly eddy fluxes into Tarim and Tian Shan respectively are seen in Figure 3.15 relative to PC4.

June Climatologically the jet moves further north in June, and the southern easterlies strengthen as does the equatorial westerly flow of the south-west monsoon. Then, only the first PC shows coherence (particularly with the Tibetan Plateau and the Tarim SPI series). Composited zonal mean flow displays strengthening of the climate mean features except in higher latitudes, where the relative westerly maximum is reduced. The increase in the mid and the decrease in the higher latitudes result in an enhanced gra-

3.4 Upstream influence on precipitation

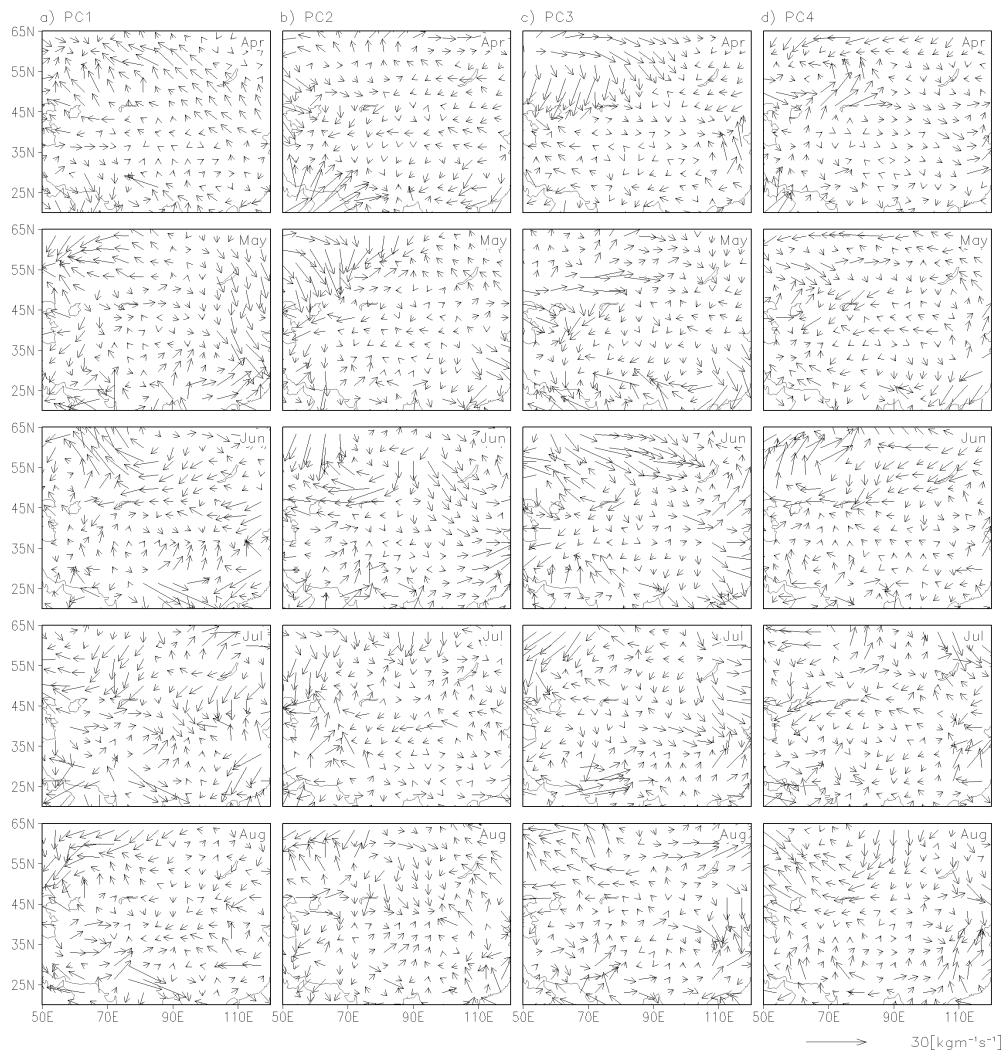


Figure 3.15. Calendar monthly composite differences for the eddy monthly mean moisture fluxes from April to August (top to bottom) for a) PC1, b) PC2, c) PC3, d) PC4.

dient in the north, while the strengthening of westerlies in mid and easterlies in low latitudes leads to a stronger contrast at the interface of both regions as well.

Monthly mean moisture flux composites relative to PC1 show strong moisture inflow from the Bay of Bengal. In addition, a large cyclonic anomaly is visible over northern Asia. The latter enhances the westerly fluxes, which also reach further to the east. As the jet stream is directly across the Caspian Sea in June, moisture fluxes from there are enhanced as well relative to PC2 but with a stronger north-eastward component. Additional north-eastward flow comes from the Persian Gulf. Relative to PC3, stronger fluxes from the Bay of Bengal are seen concurrent with slightly enhanced south-westerlies. More pronounced is an anticyclonic anomaly over northern Eurasia with an easterly jet anomaly and northerly flow. A cyclonic anomaly over the higher northern Eurasia leads

3 Central Asian precipitation – the upstream zonal wind structure

to enhanced westerly flow north of the Tian Shan. Anomalous easterly flow from further east reaches the Tian Shan, while moisture flux is enhanced onto the Tibetan Plateau from the Arabian Sea.

More moisture is transported into the Tian Shan by the monthly mean eddies from the east and north-east relative to PC1. Composites for PC2 display easterly anomalies and, collateral, the western Tibetan Plateau experiences moisture convergence. Considering PC3 composites, northerly eddy-flow is slightly enhanced into the north-western region, and this holds relative to PC4 with respect to both northern regions.

July The jet reaches its most northward latitude in July, and the zonal wind maximum is further diminished. Contrastingly, the equatorial westerlies strengthen and the easterly band in-between becomes wider. Overall not too much differences arise compared to June. So also composites relative to PC1 for July resemble those for the PC1 in June. A reduction is most conspicuous except in higher latitudes. Equatorial low level westerlies are strengthened for PC2. So are the upper level easterlies. Further enhancement is found in the flow directly north of the Iranian mountains, while even farther to the north the westerly flow is weakened. Thus, the meridional extent of the mean jet is reduced, compared to climatology. For PC3, composites appear unstructured in the south. North of the orography, westerlies are slightly stronger, but diminished further north. Easterlies and westerlies are decelerated in the lower levels south of the Iranian Plateau. The composite anomalies are even more noisy relative to PC4. Most pronounced is the decrease in the westerlies in higher latitudes and an increase south of this region. Upper level easterlies at the equator are notably reduced as well.

Stronger flow into the southern portion of the Tarim basin contributes to the coherence of Tarim SPI with PC1 and PC3. As the Tibetan Plateau is located in the same latitude belt as the unstructured composites for PC4, these suggest a more important inflow by transient disturbances or a stronger impact of the circulation downstream of the orography (for example the east Asian monsoon system). The northern regions profit most from the strengthened westerlies. South-easterly and northerly monthly mean moisture fluxes converge over the Tibetan Plateau in July relative to PC1. Stronger westerly flow reaches the studied regions and extends further eastward. Regarding composites for the PC2 time series, the only notable feature is slightly enhanced easterly flow, while for PC3 the westerly flow around the Tian Shan appears to recirculate into the area from the north-east. Relative to PC4, a cyclonic anomaly north of the Caspian Sea slightly enhances westerly flow into the north-eastern region. In addition, easterly moisture flow is enlarged. Monthly mean moisture fluxes are increased from the Arabian Sea onto the Tibetan Plateau in composites with respect to PC3 and relative to PC4.

Eddy monthly mean moisture fluxes are directed into the Tian Shan from the north and from the west (PC1) and onto the Tibetan Plateau (PC3). PC4 composites display

3.4 Upstream influence on precipitation

easterly eddy fluxes into the north-eastern region. Eddy fluxes converge on the eastern Tibetan Plateau.

August Climatologically, the mean flow is again similar to the previous months in August. The southern westerlies are slightly reduced. Significant correlations of regional August SPI series and of August PC time series with PC series for preceding months can be attributed to this persistence of the zonal flow throughout the summer season. Composites relative to PC1 show strengthened lower level westerlies and upper level easterlies equatorward of the Iranian Plateau. The zonal flow is strengthened as well north of the orography, but diminished in higher latitudes. The jet appears more meridionally confined. PC2-composites show weak anomalies in the north and in the south. A dipole of large anomalies prevails in-between, over and just north of the Iranian Plateau. Westerly flow is highly enhanced at about 50°N and strongly reduced over the orography. The latter anomaly is an expression of a northward extension or a shift of the easterlies to the north. Positive anomalies are seen north of the orography in the composite differences with respect to PC3. This is accompanied by mostly unstructured patterns between the equator and the Iranian Plateau. Additionally, the easterlies at the equator are enhanced in mid-levels. For PC4, the westerlies are strengthened north of the orography. Anomalies are again only weakly structured in the south of the domain.

The large coherence between Tibetan Plateau SPI and the concurrent PC3 for August is not effectually accounted for by the zonal wind composite differences. Slightly more distinct is the influence of strengthened flow on the SPI series for the Tarim region expressed by PC2 and PC3 composites. The identical factors influence the north-western region, weaker with respect to the anomalies summarised by PC3, stronger relative to those for PC2. The variability visualised in PC2 and PC3 further has an impact on the north-eastern region, but here coherence is larger with PC3. For all three regions, these links possibly indicate a stronger inflow from the east, a deduction supported by the strength of the correlations relative to the geographical location of the three Tian Shan subdivisions.

The jet still resides in its summer position in August associated with strong westerly moisture fluxes. Positive anomalies are seen extending to the north-eastern tip of the Tibetan Plateau with respect to PC1. Compositing relative to PC2, an anticyclonic anomaly just upstream of the Tian Shan is the most prominent feature for the monthly moisture fluxes. Additionally, easterly flow brings moisture onto the Tibetan Plateau. Strong cyclonic anomalies prevail in composites for PC3 and PC4 in northern Eurasia. Subsequently the westerly moisture flux is strengthened. For PC2, this further coincides with stronger easterly flow into the Tian Shan and stronger moisture transport from the west onto the southern Tibetan Plateau. The strong connections of the Tian Shan SPI series to the PC2 series are accounted for by the related easterly flow.

3 Central Asian precipitation – the upstream zonal wind structure

Eddy monthly mean moisture fluxes are faint, but composite differences appear enhanced from most directions relative to PC1. Northerly eddy fluxes prevail with respect to PC2. The Tibetan Plateau and the Tarim seem to receive more moisture relative to PC3, while easterly flow is found across the Tian Shan in PC4 composite differences.

Horizontal zonal wind structure and temperature

Horizontal field composites for the zonal wind on various pressure levels primarily depict the same anomalies as the vertical zonal mean sections in Figure 3.10 to Figure 3.13. Thus, zonal wind composites for the first PC in 200hPa and 600hPa (Figure 3.16 and 3.17) are essentially expressions of the meridional displacement of the mean main flow in the respective month for April to July, when PC2 measures changes in the strength of the mean flow. This relation is reversed in August. These descriptions especially hold for the upper troposphere. PC1 and PC2 composites display the variability in the mid to low latitudes, connected to the subtropical jet, while composited variations prevail in the higher latitudes for the third and fourth PCs which, thus, express the variability of the polar front jet (compare Terao, 1998; Wakabayashi and Kawamura, 2004).

The thermal-wind relation is assumed to be of primary local importance for zonal wind speed changes and, thus, for the development of displayed PC-features (compare Holton, 1992; Kuang and Zhang, 2005; Schiemann et al., 2009). Changes in the thermal-wind-relation are presented in terms of composites for temperature differences between meridionally adjacent grid points. Here, the meridional temperature difference is defined as the vertical mean of its values on the pressure levels between 500hPa and 200hPa for ERA-40. Results may be compared to Kuang and Zhang (2005), who use a slightly different definition. Koch et al. (2006) and Schiemann et al. (2009) depict, how the view of monthly mean jet climatologies deceives with regard to the 'true' zonal wind structure, and how much transient behaviour is excluded. Thus, strong anomalies of the meridional temperature difference hint to a large local thermal impact on the monthly mean zonal wind structure, while otherwise different, presumably transient, factors have to be considered.

Composites Easterly zonal wind anomalies over the Arabian Sea and westerly anomalies north of it are most pronounced in 600hPa for PC1 in April (Figure 3.17). From May to August a tripole is seen with westerly anomalies over the equatorial Indian ocean and across the Caspian Sea. In July, the northern anomalies can be traced upstream to northern Europe and the Mediterranean and downstream to the Pacific. Thus, generalising, PC1 captures the zonal wind variability not only in the section between 50° and 65°E but over the whole longitudinal extent of Eurasia. Composite anomalies in 200hPa reach from the north Atlantic to the western and central north Pacific for most months (Figure 3.16). In May and June, anomalies crossing the Caspian Sea are blocked and de-

3.4 Upstream influence on precipitation

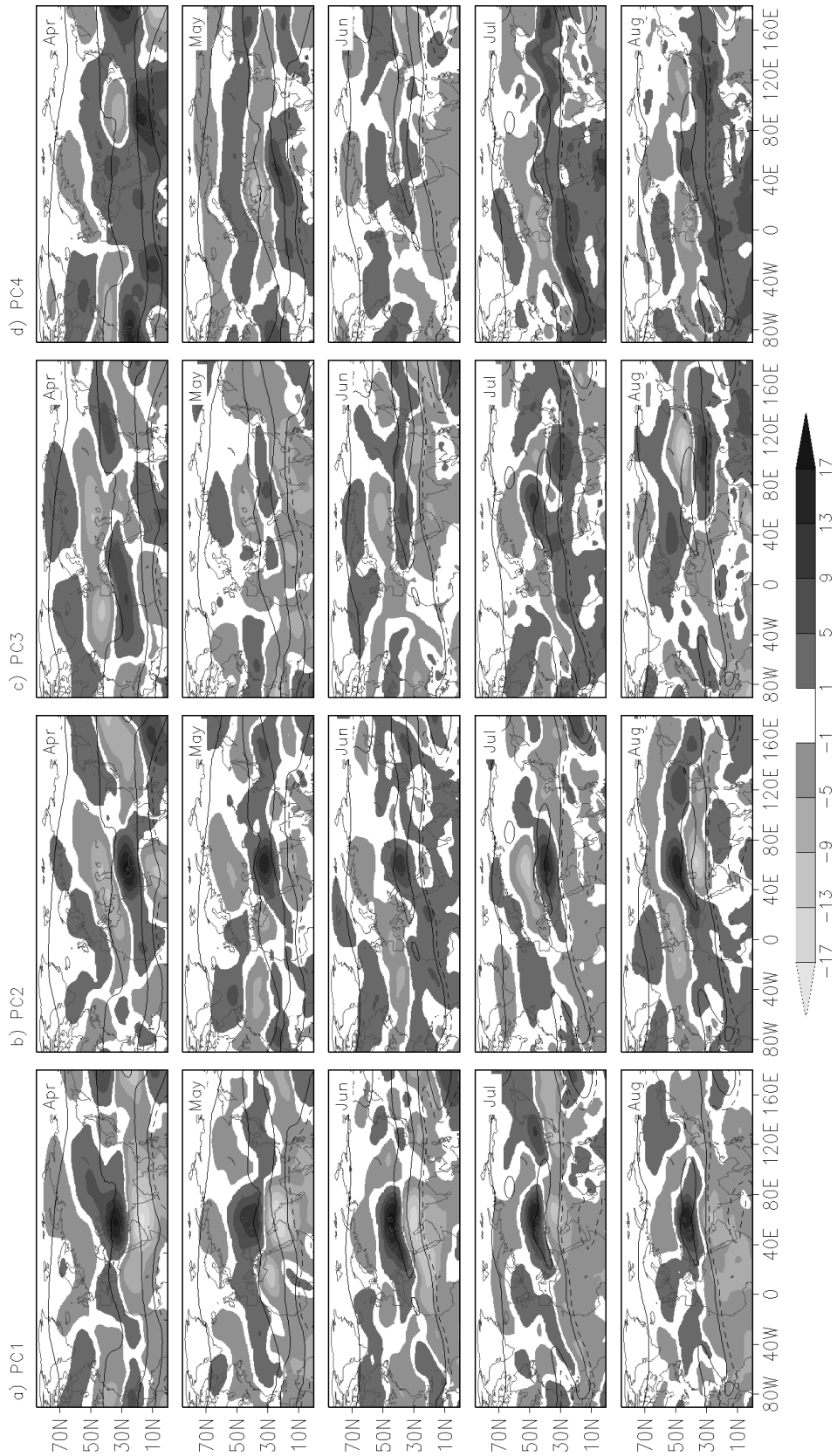


Figure 3.16. Calendar monthly composite differences for the zonal wind on $200hPa$ (shaded) from April to August (top to bottom) for a) PC1, b) PC2, c) PC3, d) PC4. Contours are the monthly mean ($\pm 20m s^{-1}$ and $\pm 2m s^{-1}$).

3 Central Asian precipitation – the upstream zonal wind structure

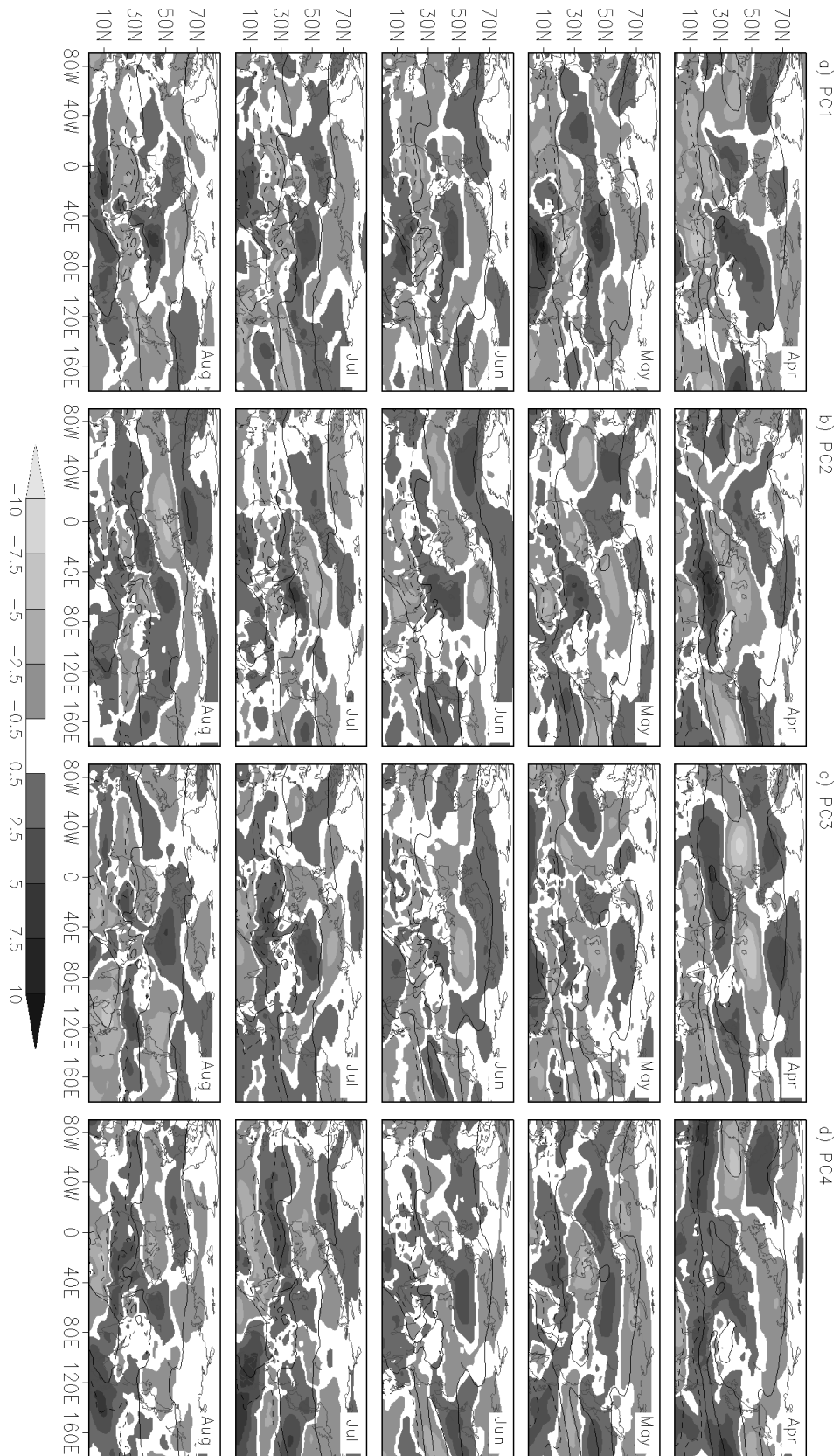


Figure 3.17. Calendar monthly composite differences for the zonal wind on 600hPa (shaded) from April to August (top to bottom) for a) PC1, b) PC2, c) PC3, d) PC4. Contours are the monthly mean ($\pm 10m s^{-1}$ and $\pm 2m s^{-1}$).

3.4 Upstream influence on precipitation

flected southward. Note the continuous easterly anomaly from the Arabian Sea to the Meiyu-Baiu-region in July and August.

Meridional temperature difference anomalies for PC1 show smaller meridional differences in the low latitudes, while these are enhanced in all months over, approximately, the Caspian Sea (Figure 3.18). In April these anomalies reach from northern Africa to the Pacific. For May, weakened differences arise over the maritime continent. The Himalayas and the Mongolian Plateau disturb the latitudinal anomaly bands in June and July. Negative anomalies are seen over Japan and Korea in August, when an otherwise uniform anomaly stretches from the eastern Mediterranean to eastern Asia. This, evidently, embodies the variability in the meridional jet position, already seen in the PCs and the horizontal zonal wind fields.

The zonal wind composites relative to PC2 depict a tripole of anomalies, that shifts northward with the mean jet position. In July and August, it is extended to a quadropole of anomalies on the $600hPa$ level. From May to August, westerly anomalies reach the Tian Shan and bifurcate around the orography in lower levels. Stronger anomalies are found in the lower levels upstream over the north Atlantic and downstream in the east Asian monsoon region. Downstream extensions of upper level anomalies are most pronounced in May and August. In April and July, the upper level flow is deflected south- and northwards, respectively. Upstream anomalies are generally anti-symmetric to anomalies in the section between 50° and $65^{\circ}E$.

For PC2 largest meridional temperature difference anomalies are found from the Caspian Sea to about $90^{\circ}E$ in summer, while they arise north of the Arabian Sea in late spring related with the transition of the jet. In April, a sign reversal is noteworthy in east Asia, and, in August, anomalies extent nearly from the Atlantic to the Pacific.

Most pronounced for PC3 are easterly zonal wind anomalies from April to June and westerly anomalies from July to August crossing the Caspian Sea. These constitute southern extensions of the stronger variability in the polar front jet as stated above. Four major bands stretch approximately along latitude circles from the Atlantic to the Pacific in April, while the anomalies are mostly confined to central Asia from May to July. Upper level anomalies are prominent over eastern Asia in August. The latitudinal bands seen in composites for April-PC3 arise similar in composites for May-PC4 and, to some extent, for July-PC4. Lower level anomalies are strong upstream over Europe in April, July and August and downstream over the north Pacific from May to July. Eastern Asian and northern Pacific anomalies are also the most prominent features from April to July in upper levels.

Composites of meridional temperature differences relative to PC3 and PC4 stand out, because large anomalies arise over east Asia. Contrasting signs are noteworthy between central and eastern Asia. Relative to PC4 anomalies are weak. Eastern Asian anomalies dominate in April and August, while eastern Mediterranean and Caspian Sea anoma-

3 Central Asian precipitation – the upstream zonal wind structure

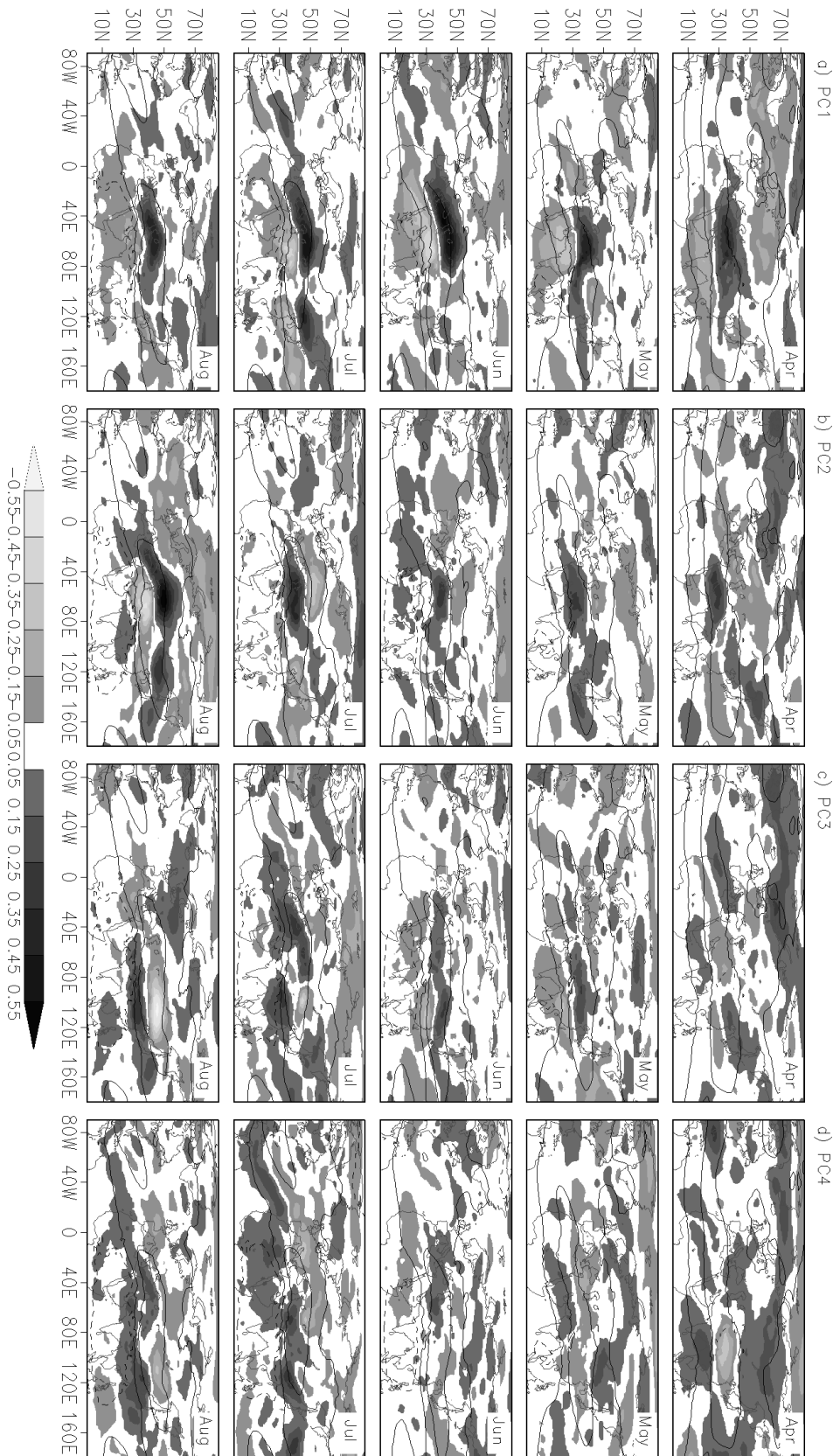


Figure 3.18. Calendar monthly composite differences for the temperature difference between meridionally adjacent grid points (shaded, averaged from 500hPa to 200hPa) from April to August (top to bottom) for a) PC1, b) PC2, c) PC3, d) PC4. Contours are the monthly mean ($\pm 0.5K$ and $\pm 0.1K$).

3.4 Upstream influence on precipitation

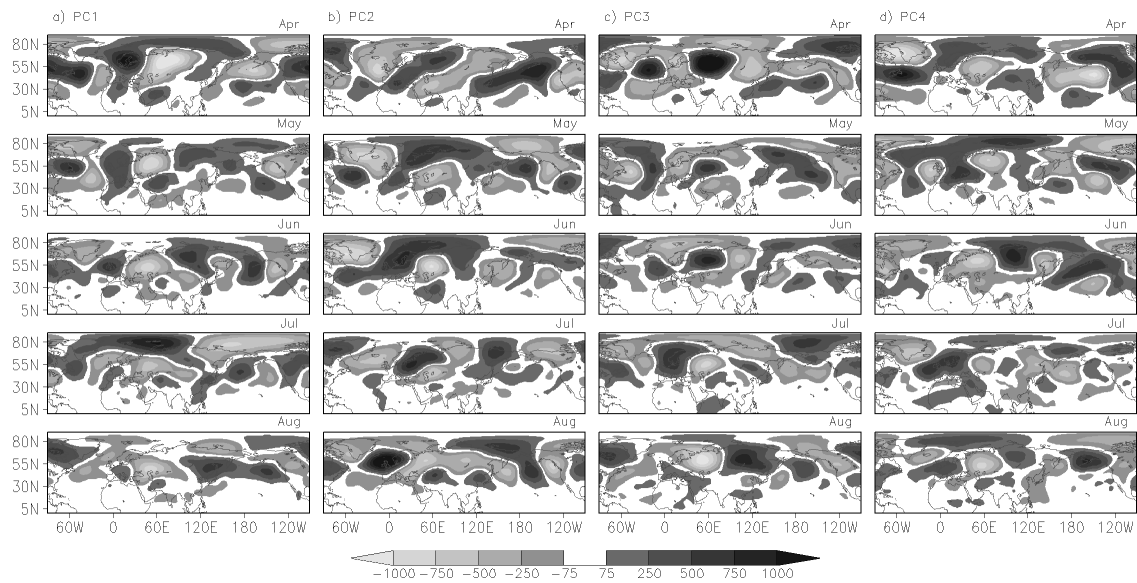


Figure 3.19. Calendar monthly composite differences for the zonally asymmetric $500hPa$ geopotential from April to August (top to bottom) for a) PC1, b) PC2, c) PC3, d) PC4.

lies are more pronounced from May to July. Prominent, spatially extended anomalies are also displayed over the northern latitudes in the Atlantic-European region in some months with respect to PC3 and PC4.

3.4.4 Teleconnections

In the following, correlations are computed between the PC time series and selected teleconnection indices. These coefficients display coherence of the zonal wind PCs with Atlantic and Pacific sector atmospheric indices and the Indian and Pacific ocean sea surface temperatures in simultaneous and preceding months. Only concurrent correlations are discussed and results are tabled in appendix C. Daily mean values of ERA-40 data for temperature and zonal and meridional wind components on selected pressure levels are interpolated onto a T21-grid ($\sim 5.6^\circ \times 5.6^\circ$), and variances and covariances are computed for the eddy components. Only correlations of monthly mean $300hPa$ and $850hPa$ eddy temperature transports are discussed.

April The zonally asymmetric $500hPa$ geopotential reflects influences of variability in the Atlantic/European sector (composited relative to PC1, Figure 3.19a). Wave train like patterns are visible from the Atlantic across northern Eurasia and arching from Scandinavia to the Arabian Sea. Composites with respect to PC2 display south-west/north-east tilted patterns over Eurasia crossing the Mediterranean and the northern latitudes. The signature of the EAWR is substantial (compare NOAA, 2005–2008) and the index

3 Central Asian precipitation – the upstream zonal wind structure

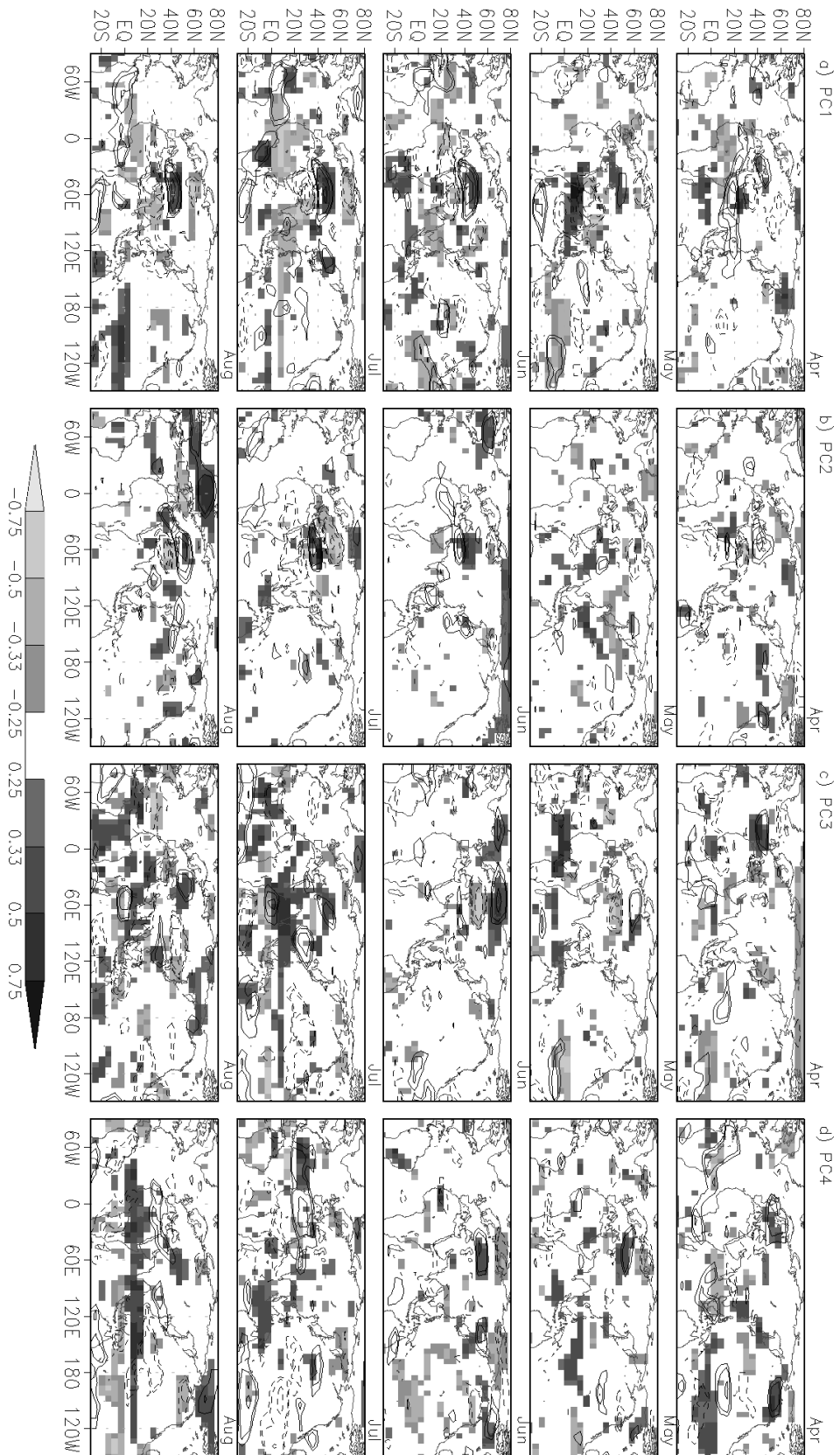


Figure 3.20. Spatial correlations from April to August (top to bottom) with $U'T'$ on 850hPa (shaded) and 300hPa (contours) for a) PC1, b) PC2, c) PC3, d) PC4.

is strongly anti-correlated. Relative to PC3, composite differences are similar to the Europe-Japan pattern (Wakabayashi and Kawamura, 2004). Central Eurasian and Atlantic features in Figure 3.19 display EA and EAWR relations, which are further substantiated by correlations (see appendix C).

Correlations of PC1 and the spatial fields of the fluxes emphasise the zonal transports in the lower latitudes in April (Figure 3.20). Additional transport from the Mediterranean region is resolved in zonal and meridional transport correlations (Figure 3.21). Zonal transport correlations for PC2 are most notable in the domain used for the PC-analyses. Thus, air-sea-interaction is especially important for the structure of the zonal wind in the western Indian ocean in April. PC3-correlations show strong coherence with meridional and zonal transports in the Atlantic/European sector. Coherence is further seen in the tropical south Atlantic. Correlations between the PC4 time series and the zonal transports also denote a connection to northern Europe and exhibit particular coherence in the central Pacific, indicating a remote influence of the Pacific ocean and the overlying atmosphere.

May Compositing geopotential anomalies are diminished in summer in agreement with the seasonally reduced atmospheric variability. Sea surface temperature indices in the tropical Pacific dominate correlation-analyses (compare table C.2). Atmospheric pattern signatures are weak. For example, the EAWR influence on PC1 is reduced to the central western Russian anomaly. However, wave trains are still visible from the Atlantic to central Asia especially for PC2 and PC3. Anomalies in northern latitudes are emphasised in composites relative to PC1 and PC4.

The spatial correlation field between PC1 and the meridional transports (Figure 3.21) indicates a wave train structure in May. Zonal transports are largest in the eastern Pacific and the Indian ocean corresponding to relations with SST-teleconnection-indices (e.g. table C.2). Correlation fields for PC3 and PC4 confirm the assumption, that these two loadings are mostly a visualisation of more northern Eurasian variability. Lower level correlations (shaded in Figures 3.20 and 3.21) additionally exhibit coherence in the tropical Pacific for PC3 and PC4.

June Weak relations to the Antarctic oscillation index (AAO, not shown) in spring are found for the summer months. For detailed discussions of the relation between the AAO and Asian climate the reader is referred to, among others, Nan et al. (2009), Wu et al. (2009), Sun et al. (2009a), Nan and Li (2003) and Xue et al. (2003).

Figure 3.19 indicates an annular structure in the zonally asymmetric geopotential compositing relative to PC1 and PC2 in the Atlantic sector. Anomalies with respect to PC2 further display the summer pattern of the EAWR (compare NOAA, 2005–2008), but relations to Eurasian-Atlantic teleconnection patterns are not deducible in the compos-

3 Central Asian precipitation – the upstream zonal wind structure

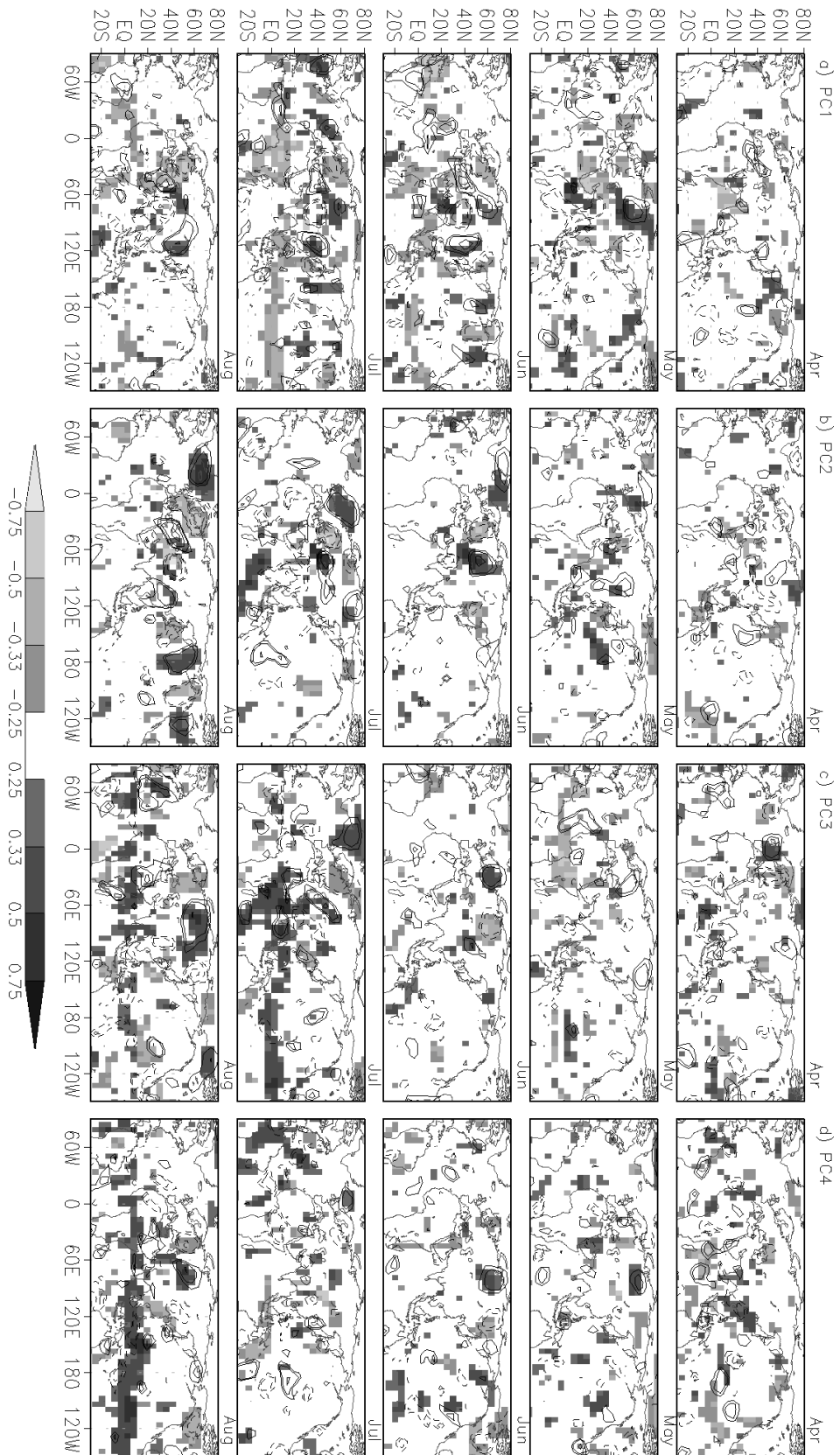


Figure 3.21. Spatial correlations from April to August (top to bottom) with $V'7'$ on 850hPa (shaded) and 300hPa (contours) for a) PC1, b) PC2, c) PC3, d) PC4.

3.4 Upstream influence on precipitation

ites for PC3 and PC4. The anomalies are oriented along higher latitude bands. In the Pacific region though, a transitional pattern or a simultaneity of WP and EPNP can be deduced from the composites for PC4.

The area utilised in the PC-analyses dominates transport correlation fields in June. Correlations extend across northern Africa to the Atlantic for PC1 and PC2 and the zonal transports (Figure 3.20), while a wave train like pattern arises in the correlation with the meridional transports for both (Figure 3.21). For PC1, this feature nearly extends circumglobal, while it is only seen from Europe to central Asia for PC2 (compare chapter 4 and Ding and Wang, 2005). PC3 and PC4 correlations are most notable in the higher latitudes. Relations with variables in the Pacific region are found in the lower levels for PC1 and PC4.

July Correlations are largest in July between teleconnection indices and the monthly zonal wind PC time series (table C.2). Compared to the patterns of Barnston and Livezey (1987) and NOAA (2005–2008), WP, EAWR and POL signatures are visible in the geopotential composites relative to PC1 (Figure 3.19). For PC2, solely a weak summer PNA pattern can be deduced in higher latitudes, which is also present in composites for the uncorrelated PC3. In addition, a wave train pattern in the Atlantic is visible. The circulation upstream and downstream appears to impact the region utilised for the zonal average (50° to 65°E). Composite differences with respect to PC4 may relate to the EA pattern, whose index is highly anti-correlated.

In July, a nearly circumglobal pattern is found in the map for the meridional temperature transport correlations with PC1. Similar features arise in the region from Europe to central Asia for PC2 and PC3. Additional correlations are noted in the higher latitudes of Eurasia. Zonal transport correlations are strongest in the domain of the PC-analysis. Further notable correlations are found with the zonal transports in the tropical north Atlantic for PC1, PC2 and PC3 and in northern Africa for PC4. Coherence of PC3 and PC4 with the upper level fluxes in the central Pacific and central Indian ocean strengthen the assumption of an Pacific influence on the westerly jet upstream of central Asia (compare correlations in table C.2). Flux-correlations are distinct for PC1, PC3 and PC4 over large areas of the tropics in the lower levels.

August The EPNP pattern is visible in the geopotential anomalies composited relative to PC1 (Figure 3.19). Signature features of the strongly correlated EAWR pattern are identifiable over Eurasia. Considering PC2, a slightly annular behavior (e.g. part of the seasonal AO pattern map) is visible in the Atlantic. Patterns further resemble a blocking NAO-feature or EA and EAWR patterns. Annular features again are seen in the composites with respect to the PC3 time series. Additionally, anomalies resemble part of the EPNP pattern downstream of central Asia and a superposition of EA and SCA

3 Central Asian precipitation – the upstream zonal wind structure

features upstream. Composited relative to PC4, a wave train bridges northern Eurasia from the Atlantic to the Okhotsk Sea and extends to the west coast of north America.

Eddy temperature transport correlations present a circumglobal pattern for PC2 in August, particularly for the meridional component. More local or small-scale wave train features are seen in the PC1-correlations. Correlations with the zonal transport component show an additional band of coherence from north Africa to east Asia and another one in the equatorial Atlantic. Multiple small scale patterns are displayed in the correlations for PC3 and PC4 in both levels in the tropics and over northern Eurasia. A possible link between PC1 and the Pacific region (compare table C.2) is emphasised by the lower level correlations. The SST-index-correlations are captured in correlations with ERA-40 heat fluxes (not shown). Although no significant correlations exist between PC4 and NINO-indices, the lower level zonal and meridional eddy temperature transports (Figures 3.20 and 3.21) are noteworthy in the central Pacific.

3.5 Summary and discussion

The zonal wind climatology is described systematically for a zonally averaged section between 50°E and 65°E. Reported results focus on its impact on central Asian precipitation. The rationale is, that precipitation variability in the Tarim river basin, the Tian Shan mountains and on the Tibetan Plateau is determined to a considerable extent by the zonal wind variability upstream of the larger Himalaya region. The validity of this assumption aids in the evaluation and predictability of the climate in central Asia. It further defines the degree to which it is suitable to employ re-analysis data and general circulation models in climate studies for this region. Using these data will always result in a mere approximate description, because a closer view can only be achieved by using regional and high resolution models, which in turn will rely on the upstream and surrounding forcing of lower resolution models (e.g. AOGCMs). Fundamental base of any such study is the validity of the precipitation climatology. Schiemann et al. (2008) concede, that the Vasclimo data can be employed for studies of the precipitation climate in larger central Asia.

The first four principal components for the section in the height-latitude-plane describe the general variability in meridional position and strength of the main subtropical jet and the variability in the mid- and high latitudes. The annual cycles of all four PC-loadings depict the transitions of the mean jet due to the seasonal evolution of solar insolation. A description is achieved of their impact on precipitation climates in the Tian Shan, on the Tibetan Plateau and in those parts of the Tarim river basin, which receive runoff from the Tian Shan. Noteworthy coherence is found between the upstream zonal flow and the monthly mean precipitation climate from April to August, while in September no coherence is seen at all. The absence of a relation in September can

be attributed to the strong change in the northern hemispheric atmospheric circulation from late summer to early autumn. The diminished coherencies in winter are related to the seasonal jet location in the south and, hence, diminished available moisture in continental air masses. Strengthened westerly moisture flow arises climatologically from April to August, that is in an extended summer season. Especially notable is the strong dependence of PCs on “modes” of the previous months, that is the found persistence.

The Tarim standardised precipitation time series is related to the position of the jet in April, June, July and August, the strength of the bifurcation around the Tian Shan in May and July and the strength of the flow at about 45°N in August. Regressing the June-SPI for the Tarim basin against three PCs for the preceding May explains nearly 50% of the variance of the June-SPI. Admittedly, this is the best result for presented multiple regression analyses.

The Tibetan Plateau precipitation (compare chapter 4) in May and June is influenced by the inter-annual variation in jet-position. This relationship on its own explains 40% of Tibetan Plateau SPI variance in May, while, in July and August, the strength of the mean jet in relation to the higher latitudinal flow is more important. These latter connection depicts the intensity of the (meridional) monsoon flow from the Arabian Sea.

The north-western region is influenced by variations in jet position, its strength and the strength of the mid- to high-latitudinal flow in April. The strength of the mean flow is also of importance for the north-east. In May, when the jet is directly over the Iranian Plateau, the variability north of the mean jet is most important for the northern areas. The variability of the meridional position affects the north-west in June. In July, variations in its strength are coherent with precipitation variations in both northern regions. Then, the north-west also is influenced by the strength of more northern zonal flow relative to the mean jet variation. Both modes are correlated with the SPI in the northern regions again in August, when a multiple regression against PC2 for the preceding July and the simultaneous PC1 and PC3 explains about 48% of the variance of the SPI series in the north-east.

It is not feasible to interpret these results as distinct physical mechanisms. Monahan and Fyfe (2009) demonstrate the inclusion of fluctuations of other modes in single principal component time series. That is, while the leading pattern arises from variations in one physical property of the jet for principal component analyses of zonal wind sections, the associated time variations include information from other properties.

The importance of the westerly inflow and inflow with a south-westerly component is emphasised in the monthly mean moisture flux composite differences, while eddy flux composites give heterogenous results. As shown by Yatagai and Yasunari (1995, 1998) northerly and southerly eddy fluxes are as present as zonal fluxes. Monthly mean flux composites additionally display contributions of easterly inflow from the east Asian monsoon region into all discussed areas, while southerly flow affects the Tarim and the

3 Central Asian precipitation – the upstream zonal wind structure

Tibetan Plateau from the Arabian Sea, but only the Plateau from the Bay of Bengal.

Composites of horizontal zonal wind and meridional temperature differences indicate upstream teleconnections with the north Atlantic sector. Correlations with teleconnection indices are only of informative value. Faulwetter (2007) discusses the subjectivity of the pattern computation, the possible mixture of patterns and the influence of seasonal changes in patterns on the resulting indices. Calculated correlation coefficients are quite variable and not usually consistent over some months. However, correlations of monthly zonal wind PCs and the atmospheric teleconnection indices establish reasonable links between the studied section and the upstream atmospheric circulation, besides the connection to the regional circulation variability and the dependence on tropical SST forcing from the Atlantic ocean (e.g. Kucharski et al., 2007, 2008), the Indian ocean (e.g. Saji et al., 1999; Hong et al., 2008) and the Pacific ocean (e.g. Webster and Yang, 1992; Hong et al., 2008).

Upstream bridges can be taken as parts of most Atlantic/European teleconnection patterns. Features stretch across northern Eurasia, across the Mediterranean to Asia or arch from northern Europe to central and eastern Asia (compare chapter 4 and Blackmon et al., 1984a,b; Ambrizzi and Hoskins, 1997; Ambrizzi et al., 1995). These patterns are most clearly depicted in the flux-correlations. In April, correlations of PC1, PC3 and PC4 with the zonal eddy temperature flux hint to wave-like patterns as do correlations between PC3 and the meridional component of the eddy temperature flux. Arching patterns are especially evident in the August correlations for PC2. Wave-like patterns are also visible in the correlations of PC1 with the meridional component in June and of all PCs in July.

The circumglobal teleconnection pattern (Ding and Wang, 2005) is closely related to temperature anomalies in the tropical Indian ocean according to recent results by Yang et al. (2009). Their findings indicate a possible atmospheric response in the northern hemisphere extratropics from northern Africa to the high latitudes of Europe in summer after an initial warming in the tropical Indian ocean. Circumglobal patterns are notable in the presented flux correlation maps in July. It is beyond the scope of this chapter to clarify the act and response relation between the upstream circulation over Europe and the state of the tropical Indian ocean. Yang et al. (2009) accentuate the necessity to resolve the connection between the larger south Asian monsoon region and the north Atlantic/Europe sector. Thorough representations of the dynamics and the forcing of these atmospheric bridges require daily, higher resolved data sets. Variability and some of the structures of north Atlantic atmospheric teleconnections are discussed in chapter 5 for simulation data and boreal summer.

4 Eurasian bridges¹

Abstract

Effects of large-scale atmospheric circulation and surface temperatures on extreme dryness and wetness on the Tibetan Plateau in summer are analysed using ERA-40 re-analysis data and observed precipitation for the 20th century. Results of IPCC-simulations with the coupled climate model ECHAM5/MPI-OM are considered to assess the ability of GCMs to reproduce observed dynamics and to evaluate possible future changes. The extreme cases of drought and wetness can be associated with circulation anomalies in the north Atlantic/European sector and wave trains bridging the Eurasian continent. Drought on the Tibetan Plateau reveals an intense high pressure anomaly over Scandinavia supported by a more south-west to north-east orientated north Atlantic storm track. This creates wave trains crossing Eurasia, which, subsequently, reduce the moisture inflow to the Tibetan Plateau. Wetness in Tibet is characterised by a more zonally oriented north Atlantic storm track. Wave trains emerging from the north Atlantic reach the subtropical jet entrance and, passing the Mediterranean-Arabian Sea route to India, interact with the monsoon's western branch to lead to ample moisture supply for Tibet. Zonal flow prevails in the extratropics in the simulations. In the observations, surface temperatures give indications for positive (negative) El Niño/Southern Oscillation and Indian Ocean Dipole episodes occurring in years of dryness (wetness) on the Tibetan Plateau. Simulated dry (wet) months concur with a warming (cooling) in the tropical Indian ocean. Future scenarios show little change of atmospheric flow composites; Tibetan Plateau droughts increase by ten percent for an A1B-scenario, and extreme wet summer months are reduced by approximately one percent.

4.1 Introduction

The Tibetan Plateau covers an area of half the size of the United States, over two million square kilometers, with an average elevation of about four kilometers. It is of outstanding relevance for the atmospheric circulation. In particular, it is of primary importance for the Eurasian and northern hemispheric climate including the Austral-Asian-monsoon circulation. From an atmospheric point of view its altitude leads to an elevated heat source and its extent (including the Himalaya Range) presents a mechanical barrier

¹This chapter incorporates the published manuscript by Bothe et al. (2009) and the manuscript by Bothe et al. (2010) which is accepted for publication.

4 Eurasian bridges

(for example Flohn, 1968; Raghavan, 1973; Hahn and Manabe, 1975; Tang and Reiter, 1984; He et al., 1987; Li and Yanai, 1996; Wu and Zhang, 1998; Held et al., 2002; Hsu and Liu, 2003; Zhang et al., 2004; Sato and Kimura, 2007; Wang et al., 2008a). Precipitation in the Tibetan Plateau area is of great importance for the hydrology and agriculture in the downstream river basins of, notably, Ganges, Indus, Mekong, Huang He, and Yangtze (Fekete et al., 1999, 2000). The Plateau is often regarded as Asia's "water tower" (Xu et al., 2008), because it serves as the water source of these large Asian rivers. Thus, Tibetan Plateau precipitation variability and the factors influencing it potentially affect the lives of more than two billion people in the bordering countries (Xu et al., 2008).

Assessment of possible future climate changes relies on the ability of coupled ocean-atmosphere general circulation models (GCMs) to capture the effects of the Tibetan Plateau and the forcings due to anomalies in the larger environment, say, for example, sea surface temperatures (SST). The model representation of precipitation depends critically on its resolution and the orography implemented (Dai, 2006). Especially in orographically pronounced regions like the Tibetan Plateau and its surroundings (e.g. the larger Asian monsoon region) large errors occur in modeled precipitation, its means and variances (Hagemann et al., 2006; Kripalani et al., 2007; Orłowsky et al., 2009).

There are three routes of moisture supply to the Tibetan Plateau (Figure 4.1 and Simmonds et al., 1999): (i) the Arabian Sea and Bay of Bengal, (ii) the South China Sea, and (iii) the mid-latitude westerlies. They are closely linked to the Asian monsoon circulation, and further are subject to the influence of long distance teleconnections and stationary wave activity: (i) On the intra-annual time scale, the North Atlantic Oscillation (NAO) has an impact on the temporal and spatial precipitation variability over the eastern part of the Tibetan Plateau (Liu and Yin, 2001) in summer and a wave train teleconnection related to the NAO bridges Eurasia in March (Li et al., 2008a). (ii) On decadal to centennial time scale the north Atlantic multidecadal and the Pacific decadal oscillations affect Eurasia (d'Orgeville and Peltier, 2007; Zhang and Delworth, 2006; Gupta et al., 2003; Ye, 2000; Goswami et al., 2006; Zhang and Delworth, 2007; Feng and Hu, 2008). (iii) A number of additional intra-annual modes are shown to link the north Atlantic and Europe to Asia, and eastern Asia to north America, respectively (Ding, 2007). Among these the results of Wakabayashi and Kawamura (2004), Ding and Wang (2005) and Sato and Takahashi (2006) are most notable, who demonstrate quasi-stationary almost circumglobal wave patterns along the northern hemispheric westerly jet and emphasise their influence over Eurasia. In addition, Wakabayashi and Kawamura (2004) find two zonally orientated wave patterns from Europe to the Okhotsk Sea crossing northern Eurasia. Ding and Wang (2005) describe a circumglobal teleconnection pattern in boreal summer, which they decompose into two conceptual scenarios. Scenario-1 incorporates an active Indian summer monsoon forcing a downstream Rossby wave train along the westerly jet, while scenario-2 describes a Rossby wave train, which is triggered

by disturbances in the upstream north Atlantic jet exit region and reaches eastward to Asia influencing the Indian summer monsoon precipitation. These remote wave train connections are usually supported by waveguides along the mid-latitude and subtropical jets (see, for example, Hoskins and Ambrizzi, 1993; Ambrizzi et al., 1995).

The routes of moisture to the plateau are furthermore modified by sea surface temperature conditions (Hong et al., 2008). Regional and remote sea surface temperature anomaly influences on Tibetan Plateau precipitation can be classified as 'direct' and 'indirect' impacts. The Indian Ocean Dipole Mode (IOD, Saji et al., 1999) and El Niño/Southern Oscillation (ENSO, Webster and Yang, 1992) directly influence the subsystems of the Asian monsoon circulation (e.g. Hong et al., 2008; Chang et al., 2000a,b; Yun et al., 2008) with subsequently reduced or enhanced moisture fluxes onto the Tibetan Plateau. Hong et al. (2008) demonstrate that positive events (positive IOD, El Niño, and both combined) reduce the moisture inflow from the southerly moisture origins (Arabian Sea, Bay of Bengal, south-east monsoon) to the Tibetan Plateau while these are strengthened during negative episodes (negative IOD, La Niña, and both combined). Kucharski et al. (2008) report the non-ENSO-forced component of the Indian monsoon variability to be driven by remote tropical Atlantic SST anomalies (primarily the Gulf of Guinea). Lau and Peng (1992) describe atmospheric teleconnections due to anomalous tropical divergence forcing in boreal summer. In their study a wave pattern emerges in the subtropics of the west Pacific that arches north-eastward via north America to the north Atlantic storm track. The latter is forced by anomalous stationary wave activity flux emerging over the north American continent. In winter an extratropical response to western Pacific ENSO-forcing arises (Shaman and Tziperman, 2005) with an eastward propagating Rossby wave. This remote influence affects snow fall over the Tibetan Plateau with subsequent impacts on the Asian monsoon.

This chapter focusses on severe and extreme drought and wetness on the Tibetan Plateau. These are analysed in their relation to large-scale disturbances. This topic is of interest not only for eastern Asian monsoon research but for climate and seasonal forecasts, and for paleoclimate studies (Zhang et al., 2008; Wang et al., 2008d). Section 4.2 describes data and methods, in section 4.3, first, composites are analysed for extreme and severe dry and wet summer months, discussing the atmospheric flow over Eurasia and the associated surface temperatures in the observed period from 1958 to 2000. Section 4.3 further demonstrates the ability of GCMs to represent the upstream impact on Tibetan Plateau precipitation, and utilises a long model run providing a larger sample size for the evaluation of circulation anomaly statistics. A further topic is the interaction of tropical forcings with upstream extratropical influences. In addition, future changes in drought and wetness occurrence are studied. Section 4.4 summarises the results and draws conclusions.

4.2 Data and methods

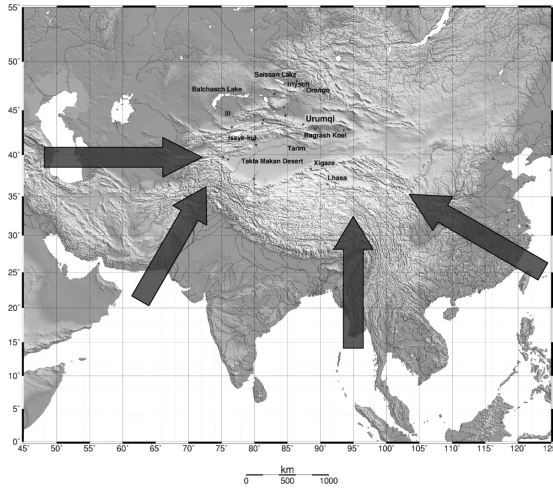


Figure 4.1. Schematic plot of the moisture paths to the Tibetan Plateau as described by Simmonds et al. (1999), background-map prepared by Frank Sielmann

Observed precipitation data is taken from the Vasclimo climatology (Variability Analysis of Surface Climate Observations, Beck et al., 2005), which spans from 1951 to 2000 with $1^\circ \times 1^\circ$ resolution. Surface (skin temperature) and upper air data (U- and V-wind-velocities, specific humidity, and geopotential on pressure levels) are obtained from ERA-40 re-analysis (September 1957 to August 2002, Uppala et al., 2005). Vasclimo precipitation and ERA-40 circulation data are analysed during the overlapping period 1958 to 2000 on a monthly basis for the summer season (June, July, August) and for preceding three months, respectively.

It is noted, that the number of upper-air and surface stations used for the precipitation climatology is low on the western Tibetan Plateau. Correlations are about 0.8 between Plateau averaged station data for the period 1961 to 2000 and the Vasclimo Plateau time series for the same period. As monthly precipitation differs strongly in various regions on the Plateau, the present study adopts the standardised precipitation index (SPI, McKee et al., 1993), which establishes reasonable agreement of point-wise and Plateau-averaged drought and wetness classifications. Many studies discuss the influence of local orography and surface conditions on heating mechanisms, precipitation amount and structure of the atmospheric boundary layer over the Plateau (Yanai and Li, 1994; Ma et al., 2002; Ueda et al., 2003). Böhner (1994) emphasises in a discussion of the representativeness of station data for precipitation and temperature on the eastern Tibetan Plateau, that a single station series is unlikely characteristic for more than a radius of a couple of hundred kilometres, if the precipitation is of a stratiform, advective origin, while data is solely locally distinctive in case of convective precipitation climates. Here the background flow for the months of extreme wetness and dryness is presented.

Additional analysis is based on IPCC-simulations of the GCM ECHAM5/MPI-OM (Roeckner et al., 2003; Marsland et al., 2003) with the IPCC AR4 emission scenarios (Nakicenovic and Swart, 2001). A triangular T63 resolution ($\approx 2^\circ \times 2^\circ$) with 31 vertical levels is applied for the atmosphere. The ocean model MPI-OM uses 1.5° resolution without flux correction. Main results are presented for the pre-industrial control-run and compared with the commitment phases of (a) 20th century (20C) and (b) A1B sce-

nario ensembles (three members with 100 years, A1B run number two has 200 years of data). The control-run (pre-industrial) has a length of 506 years. Model runs analysed are referred to as control-run (pre-industrial), 21st century (commitment phase of the 20C ensembles), and 22nd century (commitment phase of the A1B ensembles). Precipitation and atmospheric circulation data are analysed on a monthly basis for the summer season (June, July, August) and for preceding months for the full period. Precipitation is used as an area averaged time series for the Tibetan Plateau.

The Tibetan Plateau is defined in a $1^\circ \times 1^\circ$ resolution as the area above 2500m and then interpolated onto the respective grid (e.g. T63 for ECHAM5). Moisture fluxes for simulation and ERA-40 data are computed following Simmonds et al. (1999).

Standardised Precipitation Index (SPI) The SPI (introduced by McKee et al., 1993) is used to classify and monitor dryness and wetness. The calculation of the SPI is based on an “equal probability transformation”: monthly precipitation is transformed to a standard normal distribution to yield SPI values by preserving probabilities (for details see, e.g., Bordi and Sutera, 2001). Due to its standardisation the SPI gives a uniform measure for dryness and wetness in different climate regimes and on different time scales.

The transformation depends critically on the assumed statistical distribution. A false distribution type may lead to systematic errors, most pronounced for the extreme cases. That is, the commonly used gamma distribution (Bordi et al., 2007) does not necessarily hold for all months; better fits can be achieved using the Weibull distribution. In order to still use a single unifying distribution type, the “Generalised Gamma Distribution” is applied instead, employing a re-parameterised version (Sienz et al., 2007).

The SPI can be constructed for different time scales characterising periods of meteorological (months), hydrological (season) and agricultural (year) dryness or wetness. Here the monthly time scale is chosen as a meteorologically relevant lower bound for dry and

Table 4.1. Standardised Precipitation Index classification and event-probability (P in %).

| SPI-Intervals | SPI-Classes | P-Values |
|----------------------|--------------------|-----------------|
| $SPI \geq 2$ | extremely wet | 2.3 |
| $2 > SPI \geq 1.5$ | severely wet | 4.4 |
| $1.5 > SPI \geq 1$ | moderately wet | 9.2 |
| $1 > SPI > -1$ | normal | 68.2 |
| $-1 \geq SPI > -1.5$ | moderately dry | 9.2 |
| $-1.5 \geq SPI > -2$ | severely dry | 4.4 |
| $SPI \leq -2$ | extremely dry | 2.3 |

wet spells and their extremes (Dracup et al., 1980). The SPI classification accords with McKee et al. (1993, see Table 4.1).

The transformation of precipitation to SPI is also utilised to assess future changes in dryness and wetness (following Sienz et al., 2007) on the Tibetan Plateau in the scenario data for ECHAM5/MPI-OM. Therefore, the scenario-run Tibetan Plateau precipitation is transformed using the parameters of the transformation of the control-run precipitation. Thus, the same monthly precipitation amount in the future results in the same SPI-value, but the ‘equal probabilities’ are now representing the scenario-run-precipitation distribution. This results in deviations from the standard normal distribution, which can be expressed as future precipitation changes.

4.3 Tibetan Plateau

4.3.1 Climatological setting

The circulation above the Tibetan Plateau is characterised by the upper level outflow associated with the Tibetan anticyclone and the lower tropospheric flow providing the moisture inflow. The main features of the former are summarised as follows: (i) the divergent flow associated with the tropical Walker type circulation expands over the entire region (Figure 4.2a,b), (ii) the Tibetan Plateau is “sandwiched” by the summer westerly jet passing to its north and the tropical easterly jet to the south of the Himalayas (Figure 4.2c), and (iii) a warm anticyclone controls the Plateau outflow, as indicated by the 300 – 500hPa thickness (Figure 4.2c,d). The zonally asymmetric barotropic component of the upper-tropospheric circulation (Figure 4.2e,f) is displayed for comparison. The stationary wave activity flux climatology (Plumb, 1985) demonstrates the influence of the circulation upstream and downstream of the Tibetan Plateau. Notable are the strong wave activity sources induced by the Himalaya Range and over the eastern Mediterranean region (Figure 4.2e,f). The re-analysis ERA-40 (Figure 4.2; Kållberg et al., 2005) and simulated ECHAM5/MPI-OM climatologies (Figure 4.2, 506 year control-run) show similarity of the basic flow patterns and the underlying dynamics; differences occur in the intensity and location of the continental scale wave activities, storm tracks and jets. The summer westerly jet is stronger over the north Atlantic and over Asia in ECHAM5/MPI-OM (Figure 4.2d) compared to ERA-40 (Figure 4.2c) which is accompanied by a more zonal orientation of the north Atlantic storm track (Figure 4.2e,f).

The three origins of moisture supply (compare Figure 4.1) appear clearly in Figure 4.2g to j (compare to Simmonds et al., 1999): (i) The Indian monsoon transports moisture from the Arabian Sea and Bay of Bengal onto the Tibetan Plateau. This transport becomes particularly important where over the Plateau westerly wind and “gaign” (winds ascending along the western slopes) merge. (ii) The south-eastern Asian monsoon and the western north Pacific subtropical high direct warm moist air from the South China

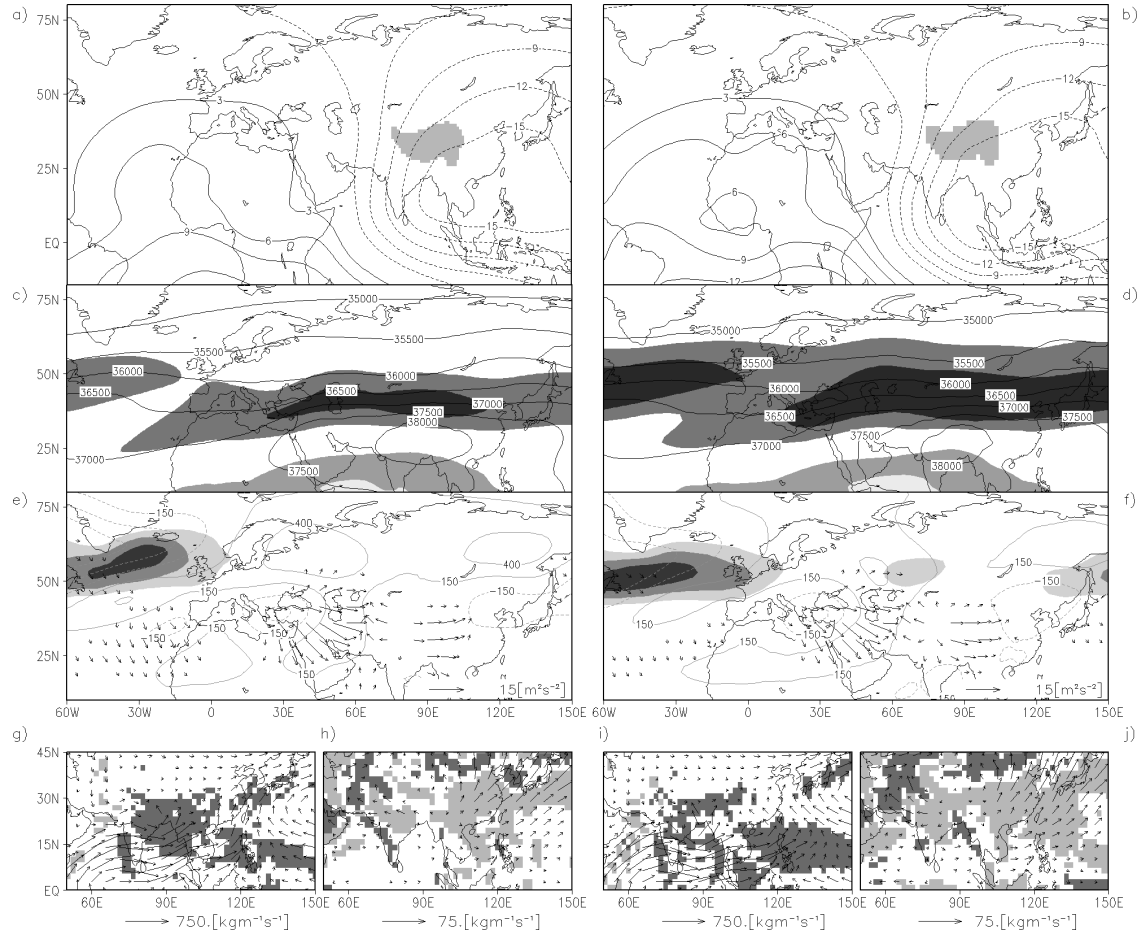


Figure 4.2. Climatologies of ERA-40 re-analysis (left) and ECHAM5/MPI-OM control-run (right) data (Tibetan Plateau shaded in panels a and b): a) and b) 200hPa velocity potential (in $10^6 m^2 s^{-1}$, contours), c) and d) 200hPa zonal wind (in $m s^{-1}$), shaded, the 300hPa – 500hPa layer thickness (contours), e) and f) 500hPa storm track (in $10^2 m^4 s^{-4}$), shaded, zonal asymmetric barotropic upper tropospheric circulation component ($0.5 \cdot (300hPa + 500hPa)$ geopotential) in $m^2 s^{-2}$, contours), Plumb’s stationary wave flux in 500hPa (in $m^2 s^{-2}$, arrows), g) and i) monthly mean of vertically integrated moisture flux and its divergence (in mm per day), h) and j) eddy contribution of vertically integrated moisture flux and its divergence. Shades are from light to dark grey in b), c) $-20, -10, 10$ and 20 and in e), f) $900, 1200$ and 1500 . In g) and i) (h and j) divergence and convergence of moisture flux are shaded in light and dark grey above and below $+5$ ($+0.5$) and -5 (-0.5). Arrows of magnitude smaller 1.5 (in panels e, f), 26 (g, i) and 2.5 (h, j) are omitted. Grids for the fluxes have been adjusted to facilitate comparison.

4 Eurasian bridges

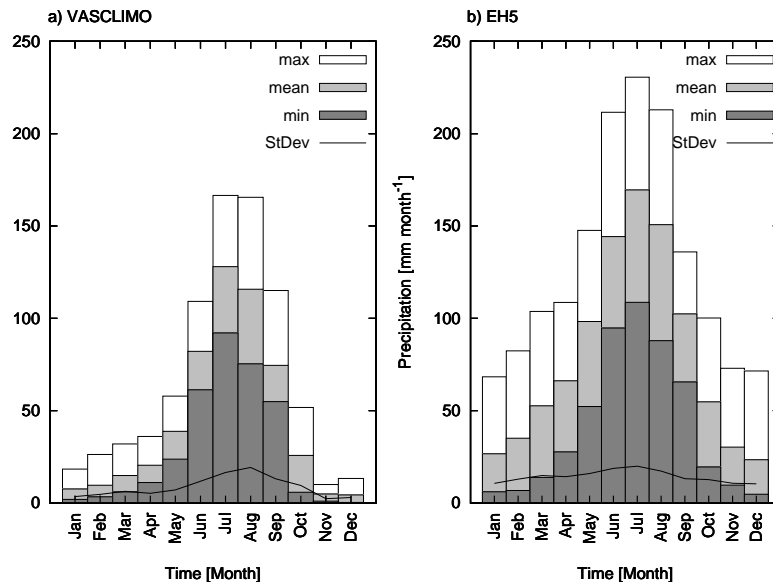


Figure 4.3. Tibetan Plateau averaged annual cycle of precipitation (mm per month), a) Vasclimo climatology, b) ECHAM5 control-run (dark shading minimal amount per month, light shading mean amount, clear boxes maximal amount, line standard deviation).

Sea onto the Plateau. (iii) The mid-latitude westerlies supply the northern parts of the Plateau with moisture. Most areas of Tibet are controlled by convergence (Figure 4.2g,i). The eddy water transport (Figure 4.2h,j) recycles the mean moisture flux and displays divergence for most parts of China and the Plateau. Note that the mean eddy flow is an order of magnitude smaller than the monthly mean flow.

The monthly mean precipitation averaged over the Tibetan Plateau (above 2500m) is mainly provided during boreal summer, about 8 to 13 cm per month, contributing about 70% of the annual mean (Figure 4.3a, based on Vasclimo). Its standard deviation is about one to two cm per month linked to the varying number of synoptic scale systems; for example, one disturbance more (less) may suffice to generate severe wetness (or dryness). The area averaged precipitation climatology for the control-run (Figure 4.3b) differs notably from the observed climatology (Figure 4.3a): The model simulation shows larger monthly precipitation and a shift in the annual cycle (Figure 4.3) with notable deviations in monthly minima, maxima and standard deviations. Note again, that the observed precipitation climatology suffers from the low station density on the western Tibetan Plateau. Hagemann et al. (2006) report too strong monsoon precipitation on the south-eastern slopes of the Himalaya Range in ECHAM5, which contribute to the Tibetan Plateau as defined here.

Future changes Projected 21st century (20C commitment phase) and 22nd century (A1B commitment phase) annual cycles of precipitation do not differ considerably from

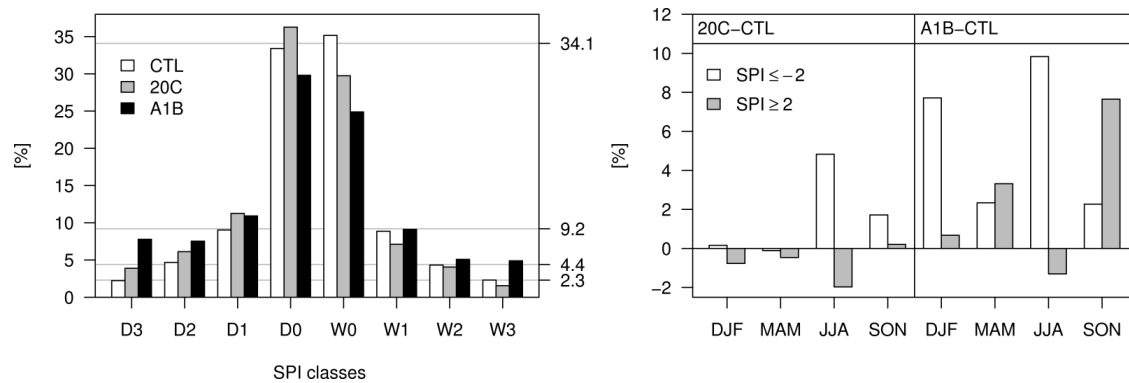


Figure 4.4. SPI class frequencies as in table 4.1. Left: for the ECHAM5 pre-industrial control-run (CTL), present day scenario (20C) and future scenario climate (A1B), SPI event probabilities in % on right vertical axis. Right: Differences in frequencies of extreme SPI classes per season.

the control-run (Figure 4.3b): the maxima of monthly precipitation increase for all seasons except the A1B-ensemble summers (not shown). The following changes in SPI-classes (compare table 4.1) are noted: (i) For the 21st century climate (20C commitment phase) compared to the pre-industrial climate an increase in all dry classes is compensated by a decrease in normal and moderate wet classes (Figure 4.4). (ii) The 21st century increase in extreme and severe dry cases is most pronounced in the summer season with approximately 5 percent more extreme dry months and about two percent less extreme wet months. A weak increase in extreme dryness is also found in autumn. (iii) In the A1B scenario (commitment phase, years 2101 to 2200) only the normal classes decrease. Wet and dry classes increase with particularly more extreme dry cases. (iv) The model projects a strong rise of extreme dry classes for the 22nd century in winter and summer with about eight and ten percent, respectively. In spring and fall about two percent more extreme dry cases are found. This is accompanied by an increase of about three percent in extreme wet spring-months and of nearly eight percent in extreme autumn-months.

Note that the SPI-classes used are those relative to the probability density function (pdf) of the control-run. Thus the pdf for the 21st century commitment period is shifted towards dry cases; the pdf for the 22nd century commitment phase appears flatter with larger tails, that is more extreme cases.

Tibetan Plateau drought and wetness The geopotential and zonal wind fields are regressed onto the SPI to show the synoptic scale flow pattern related to observed Tibetan Plateau dryness and wetness (Figure 4.5a). Under wet (dry) conditions both the subtropical jet over continental Europe and the tropical easterly jet over north Africa shift poleward (equatorward). Over the Tibetan Plateau the subtropical jet is enhanced (reduced) accompanied by an equatorward (poleward) shift. Simultaneously two anticyclone-cyclone (cyclone-anticyclone) dipoles occur over east Asia and western Europe. The

4 Eurasian bridges

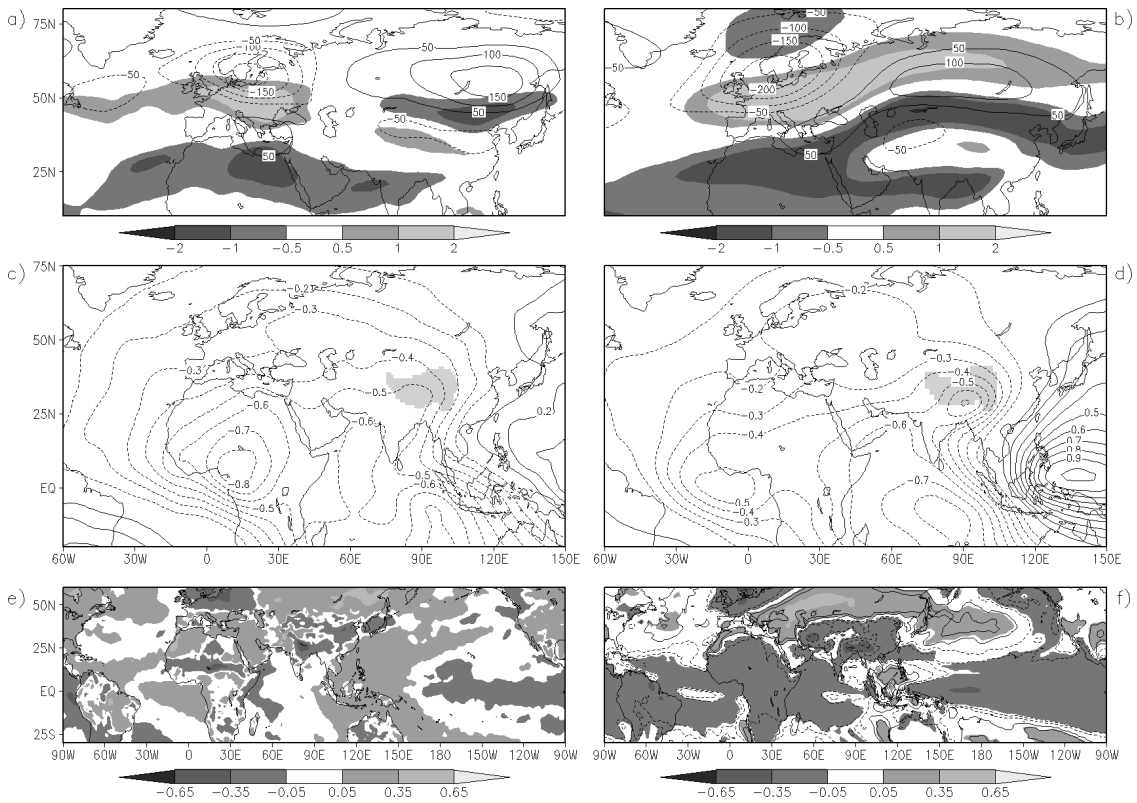


Figure 4.5. Linear regression analysis (left: ERA-40, right: ECHAM5): a) and b) 200hPa zonal wind in $m s^{-1}$, shaded, and the 300hPa geopotential in $m^2 s^{-2}$, contours, c) and d) 200hPa velocity potential in $10^6 m^2 s^{-1}$, contours, Tibetan Plateau is marked shaded, and e) skin temperature and f) surface temperature in K against the respective Tibetan Plateau SPI series.

center of the monsoon system shifts westward (eastward) under wet (dry) conditions (Figure 4.5c), affected by the sea surface temperature anomalies of the neighbouring oceans (e.g. Indian Ocean Dipole, IOD, or El Niño/Southern Oscillation, ENSO, see skin temperature regression in Figure 4.5e). The western north Pacific monsoon and the Indian summer monsoon (Wang and Fan, 1999; Wang et al., 2001, 2008b) are expected to influence Tibetan Plateau precipitation. The correlation of summer monthly SPI and the monthly western north Pacific monsoon index is highly significant (at 99% level), however, no close relationship with extreme wet or dry episodes is found. Correlations between the Indian summer monsoon index and Plateau SPI are not significant (90% level). Both index time series are obtained from the International Pacific Research Center (<http://iprc.soest.hawaii.edu/~ykaji/monsoon/index.html>).

For simulations, regressing the 300hPa geopotential and 200hPa zonal wind fields onto the Tibetan Plateau SPI variability displays a large negative (positive) geopotential pattern over northern Europe for wet (dry) conditions on the Tibetan Plateau with a positive (negative) anomaly stretching from the eastern Mediterranean to north-eastern

Eurasia and another negative (positive) one directly upstream of the Himalayas (Figure 4.5b). This hints to a wave-train-like structure connecting the north Atlantic and south-east Asia. Under wet (dry) conditions the westerly jet over Europe is intensified (weakened) as is the zonal wind over northern Eurasia and the subtropical easterly jet (Figure 4.5b). The westerly jet north of and above the Tibetan Plateau is weakened (intensified) while strong easterly anomalies prevail over northern Africa (Figure 4.5b). The $200hPa$ velocity potential shows a weakening (strengthening) of the cells over west Africa and in the Pacific region for wetness (dryness), while over the Himalayas, India, and the Tibetan Plateau the circulation is strengthened (weakened, Figure 4.5d). The Tibetan Plateau control-run summer monthly SPI is negatively (99.99% significance level) correlated with monthly summer indices of the western north Pacific monsoon and the Indian monsoon as defined by Wang and Fan (1999) and Wang et al. (2001). Mid-latitude surface temperature regressions correspond to the $300hPa$ geopotential regressions with cold (warm) anomalies, where negative (positive) geopotential anomalies occur (Figure 4.5f). In nearly all tropical ocean regions, especially the eastern equatorial Pacific and the western Indian ocean, cold (warm) anomalies arise in the Tibetan Plateau wet (dry) months. Considering the tropical ocean variability, Jungclaus et al. (2006) describe a 0.5K higher standard deviation in ECHAM5/MPI-OM for the Niño-3 region compared to observations. According to their study the model underestimates the non-linearity and the non-normality in ENSO, while the modeled period is also smaller. However, van Oldenborgh et al. (2005) find the simulated ENSO in ECHAM5/MPI-OM fairly robust.

Tibetan Plateau SPI-regressions are computed for each scenario-run's commitment phase separately to assess possible linearly related future flow changes. For the commitment periods of the ECHAM5/MPI-OM 20C and A1B scenarios, they mainly agree with the control-run (not shown). Major exceptions are $200hPa$ zonal wind regressions with partially more pronounced jets and $200hPa$ velocity potential regressions with differing extent of anomalies. In addition, considering surface temperatures, one 21st century projection considerably deviates from the control-run.

4.3.2 Observations and ERA-40 re-analysis

Tibetan Plateau dryness and wetness: Eurasian flow regimes

The linear regression analysis is complemented with a composite analysis of dry and wet months focussing on the dynamical flow patterns and the boundary conditions. Regional features of the moisture supply and the larger scale embedding are discussed.

Extreme and severe dryness Six months of severe and extreme drought ($SPI \leq -1.5$) are identified: June 1961, June 1965, June and August 1972, August 1984 and July 1994. Main features from the anomaly field composites of drought characteristics are sum-

4 Eurasian bridges

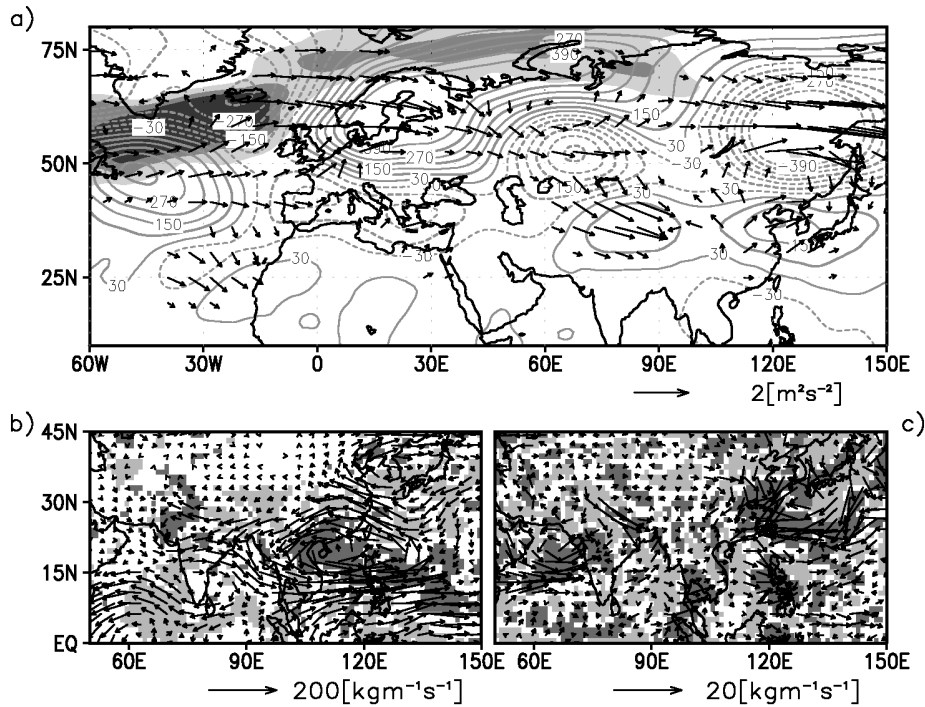


Figure 4.6. Dry case composites: a) the storm track on $500hPa$ as variance of geopotential (shaded, shades are 900 , 1200 and $1500 m^4 s^{-4}$), zonally asymmetric barotropic upper tropospheric circulation component ($\frac{1}{2} \cdot (300hPa + 500hPa)$ geopotential) anomalies (contour intervals are $60 m^2 s^{-2}$), and anomalies of Plumb's stationary wave flux in $500hPa$ (in $m^2 s^{-2}$, arrows), b) monthly mean contribution of vertically integrated moisture flux and its divergence (in mm per day), and c) eddy contribution of vertically integrated moisture flux and its divergence. In b) (c) divergence and convergence of moisture flux are shaded in light and dark grey above and below $+1.25$ ($+0.25$) and -1.25 (-0.25). Arrows of magnitude smaller 0.2 , 2.5 and 0.25 are omitted in a), b) and c), respectively.

marised as follows:

(i) Over the Tibetan Plateau, in particular its central and eastern areas, the water vapour convergence is reduced, associated with a region-wide weakening of the monsoon moisture transport (Figure 4.6b). The characteristic Indian monsoon and the north-eastward east Asian monsoon moisture flows are reduced. The conflicting positive moisture flux anomaly (Figure 4.6b) is restricted to the south of the Plateau. The upper level moisture flow (not shown) is deflected due to enhanced anticyclonic circumflow around the Himalaya Range associated with an anomalous high pressure zone in the larger Plateau region (Figure 4.6a). In addition, the monthly mean moisture routes from the south-east and through the Bay of Bengal are suppressed (Figure 4.6b). These negative flux anomalies are due to enhanced cyclonic activity over the South China Sea. The reduced moisture supply to the Plateau coincides with the reduction of upper air outflow and

tropical easterly jet (e.g. regression, Figure 4.5a). In addition, the eddy mean component (Figure 4.6c) indicates moisture transport from the western to the eastern Plateau and to the Bay of Bengal.

(ii) The dry case dynamics is related to stationary and transient eddy activity bridging the north Atlantic and the Eurasian continent (Figure 4.6a). A marked wave train commences from a high pressure anomaly over Scandinavia and extends to the South China Sea. There, a cyclonic anomaly affects (the eastern/south-eastern part of) the Tibetan Plateau (Figure 4.6a). This anomalous cyclone deflects the moisture supply from the South China Sea and Bay of Bengal (Figure 4.6b). The wave train is a manifestation of basically (equivalent) barotropic dynamics (not shown). This Rossby-like wave train is initiated by the strong anticyclonic anomaly over northern Europe/Scandinavia (Figure 4.64a): this corresponds to the reduction of the mid-latitude westerly jet intensity over Europe and a strong northern European anticyclone as shown in the regression analysis (Figure 4.5a). This wave train is clearly detectable in the stationary wave activity flux anomalies (Figure 4.6a) and in the extended horizontal Eliassen-Palm-Flux (Hoskins et al., 1983, not shown). The anomalous anticyclone over Scandinavia is supported by transient eddy activity (not shown) of the south-west/north-east orientated north Atlantic storm track which, in turn, is influenced by a large positive surface pressure anomaly in the central north Atlantic (not shown). The wave train transports stationary wave energy from Scandinavia via the Caspian Sea region to the Tibetan Plateau.

Fraedrich and Müller (1992) and Fraedrich (1994) report northern winter and spring anomalous European circulation features affected by ENSO extremes (similar to the Scandinavian high anomalies found for extreme dryness) which persist throughout the following boreal spring and summer seasons. While the influence of ENSO on Europe is subject to ongoing research (Brönnimann, 2007), the present analysis finds no Scandinavian geopotential anomalies in boreal summer simultaneous with ENSO, nor a leading role of ENSO.

Extreme and severe wetness The eleven summer months of Tibetan Plateau wetness (severe and extreme wet SPI-classes) are August 1958 and 1962, June 1971, 1973 and 1978, July 1981, June 1984, August 1991, July 1996, August 1998 and June 2000. The occurrence of comparatively fewer (six) months of severe and extreme drought (Vasclimo-ERA-40 period) is related to an increase of very wet summer months in the late 20th century (1996 to 2000). The following results are obtained:

(i) The moisture inflow onto the Plateau through all three pathways is enhanced (Figure 4.7): (a) In the mid-levels a westward enlarged western north Pacific subtropical high allows moist air from the South China Sea to reach the Plateau but, more importantly, (b) wet air is directed from the Arabian Sea onto the Plateau along the mid-level cyclonic anomaly over the Arabian region and central Asia. (c) In low levels this anomaly reaches

4 Eurasian bridges

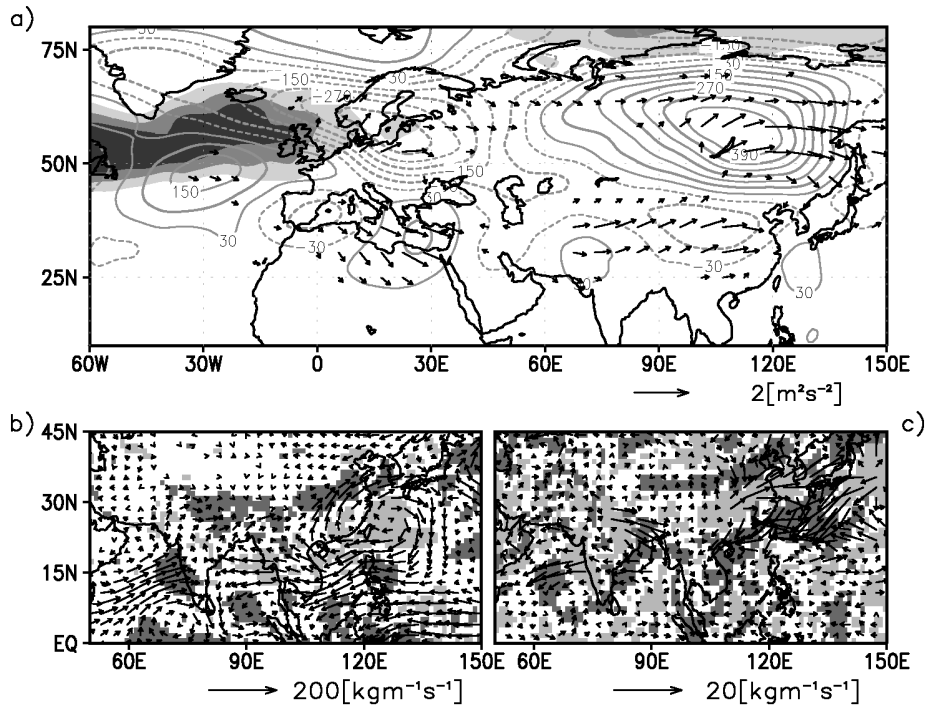


Figure 4.7. Wet case composites: a) the storm track on $500hPa$ as variance of geopotential (shaded, shades are $900, 1200$ and $1500 m^4 s^{-4}$), zonally asymmetric barotropic upper tropospheric circulation component ($\frac{1}{2} \cdot (300hPa + 500hPa)$ geopotential) anomalies (contour intervals are $60 m^2 s^{-2}$), and anomalies of Plumb's stationary wave flux in $500hPa$ (in $m^2 s^{-2}$, arrows), b) monthly mean contribution of vertically integrated moisture flux and its divergence (in mm per day), and c) eddy contribution of vertically integrated moisture flux and its divergence. In b) c) divergence and convergence of moisture flux are shaded in light and dark grey above and below $+1.25$ ($+0.25$) and -1.25 (-0.25). Arrows of magnitude smaller $0.2, 2.5$ and 0.25 are omitted in a), b) and c), respectively.

the Bay of Bengal deflecting moist southerly flow onto the Plateau. Thus the eleven summer months of (at least severe) wetness are characterised by larger-than-average moisture inflow along these anomalies accompanied by strengthened Asian monsoon water vapour transport.

(ii) The water vapour flux anomalies described above are influenced by transient and stationary wave activity. A zonally orientated wave like pattern emerges from the north Atlantic region, extends along $30^\circ N$ and stretches to the western north Pacific south of the large cyclone-anticyclone dipole over northern Eurasia (Figure 4.7a). This wave train commences in the southern part of the north Atlantic storm track and extends along the jet to the eastern Mediterranean (Figure 4.75a). The stationary wave activity flux anomaly is weaker than in the dry case. The flux from the Atlantic to the eastern Mediterranean and from the Tibetan Plateau region eastwards is evident. Thus the wave

train diffuses between the subtropical and the tropical easterly jet at the critical latitude of zero zonal velocity (not shown). A secondary wave train emerges from the larger Arabian region and western Asia, where cyclonic anomalies prevail, and stretches along the border between the northward displaced subtropical westerly and tropical easterly jet (compare Figure 4.5a). Although these two patterns are not marked as significant (90% level, t-test) on all pressure levels, the Mediterranean wave train is fully established in the 850hPa geopotential (not shown) and the full range of both patterns is best visible in the zonally asymmetric component of the 300hPa geopotential (compare later Figure 4.9h). Note that, simultaneously, the upper outflow and the tropical easterly jet are strengthened as depicted by the regression analysis (Figure 4.5).

Identification of wave trains on sub-seasonal scale This paragraph presents the sub-seasonal atmospheric features for dry and wet episodes on the Tibetan Plateau. Summer 1984 is selected as a case study to trace the (i) Scandinavia-East-Asia wave train for severe dryness in August and (ii) the Mediterranean wave train for severe wetness in June 1984 in terms of zonally asymmetric 500hPa and 300hPa geopotential.

(i) Scandinavia-East-Asia wave train: Staggered sections (Figure 4.8c) for the Hovmöller diagram of daily 500hPa geopotential anomalies (Figure 4.8a) demonstrate the dry wave train connecting northern Europe and south Asia (compare Figure 4.6a). In the severe dry August 1984 (Figure 4.8a, days 62 to 92) an anticyclonic anomaly persists over northern and central Europe, cyclonic anomalies exist over central Eurasia and eastern China while north of Tibet and on the Tibetan Plateau an anomalous anticyclonic circulation prevails. For June and July (Figure 4.8a, day 1 to 61) anomalies are less persistent, interrupted by wave train activity, and shifted westward. Lag-correlations (not shown) of area-averaged 500hPa geopotential (80° to 100°E, 30° to 36°N) with the geopotential field for August 1984 confirm the development of the anomaly in the Plateau region following the formation of the Scandinavian high anomaly. The maximum correlation is found for the Scandinavian anomaly leading the Tibetan Plateau anomaly by five days.

(ii) Mediterranean wave train: The wet wave train (in June 1984) is clearly seen in the Hovmöller diagram (Figure 4.8b) along the section about 30°N (daily 300hPa geopotential anomalies averaged over 25° to 40°N, see Figure 4.8d). In June 1984 (Figure 4.8b, days 1 to 30) it displays alternating anticyclonic and cyclonic disturbances along 30°N with positive anomalies near 15°W, 40°E and 120°E, negative ones at 0° and occasionally near 60°E and 90°E. This is emphasised by comparing the dry August (days 62 to 92) and the wet June (days 1 to 30). In August (with severe dryness), disturbances travel westward from eastern Europe/central Asia (30°E to 60°E) to the Atlantic region.

Surface temperature conditions Here, persistent surface (skin) temperature anomalies preceding Tibetan Plateau dryness and wetness are analysed up to three months, which

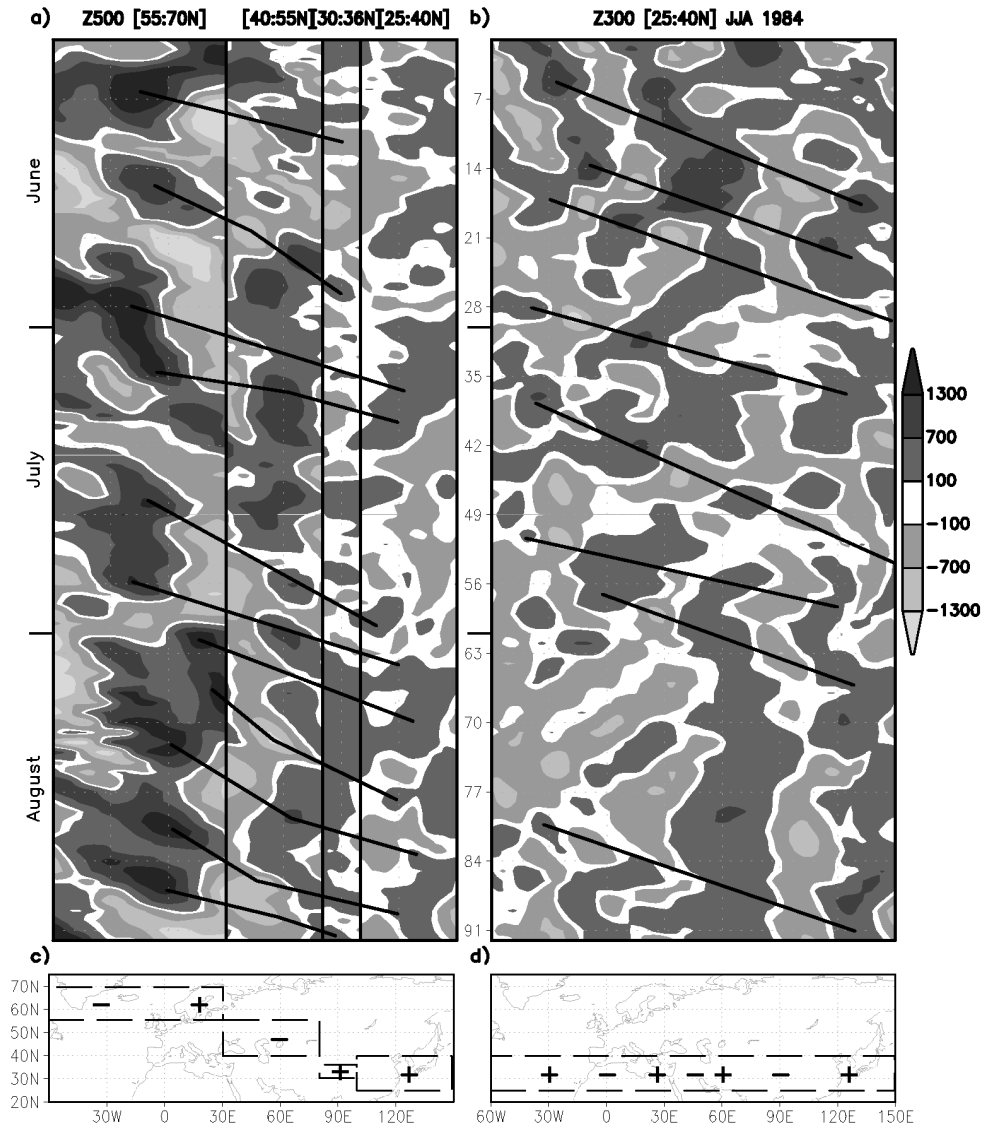


Figure 4.8. Longitude-time sections (Hovmöller diagram) of zonally asymmetric geopotential (annual cycle subtracted) for summer 1984: a) staggered section for 500hPa, 60°W to 30°E averaged 55° to 70°N, 30° to 80°E mean for 40° to 55°N, 80° to 100°E average for 30° to 36°N, 100° to 150°E average for 25° to 40°N, b) 300hPa section averaged over 25° to 40°N, c) description of boxes used in panel (a), d) description of section used in (b). In c) and d) plus (minus) indicates anticyclonic (cyclonic) anomalies in Figure 4.6a and Figure 4.7a. Lines in a), b) indicate occurrences of Scandinavia-East-Asia pattern or Mediterranean pattern.

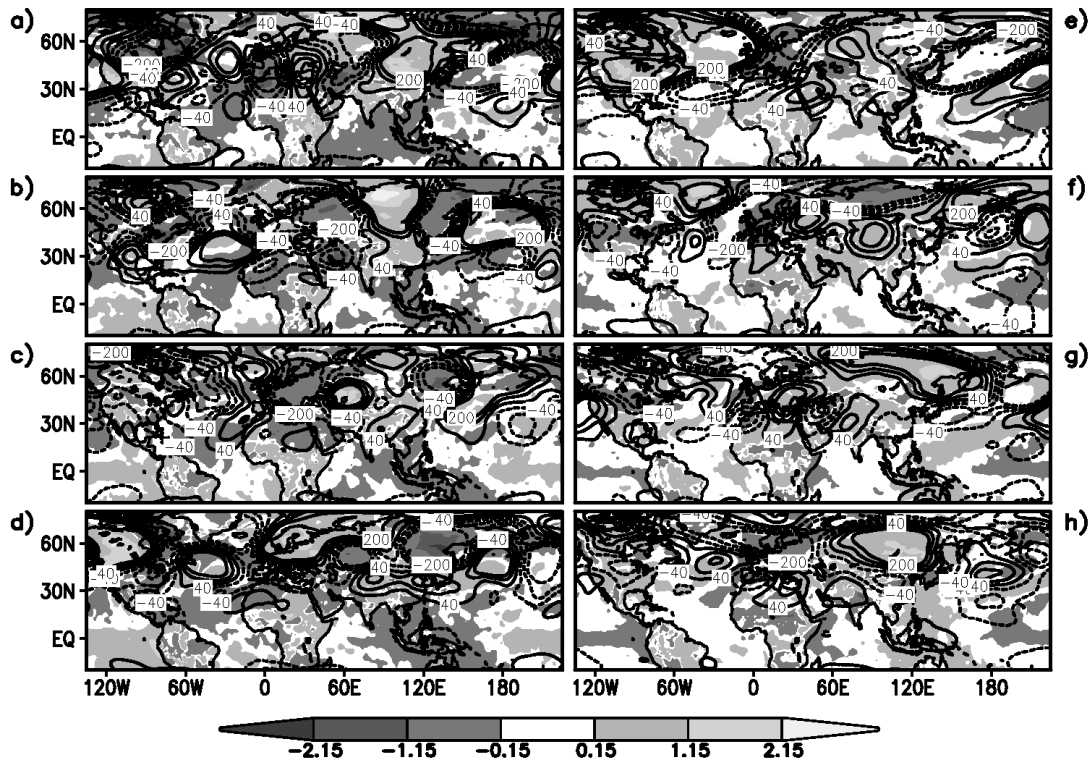


Figure 4.9. Composites anomalies for months preceding wet and dry episodes of ERA-40 skin temperature (in K, shaded) and zonally asymmetric 300hPa geopotential (in $m^2 s^{-2}$, contours): a) dry-3 months, b) dry-2, c) dry-1, d) dry, e) wet-3 months, f) wet-2, g) wet-1, h) wet.

influence the monsoon and the hemispheric circulation.

Extreme and severe dryness: The simultaneous skin temperature composite (Figure 4.9d) reflects the overlying atmospheric flow anomalies: anomalous warm conditions over Scandinavia, Tibet, and East China, and cold anomalies in East Siberia, South China, the Mediterranean and central Eurasia. In the tropical north Atlantic a large statistically significant cold SST-anomaly occurs. This anomalous cold pool is seen in months preceding dryness (dry-1, dry-2, dry-3, Figure 4.9a to c) and extends temporarily from the tropical north Atlantic to the western slope of the Himalayas. Apparently, this north Atlantic cooling initiates atmospheric anomalies (blocking, Figure 4.9a to d) deflecting the jet and storm track positions. That is, a persistent cooler state of the tropical Atlantic acts as the necessary precursor of a northward deflected storm track and, subsequently, a strong Scandinavian high. This view agrees with the vertical anomaly structure (not shown) which presents a significant cooling throughout the troposphere. This negative anomaly is interpreted as cold-monopole forcing (Walter et al., 2001). Simmons et al. (1983) and Walter and Graf (2002) discuss possible influences of tropical north Atlantic SST-anomalies on north Atlantic climate teleconnections for

4 Eurasian bridges

boreal winter. How tropical north Atlantic SST and other factors interact in boreal summer to force north Atlantic and Eurasian teleconnection patterns is subject of ongoing research. Kucharski et al. (2007, 2008) emphasise an Atlantic forced component of the Indian summer monsoon. They localise the main forcing for the non-ENSO-driven variability of the Indian monsoon rainfall in the region of the Gulf of Guinea. This region is prominently represented in the regression analysis (Figure 4.5e), which represents the linear influence on Tibetan Plateau precipitation, but there is no signal in the composite analysis for wet and dry extreme episodes.

Tropical skin temperature composites (Figure 4.9d) indicate a positive IOD phase with warming (cooling) in the equatorial western (eastern) Indian ocean and an El Niño. Three (out of the six) dry months during the ERA-40 period coincide with positive IOD events (1961, 1972, 1994) and, superimposed, two of them (1972, 1994) with positive ENSO-events (Niño Index of NOAA's Climate Prediction Center, NOAA, 2008). The most persistent of the regional tropical anomalies is the significantly cooler maritime continent (Figure 4.9a to d). Tropical SST anomalies (e.g. positive IOD, warm ENSO) appear to have a strong effect on the three moisture paths to the Tibetan Plateau (Hong et al., 2008). Both, positive IOD or ENSO events, prohibit moisture inflow from the south-east and, if concurrent, they strongly deflect the inflow through the Arabian Sea and the Bay of Bengal. Especially the cold anomalies from the maritime continent to the Bay of Bengal and the East China Sea promote anomalous moisture divergence on the Tibetan Plateau (northerly wind anomalies from the continent to the Bay of Bengal, anomalous cyclonic circulation over the South China Sea).

Extreme and severe wetness: Wetness composites show northern Europe to be slightly colder compared to the climatology, while northern Asia is warmer (Figure 4.9h, skin temperature) reflecting the atmospheric anomalies. Additionally, an anomalous warm pool is visible in the tropical to subtropical western Pacific.

More importantly, a negative IOD phase (cold western tropical Indian ocean, warm eastern tropical Indian ocean) may coincide with La Niña (Figure 4.9h). Associated warm anomalies in the maritime continent are extending northward to the East China Sea (Figure 4.9h). These significant warm anomalies influence the moisture transport to the Tibetan Plateau (see below and Hong et al., 2008). Scatter diagrams of the IOD-Mode index and various ENSO-indices versus the Tibetan Plateau SPI show that months of extreme and severe wetness tend to coincide with negative IOD and cold ENSO events (not shown). Correlation coefficients are significant at the 95% level; thus, it cannot be excluded, that IOD and ENSO are linked to the extreme and severe pluvial events.

Hong et al. (2008) support the above statements: La Niña combined with a negative Indian Ocean Dipole enhances moisture inflow through all southerly routes. A warmer eastern Indian Ocean and maritime continent (extending to the East China Sea) enhance the local convective activity: the enhanced western north Pacific subtropical

high extends further west carrying more moisture from the warmer western Pacific via the Indochinese Peninsula into the Bay of Bengal and to the Plateau.

Shaman and Tziperman (2005) describe, how wintertime ENSO affects the accumulation of snow on the Plateau. Thus the meridional land–sea temperature contrast is changed, which drives the south Asian summer monsoon circulation. In addition, the Plateau’s sensible and latent heating are modified. However, the present study shows no strong relations (correlations and conditional composites, not shown) between wet and dry conditions on the Plateau and preceding wintertime ENSO or snow depth.

4.3.3 ECHAM5/MPI-OM simulations for the IPCC AR4

With respect to the simulation data, already the regression analysis suggests a dynamical link between dryness and wetness on the Tibetan Plateau and the upstream circulation on a linear basis (Figure 4.5). The following composites present regional moisture flux anomalies and large-scale flow patterns related to the severe and extreme episodes.

Composite analysis

Of the 1518 summer months (control-run) 100 are classified as severe or extreme wet and 103 as severe or extreme dry. Composites reveal the following major features:

(i) Water vapour convergence is reduced over the Tibetan Plateau with weakened moisture fluxes reaching the Tibetan Plateau (Figure 4.10b,c) for dry months. In addition, the moisture fluxes related with the east Asian summer monsoon are reduced along the eastern coast of Asia and enhanced towards the Philippines and the Pacific warm pool. The situation for wetness is the opposite (Figure 4.11b,c): More moisture reaches the Tibetan Plateau via the Arabian Sea and the Bay of Bengal; the south-east Asian moisture flux is weakened; India and the Indochinese peninsula receive less moisture.

(ii) Dry case circulation composites show a pronounced stationary wave (Figure 4.10a). Commencing from a high pressure anomaly over the eastern north Atlantic it stretches towards central western Asia and the Tibetan Plateau region. The anomalous eastern north Atlantic anticyclone is supported by transient eddy activity of a slightly anomalous south-west/north-east orientated north Atlantic storm track. Stationary wave flux anomalies (Plumb, 1985) document the downstream energy flux (Figure 4.10a). The related western Asian positive geopotential anomaly inhibits the moisture flux from the Arabian Sea. A negative flow anomaly over the oceans from the Bay of Bengal to the South China Sea combined with a positive one over the lower Yangtze reduce the moisture flux from there into the Tibetan Plateau and the east Asian summer monsoon.

(iii) Severe wet months (Figure 4.11a) are characterised by a continental scale (Europe-Asia) quadrupole-like anomaly of the (barotropic) circulation. The northern dipole of this pattern is supported by a more zonally directed north Atlantic storm track (up-

4 Eurasian bridges

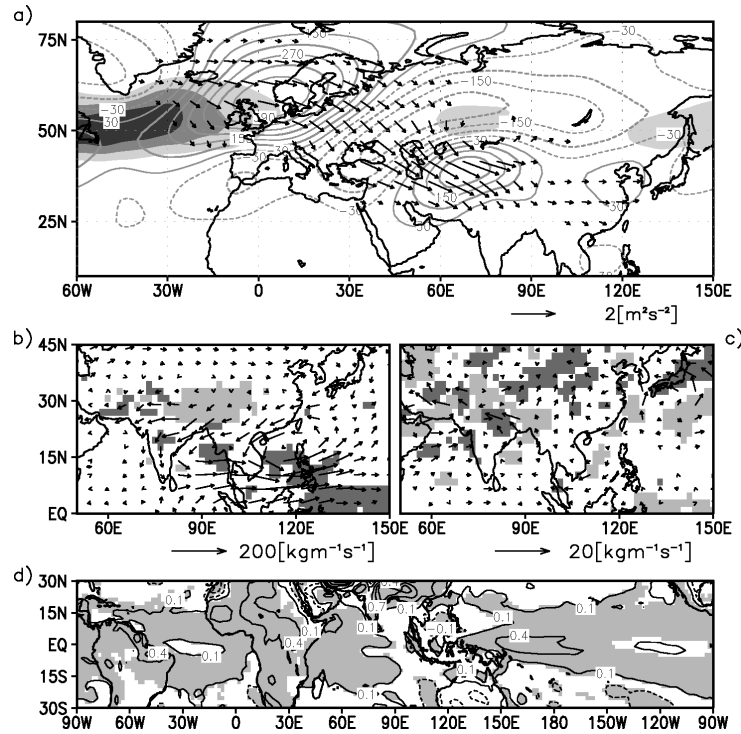


Figure 4.10. Control-run dry case composites: a) the storm track on 500hPa as variance of geopotential (shaded, shades are 900, 1200 and 1500 $m^4 s^{-4}$), zonally asymmetric barotropic upper tropospheric circulation component, $0.5 \cdot (300hPa + 500hPa \text{ geopotential})$, anomalies (contour intervals are $60 m^2 s^{-2}$), and anomalies of Plumb's stationary wave flux in 500hPa (in $m^2 s^{-2}$, arrows), b) monthly mean contribution of vertically integrated moisture flux and its divergence (in mm per day), c) eddy contribution of vertically integrated moisture flux and its divergence, and d) surface temperature (in K, contours), shading indicates 90% significance level. In b) (c) divergence and convergence of moisture flux are shaded in light and dark grey above and below $+1.25$ ($+0.25$) and -1.25 (-0.25). Arrows of magnitude smaller 0.2, 2.5 and 0.25 are omitted in a), b) and c), respectively.

stream) leading to more zonally directed stationary wave fluxes (downstream). From the south-eastern pole (Tibetan Plateau) of the pattern wave flux anomalies emerge over eastern China (Figure 4.11a) as an atmospheric response to the thermal heating over the wet Tibetan Plateau (Wang et al., 2008a).

(iv) The surface temperature anomalies over land are associated with the overlying atmospheric features for wetness and dryness (not shown). Tibetan Plateau dryness (wetness) is accompanied by a significant near circumglobal warm (cold) anomaly in the tropics (Figure 4.10d, Figure 4.11d). In months preceding dryness (wetness) this feature (not shown) remains basically unchanged, but with an eastward phase-shift.

(v) Future scenario composites do not show substantial differences to the results presented for the control-run.

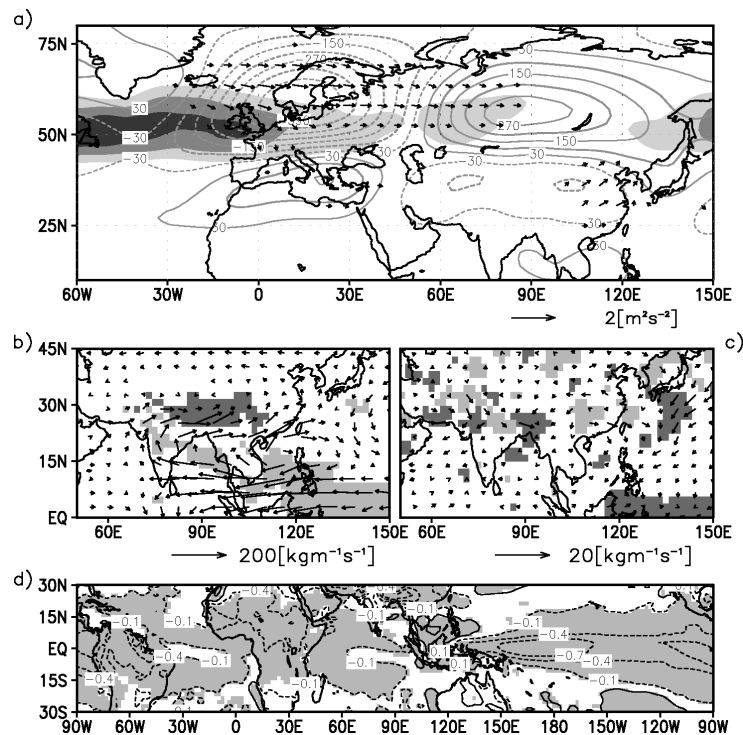


Figure 4.11. Control-run wet case composites: a) the storm track on 500hPa as variance of geopotential (shaded, shades are 900, 1200 and 1500 $m^4 s^{-4}$), zonally asymmetric barotropic upper tropospheric circulation component, $0.5 \cdot (300hPa + 500hPa)$ geopotential, anomalies (contour intervals are $60 m^2 s^{-2}$), and anomalies of Plumb's stationary wave flux in 500hPa (in $m^2 s^{-2}$, arrows), b) monthly mean contribution of vertically integrated moisture flux and its divergence (in mm per day), c) eddy contribution of vertically integrated moisture flux and its divergence, and d) surface temperature (in K, contours), shading indicates 90% significance level. In b) (c) divergence and convergence of moisture flux are shaded in light and dark grey above and below $+1.25 (+0.25)$ and $-1.25 (-0.25)$. Arrows of magnitude smaller 0.2, 2.5 and 0.25 are omitted in a), b) and c), respectively.

Comparison to observations (ERA-40) Control-run and ERA-40 dry and wet case composites are compared for vertically averaged geopotential fields (mean over five isobaric levels from 100hPa to 500hPa, Figure 4.12). The dry case composites (contours in Figure 4.12a and b) show similar patterns, except for the zonally oriented negative anomaly over the Mediterranean which, in the simulation, extends further to the west and connects with the north-eastern Eurasian anomaly.

Wet case circulation anomalies (shaded in Figure 4.12a and b) are qualitatively very similar over northern Eurasia, with the northern European anomaly extending to about $45^\circ E$. Further downstream, the eastern Asian anticyclone stretches to the Pacific. Deviations occur along $30^\circ N$: ECHAM5/MPI-OM composites do not feature the wave train structure from the north Atlantic to the Pacific as clearly as in ERA-40. The wet-dry anti-

4 Eurasian bridges

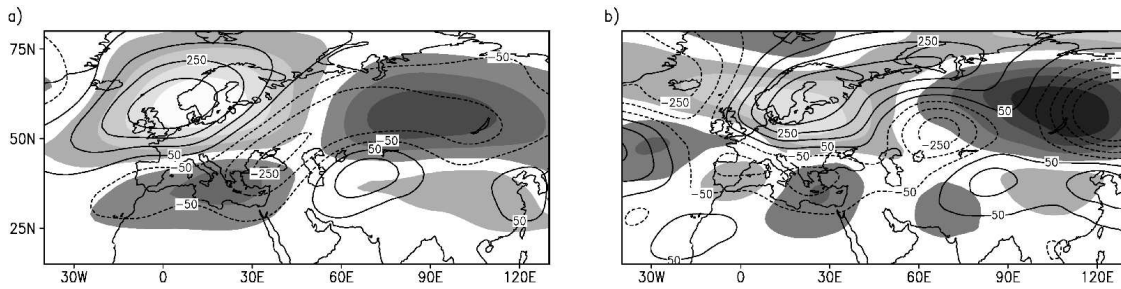


Figure 4.12. Composite comparison between (a) ECHAM5/MPI-OM control-run simulation and (b) ERA-40 re-analysis. Displayed is the vertical mean of zonally asymmetric geopotential (in $m^2 s^{-2}$) on the 100, 200, 300, 400 and 500hPa levels. Wet case anomalies are displayed shaded, dry case anomalies in contours. Shadings are from light to dark grey $-350, -250, -150, -50, 50, 150, 250, 350$.)

symmetry, which is notable in the simulation composites, does not occur as pronounced in ERA-40, if at all.

Mid-latitude and tropical impacts and dynamical interpretation

The regression and composite flow patterns related to Tibetan Plateau drought and wetness are supplemented by analyses of the dynamics of mid-latitude teleconnections embedded in the global atmospheric circulation. They are also responding to tropical SST-anomalies, which induce local centers of action in terms of convectively forced heat sources or sinks.

Mid-latitude influence Upstream and downstream of the Tibetan Plateau the large-scale dynamics is suitably represented by the hemispheric meridional wind field to capture wave dynamics. Space-time lag-correlations of the 300hPa meridional wind, centered over the Tibetan Plateau (30° to 35° N, 86° to 96° E), with the whole hemispheric field are computed on a day-to-day basis up to ± 10 day lags (June 1 to August 31). First, the summer climate mean is presented based on the last 200 years of the control-run (Figure 4.13 and Figure 4.14), before four summer seasons are selected, each characterised by two months of severe and extreme wetness (dryness). The deviations from summer climate (Figure 4.15 and 4.16) are analysed, revealing the following results:

(i) The summer climate displays a circumglobal teleconnection in the 300hPa meridional wind upstream and downstream of the Tibetan Plateau. The time-longitude lag-correlation cross-sections (Figure 4.13, averaged from 35° N to 55° N) indicate a wave train commencing in the north Atlantic region. This wave train reaches the Tibetan Plateau via Eurasia continues across the north Pacific to America reinforcing the north Atlantic storm track after about 20 days. This circumglobal perspective fits the teleconnection pattern described by Ding and Wang (2005) and the description of Uno et al.

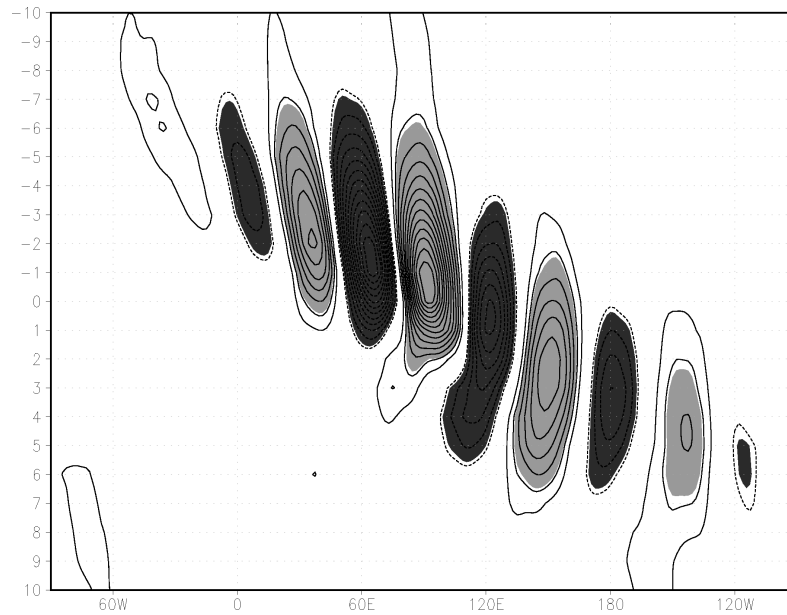


Figure 4.13. Control-run longitude time lag diagrams for Tibetan Plateau averaged and hemisphere-wide 300hPa meridional wind correlations, from -10 to $+10$ days. Dark (light) shadings are significance level of positive (negative) correlation coefficients at the 99.99% level for an estimated effective number of degrees of freedom. Contour intervals are 0.025.

(2009) regarding the transport of mineral dust from a dust storm event in the Taklamakan in May 2007.

(ii) The summer climate lag-correlation fields (Figure 4.14, selected lags ± 9 , ± 6 , ± 3 and 0 days) show the preferred teleconnection route stretching from north America via the north Atlantic storm track to the Tibetan Plateau; even further upstream, signals appear in the transient eddies over the north Pacific reaching north America. Therefore, a circumglobal influence of tropical Pacific SST-anomalies, initially, on the north Pacific storm track and, further downstream, on the Tibetan Plateau can be envisaged (Figure 4.14) in the sense that storm tracks respond to tropical forcing over the oceans and subsequently can act as wavemakers of cross-continental wave trains.

(iii) Severe and extreme dry events show upstream circulation patterns of similar spatial structure (Figure 4.15, lags -9 , -6 , -3 , 0 and $+3$ days) which is dominated by the link from the north Atlantic storm track to the Tibetan Plateau. This structure is modulated by a wave train emerging from the subtropical north Pacific crossing north America and reaching the north Atlantic. For wet events, however, the correlations are less distinct (Figure 4.16). The upstream teleconnection route is more zonally oriented and commences near the Mediterranean. A mechanism described by Rodwell and Hoskins (1996, 2001) may operate here.

4 Eurasian bridges

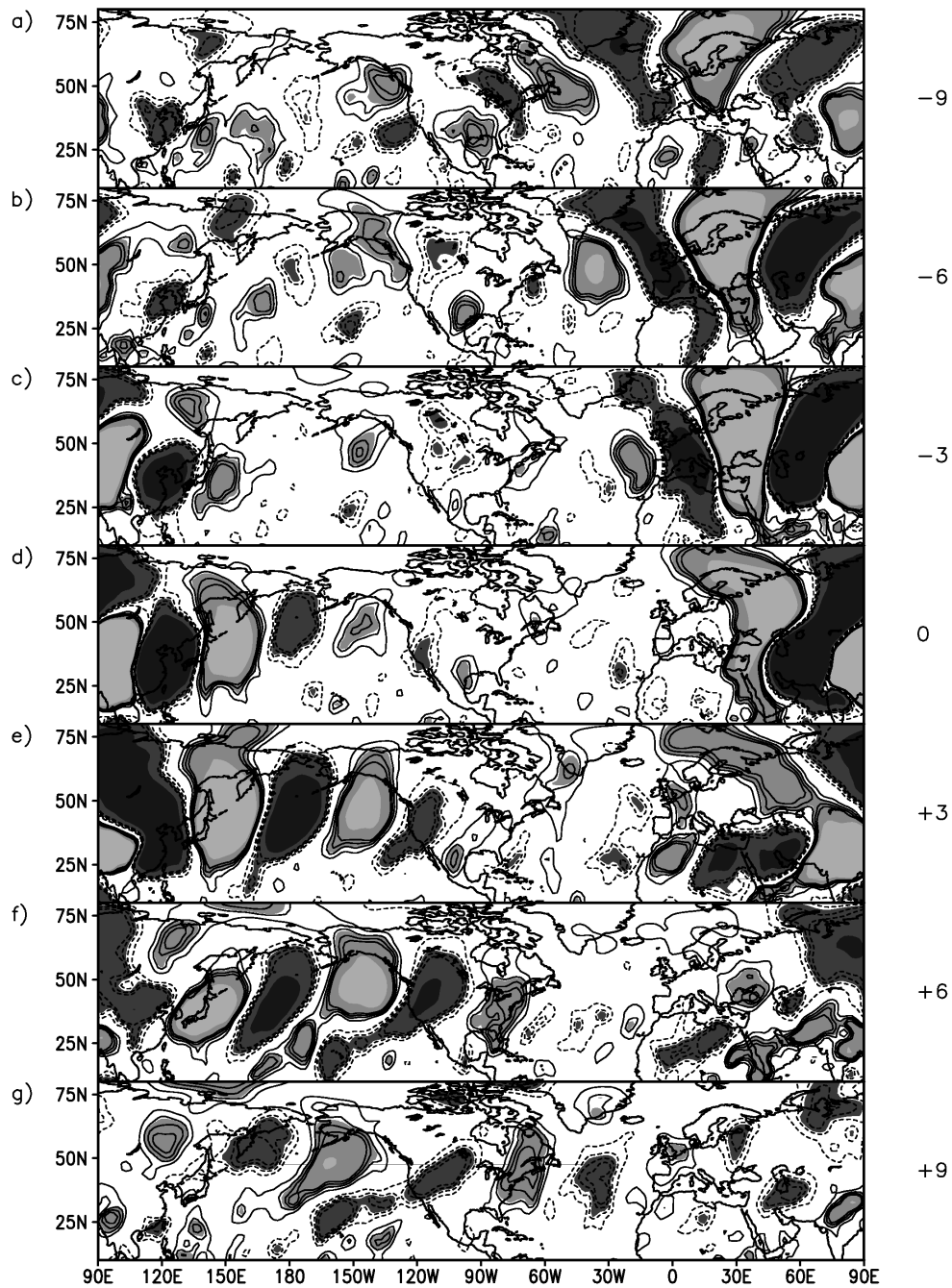


Figure 4.14. Control-run correlations for Tibetan Plateau averaged (June 11th to August 21st, last 200 years of control-run) and hemisphere-wide 300hPa meridional wind for lags ± 9 days (a,g), ± 6 days (b,f), ± 3 days (c,e), and concurrent (d). Dark (light) shadings indicate significance of positive (negative) correlation coefficients at the 90% and 99.99% levels for an approximation of effective degrees of freedom. Contours are 90%, 99%, 99.9%, 99.99% levels neglecting potential stochastic dependencies.

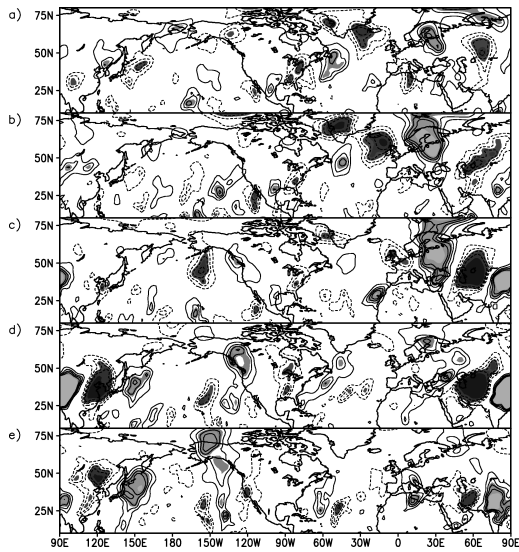


Figure 4.15. Control-run dry case lag-correlations for Tibetan Plateau averaged (June 11th to August 21st) and hemisphere-wide 300hPa meridional wind for lags -9 (a), -6 (b), ± 3 days (c,e), and concurrent (d). Contours: significant positive (negative) correlations at the 90%, 99%, 99.9%, 99.99% levels neglecting stochastic dependencies. Dark (light) shades: positive (negative) correlations at the 90%, 95% and 99% levels relative to estimated effective degrees of freedom.

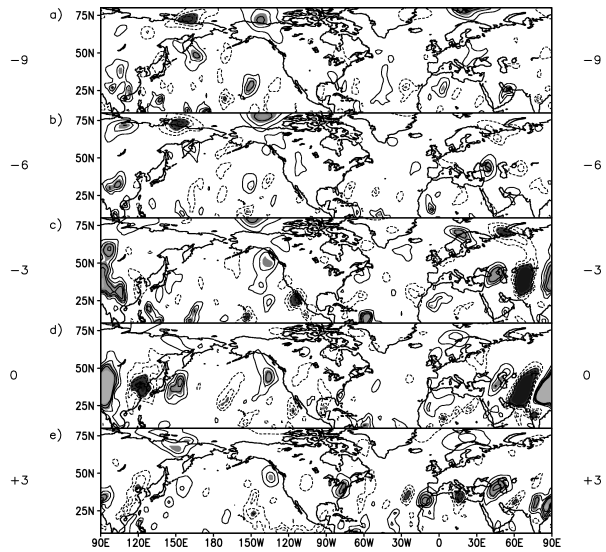


Figure 4.16. Control-run wet case lag-correlations for Tibetan Plateau averaged (June 11th to August 21st) and hemisphere-wide 300hPa meridional wind for lags -9 (a), -6 (b), ± 3 days (c,e), and concurrent (d). Contours: significant positive (negative) correlations at the 90%, 99%, 99.9%, 99.99% levels neglecting stochastic dependencies. Dark (light) shades: positive (negative) correlations at the 90%, 95% and 99% levels relative to estimated effective degrees of freedom.

Tropical steering Tropical SST-anomalies in the Indian and Pacific ocean affect south-east Asian precipitation (Hong et al., 2008) by modulating the lower tropospheric flow patterns and, therefore, the regional water supply. These SST anomalies can be associated with “centres of action” which, depending on their strength, influence the tropical flow and, subsequently, may affect the mid-latitude circulation (Simmons et al., 1983; Lau and Peng, 1992; Walter and Graf, 2002). Here it should be noted that the tropical surface temperature fields composited with respect to Tibetan Plateau drought and wetness appear to be biased by the ENSO variability in ECHAM5/MPI-OM (Jungclaus et al., 2006), which is more intense than observed. The following SST-induced anomaly-centres appear to affect the Tibetan Plateau.

(i) Cold SST-anomalies extending from the Indian Ocean to the tropical Pacific (Figure 4.11d) lead to subsidence induced low level anticyclonic circulation enhancing the moisture-transport to the Tibetan Plateau along their southern routes (Simmonds et al., 1999). This tropical anticyclonic anomaly also affects the South China Sea (Figure 4.11a)

4 Eurasian bridges

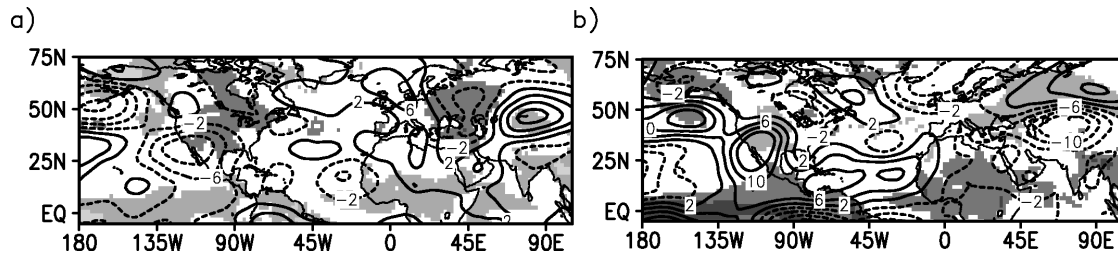


Figure 4.17. Control-run composites for the month before dry events (a) and wet events (b). Shades are surface temperatures (dark grey -0.6 and -0.2 K, light grey 0.2 and 0.6 K), contours are zonally asymmetric streamfunction anomalies (in $10^5 m^2 s^{-1}$).

and, concurrent with a weaker north Pacific subtropical high, enhances the moisture flux and precipitation in south-east China.

(ii) Warm anomalies extending from the Indian to the Pacific Ocean show the opposite effect (Figure 4.10d): For dry months a warmer Indian ocean induced regional cyclonic anomaly suppresses moisture inflow to the Tibetan Plateau by enhanced low level west-lies. Again, the anomalies extend to the South China Sea. Concurrent with anticyclonic anomalies over north-eastern China and a strengthened north Pacific subtropical high they modify the east Asian summer monsoon reducing moisture inflow from the south-east and through the Bay of Bengal.

(iii) The months preceding severe and extreme Tibetan Plateau wetness (dryness) display anticyclonic (cyclonic) anomalies over the Gulf of Alaska and south-western United States (Figure 4.17); from here a wave train of alternating cyclonic- and anticyclonic anomalies emerges reaching the eastern north Atlantic, which is weak for dry but distinct for wet events. Numerical GCM experiments (Lau and Peng, 1992) show the response of the large-scale flow to divergence anomalies in the tropical Indian and Pacific Ocean, which act as wavemakers and lead to wave trains affecting the extratropical flow in the northern hemisphere. These wave trains can extend, under favourable flow conditions, further eastward modifying the circulation over north America and the north Atlantic storm track region. In this sense they may be interpreted as predecessors for Tibetan Plateau drought and wetness.

4.4 Summary

The present chapter analyses processes affecting boreal summer variability of pluvial conditions on the Tibetan Plateau, first in observations, then in pre-industrial and IPCC-scenario climate simulations with a state-of-the-art coupled Atmosphere-Ocean GCM (ECHAM5/MPI-OM). Observed dryness (wetness) on the Plateau is accompanied by reduced (enhanced) water vapour convergence (Figure 4.6b,c and Figure 4.7b,c) due to weakened (amplified) moisture transport (Figure 4.6a, 4.7a) from all three climatological

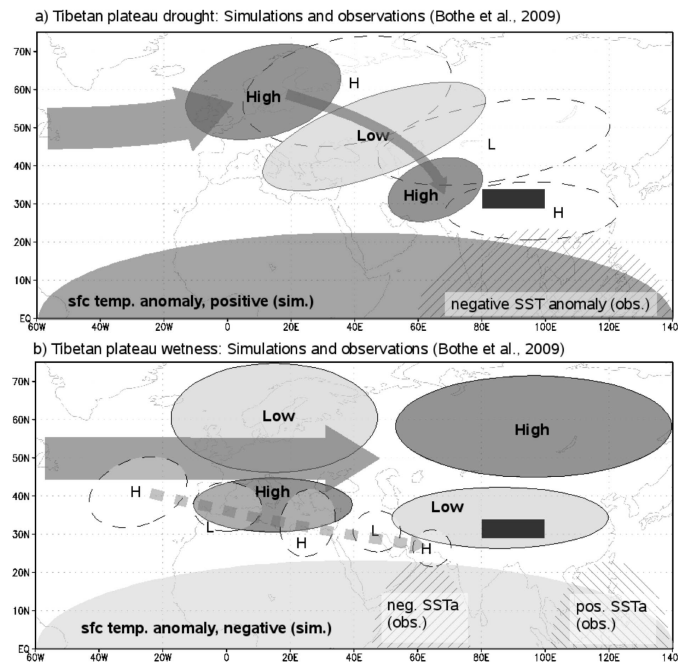


Figure 4.18. Schematic diagram of the dynamics related to drought (a) and wetness (b) on the Tibetan Plateau for model scenarios and observations. Circulation anomalies (model) are shown as ellipses with solid lines. Dark (light) grey are anticyclonic (cyclonic) patterns. Observation anomalies differing from model scenarios are dashed. The storm track (model and observations do not differ significantly) is presented as thick arrow in the north Atlantic. The main wave flux is shown as thin arrow (solid for model, dashed for observations). Tropical surface temperature anomalies are shaded (hatched) for model (observations). Moisture flux anomalies are (not shown) in a) stronger transport from the Indian to the Pacific ocean with subsequent larger reflow into south-east China and in b) weakened flow from the Indian to the Pacific ocean with enhanced southerly flow onto the Tibetan Plateau.

inflow routes associated with the combined effects of the surface temperature and large-scale atmospheric circulation anomalies.

Related zonal shifts of the monsoon circulation (Figure 4.5c) are connected with sustained thermal anomalies of the maritime continent (Figure 4.9), which, in turn, can be attributed to concurrent episodes of IOD and/or ENSO. Tropical ocean surface conditions (Figure 4.9) fit the description by Hong et al. (2008) of IOD and ENSO impacts on Asian moisture fluxes. Surface temperature anomalies reach northward to the East China Sea and modify the western north Pacific subtropical high (e.g. Figure 4.7b) leading to additional moisture flux (see also Chang et al., 2000a,b).

Upstream and mid-latitude modification of the Asian monsoon is subject to intense research. For Tibetan Plateau drought a wave train bridges Eurasia from Scandinavia to east China (Figure 4.6a, 4.8a, 4.9d). During months of wetness (Figure 4.7a, 4.8b, 4.9h)

4 Eurasian bridges

conditions in the north Atlantic favour the development of an anomalous short zonal wavelength wave train in the Mediterranean region due to enhanced mid-latitude flow over Europe between 50° and 60° N (consistent with Liu and Yin, 2001). This pattern occurs prior to the Tibetan Plateau wetness events (Figure 4.9g). Considering the Eurasian bridging, transient eddy activity in the north Atlantic storm track supports a Scandinavian anticyclone. A cold surface anomaly in the tropical north Atlantic (Figure 4.9a to d) contributes to the position and orientation of the storm track via associated persistent atmospheric anomalies, which are best seen in the surface pressure (not shown) and the overlying circulation (Figure 4.9a to d). A northward displacement of the westerly jet in east Asia due to contrasting thermal anomalies in middle and high latitudes supports the dry event wave train in the proximity of the Plateau.

The sub-monthly development of the wave train patterns (Figure 4.6a, 4.7a, 4.8b, 4.9d, h) remains for further studies. Striking is their similarity to prevalent atmospheric fluctuations in boreal winter. Blackmon et al. (1984b) describe *inter alia* “intermediate” mobile wave trains with north-west/south-east orientation (zonal wavenumber four to six, period of under a month) and zonal high frequent baroclinic fluctuations (zonal wavenumber six to nine, period lower than a week). The former is similar to the dry event wave train (Figure 4.6a, 4.9d) and the latter to the wetness Mediterranean wave train (Figure 4.7a, 4.9h). One or two occurrences of the “fast” wave train could classify a month as being wet, while only one geographically and temporally persistent “intermediate” pattern could cause a drought event on the Tibetan Plateau. Although wave train patterns connecting Europe and Asia have been found previously, the explicit links between dryness and wetness on the Tibetan Plateau and the Atlantic sector via wave train features has not been noted so far.

The Scandinavia-East-Asia pattern resembles the European part of the circumglobal teleconnection described by Ding and Wang (2005). According to them, barotropic instability in the north Atlantic jet exit triggers anomalous high pressure over north or west Europe, which affects the Asian monsoon via Rossby wave trains. As the storm track shows an anomalous south-west/north-east orientation for drought events on the Tibetan Plateau, the dry pattern may be interpreted as spatially shifted occurrence of this mechanism. This is in accordance with Ding and Wang (2005), who accept the possibility, that the upstream (Eurasian) part of the circumglobal teleconnection triggers a strong upper level anticyclonic anomaly and, subsequently, a strong Indian monsoon.

James and Hoskins (1985) identify the eastern Mediterranean as possible example for an internal baroclinic instability mechanism. Rodwell and Hoskins (1996, 2001) describe a connection between Asian monsoon heating and the dynamics of deserts as well as the atmospheric circulation in the Mediterranean region. There, Ziv et al. (2004) find negative correlations with the monsoon (leading by 1 day) using interdiurnal vertical pressure-velocity variations. In the present study computing correlations between ERA-

40 daily summer monsoon ascent and Mediterranean descent (same regions as Ziv et al., 2004, different level) yields no significance for most years with Tibetan extreme episodes (not shown). For example, in the case study of 1984 only the dry August displays the monsoon leading as described by Ziv et al. (2004). The impact of extreme daily as well as climatological episodes of monsoon heating remains for further research.

In the simulations dry events on the Tibetan Plateau are related to a warming in the tropical oceans (Figure 4.10d) because over the Indian ocean region tropical upper level easterlies are reduced and lower level westerlies are enhanced which prohibit moisture flow onto the Tibetan Plateau. Weaker moisture inflow from the south-east relates to a concurrent anomalous anticyclone over north-eastern China and a strengthened north Pacific subtropical high. A conceptual sketch (Figure 4.18a) displays the principle results for dry events found in simulation data, and how they compare to the observations (e.g. Figure 4.12b): Circulation composites (Figure 4.10a) show a pronounced upstream wave-pattern, forced and maintained by transient eddies of the north Atlantic storm track (compare Bueh and Nakamura, 2007); that is, a more south-west/north-east orientation of the north Atlantic storm track is observed with enhanced zonal winds east of Greenland (Figure 4.10). The trans-Eurasian wave train ends in a high pressure anomaly west of the Tibetan Plateau which, in combination with the mechanical barrier of the Himalaya Range, reduce the moisture inflow from the Arabian Sea. Locations of related flow anomalies differ between model and observations (Figure 4.12), but the mechanisms obviously match (Figure 4.18a). Similar circulation features are noted by Sato and Takahashi (2006) and Wakabayashi and Kawamura (2004). A circumglobal picture (see also Ding and Wang, 2005) emerges, when following the circulation further downstream.

The wet events on the Tibetan Plateau in the ECHAM5/MPI-OM simulations are associated with strong near global tropical cold SST-anomalies (Figure 4.11d). In the Indian ocean this cooling leads to more intense moisture-transport through the Arabian Sea and the Bay of Bengal onto the Tibetan Plateau, because the more zonally oriented hemispheric circulation (compared to the summer mean) reduces mid-latitude influences. Observations show a zonally oriented wave train commencing from the Atlantic and crossing the Mediterranean to Asia and even the Pacific (dashed ellipses in Figure 4.18b). Lag-correlations ($300hPa$ meridional wind, Figure 4.16) for wet months display zonally oriented patterns upstream of the Tibetan Plateau commencing near the Mediterranean. The schematic diagram (Figure 4.18b) summarises the main anomalies.

The circumglobal perspective comprises upstream and downstream circulation patterns in the summer lag-correlations centred on the Tibetan Plateau (Figure 4.13). The upstream wave train bridging Eurasia from the north Atlantic to the Asian monsoon regions interacts with the regionally SST-forced circulation anomalies. This interaction provides the conditions of precipitation variability on a monthly time scale. The upstream influence dominates in dry months (Figure 4.15), but is weakened for wet events

4 Eurasian bridges

(Figure 4.16). Downstream lag-correlation patterns exhibit a Pacific-north American wave pattern which can be interpreted as forced by the Tibetan Plateau (Lau and Peng, 1992; Held et al., 2002; Wang et al., 2008a) or emerging from thermodynamical steering in the tropics of the Indian or Pacific ocean (Lau and Peng, 1992). This further resembles the Pacific-Japan-pattern described by Nitta (1987).

Atmospheric composites for IPCC future scenarios (ECHAM5/MPI-OM, not shown) and for selected periods of the control-run (not shown) confirm the circulation patterns presented here, but give stronger indications for a symmetric relation between Tibetan Plateau SPI and hemispheric circulation in summer. Analysed data of other models included in the IPCC fourth assessment report (obtained from the IPCC data distribution centre, not shown) demonstrate a wave train bridge from larger Scandinavia to central or eastern Asia as the most common anomalous atmospheric flow feature for Tibetan Plateau wetness and drought. Differences in the results of the various models may be due to the representation of the Tibetan Plateau; that is, different model resolutions and implementation of orography.

In summarising, the present chapter shows that concurrent conditions upstream (the anomalous state of the north Atlantic ocean) and downstream (SST-anomalies in the Indo-Pacific region) of the Tibetan Plateau are relevant for the development of south-eastern Asian rainfall. As the persistence of these anomalies matters, they influence the Asian region on longer time scales. Further examination of the impact of the seasonal and annual mean circulations on the regional climate is necessary to resolve the initiating dynamics. Finally, higher resolution model simulations may lead to a more realistic representation of the cross Eurasian and circumglobal flow, which is provided by coherent large-scale circulation patterns like wavemakers and wave trains. These are few “low dimensional” features relevant to the bridging process which, to be generated, require higher resolution processes. Capturing these mechanisms may lead to more consistency between model results and observations in future present day and scenario simulations.

5 Synopsis and outlook

The origin of the present thesis is the necessity to evaluate impact factors on the characteristics of precipitation in certain regions as a background for the management of water resources and the estimation of potential present and future risks of hydrological severe and extreme conditions. For example, the Yangtze river basin in China is subject to recurrent flooding and drought in summer due to (i) decadal variability of the east Asian summer monsoon and (ii) external impacts from inter-annual large-scale atmospheric and oceanic variability. In contrast, the Indus river and water reservoirs of groundwater and glaciers are utilised in the agriculture of northern India and Pakistan to the effect, that the demand on water enforces improved assessments of available water on monthly, seasonal and inter-annual time scales. In summer, subsystems of the Asian and global monsoon circulation influence these river catchments and constitute the main annual source of precipitation. The thermal state of the Tibetan Plateau and the overlying atmosphere are possibly pivotal forcings of the monsoon circulations in Asia. In turn, the hydrological state of the Plateau affects the thermal conditions. Hence, the research focusses on the Tibetan Plateau and pays additional attention to the larger Tian Shan region and the river catchments of Yangtze and Indus.

A simple rationale underlies the examination of covariability of precipitation in these regions with external factors in the atmospheric and oceanic circulations: The spatially and temporally small-scale phenomenon precipitation is to some extent regionally conditioned by influences on larger spatio-temporal scales. The assumption is considered from the viewpoints of time series and dynamical composite analyses in boreal summer. The covariability of regional precipitation in terms of the standardised precipitation index with atmospheric and oceanic teleconnection indices is described in chapter 2 with a previous discussion of the teleconnectivity of the summer precipitation. The study of coherence between standardised precipitation in Asia is extended in chapter 3 to evaluate the impact of the zonal wind structure upstream of the central Asian orography on precipitation in central Asia. Owing to its position in Asia and its effects on the regional to hemispheric atmospheric circulations, the Tibetan Plateau is subject to a detailed discussion of the dynamical factors, which influence moisture fluxes to and precipitation above its territory in chapter 4. These discussions are subsumed under the title of “teleconnections for precipitation”, where ‘teleconnection’ refers to covariability in the field of the parameter considered, to remote covariations in different fields and to patterns

found to influence a meteorological variable in a certain region. Precipitation, as the studied measure, is employed in the transformed and standardised design of the Standardised Precipitation Index (SPI) following McKee et al. (1993).

5.1 Synopsis

All chapters present prominent connections between precipitation over Asia and the atmospheric circulation in the upstream north Atlantic/European sector. Put figuratively, bridges are found from the north Atlantic to central and east Asia, which deflect moisture fluxes from or direct them into the regions of interest. The most distinct of such features is the Scandinavia-East-Asia bridging in chapter 4 for dryness on the Tibetan Plateau in model and re-analysis data. This pattern and its zonal counterpart, the Mediterranean wave train, for observed above normal precipitation on the Plateau, serve as example of possibly asymmetric mechanisms influencing the precipitation in a region of climatic significance. Indeed, simulation data indicate a more symmetric relationship in a larger sample size.

Upstream wave train links and associated anomalies, which deflect the moisture inflow not only from the south, confirm the findings of chapter 3 on the impact of the zonal wind structure in a zonally averaged section between 50°E and 65°E on central Asian precipitation in the Tarim river basin, the Tian Shan mountains and on the Tibetan Plateau. Leading principal components for the section describe meridional position and strength of the main subtropical jet and its mid- to high latitude counterpart. Coherence of jet variations and regional precipitation is found in summer, when strengthened westerly moisture flow arises climatologically. Principal components exhibit notable persistence. Position and bifurcation of the flow around the Tian Shan affect precipitation in the Tarim basin, mean jet position and relative strength of the subtropical and polar jets are most important for summer precipitation on the Tibetan Plateau. Upstream bridges from the north Atlantic sector are weak but perseverative in composites and are interpreted as components of Atlantic/European teleconnection patterns (compare Barnston and Livezey, 1987; NOAA, 2005–2008), that stretch across northern Eurasia, cross the Mediterranean to Asia or arch from northern Europe to central and eastern Asia (Blackmon et al., 1984a,b; Ambrizzi and Hoskins, 1997; Ambrizzi et al., 1995). In addition, circumglobal patterns (compare Ding and Wang, 2005) can be depicted. Correlations of PC time series and common teleconnection indices consolidate the links between the studied zonal section and the upstream atmospheric circulation.

The relationship between precipitation in central Asia and the upstream circulation is already reflected in such a simple measure as teleconnectivity maps (Wallace and Gutzler, 1981) in chapter 2. The standardised precipitation index in Europe co-varies with the SPI field at the southern flank of the Himalaya southwards to the Arabian Sea and

on the Tibetan Plateau. The SPI fields in the Yangtze basin, the Indus catchment and on the Tibetan Plateau are strongly correlated with the North Atlantic Oscillation, the Arctic Oscillation and the Scandinavia pattern index.

Area averaged and subsequently standardised precipitation time series display the most stable relations in moving window correlations as follows: (i) The Indian summer monsoon is the strongest impact on precipitation in the Indus catchment, but variances for both indices develop opposite in the late 20th century. Additionally, the covariability with ENSO is noteworthy and the correlations with the AO increase in later decades, when slightly more positive AO summers occur. (ii) On the Tibetan Plateau, the Indian Ocean Dipole mode exerts an influence on precipitation, but significant non-stochastic changes in IOD DMI variance result in fluctuations. Changes in NAO mean and variance in the late 1970s initiate a period of coherence between the Plateau summer SPI and the NAO. (iii) The Yangtze basin SPI relations to remote features undergo strong changes consistent with the decadal variability of precipitation in eastern Asia (e.g. Ding et al., 2008). The relationship is coherent between the upper reaches summer SPI and the NAO in early and late decades of the period 1951 to 2000 and interrupted in-between. Solely the Scandinavia pattern index co-varies significantly throughout the 50 years with the upper reaches standardised area averaged precipitation, and, in addition, is found to correlate weakly with the rainfall in the lower reaches. There, the constantly changing relation to sea surface temperature indices is particularly conspicuous, with possibly significant negative correlations in early decades and nearly as strong positive coherence in late decades of the second half of the 20th century. The variations in covariability of SPI and common teleconnections corroborate the conclusion, that it is not feasible to apply the noticed coherence in water resources management (Archer and Fowler, 2004).

5.2 Discussion

The extent of north Atlantic variability patterns downstream is commonly noticed, and the presently taken systematic approaches stress the importance to identify underlying triggers. Displayed bridges and their variability allow a better estimation of the relative importance of regional and large-scale influences on the summertime Asian (monsoon) circulation, which in future may allow to improve the projection of upcoming monthly and seasonal precipitation. However, the presented results lack the evaluation of two topics: (i) no attempt is made to employ the results in a predictability study of (standardised) precipitation on regional scale or for single locations, and, possibly superordinate and prerequisite to such an approach, (ii) no reasonable mechanistic explanation is presented for, e.g., the differing connections which result in contrary pluvial conditions (for example on the Tibetan Plateau). With regard to the potential to estimate the standardised precipitation based on stable teleconnections, preliminary results indicate no

5 Synopsis and outlook

or at least not much skill (not shown, tested is an approach following Rimbu et al., 2005; Ionita et al., 2008).

Concerning the trans-Eurasian teleconnections, it, first of all, has to be mentioned, that such features are found to be of influence for the east Asian climate (e.g. Watanabe, 2004), the Indian summer monsoon (e.g. Ding and Wang, 2005), the climate of the Tibetan Plateau (Liu and Yin, 2001; Li et al., 2008a) and the climate of Japan (e.g. Enomoto et al., 2003, 2009). These results are similar in the anomaly structure of described features, but differ in their origin and their main effect. Possible redundancies in mechanisms and the importance to ascertain triggers are highlighted, if the spatio-temporal structures of atmospheric circulation fluctuations are revisited (Blackmon et al., 1984a,b). Wave train features in chapters 3 and 4 and the patterns just mentioned can to some extent be subsumed in the dynamical scenarios for the circumglobal teleconnection of Ding and Wang (2005). The most impressive emergence of a circumglobal extent wave pattern is reported by Uno et al. (2009) in their observations and simulations of a dust storm event in the Taklamakan desert in May 2007. Mineral dust is transported in the upper troposphere from its origin in a horizontally oscillating current across the Pacific and then nearly zonally across north America and the Atlantic to Europe. There, the current splits, some air passes over Scandinavia and arches south-eastward, while another portion enters the subtropical jet in the Mediterranean. The northern and southern currents reunite in central Asia. According to Yang et al. (2009), the circumglobal wave train pattern is closely related to temperature anomalies in the tropical Indian ocean, from where an atmospheric response in the upstream northern hemispheric extratropics can be excited by an initial warming.

Results in the present thesis basically revert to the question, whether the monsoon-desert and monsoon-subtropical-anticyclone mechanisms of Rodwell and Hoskins (1996, 2001) are the driving forces in the interaction between the heating of the Asian monsoon circulation and the upstream circulation in the north Atlantic/European sector or whether a re-evaluation is necessary of the connection between the climates in Asia and Europe. Rodwell and Hoskins depict inter alia how the boreal summer heating of the monsoon and the subsequent ascent possibly forces the climate in the eastern Mediterranean by excitation of a westward travelling Rossby wave and its associated descent in the eastern Mediterranean region. This mechanism is the primary forcing for the regional climate (Ziv et al., 2004) with a nearly closed zonal circulation for July and August (averaged between 20° and 35°N). A second cell to the west links the region further to the Atlantic subtropical anticyclone. Ziv et al. (2004) present significant negative correlations for the late summer of 1989 between interdiurnal variations of vertical velocities in the two areas (Asian monsoon, Mediterranean) which are maximized with the monsoon leading by 1 day. If ERA-40 daily vertical pressure velocity data is considered in summer, a wide range of correlation values is found on various monthly and seasonal

time scales. In 1984 for example, the month of June (severely wet conditions on the Tibetan Plateau) or the full summer display no significant correlations between both areas. However, the August 1984 displays the monsoon leading as described. The month is characterised as severely dry on the Tibetan Plateau. It appears justified to assume the anomalous wave train in the Mediterranean, that is central to the dynamics of wetness on the Tibetan Plateau, to be largely independent of the monsoonal heating.

Revisiting the structures of 500hPa geopotential height anomalies An assessment of the variability of the 500hPa geopotential heights in the north Atlantic sector (revisiting the results of Blackmon et al., 1984a,b, for summer and simulations with ECHAM5/MPI-OM) exhibits the following initiatory results for structure, variability and remote coherence of 500hPa geopotential height. Based on twice daily data, fluctuations range from short lived eddies to long inter-annual climate variations.¹

Standard deviations of northern hemisphere 500hPa geopotential heights on various time scales show common maxima, for example, over the exit region of the north Atlantic storm track at the British Isles (not shown). On long time scales, minima are visible in the central Mediterranean and the north Atlantic storm track. In variance ratios of different time scales, the annual cycle dominates the monsoon affected regions of north-western Africa and east Asia. The average annual cycle is nearly neglectable considering the variance over northern Europe, India and central Asia.

Two main centres for variability arise: short fluctuations are most prominent in the north Atlantic storm track, while data on all other time scales vary maximally in the storm track exit region stretching further across the British Isles, the North Sea and the Baltic Sea. In teleconnectivity maps, a dipole links the eastern Mediterranean to the region from the British Isles to Scandinavia (compare Figure 1.7). One-point-correlations with central Europe display the short wave-length wave train specified by Blackmon et al. (1984a,b) for short time scales. It is traceable upstream back to the east coast of north America and reaches downstream to the Arabian Peninsula. Intermediate time scale data presents the associated pattern described by Blackmon et al. (1984a,b). The pattern arches from the central north Atlantic to Europe and then equatorwards to north Africa. Indeed all downstream components, except for short fluctuations, orientate zonally and equatorward.

The dependence on the position of the correlation-centre can be represented in multiple one-point-correlation maps (selected for their visual image, see appendix D). Short time scale patterns (Figure D.1) attain nearly a semi-hemispheric extent with only slight arching. Centred over northern central Europe, the wave trains originate in the western

¹Twice daily geopotential heights are considered with and without annual cycle. Various filters are applied to the adjusted data of which three are to be mentioned: a bandpass filter (2.5 to 6 days, Blackmon and Lau, 1980) and fourier transforms of the seasonal daily data with consideration of intermediate (~ 10 to ~ 23 days) and long fluctuations (~ 14 to 92 days).

5 Synopsis and outlook

north Atlantic and emanate to western central Asia. Other patterns reach the summer westerly jet above the Mediterranean. Mediterranean centres are related to distinct wave trains crossing the Black Sea or diffusing over Arabia. Intermediate time scale one-point-correlations are nearly zonal for centres over central Europe (Figure D.2). Northern centres relate to downstream south-eastward arching anomalies and appear to be initiated to the south-west. South-eastern centres are downstream components of these patterns. Intermediate wave trains extend nearly hemispheric. The long time scale correlation patterns are equivalent to monthly patterns (see Wallace and Gutzler, 1981) flanking maxima of variance and displaying significant correlations across the Eurasian land-mass. Lagged correlations reinforce these results. Noteworthy lagged patterns for long time scales originate in the northern mid-latitudes of the north Atlantic, subsequently stretch along the summer subtropical jet and bend around the Tibetan Plateau.

Sub-seasonal circulation features are, to some extent, defined by the wave guide effect of the jets and in turn depend on the persistent position of the jets in summer, the variability of the jets and external impacts on the jets. Features tend to evolve in and align along the jet. On short time scales, travelling wave trains develop in the north Atlantic storm track. Their downstream directions include (i) the development along the subtropical jet across the Mediterranean, (ii) the bridging of Europe in the extension of the storm track and (iii) subsequently the passing along the polar front jet or (iv) the south-eastward bend to central and eastern Asia.

5.3 Outlook

Results and discussions detail remote interactions between the upstream circulation, emanating wave trains and the Asian monsoon circulations. A central question remains undiscussed, which has to be addressed to quantify these upstream factors in their impact on the monsoon circulations and, hence, to utilise them as potential predictors for regional precipitation. Which factors influence the shape and development of Eurasian bridgings in different events? Surface factors have to be identified, which have potential to deflect atmospheric flows and wave activity or direct them along a certain route on time scales from days to months. Possible triggers are north or central Atlantic sea surface temperature and flux anomalies, the course of the Gulf Stream or the intensity of the meridional overturning circulation (e.g. Jungclaus et al., 2005; Kuhlbrodt et al., 2007). Besides the influence of tropical Atlantic SSTs on the decadal variability of the NAO (Sun et al., 2009b), preliminary results indicate a central role of the variability in the eastern Mediterranean interacting with the atmospheric variations in central northern Europe as possible triggering or regulating feature. Hence, the atmospheric state is possibly less important directly upstream of the Himalaya (compare chapter 3) where the jet is close to purely zonal, but rather the relations between the location of the north

Atlantic storm track exit and the continuity or break up of the subtropical jet (across Arabia and western Asia) define an upstream influence on the Asian monsoon.

In the consideration of factors available for prediction, the Atlantic Multidecadal Oscillation (AMO, period of about 70 years, Kerr, 2005) is an upcoming choice. It describes the decadal variability of Atlantic basin averaged sea surface temperatures. Asian precipitation data is mostly limited to the second half of the 20th century, and therefore, a discussion of the AMO in the present context is of limited value. Various studies detail the influence of the AMO on rainfall and streamflow in the U.S.A (Enfield et al., 2001), the north American summer monsoon (Hu and Feng, 2008), rainfall in the Sahel (Zhang and Delworth, 2006), precipitation in India (Zhang and Delworth, 2006; Li et al., 2008b), the Indian summer monsoon (Feng and Hu, 2008), Arctic air temperatures (Chylek et al., 2009) and how the AMO is linked to the Pacific variability (d'Orgeville and Peltier, 2007; Zhang and Delworth, 2007) and to the whole of the Asian summer monsoon (Wang et al., 2009). A short initiating consideration reveals notable coherence between an AMO index constructed from annual mean surface temperatures for the ERA-40 re-analysis data and summer SPI in some of the considered regions. Regressions of atmospheric summer fields against the annual AMO give a wave train structure similar to discussed bridges. Thus, the impact of the decadal Atlantic variability should be thoroughly and systematically depicted, to quantify its potential as a predictor of regional precipitation in eastern and central Asia. In particular, a trustworthy estimation of the summer precipitation with respect to the Tibetan Plateau can help to subsequently assess seasonal precipitation on the Indian subcontinent and China due to the effect of the plateau as an elevated heat source. According to Levermann et al. (2009) only weak external influences suffice possibly to trigger abrupt monsoon transitions because of a moisture-advection feedback in the seasonal heat balance.

A Methods and third party software

A.1 Significances of moving window analyses

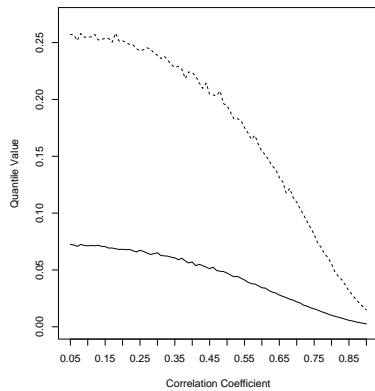


Figure A.1. Bootstrap estimate of quantiles for window correlations (see text for details).

This section repeats the note of chapter 2 on how to distinguish noise and signal related variability in moving window correlation analyses. Following the comments of Wunsch (1999) on the interpretation of short climate records, Gershunov et al. (2001) systematically discuss the claimed weakening in the relationship between the Indian monsoon and El Niño/Southern Oscillation (e.g. Krishnamurthy and Goswami, 2000; Kumar et al., 1999) and are not able to dismiss the hypothesis, that the variability in the relationship is attributable purely to stochastic processes. Therefore they recommend to use a bootstrap approach (Efron and Tibshirani, 1993) in any research on decadal variability in the linkage between time series, particularly in any utilisation of running window correlations.

First, the “best” autoregressive model is established to fit the data. If this results in zero order assumptions, and the time series are supposed to be independent random variables, the natural variability of the coherence of such two time series is easily evaluated by simulating pairs of correlated white noise time series: Is $x_1(t)$ a time series equaling ε_1 , then a series correlated with a correlation coefficient c can be constructed by $x_2(t) = cx_1(t) + \varepsilon_2$, with ε_i being random normal distributed variables with zero mean and unit variance (σ_1^2) for ε_1 and $\sigma_2^2 = 1 - c^2$ for ε_2 because x_1 , due to the correlation, explains c^2 of the variance of x_2 . The correlation coefficient c refers to the full length time series, which is in this case 50 year or 50 data points. The simulation is done for correlation coefficients from 0.05 to 0.9 in 0.01 intervals. Afterwards moving window correlations, means and variances are computed for a window length of 21 data points. Standard deviations are computed for each correlation coefficient over the running measures. If this simulation is repeated M times in an bootstrap approach, the 95% and 5% percentiles of the standard deviations of moving window correlations (and means and variances) serve as 95% significance levels for one-tailed tests. The tested hypothesis is: Variabilities of the running measures are purely stochastic. Variability exceeding the

95% percentile is significantly enlarged relative to a pure random white noise process, and it is significantly smaller than in a pure random white noise process, if it is below the 5% percentile. The 95% percentile is included in the respective figures relative to the correlation over the full period and the estimates for the correlation coefficients are plotted in Figure A.1. The stippled (continuous) line represents the 95% (5%) percentile with respect to the full period correlation coefficients as depicted by the abscissa. $M = 5000$ is utilised. As an example, a window correlation coefficient of 0.69 is possible due to pure stochastic variability for windows of 21 data points and a correlation coefficient of $c = 0.5$ between two base time series with 50 data points. According to the bootstrap estimate, the moving window (length of 21 values) means of a random normal process with zero mean (full period 50 values) may vary about ± 0.25 before the variation in mean is conspicuous. Variations of less than about ± 0.07 are again peculiar. Moving window variances are unremarkable between $\sim 1 \pm 0.09$ and $\sim 1 \pm 0.36$ for the assumed setting.

A.2 Calculation of vertically integrated moisture fluxes

Vertically integrated moisture fluxes are presented for ERA-40 (Uppala et al., 2005) and ECHAM5/MPI-OM (Roeckner et al., 2003) data. These are computed following the procedure presented by Simmonds et al. (1999). Surface pressure and pressure level data is employed for meridional wind, zonal wind and specific humidity. The levels are $100hPa$, $150hPa$, $200hPa$, $250hPa$, $300hPa$, $400hPa$, $500hPa$, $600hPa$, $700hPa$, $775hPa$, $850hPa$, $925hPa$ and $1000hPa$. Data is available in a temporal six hour resolution. Simmonds et al. (1999) apply an approach previously discussed by Trenberth (1991). The vertical integration on pressure levels neglects the possible imbalances or residuals, which arise in the processing of re-analysis model output onto the pressure levels. The procedure integrates not over continuous layer contents but over values, which represent the level of the three dimensional grid point. Thus, the moisture balance is not necessarily closed with regard to the pressure levels. Imbalances subsequently also exist in the vertically integrated components.

The calculation distinguishes between stationary and transient flux-components with transients defining anomalies for each ongoing month:

$$\overline{q \mathbf{u}} = \overline{q} \overline{\mathbf{u}} + \overline{q' \mathbf{u}'}$$

q is the specific humidity and \mathbf{u} the horizontal wind vector, over-bar and prime denote time mean and deviation, respectively. The vertical integration is performed in finite differences with a trapezoidal setup. That is, the incorporated atmospheric column from the surface to the $100hPa$ level is divided into 13 new layers, whose borders are set by the new lowermost level at $1100hPa$ and the uppermost one at $75hPa$. The pressure levels

A.3 Empirical Orthogonal Functions or Principal Component Analysis

reside in the middle of two new levels. The finite difference integration becomes:

$$\mathbf{F} = \frac{1}{g} \sum_{j=1}^J \beta_j q_j \mathbf{u}_j \Delta p_j$$

with g , gravity acceleration, J , the number of layers, and Δp_j the pressure thickness of the j th layer. The trapezoidal setup necessitates a factor to account for the position of earth's surface in the vertical column. β_j is assigned for each level at each time step anew to correct the amount of each layer, that is above the surface (p_s , surface pressure, p_j^t , top of j th layer)

$$\beta_j = \begin{cases} 0 & \text{if the } j\text{th layer's top is below the surface,} \\ 1 & \text{if the } j\text{th layer's top is above the surface,} \\ \frac{p_j - p_j^t}{\Delta p_j} & \text{if the surface is in the } j\text{th layer.} \end{cases}$$

A.3 Empirical Orthogonal Functions or Principal Component Analysis

Since Lorenz (1956) introduced empirical orthogonal functions (for an extensive introduction, see von Storch and Zwiers, 1999) into atmospheric sciences in his work on statistical weather prediction, scientists and students utilise the technique in scores of scores of studies to determine co-varying patterns in extended multi-dimensional data sets. While North et al. (1982) and others discuss the statistical uncertainties in the estimation of modes, patterns or loadings, a number of recent reviews and "caveat"-publications (e.g. Dommenges and Latif, 2002; Hannachi et al., 2007; Dommenges, 2007) stress the intrinsic problems of the method. Monahan et al. (2009) put it to the catch phrase, one should not mistake the medium for the message. This appendix shortly details the mathematics of principal component analysis and the inherent "caveats".

Principal Component Analysis The phase space of atmospheric data is, from a human point of view, close to infinite, that is, an interpretation is not easily achieved. The solution would be a statistical technique, that reduces the phase space and clearly discriminates between the significant major "modes" and the "leftovers". Principal component analysis is the technique most commonly applied with the intention to determine the relevant features from the residual. Thus, the start for the short description is a vector $\mathbf{X}(t)$ that evolves in time and may represent any data field of interest. We assume N time steps and a spatial dimension of M grid points. \mathbf{X} is assumed to be of zero mean; a suitable mean is subtracted before utilisation. The vector can be expanded into a finite series of time coefficients α_n and pattern vectors \mathbf{e}_n :

$$\mathbf{X}(t) = \sum_{n=1}^{N-1} \alpha_n \mathbf{e}_n + \epsilon_n.$$

The base vectors or patterns are chosen to be orthogonal and to minimise the residual ϵ_n . Thus, the coefficients, α_n , varying in time, are projections of the vector \mathbf{X} onto the pattern vector \mathbf{e}_n .

An eigenvalue problem can be formulated to find the base vectors

$$\mathbf{C} \mathbf{e}_n = \lambda_n \mathbf{e}_n$$

for the covariance matrix

$$\mathbf{C} = \frac{1}{N-1} \mathbf{X}^T \mathbf{X}$$

with, ordered by size, the eigenvalues $\lambda_1 \geq \lambda_2 \geq \dots \geq \lambda_{N-1}$ and the eigenvectors \mathbf{e}_n . The time coefficients are the principal components of the vector \mathbf{X} and the eigenvectors are called the loadings or Empirical Orthogonal Functions. Then the original field \mathbf{X} is expressed based on a new set of orthogonal base pattern vectors and their uncorrelated time series. The total variance of \mathbf{X} is the sum of the eigenvalues λ_n and it is common to write the variance “explained” by each eigenvalue as percentage

$$\frac{100\lambda_i}{\sum_{n=1}^{N-1} \lambda_n} \%.$$

Here, latitudinal weights are used according to the field grids, and principal components are computed with the PINGO package of the Model & Data group at the Max Planck Institute for Meteorology.

Caveat Principal component analysis is a most useful tool for identifying prominent patterns of variability and reducing the dimensionality of data. However, it is a tool and one with notable problems, when the interpretation of the mathematical results is considered. Spatial and temporal auto-correlations in the data and the suggested coherence in large-scale patterns are always just due to the correlations of neighbouring locations (e.g. Hannachi et al., 2007). For example, the Arctic Oscillation pattern is identified as leading mode in northern hemispheric PC studies, that links the Atlantic and the Pacific sector, but some studies employing different methods find no significant correlative relationship between the two basins (e.g. Ambaum et al., 2001; Dommenges, 2007; Vallis and Gerber, 2008). The weaknesses of the PC analysis are to identify the dominant variability centre and the interdependencies between multiple centres in multivariate data (Dommenges and Latif, 2002). The difficulty arises from the definition of the tool, that requires orthogonality in time and space of the variability modes, which in nature is often not a feasible assumption.

Dommenget (2007) suggests to implement a null hypothesis to test PC analysis techniques. In much the same way as Hasselmann (1976) describes a null hypothesis for time series, it is proposed to fit an $AR(n)$ process or a representative physical model to the spatial fields. The spatial equivalent to an $AR(1)$ process, like in time series analysis, would be an isotropic diffusion process (Dommenget, 2007). PC loadings of the process, or an $AR(n)$ -field, and of the original data can be compared to one another and “fingerprints” of the observed data can be defined as deviations from the null hypothesis in the phase space.

Monahan et al. (2009) stress that the individual interpretation of PC loadings is not feasible. Often, EOF modes are interpreted individually, independent of other modes, but, generally, the loadings will not represent individual dynamical modes nor be equivalent to kinematic degrees of freedom nor statistically independent. Especially influential is the demand, that the loadings shall maximise variance over the full analysis domain. Of course, the results are expression of the variability of the data and the physics involved. However, they are not necessarily independent or individually meaningful and have to be re-examined with other methods and a thorough application of the physical laws. Furthermore, patterns from PC analyses are not necessarily expression of one or more readily identifiable physical processes. The heterodyne of distinct physical modes in one loading (or pattern or mode) is demonstrated on the example of the zonal jet (Monahan et al., 2009; Monahan and Fyfe, 2009). For example, while the leading dipole pattern PC loading is due to the strong variations in position, the associated time series also includes information of fluctuations in strength and width. A fact, that has to be considered in the evaluation of the results obtained in chapter 3.

PCA or EOF analysis are filters: The “tool” imprints itself on the data. Multiple tools should be applied relative to the problem at hand. Then, the various achieved representations can be tested against one another.

A.4 Third party software

SPI transformations and statistical analyses are primarily performed with the statistical software R provided by “The R Project for Statistical Computing” (R Development Core Team, 2005). It is available under terms of the Free Software Foundation’s GNU General Public License from <http://www.r-project.org/>. The respective scripts are to substantial extent due to work by Frank Sienz.

Various software packages are employed available from the Model & Data group at the Max Planck Institute for Meteorology. These are: PINGO, cdo, GrADS, gnuplot. Teleconnectivity following Wallace and Gutzler (1981) is computed with, among others, a utility programmed by Martin Doege. This and further routines for computing the variances and covariances (fluxes) of stationary and transient eddy measures and for

A Methods and third party software

calculating the stationary wave activity flux according to Plumb (1985) are available from the Theoretical Meteorology group at the Meteorological Institute of the University of Hamburg (<http://www.mi.uni-hamburg.de/Tools.252.0.html>). A routine for multiple regression analysis is provided by Sielmann (2008).

B Supplement to chapter 2: Teleconnections of the northern hemisphere SPI field

This appendix displays supplementary information on properties of considered indices and standardised precipitation series. Figures B.1 and B.2 re-plot the moving window means and variances in more detail, and Figure B.3 shows the moving window correlations for the whole Yangtze as comparison to the results for the sub-catchments in Figures 2.11 and 2.12 in chapter 2. The correlations of the summer SPI series among each other are displayed in table B.1. Indices for the Pacific Transition pattern and the Tropical/Northern Hemisphere pattern are not considered, as they are only defined for few months (NOAA, 2005–2008).

The SPI-3 for summer (June, July, August) is calculated for the whole period of 50 years. Thus, variances and means will change for different window sizes and from window to window. Similarly other indices (that is the teleconnections) are normalised over the whole 50 year time series. Large shifts in the late 20th century may be attributed to the impact of the 1997/1998 El Niño. Precipitation time series and all other time series are not detrended due to the decadal variability in summer rainfall in the Yangtze river catchment (compare Ding et al., 2008) which is of special interest. Figure A.1 in appendix A displays the natural random variability of correlation coefficients obtained from a bootstrap approach (Efron and Tibshirani, 1993; Gershunov et al., 2001) under the assumption of white noise processes.

Table B.1. Correlation coefficients for the regional summer SPI-3 series among another.

| | Indus basin | Tibetan Plateau | Whole Yangtze | Upper Yangtze | Lower Yangtze |
|-----------------|----------------|--------------------|------------------|------------------|------------------|
| Indus basin | 1. | −0.03 | −0.24 | −0.32 | −0.14 |
| Tibetan Plateau | | 1. | 0.52 | 0.56 | 0.38 |
| Whole Yangtze | | | 1. | 0.81 | 0.95 |
| Upper Yangtze | | | | 1. | 0.60 |
| Lower Yangtze | | | | | 1. |

B Supplement to chapter 2

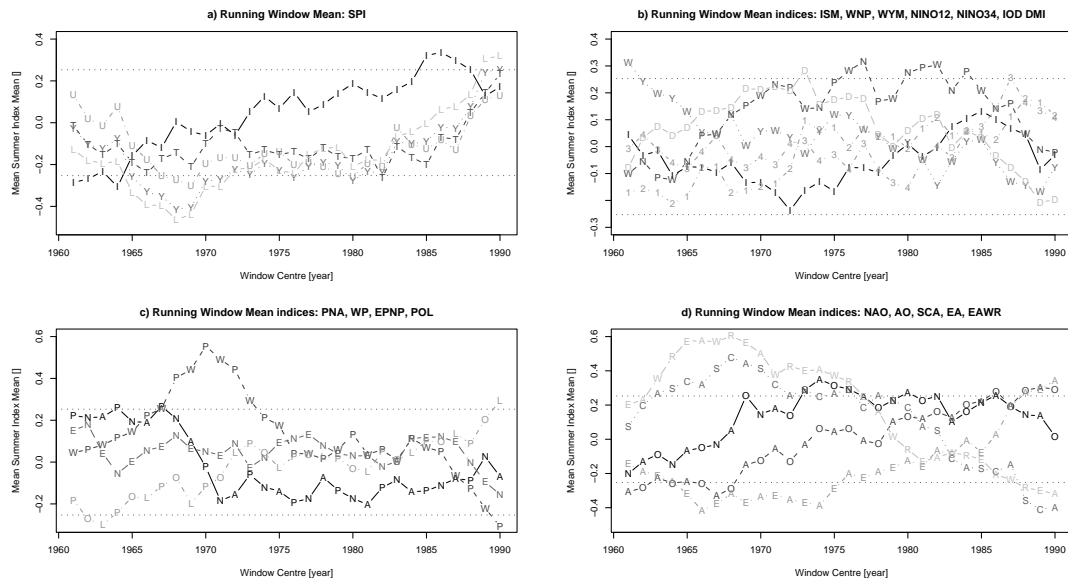


Figure B.1. Moving window means for a) the regional summer SPI time series (labels: I, Indus, T, Tibetan Plateau, W, Whole Yangtze, U, Upper Yangtze, L, Lower Yangtze), b) monsoon indices, ISM (I), WNP (WNP), WYM (WY) and SST-indices, NINO12 (12), NINO34 (34), IOD DMI (D), c) atmospheric indices PNA (PNA), WP (WP), EPNP (EN), POL (POL), d) NAO (NAO), AO (AO), SCA (SCA), EA (EA), EAWR (EAWR).

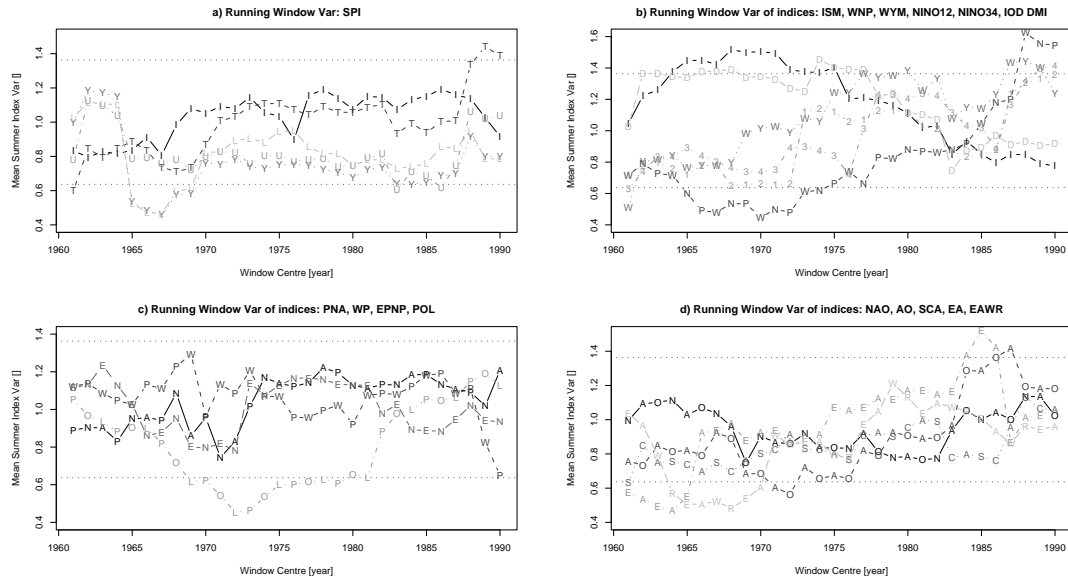


Figure B.2. Moving window variances for a) the regional summer SPI time series (labels: I, Indus, T, Tibetan Plateau, W, Whole Yangtze, U, Upper Yangtze, L, Lower Yangtze), b) monsoon indices, ISM (I), WNP (WNP), WYM (WY) and SST-indices, NINO12 (12), NINO34 (34), IOD DMI (D), c) atmospheric indices PNA (PNA), WP (WP), EPNP (EN), POL (POL), d) NAO (NAO), AO (AO), SCA (SCA), EA (EA), EAWR (EAWR).

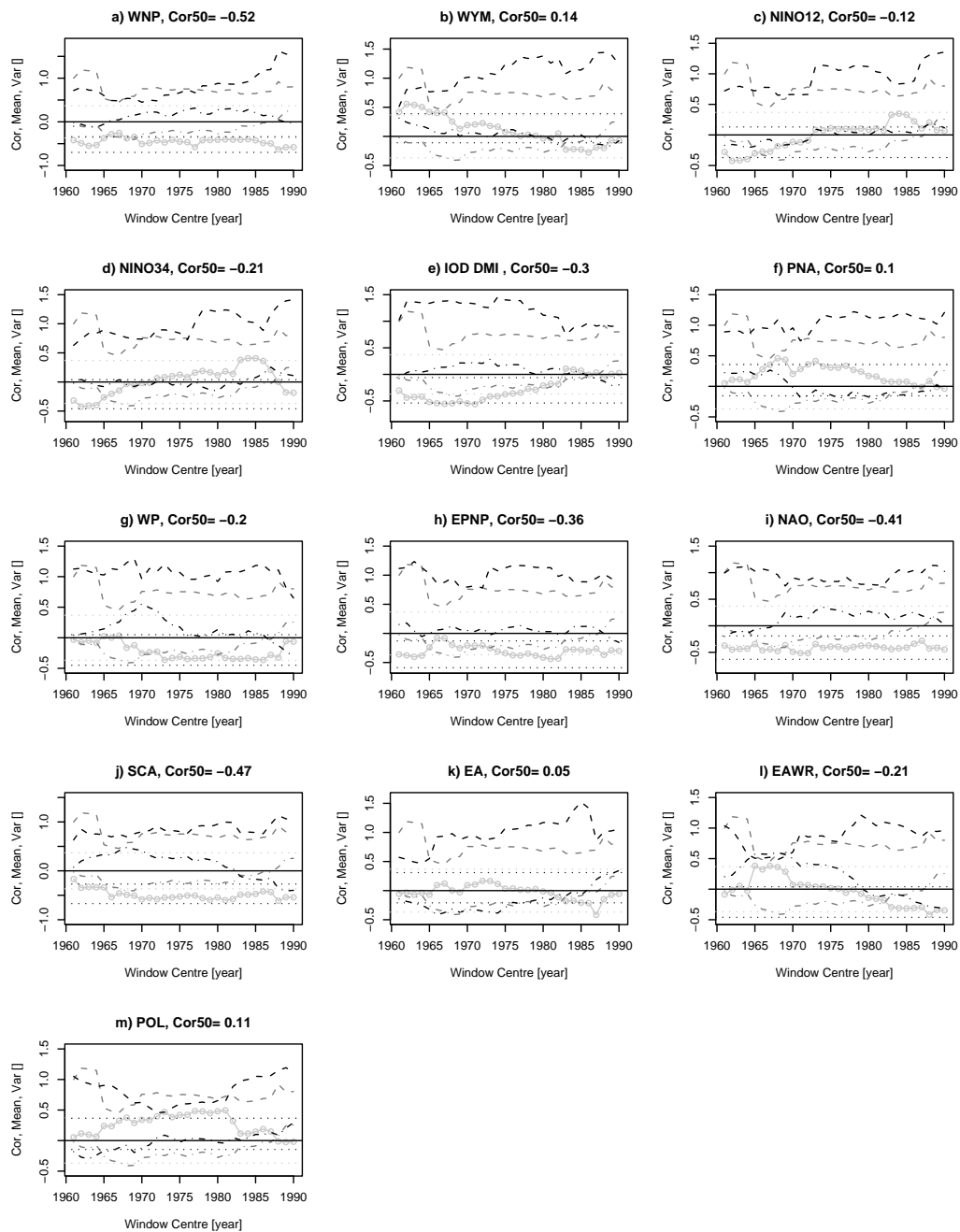


Figure B.3. Whole Yangtze basin summer SPI covariability 1951 to 2000: a) WNP, b) WYM, c) NINO12, d) NINO34, e) DMI, f) PNA, g) WP, h) EPNP, i) NAO, j) SCA, k) EA, l) EAWR, m) POL. Plotted are moving window correlations (line-points), moving variances (dashed), moving means (dash dotted, SPI-means and variances, grey, index means and variances, black). Horizontal lines are t-test significances (90% level, grey dotted) and bootstrap estimates of correlation variability (95%, black dotted).

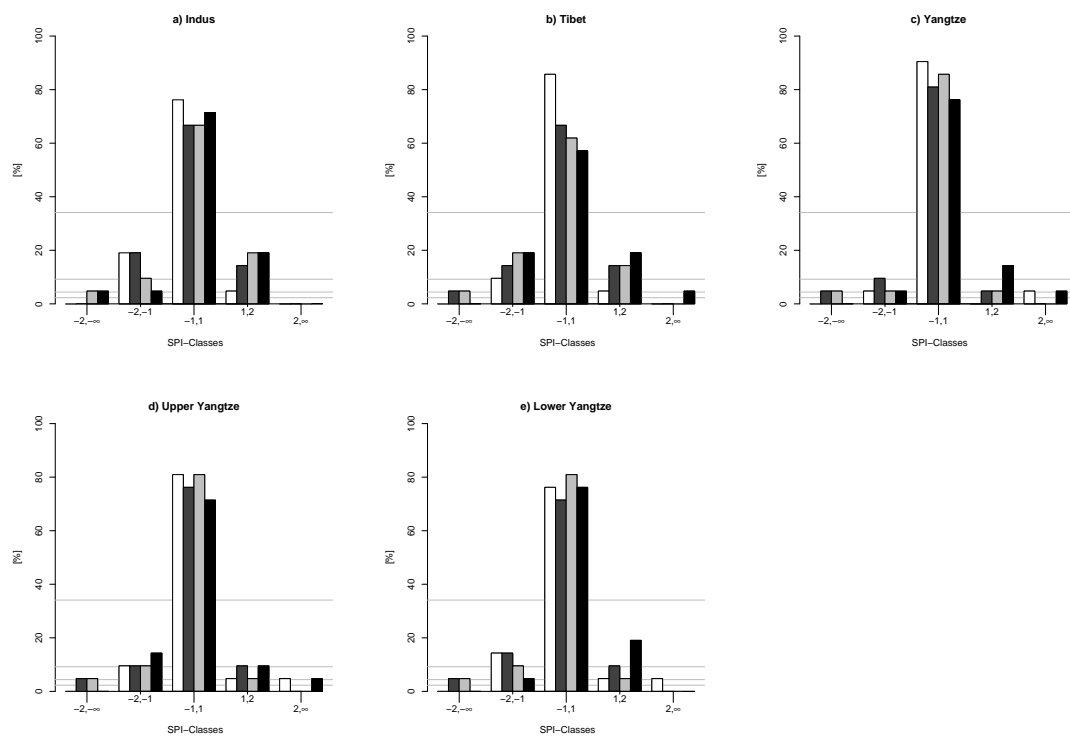


Figure B.4. Change assessment for area averaged summer SPI series, a) Indus, b) Tibetan Plateau, c) whole Yangtze basin, d) upper Yangtze reaches, e) lower Yangtze reaches. Four 21 year windows are considered: 1951 to 1971 (white), 1961 to 1981 (darker grey), 1971 to 1991 (lighter grey), 1980 to 2000 (black).

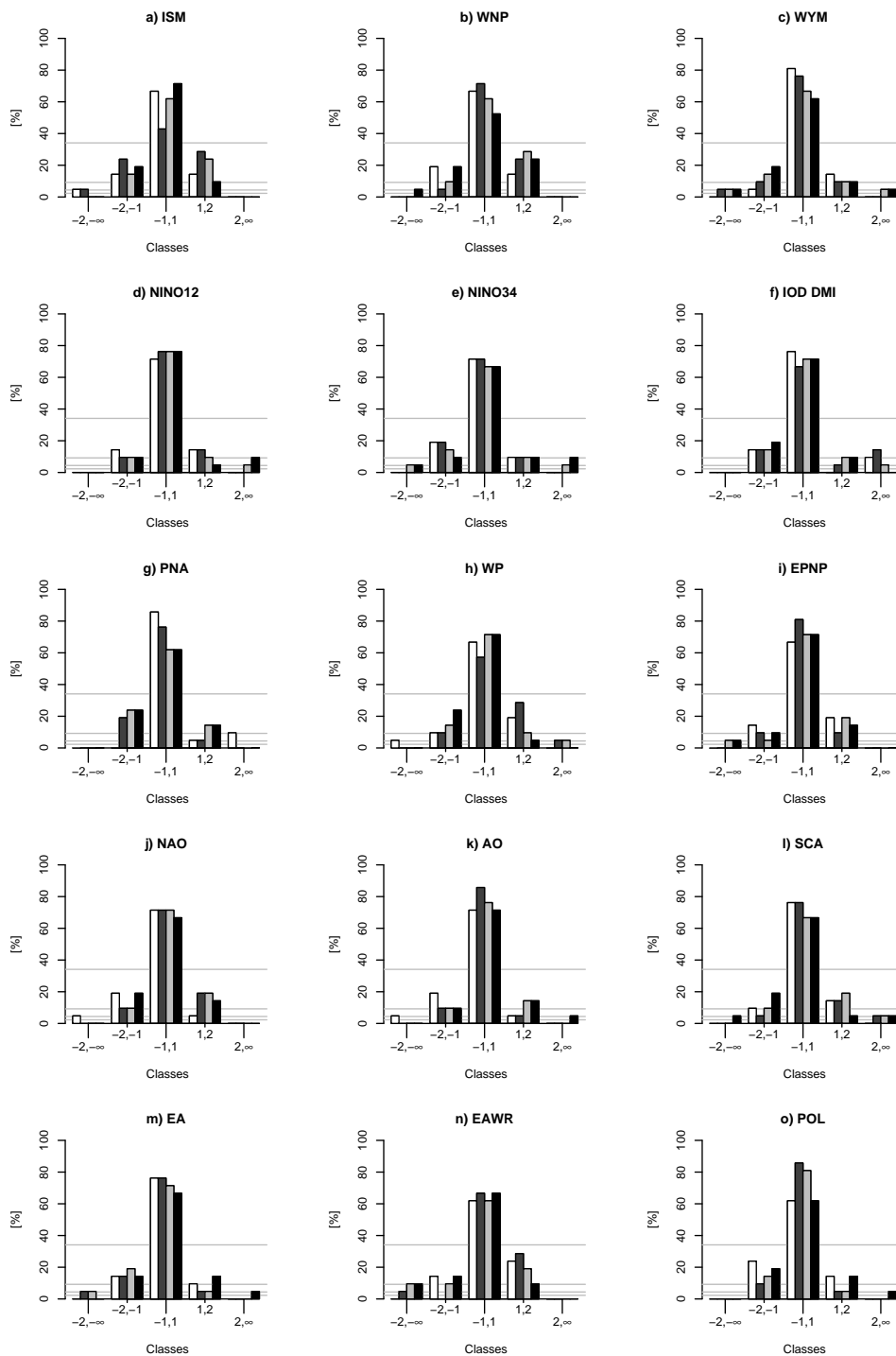


Figure B.5. Change assessment for summer monsoon and teleconnection indices. Four 21 year windows are considered: 1951 to 1971 (white), 1961 to 1981 (darker grey), 1971 to 1991 (lighter grey), 1980 to 2000 (black).

C Supplement to chapter 3: Central Asian precipitation – the upstream zonal wind

This appendix presents further figures to supplement the findings of chapter 3. The zonal wind ($200hPa$) climatology is displayed in Figure C.1, and Figure C.2 gives details considering the climatology of eddy monthly mean moisture fluxes. Figures C.3 to C.6 present the PC-loadings and table C.1 shows their explained variances. Further, correlations are shown between the principal component time series and teleconnection indices. Significance is described in terms of the assumptions detailed in section 3.2. Table C.2 depicts the correlations for the five months discussed.

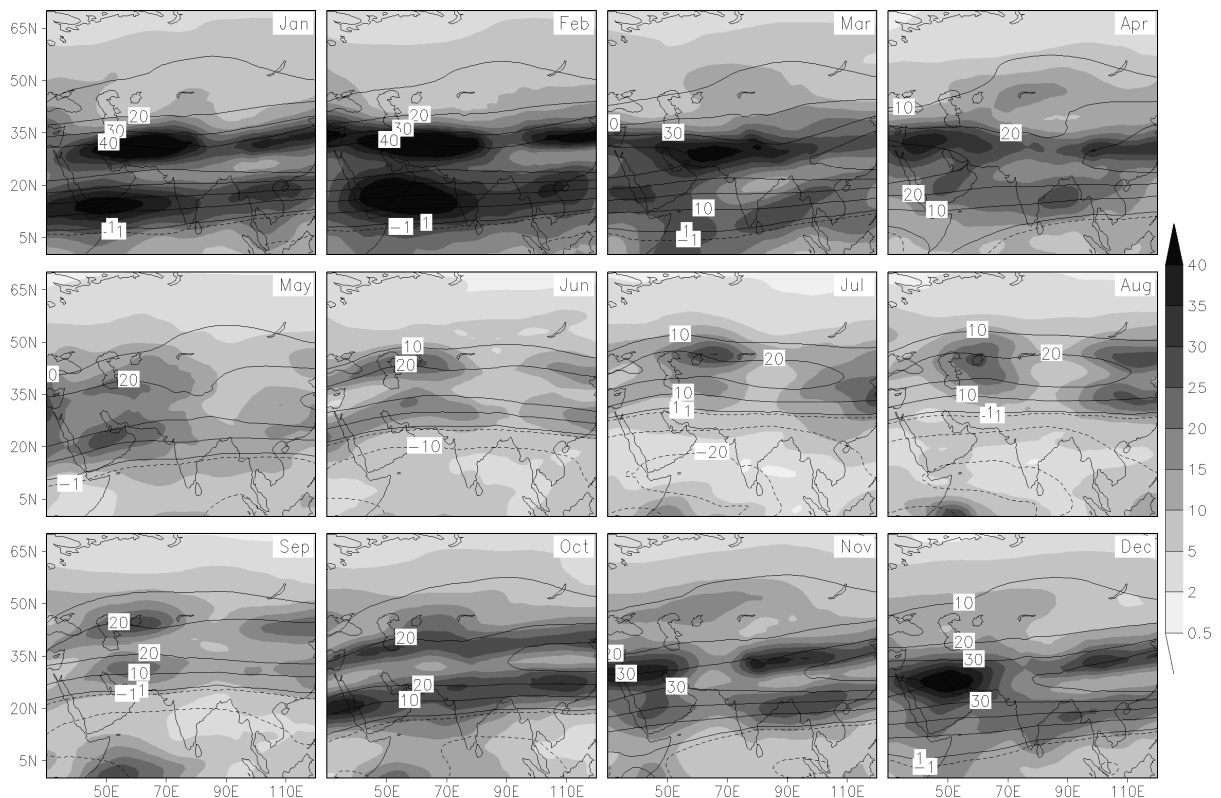


Figure C.1. Annual cycle for the monthly mean zonal wind in $m s^{-1}$ on the $200hPa$ level: mean (contours) and variance (shades).

C Supplement to chapter 3

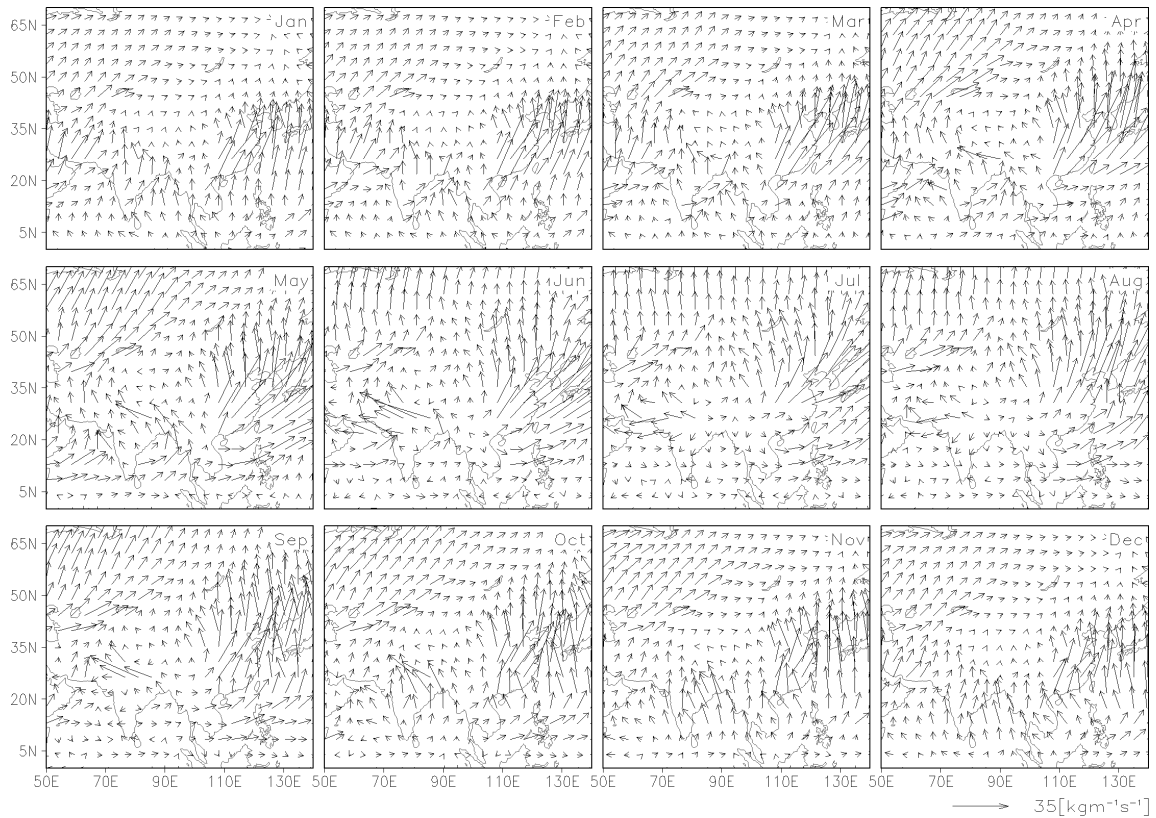


Figure C.2. Annual cycle of eddy monthly mean vertically integrated moisture fluxes from the ERA-40 re-analysis for the larger Asian region.

Table C.1. Variance explained by the first seven PC loadings by month.

| Month | PC-Rank, Eigenvalue (%) | | | | | | | ... |
|-------|-------------------------|-------|-------|------|------|------|------|-----|
| | 1 | 2 | 3 | 4 | 5 | 6 | 7 | |
| Jan | 49.99 | 19.93 | 7.30 | 5.77 | 3.97 | 2.83 | 1.41 | ... |
| Feb | 52.68 | 18.11 | 8.01 | 5.20 | 3.59 | 2.59 | 1.74 | ... |
| Mar | 38.06 | 23.08 | 12.67 | 6.52 | 4.64 | 3.07 | 2.47 | ... |
| Apr | 34.73 | 24.24 | 10.01 | 7.92 | 6.76 | 2.78 | 2.15 | ... |
| May | 46.69 | 17.19 | 9.43 | 5.55 | 3.97 | 2.74 | 2.25 | ... |
| Jun | 38.42 | 12.50 | 9.85 | 7.85 | 5.43 | 4.66 | 3.84 | ... |
| Jul | 31.64 | 22.53 | 9.93 | 7.51 | 4.61 | 3.73 | 2.98 | ... |
| Aug | 31.16 | 21.01 | 11.30 | 7.54 | 6.02 | 3.98 | 3.38 | ... |
| Sep | 44.44 | 16.78 | 10.85 | 6.72 | 3.11 | 2.96 | 2.42 | ... |
| Oct | 45.40 | 17.68 | 9.83 | 6.79 | 5.75 | 2.99 | 1.77 | ... |
| Nov | 35.88 | 22.05 | 10.92 | 8.52 | 6.14 | 3.11 | 2.22 | ... |
| Dec | 35.74 | 25.68 | 10.86 | 9.53 | 4.21 | 2.42 | 2.02 | ... |

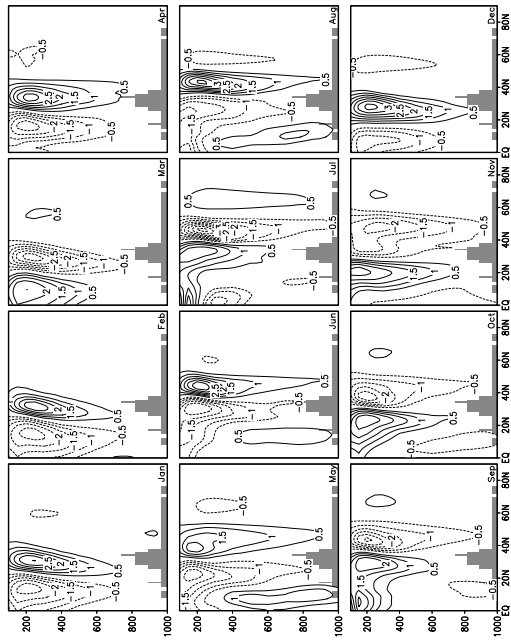


Figure C.3. First loadings of the monthly PC-analyses.

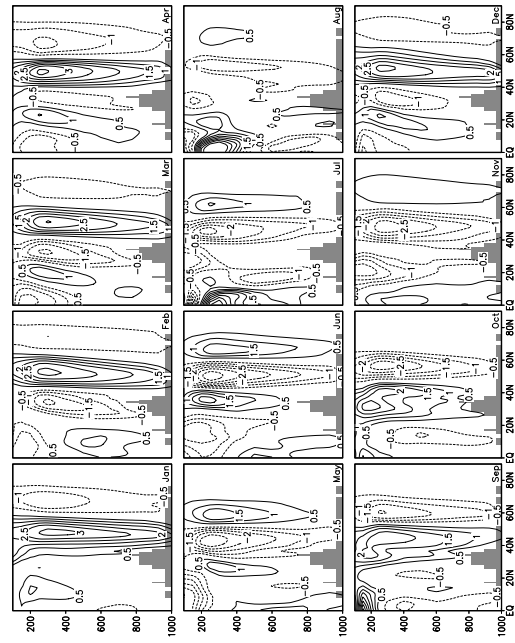


Figure C.5. Third loadings of the monthly PC-analyses.

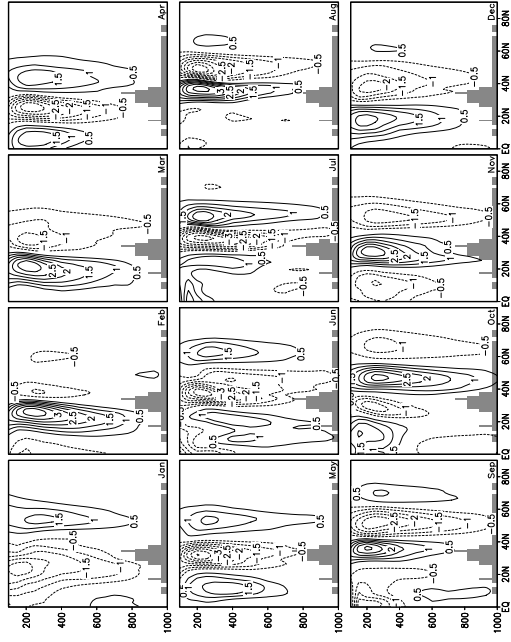


Figure C.4. Second loadings of the monthly PC-analyses.

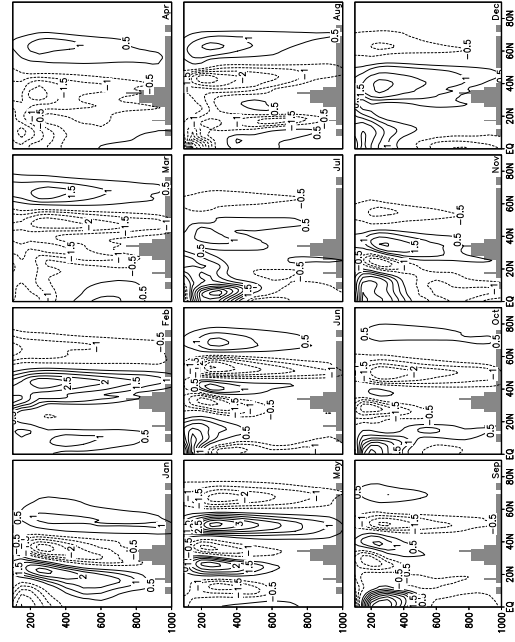


Figure C.6. Fourth loadings of the monthly PC-analyses.

Table C.2. Correlations of monthly PC time series with concurrent teleconnection indices. * and boxes denote, respectively, 90% significance levels relative to 41 degrees of freedom and calculated minimal effective degrees of freedom.

| Month | PCs | Teleconnection index | | | | | | | | | | | | |
|--------|-----|----------------------|-------|-------|--------|--------|--------|--------|--------|--------|-------|-------|-------|--|
| | | NAO | AO | PNA | NI12 | NI34 | DMI | EA | WP | EPNP | EAWR | SCA | POL | |
| April | PC1 | 0.31* | 0.03 | 0.22 | 0.00 | -0.27* | -0.06 | 0.10 | 0.06 | -0.1 | 0.33* | 0.28* | -0.15 | |
| | PC2 | -0.00 | 0.14 | -0.12 | 0.08 | -0.03 | -0.21 | 0.13 | 0.06 | 0.13 | -0.39 | 0.00 | 0.16 | |
| | PC3 | 0.13 | 0.17 | 0.00 | -0.31* | -0.15 | 0.23 | -0.49 | 0.16 | 0.04 | -0.47 | -0.22 | 0.36 | |
| | PC4 | 0.29* | -0.16 | 0.30* | 0.32* | 0.44 | -0.20 | -0.29* | 0.04 | 0.37 | 0.23 | 0.17 | -0.11 | |
| May | PC1 | 0.26* | 0.22 | -0.02 | -0.31* | -0.46 | -0.30* | 0.01 | -0.21 | -0.23 | 0.35 | -0.00 | -0.23 | |
| | PC2 | 0.31* | 0.17 | 0.00 | -0.12 | -0.25 | 0.00 | 0.25 | -0.27* | -0.09 | -0.20 | -0.10 | -0.07 | |
| | PC3 | -0.30* | -0.05 | -0.22 | -0.36 | -0.38 | -0.18 | -0.22 | -0.11 | 0.07 | -0.05 | 0.09 | 0.17 | |
| | PC4 | 0.17 | -0.19 | 0.09 | 0.28* | 0.16 | -0.24 | 0.35 | 0.29* | 0.27* | 0.26* | 0.30* | -0.21 | |
| June | PC1 | 0.27* | 0.44 | -0.22 | -0.56 | -0.41 | -0.10 | 0.03 | 0.16 | -0.05 | -0.05 | -0.09 | -0.11 | |
| | PC2 | 0.48 | 0.26* | 0.07 | 0.12 | 0.12 | 0.23 | 0.07 | 0.07 | -0.15 | 0.31* | 0.07 | -0.08 | |
| | PC3 | 0.06 | 0.21 | -0.03 | -0.39 | -0.34 | -0.08 | -0.08 | -0.1 | 0.02 | -0.47 | -0.22 | 0.33* | |
| | PC4 | 0.06 | 0.05 | 0.03 | -0.21 | -0.01 | -0.21 | 0.37 | 0.43 | 0.37 | 0.10 | -0.09 | -0.01 | |
| July | PC1 | 0.10 | -0.04 | 0.00 | -0.15 | -0.14 | 0.13 | 0.08 | 0.32* | 0.09 | 0.57 | 0.10 | -0.37 | |
| | PC2 | 0.04 | 0.1 | 0.46 | -0.03 | -0.08 | 0.11 | 0.18 | -0.23 | -0.20 | 0.20 | 0.09 | 0.05 | |
| | PC3 | 0.22 | 0.03 | 0.16 | 0.28* | 0.13 | 0.27* | 0.02 | -0.20 | -0.01 | 0.20 | 0.19 | 0.03 | |
| | PC4 | 0.02 | -0.23 | -0.00 | 0.30* | 0.56 | 0.40 | -0.52 | 0.07 | 0.12 | 0.28* | 0.16 | -0.05 | |
| August | PC1 | -0.08 | 0.06 | 0.06 | -0.35 | -0.29* | -0.05 | 0.11 | -0.08 | -0.28* | 0.45 | 0.01 | -0.04 | |
| | PC2 | 0.38 | 0.28* | -0.21 | 0.12 | -0.01 | 0.04 | -0.45 | -0.08 | -0.17 | 0.26* | 0.21 | 0.06 | |
| | PC3 | -0.07 | 0.37 | -0.11 | -0.05 | -0.23 | -0.20 | 0.38 | -0.11 | -0.50 | 0.14 | -0.49 | 0.06 | |
| | PC4 | 0.06 | 0.09 | -0.18 | 0.13 | 0.24 | -0.09 | 0.15 | 0.00 | 0.10 | -0.07 | -0.16 | -0.05 | |

D Revisiting the structures of $500hPa$ geopotential height fluctuations

The structure, variability and remote coherence of $500hPa$ geopotential height fluctuations is classified following Blackmon et al. (1984a,b) using results of the coupled climate model ECHAM5/MPI-OM for northern hemisphere summer. Based on twice daily data, fluctuations on various time scales range from short lived eddies to long inter-annual climate variations. Three figures depict the discussion in chapter 5.

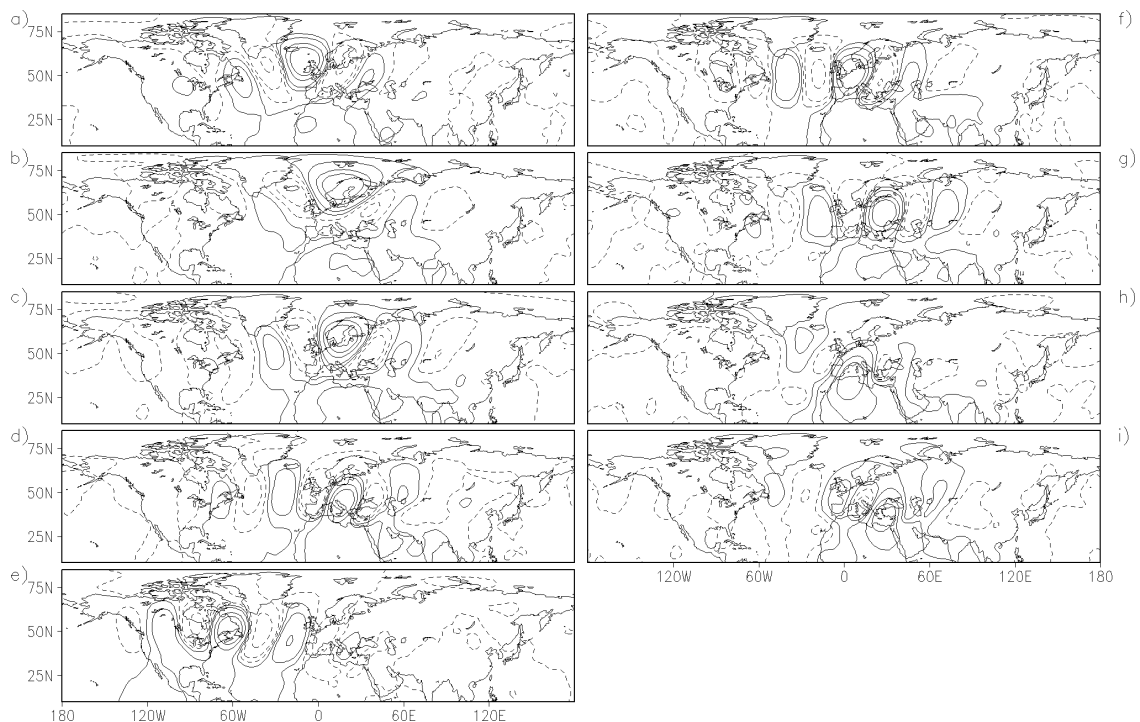


Figure D.1. Selected one point correlation maps for short time scale fluctuations (2.5 to 6 days) in the domain $80^{\circ}W$ to $30^{\circ}E$ and $20^{\circ}N$ to $80^{\circ}N$.

D Revisiting the structures of 500hPa geopotential anomalies

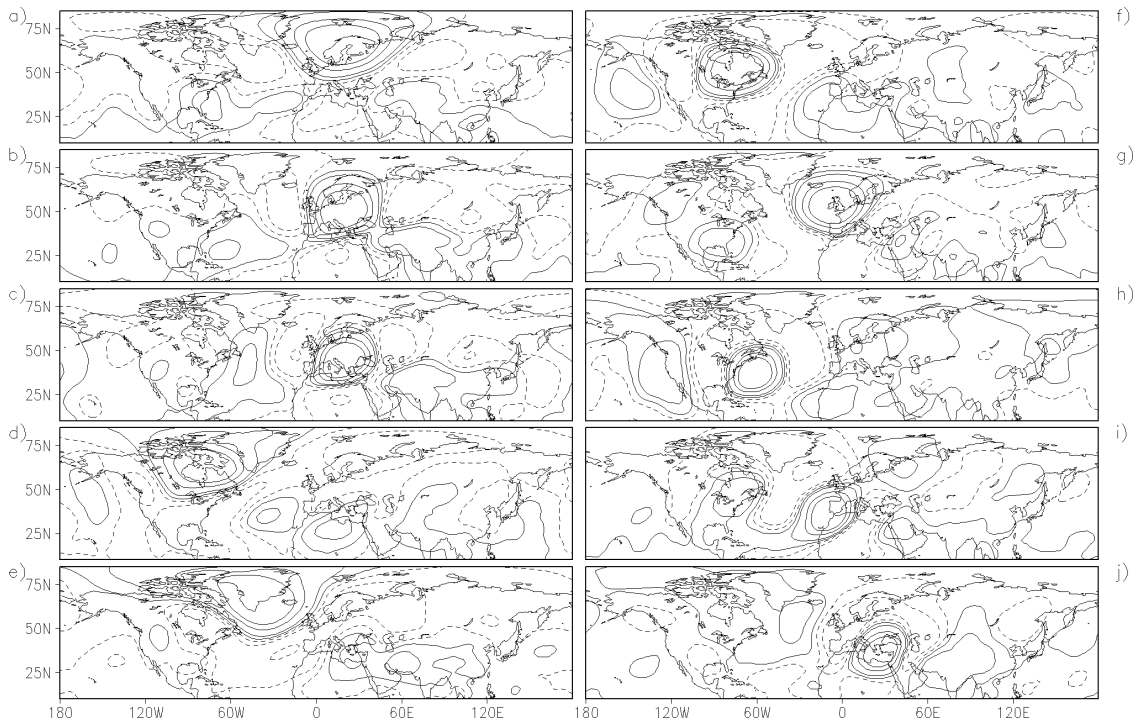


Figure D.2. Selected one point correlation maps for intermediate time scale fluctuations (~ 10 to ~ 23 days).

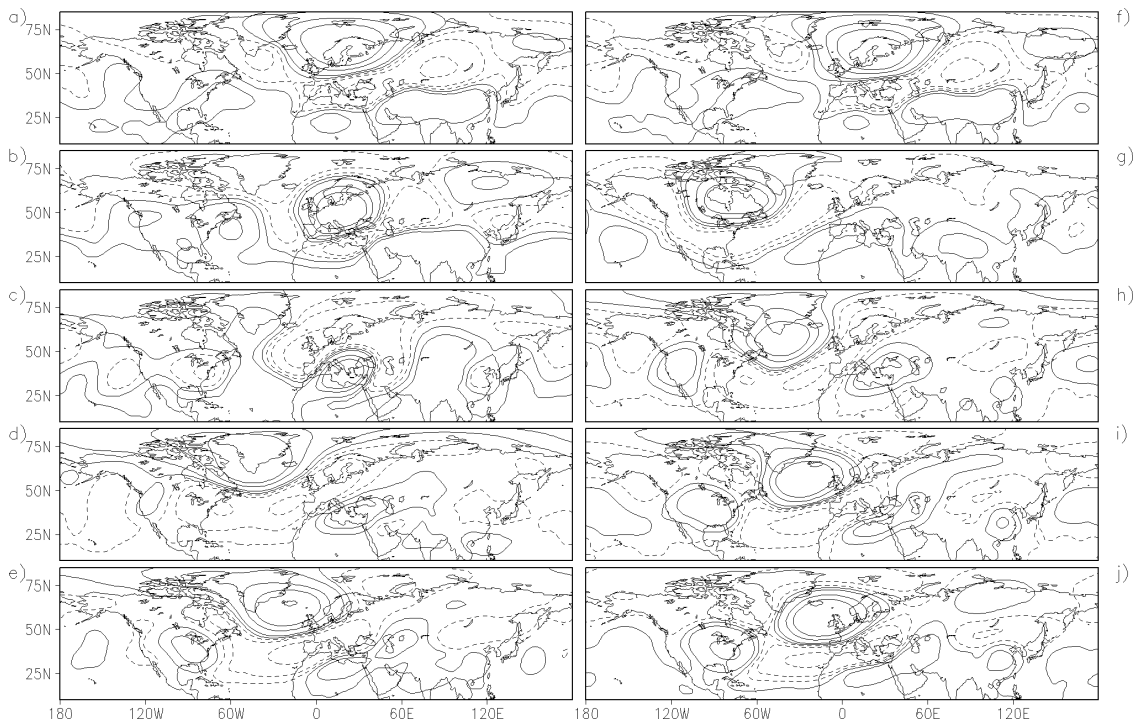


Figure D.3. Selected one point correlation maps for long time scale fluctuations (~ 14 to 92 days).

Bibliography

- Academica Sinica, 1957: On the general circulation over eastern Asia (I). *Tellus*, **9**, 432–446, Staff Members of the Section of Synoptic and Dynamic Meteorology, Institute of Geophysics and Meteorology, Academia Sinica, Peking.
- Academica Sinica, 1958: On the general circulation over eastern Asia (II). *Tellus*, **10**, 58–75, Staff Members of the Section of Synoptic and Dynamic Meteorology, Institute of Geophysics and Meteorology, Academia Sinica, Peking.
- Adler, R. F., G. J. Huffman, A. Chang, R. Ferraro, P. Xie, J. Janowiak, B. Rudolf, U. Schneider, S. Curtis, D. Bolvin, A. Gruber, J. Susskind, P. Arkin and E. Nelkin, 2003: The version-2 global precipitation climatology project (GPCP) monthly precipitation analysis (1979–present). *Journal of Hydrometeorology*, **4**, 1147–1167.
- Ali, K. F. and D. H. De Boer, 2007: Spatial patterns and variation of suspended sediment yield in the upper Indus river basin, northern Pakistan. *Journal of Hydrology*, **334**, 368–387, doi:10.1016/j.jhydrol.2006.10.013.
- Ambaum, M. H. P., B. J. Hoskins and D. B. Stephenson, 2001: Arctic Oscillation or North Atlantic Oscillation? *Journal of Climate*, **14**, 3495–3507.
- Ambrizzi, T. and B. J. Hoskins, 1997: Stationary Rossby-wave propagation in a baroclinic atmosphere. *Quarterly Journal of the Royal Meteorological Society*, **123**, 919–928, doi:10.1002/qj.49712354007.
- Ambrizzi, T., B. J. Hoskins and H.-H. Hsu, 1995: Rossby wave propagation and teleconnection patterns in the austral winter. *Journal of the Atmospheric Sciences*, **52**, 3661–3672.
- Ångström, A., 1935: Teleconnections of climatic changes in present time. *Geografiska Annaler*, **17**, 242–258, available online at <http://www.jstor.org/stable/519964>.
- Archer, D. R. and H. J. Fowler, 2004: Spatial and temporal variations in precipitation in the upper Indus basin, global teleconnections and hydrological implications. *Hydrology and Earth System Sciences*, **8** (1), 47–61.
- Barlow, M. A. and M. K. Tippett, 2008: Variability and predictability of central Asia river flows: Antecedent winter precipitation and large-scale teleconnections. *Journal of Hydrometeorology*, **9**, 1334–1349, doi:10.1175/2008JHM976.1.
- Barnston, A. G. and R. E. Livezey, 1987: Classification, seasonality and persistence of low-frequency atmospheric circulation patterns. *Monthly Weather Review*, **115**, 1083–1126.
- Beck, C., J. Grieser and B. Rudolf, 2005: A new monthly precipitation climatology for the global land areas for the period 1951 to 2000. *Climate Status Report 2004*, German Weather Service, Offenbach, Germany, 181–190.
- Bjerknes, J., 1969: Atmospheric teleconnections from the equatorial Pacific. *Monthly Weather Review*, **97**, 163–172.

Bibliography

- Blackmon, M. L. and N. C. Lau, 1980: Regional characteristics of the northern hemisphere wintertime circulation: A comparison of the simulation of a GFDL general circulation model with observations. *Journal of the Atmospheric Sciences*, **37**, 497–514.
- Blackmon, M. L., Y.-H. Lee and J. M. Wallace, 1984a: Horizontal structure of 500 mb height fluctuations with long, intermediate and short time scales. *Journal of the Atmospheric Sciences*, **41**, 961–980.
- Blackmon, M. L., Y.-H. Lee, J. M. Wallace and H.-H. Hsu, 1984b: Time variation of 500 mb height fluctuations with long, intermediate and short time scales as deduced from lag-correlation statistics. *Journal of the Atmospheric Sciences*, **41**, 981–991.
- Böhner, J., 1994: Circulation and representativeness of precipitation and air temperature in the southeast of the Qinghai–Xizang plateau. *Geojournal*, **34**, 55–66.
- Böhner, J., 2006: General climatic controls and topoclimatic variations in central and high Asia. *Boreas*, **35**, 279–295, doi:10.1080/03009480500456073.
- Böhner, J. and F. Lehmkuhl, 2005: Environmental change modelling for central and high Asia: Pleistocene, present and future scenarios. *Boreas*, **34**, 220–231, doi:10.1080/03009480510012917.
- Bordi, I., K. Fraedrich, M. Petitta and A. Sutera, 2007: Extreme value analysis of wet and dry periods in Sicily. *Theoretical and Applied Climatology*, **87**, 61–71, doi:10.1007/s00704-005-0195-3.
- Bordi, I., K. Fraedrich and A. Sutera, 2008: Multiple jets observed in the summer northern hemisphere troposphere. *Il Nuovo Cimento C*, **30**, 587–604, doi:10.1393/ncc/i2007-10271-5.
- Bordi, I. and A. Sutera, 2001: Fifty years of precipitation: Some spatially remote teleconnections. *Water Resources Management*, **15**, 247–280.
- Bothe, O., K. Fraedrich and X. Zhu, 2009: Summer drought and wetness on the Tibetan plateau: A composite analysis. *International Journal Of Climatology*, doi:10.1002/joc.1946, in press.
- Bothe, O., K. Fraedrich and X. Zhu, 2010: Large scale circulations and Tibetan Plateau summer drought and wetness in a high resolution climate model. *International Journal Of Climatology*, in press.
- Brönnimann, S., 2007: Impact of El Niño–Southern Oscillation on European climate. *Reviews of Geophysics*, **45**, RG3003, doi:10.1029/2006RG000199.
- Brutsaert, W., 2005: *Hydrology: an introduction*. Cambridge University Press, Cambridge, New York, 605 pp.
- Bueh, C. and H. Nakamura, 2007: Scandinavian pattern and its climatic impact. *Quarterly Journal of the Royal Meteorological Society*, **133**, 2117–2131.
- Chang, C.-P., Y. Zhang and T. Li, 2000a: Interannual and interdecadal variations of the east Asian summer monsoon and tropical Pacific SSTs. Part I: Roles of the subtropical ridge. *Journal of Climate*, **13**, 4310–4325.
- Chang, C.-P., Y. Zhang and T. Li, 2000b: Interannual and interdecadal variations of the east Asian summer monsoon and tropical Pacific SSTs. Part II: Meridional structure of the monsoon. *Journal of Climate*, **13**, 4326–4340.
- Chen, M., P. Xie, J. E. Janowiak and P. A. Arkin, 2002: Global land precipitation: A 50-yr monthly analysis based on gauge observations. *Journal of Hydrometeorology*, **3**, 249–266.

- Chen, T. C., S. Y. Wang, W. R. Huang and M. C. Yen, 2004: Variation of the east Asian summer monsoon rainfall. *Journal of Climate*, **17**, 744–762.
- Chow, K. C., H.-W. Tong and J. C. L. Chan, 2008: Water vapor sources associated with the early summer precipitation over China. *Climate Dynamics*, **30**, 497–517, doi:10.1007/s00382-007-0301-6.
- Chylek, P., C. K. Folland, G. Lesins, M. K. Dubey and M. Wang, 2009: Arctic air temperature change amplification and the Atlantic Multidecadal Oscillation. *Geophysical Research Letters*, **36**, L14 801, doi:10.1029/2009GL038777.
- Dai, A., 2006: Precipitation characteristics in eighteen coupled climate models. *Journal of Climate*, **19**, 4605–4630.
- De Geer, G., 1926: On the solar curve: As dating the ice age, the New York moraine, and Niagara Falls through the Swedish timescale. *Geografiska Annaler*, **8**, 253–283, available online at <http://www.jstor.org/stable/519727>.
- Defant, A., 1924: Die Schwankungen der atmosphärischen Zirkulation über dem nordatlantischen Ozean im 25-jährigen Zeitraum 1881–1905. *Geografiska Annaler*, **6**, 13–41, available online at <http://www.jstor.org/stable/519605>.
- Ding, Q. and B. Wang, 2005: Circumglobal teleconnection in the northern hemisphere summer. *Journal of Climate*, **18**, 3483–3505, doi:10.1175/JCLI3473.1.
- Ding, Y., 2007: The variability of the Asian summer monsoon. *Journal of the Meteorological Society of Japan. Ser. II*, **85B**, 21–54.
- Ding, Y. and J. C. L. Chan, 2005: The east Asian summer monsoon: an overview. *Meteorology and Atmospheric Physics*, **89**, 117–142, doi:10.1007/s00703-005-0125-z.
- Ding, Y., Y. Sun, Z. Wang, Y. Zhu and Y. Song, 2009: Inter-decadal variation of the summer precipitation in China and its association with decreasing Asian summer monsoon part II: Possible causes. *International Journal of Climatology*, 1926–1944, doi:10.1002/joc.1759.
- Ding, Y., Z. Wang and Y. Sun, 2008: Inter-decadal variation of the summer precipitation in east China and its association with decreasing Asian summer monsoon. Part I: Observed evidences. *International Journal of Climatology*, **28**, 1139–1161, doi:10.1002/joc.1615.
- Dinku, T., S. J. Connor, P. Ceccato and C. F. Ropelewski, 2008: Comparison of global gridded precipitation products over a mountainous region of Africa. *International Journal of Climatology*, **28**, 1627–1638, doi:10.
- Dirmeyer, P. A. and K. L. Brubaker, 2007: Characterization of the global hydrologic cycle from a back-trajectory analysis of atmospheric water vapor. *Journal of Hydrometeorology*, **8**, 20–37.
- Doberitz, R., 1968: Cross spectrum analysis of rainfall and sea temperature at the equatorial Pacific ocean. *Bonner Meteorologische Abhandlungen*, **8**, 1–61.
- Dommenges, D., 2007: Evaluating EOF modes against a stochastic null hypothesis. *Climate Dynamics*, **28**, 517–531, doi:10.1007/s00382-006-0195-8.
- Dommenges, D. and M. Latif, 2002: A cautionary note on the interpretation of EOFs. *Journal of Climate*, **15**, 216–225.
- Domrös, M. and G. Peng, 1988: *The Climate of China*. Springer, Berlin, 360 pp.

Bibliography

- d'Orgeville, M. and W. R. Peltier, 2007: On the Pacific Decadal Oscillation and the Atlantic Multidecadal Oscillation: Might they be related? *Geophysical Research Letters*, **34**, L23705, doi:10.1029/2007GL031584.
- Dracup, J. A., K. S. Lee and E. G. Paulson Jr., 1980: On the definition of droughts. *Water Resources Research*, **16**, 297–302.
- Duan, A. M. and G. X. Wu, 2005: Role of the Tibetan plateau thermal forcing in the summer climate patterns over subtropical Asia. *Climate Dynamics*, **24**, 793–807, doi:10.1007/s00382-004-0488-8.
- Dugam, S. S., S. D. Bansod and S. B. Kakade, 2009: Pre-monsoon zonal wind index over Tibetan plateau and sub-seasonal Indian summer monsoon rainfall variability. *Geophysical Research Letters*, **36**, L11809, doi:10.1029/2009GL038207.
- Efron, B. and R. J. Tibshirani, 1993: *An introduction to the Bootstrap*, Monographs on Statistics and Applied Probability, Vol. 57. Chapman & Hall/CRC, 436 pp.
- Enfield, D. B., A. M. Mestas-Nuñez and P. J. Trimble, 2001: The Atlantic Multidecadal Oscillation and its relation to rainfall and river flows in the continental U.S. *Geophysical Research Letters*, **28**, 2077–2080.
- Enomoto, T., H. Endo, Y. Harada and W. Ohfuchi, 2009: Relationship between high-impact weather events in Japan and propagation of Rossby waves along the Asian jet in July 2004. *Journal of the Meteorological Society of Japan. Ser. II*, **87** (1), 139–156.
- Enomoto, T., B. J. Hoskins and Y. Matsuda, 2003: The formation mechanism of the Bonin high in August. *Quarterly Journal of the Royal Meteorological Society*, **129**, 157–178, doi:10.1256/qj.01.211.
- Faulwetter, R., 2007: The seasonal cycle of northern hemispheric teleconnection patterns, unpublished, compare abstract to talk given at 8th annual meeting of the EMS 2008 <http://www.cosis.net/abstracts/EMS2008/00215/EMS2008-A-00215.pdf>.
- Fekete, B. M., C. J. Vörösmarty and W. Grabs, 1999: Global, composite runoff fields based on observed river discharge and simulated water balances. Tech. Rep. 22, Global Runoff Data Center, Koblenz, Germany, 115 pp.
- Fekete, B. M., C. J. Vörösmarty and W. Grabs, 2000: UNH/GRDC composite runoff fields V 1.0. <http://www.grdc.sr.unh.edu/>.
- Feng, S. and Q. Hu, 2008: How the North Atlantic Multidecadal Oscillation may have influenced the Indian summer monsoon during the past two millenia. *Geophysical Research Letters*, **35**, L01707, doi:10.1029/2007GL032484.
- Flohn, H., 1968: Contributions to a meteorology of the Tibetan highlands. *Atmospheric Science Paper*, (130).
- Fowler, H. J. and D. R. Archer, 2005: Hydro-climatological variability in the upper Indus basin and implications for water resources. *Regional Hydrological Impacts of Climatic Change – Impact Assessment and Decision Making*, IAHS Publication 295, 131–138.
- Fowler, H. J. and D. R. Archer, 2006: Conflicting signals of climatic change in the upper Indus basin. *Journal of Climate*, **19**, 4276–4293, doi:10.1175/JCLI3860.1.
- Fraedrich, K., 1990: European Grosswetter during warm and cold extremes of El Niño/Southern Oscillation. *International Journal of Climatology*, **10**, 21–31, doi:10.1002/joc.3370100104.

- Fraedrich, K., 1994: An ENSO impact on Europe? *Tellus A*, **46**, 541–552, doi:10.1034/j.1600-0870.1994.00015.x.
- Fraedrich, K. and K. Müller, 1992: Climate anomalies in Europe associated with ENSO extremes. *International Journal of Climatology*, **12**, 25–31, doi:10.1002/joc.3370120104.
- Franzke, C. and S. B. Feldstein, 2005: The continuum and dynamics of northern hemisphere teleconnection patterns. *Journal of the Atmospheric Sciences*, **62**, 3250–3267, doi:10.1175/JAS3536.1.
- Frisius, T., K. Fraedrich, H. Borth, O. Bothe and X. Zhu, 2009: Flow around the Tibetan plateau: a shallow water model approach. *Geophysical Research Abstracts*, **11**, EGU2009-7248.
- Fujinami, H. and T. Yasunari, 2009: The effects of midlatitude waves over and around the Tibetan plateau on submonthly variability of the east Asian summer monsoon. *Monthly Weather Review*, **137**, 2286–2304.
- Garreaud, R. D., 2007: Precipitation and circulation covariability in the extratropics. *Journal of Climate*, **20**, 4789–4797, doi:10.1175/JCLI4257.1.
- Gershunov, A., N. Schneider and T. Barnett, 2001: Low-frequency modulation of the ENSO–Indian monsoon rainfall relationship: Signal or noise? *Journal of Climate*, **14**, 2486–2492.
- Gerstengarbe, F.-W., P. C. Werner and U. Rüge, 1999: *Katalog der Grosswetterlagen Europas 1881–1998 nach P. Hess und H. Brezowsky*. 5th ed., Potsdam-Institut für Klimafolgenforschung, Potsdam, Germany, 138 pp.
- Glickman, T. S., (Ed.) , 2000: *Glossary of Meteorology*. 2d ed., American Meteorological Society, 855 pp., available online at <http://amsglossary.allenpress.com/>.
- Gong, D.-Y. and C.-H. Ho, 2002: Shift in the summer rainfall over the Yangtze river valley in the late 1970s. *Geophysical Research Letters*, **29**, 1436, doi:10.1029/2001GL014523.
- Gong, D.-Y. and C.-H. Ho, 2003: Arctic oscillation signals in the east Asian summer monsoon. *Journal of Geophysical Research*, **108(D2)**, 4066, doi:10.1029/2002JD002193.
- Goswami, B. N., M. S. Madhusoodanan, C. P. Neema and D. Sengupta, 2006: A physical mechanism for north Atlantic SST influence on the Indian summer monsoon. *Geophysical Research Letters*, **33**, L02706, doi:10.1029/2005GL024803.
- Gruber, A. and V. Levizzani, 2008: Assessment of global precipitation products. A project of the world climate research programme global energy and water cycle experiment (GEWEX) radiation panel. WMO/TD 1430, World Climate Research Program Report No. 128, 50 pp.
- Gupta, A. K., D. M. Anderson and J. T. Overpeck, 2003: Abrupt changes in the Asian southwest monsoon during the Holocene and their links to the north Atlantic ocean. *Nature*, **421**, 354–357, doi:10.1038/nature01340.
- Guttman, N. B., 1998: Comparing the Palmer drought index and the standardized precipitation index. *Journal of the American Water Resources Association*, **34**, 113–121, doi:10.1111/j.1752-1688.1998.tb05964.x.
- Guttman, N. B., 1999: Accepting the standardized precipitation index: A calculation algorithm. *JAWRA Journal of the American Water Resources Association*, **35**, 311–322, doi:10.1111/j.1752-1688.1999.tb03592.x.
- Hagemann, S., K. Arpe and L. Bengtsson, 2005: Validation of the hydrological cycle of ERA40. ECMWF ERA-40 Project Report Series 24, European Centre for Medium-Range Weather Fore-

Bibliography

- casts, Shinfield, Reading, UK. Available from <http://www.ecmwf.int/publications>.
- Hagemann, S., K. Arpe and E. Roeckner, 2006: Evaluation of the hydrological cycle in the ECHAM5 model. *Journal of Climate*, **19**, 3810–3827.
- Hahn, D. G. and S. Manabe, 1975: The role of mountains in the south Asian monsoon circulation. *Journal of the Atmospheric Sciences*, **32**, 1515–1541.
- Hannachi, A., I. T. Jolliffe and D. B. Stephenson, 2007: Empirical orthogonal functions and related techniques in atmospheric science: A review. *International Journal of Climatology*, **27**, 1119–1152, doi:10.1002/joc.1499.
- Hasselmann, K., 1976: Stochastic climate models part I. Theory. *Tellus*, **28**, 473–485.
- Hatzaki, M., H. A. Flocas, D. N. Asimkopoulos and P. Maheras, 2007: The eastern Mediterranean teleconnection pattern: identification and definition. *International Journal of Climatology*, **27**, 727–737, doi:10.1002/joc.1429.
- He, H., J. W. McGinnis, Z. Song and M. Yanai, 1987: Onset of the Asian summer monsoon in 1979 and the effect of the Tibetan plateau. *Monthly Weather Review*, **115**, 1966–1995.
- He, J., J. Ju, Z. Wen and J. Lü, 2007: A review of recent advances in research on Asian monsoon in China. *Advances in Atmospheric Sciences*, **24**, 972–992, doi:10.1007/s00376-007-0972-2.
- Held, I. M., M. Ting and H. Wang, 2002: Northern winter stationary waves: Theory and modeling. *Journal of Climate*, **15**, 2125–2144.
- Holton, J. R., 1992: *An Introduction to Dynamic Meteorology*. 3d ed., Academic Press.
- Hong, C.-C., M.-M. Lu and M. Kanamitsu, 2008: Temporal and spatial characteristics of positive and negative Indian ocean dipole with and without ENSO. *Journal of Geophysical Research*, **113**, D08 107, doi:10.1029/2007JD009151.
- Hoskins, B. J. and T. Ambrizzi, 1993: Rossby wave propagation on a realistic longitudinally varying flow. *Journal of the Atmospheric Sciences*, **50**, 1661–1671.
- Hoskins, B. J., I. N. James and G. H. White, 1983: The shape, propagation and mean-flow interaction of large-scale weather systems. *Journal of the Atmospheric Sciences*, **40**, 1595–1612.
- Hsu, H. H. and S. M. Lin, 2007: Asymmetry of the tripole rainfall pattern during the east Asian summer. *Journal of Climate*, **20**, 4443–4458, doi:10.1175/JCLI4246.1.
- Hsu, H.-H. and X. Liu, 2003: Relationships between the Tibetan plateau heating and east Asian summer monsoon rainfall. *Geophysical Research Letters*, **30(20)**, 2066, doi:10.1029/2003GL017909.
- Hu, Q. and S. Feng, 2008: Variation of the north American summer monsoon regimes and the Atlantic Multidecadal Oscillation. *Journal of Climate*, **21**, 2371–2383, doi:10.1175/2007JCLI2005.1.
- Husak, G. J., J. Michaelsen and C. Funk, 2007: Use of the gamma distribution to represent monthly rainfall in Africa for drought monitoring applications. *International Journal of Climatology*, **27**, 935–944, doi:10.1002/joc.1441.
- Ionita, M., G. Lohmann and N. Rimbu, 2008: Prediction of spring Elbe discharge based on stable teleconnections with winter global temperature and precipitation. *Journal of Climate*, **21**, 6215–6226, doi:10.1175/2008JCLI2248.1.

- James, I. N., 2007: An objective classification method for Hess and Brezowsky Grosswetterlagen over Europe. *Theoretical and Applied Climatology*, **88**, 17–42, doi:10.1007/s00704-006-0239-3.
- James, I. N. and B. J. Hoskins, 1985: Some comparisons of atmospheric internal and boundary baroclinic instability. *Journal of the Atmospheric Sciences*, **42**, 2142–2155.
- Jiang, J., D. Zhang and K. Fraedrich, 1997: Historic climate variability of wetness in east China (1960–1992): a wavelet analysis. *International Journal of Climatology*, **17**, 969–981.
- Jungclaus, J. H., H. Haak, M. Latif and U. Mikolajewicz, 2005: Arctic-North Atlantic interactions and multidecadal variability of the Meridional Overturning Circulation. *Journal of Climate*, **18**, 4013–4031, doi:10.1175/JCLI3462.1.
- Jungclaus, J. H., N. Keenlyside, M. Botzet, H. Haak, J. J. Luo, M. Latif, J. Marotzke, U. Mikolajewicz and E. Roeckner, 2006: Ocean circulation and tropical variability in the coupled model ECHAM5/MPI-OM. *Journal of Climate*, **19**, 3952–3972.
- Källberg, P., P. Berrisford, B. Hoskins, A. Simmons, S. Uppala, S. Lamy-Thépaut and R. Hine, 2005: ERA-40 Atlas. ECMWF ERA-40 Project Report Series 19, European Centre for Medium-Range Weather Forecasts, Shinfield, Reading, UK. Available online at <http://www.ecmwf.int/publications>.
- Kaplan, A., M. Cane, Y. Kushnir, A. Clement, M. Blumenthal and B. Rajagopalan, 1998: Analyses of global sea surface temperature 1856–1991. *Journal of Geophysical Research*, **103**, 18 567–18 589.
- Kerr, R. A., 2005: Atlantic climate pacemaker for millennia past, decades hence? *Science*, **309** (5731), 41–43, doi:10.1126/science.309.5731.41.
- Koch, P., H. Wernli and H. C. Davies, 2006: An event-based jet-stream climatology and typology. *International Journal of Climatology*, **26**, 283–301, doi:10.1002/joc.1255.
- Kottek, M., J. Grieser, C. Beck, B. Rudolf and F. Rubel, 2006: World map of the Köppen-Geiger climate classification updated. *Meteorologische Zeitschrift*, **15**, 259–263, doi:10.1127/0941-2948/2006/0130.
- Kripalani, R. H., J. H. Oh and H. S. Chaudhari, 2007: Response of the east Asian summer monsoon to doubled atmospheric CO₂: Coupled climate model simulations and projections under IPCC AR4. *Theoretical and Applied Climatology*, **87**, 1–28, doi:10.1007/s00704-006-0238-4.
- Krishnamurthy, V. and B. N. Goswami, 2000: Indian Monsoon–ENSO relationship on interdecadal timescale. *Journal of Climate*, **13**, 579–595.
- Kuang, X. and Y. Zhang, 2005: Seasonal variation of the east Asian subtropical westerly jet and its association with the heating field over east Asia. *Advances in Atmospheric Sciences*, **22**, 831–840, doi:10.1007/BF02918683.
- Kucharski, F., A. Bracco, J. H. Yoo and F. Molteni, 2007: Low-frequency variability of Indian monsoon–ENSO relationship and the tropical Atlantic: The “weakening” of the 1980s and 1990s. *Journal of Climate*, **20**, 4255–4266.
- Kucharski, F., A. Bracco, J. H. Yoo and F. Molteni, 2008: Atlantic forced component of the Indian monsoon interannual variability. *Geophysical Research Letters*, **35**, L04706, doi:10.1029/2007GL033037.
- Kuhlbrodt, T., A. Griesel, M. Montoya, A. Levermann, M. Hofmann and S. Rahmstorf, 2007: On the driving processes of the Atlantic meridional overturning circulation. *Reviews of Geophysics*,

Bibliography

- 45, RG2001, doi:10.1029/2004RG000166.
- Kumar, K., B. Rajagopalan and M. A. Cane, 1999: On the weakening relationship between the Indian monsoon and ENSO. *Science*, **284**, 2156–2159, doi:10.1126/science.284.5423.2156, <http://www.sciencemag.org/cgi/reprint/284/5423/2156.pdf>.
- Kushnir, Y. and J. M. Wallace, 1989: Low-frequency variability in the northern hemisphere winter: Geographical distribution, structure and time-scale dependence. *Journal of the Atmospheric Sciences*, **46**, 3122–3143.
- Kutzbach, J. E., 1970: Large-scale features of monthly mean northern hemisphere anomaly maps of sea-level pressure. *Monthly Weather Review*, **98**, 708–716.
- Lau, K. M. and M. T. Li, 1984: The monsoon of east Asia and its global associations—a survey. *Bulletin of the American Meteorological Society*, **65**, 114–125.
- Lau, K. M. and L. Peng, 1992: Dynamics of atmospheric teleconnections during the northern summer. *Journal of Climate*, **5**, 140–158.
- Lau, K.-M. and H. Weng, 2002: Recurrent teleconnection patterns linking summertime precipitation variability over east Asia and north America. *Journal of the Meteorological Society of Japan*, **80**, 1309–1324, doi:10.2151/jmsj.80.1309.
- Lau, K. M., G. Yang and S. Shen, 1988: Seasonal and intraseasonal climatology of summer monsoon rainfall over east Asia. *Monthly Weather Review*, **116**, 18–37.
- Lee, S. and H. Kim, 2003: The dynamical relationship between subtropical and eddy-driven jets. *Journal of the Atmospheric Sciences*, **60**, 1490–1503.
- Legates, D. R. and C. J. Willmott, 1990: Mean seasonal and spatial variability in gauge-corrected, global precipitation. *International Journal of Climatology*, **10**, 111–127, doi:10.1002/joc.3370100202.
- Levermann, A., J. Schewe, V. Petoukhov and H. Held, 2009: Basic mechanism for abrupt monsoon transitions. *Proceedings of the National Academy of Sciences USA*, doi:10.1073/PNAS.0901414106, in press.
- Li, C. and M. Yanai, 1996: The onset and interannual variability of the Asian summer monsoon in relation to land–sea thermal contrast. *Journal of Climate*, **9**, 358–375.
- Li, J., R. Yu and T. Zhou, 2008a: Teleconnection between NAO and climate downstream of the Tibetan plateau. *Journal of Climate*, **21**, 4680–4690.
- Li, S., L. Ji and W. Lin, 2001a: On the formation and maintenance of the persistent anomalies of summertime circulation over Ural mountains. *Advances in Atmospheric Sciences*, **18**, 819–830.
- Li, S., L. Ji, W. Lin and Y. Ni, 2001b: The maintenance of the blocking over the Ural mountains during the second Meiyu period in the summer of 1998. *Advances in Atmospheric Sciences*, **18**, 87–105, doi:10.1007/s00376-001-0006-4.
- Li, S., J. Perlwitz, X. Quan and M. P. Hoerling, 2008b: Modelling the influence of north Atlantic multidecadal warmth on the Indian summer rainfall. *Geophysical Research Letters*, **35**, L05 804, doi:10.1029/2007GL032901.
- Liu, X. and Z.-Y. Yin, 2001: Spatial and temporal variation of summer precipitation over the eastern Tibetan plateau and the North Atlantic Oscillation. *Journal of Climate*, **14**, 2896–2909.

- Liu, Y., B. Hoskins and M. Blackburn, 2007: Impact of Tibetan orography and heating on the summer flow over Asia. *Journal of the Meteorological Society of Japan. Ser. II*, **85B**, 1–19.
- Liu, Z. and M. Alexander, 2007: Atmospheric bridge, oceanic tunnel, and global climatic teleconnections. *Reviews of Geophysics*, **45**, RG2005, doi:10.1029/2005RG000172.
- Lockyer, N. and W. J. S. Lockyer, 1902: On some phenomena which suggest a short period of solar and meteorological changes. *Proceedings of the Royal Society of London*, **70**, 500–504, available online at <http://www.jstor.org/stable/116642>.
- Lorenz, E. N., 1956: Empirical orthogonal functions and statistical weather prediction. Statistical Forecasting Project, Scientific Report 1, Massachusetts Institute of Technology, Department of Meteorology, Cambridge, Massachusetts. Available online at <http://eapsweb.mit.edu/research/Lorenz/publications.htm>.
- Lu, M.-M. and C.-P. Chang, 2009: Unusual late-season cold surges during the 2005 Asian winter monsoon: Roles of Atlantic blocking and the central Asian anticyclone. *Journal of Climate*, **22**, 5205–5217, doi:10.1175/2009JCLI2935.1.
- Ma, Y., Z. Su, Z.-L. Li, T. Koike and M. Menenti, 2002: Determination of regional net radiation and soil heat flux over heterogeneous landscape of the Tibetan Plateau. *Hydrological Processes*, **16**, 2963–2971.
- Mao, J. and G. Wu, 2006: Intraseasonal variations of the Yangtze rainfall and its related atmospheric circulation features during the 1991 summer. *Climate Dynamics*, **27**, 815–830, doi:10.1007/s00382-006-0164-2.
- Marsland, S., H. Haak, J. Jungclaus, M. Latif and F. Röske, 2003: The Max-Planck-Institute global ocean/sea ice model with orthogonal curvilinear coordinates. *Ocean Modelling*, **5**, 91–127.
- McKee, T. B., N. J. Doeskin and J. Kleist, 1993: The relationship of drought frequency and duration to time scales. *8th Conference on applied climatology*, American Meteorological Society, Anaheim, Canada, 179–184.
- Mitchell, T. D. and P. D. Jones, 2005: An improved method of constructing a database of monthly climate observations and associated high-resolution grids. *International Journal of Climatology*, **25**, 693–712, doi:10.1002/joc.1181.
- Monahan, A. H. and J. C. Fyfe, 2009: How generic are dipolar jet EOFs? *Journal of the Atmospheric Sciences*, **66**, 541–551, doi:10.1175/2008JAS2814.1.
- Monahan, A. H., J. C. Fyfe, M. H. P. Ambaum, D. B. Stephenson and G. R. North, 2009: Empirical orthogonal functions: The medium is the message. *Journal of Climate*, doi:10.1175/2009JCLI3062.1, in press.
- Nakicenovic, N. and R. Swart, 2001: *IPCC Special Report on Emissions Scenarios*. Cambridge University Press: Cambridge, UK.
- Nan, S. and J. Li, 2003: The relationship between the summer precipitation in the Yangtze river valley and the boreal spring southern hemisphere annular mode. *Geophysical Research Letters*, **30**, 2266, doi:10.1029/2003GL018381.
- Nan, S., J. Li, X. Yuan and P. Zhao, 2009: Boreal spring southern hemisphere annular mode, Indian ocean sea surface temperature, and east Asian summer monsoon. *Journal of Geophysical Research*, **114**, D02 103, doi:10.1029/2008JD010045.

Bibliography

- Ninomiya, K. and Y. Shibagaki, 2007: Multi-scale features of the Meiyu-Baiu front and associated precipitation systems. *Journal of the Meteorological Society of Japan*, **85B**, 103–122.
- Nitta, T., 1987: Convective activities in the tropical western Pacific and their impact on the northern hemisphere summer circulation. *Journal of the Meteorological Society of Japan. Ser. II*, **65**, 373–390.
- NOAA, 2005–2008: Northern hemisphere teleconnection patterns. <http://www.cpc.noaa.gov/data/teledoc/telecontents.shtml>.
- NOAA, 2006: AAO, NAO, PNA & AO. http://www.cpc.noaa.gov/products/precip/CWlink/daily_ao_index/teleconnections.shtml.
- NOAA, 2008: Previous ENSO events. http://www.cpc.noaa.gov/products/monitoring_and_data/ENSO_connections.shtml.
- North, G. R., T. L. Bell, R. F. Cahalan and F. J. Moeng, 1982: Sampling errors in the estimation of empirical orthogonal functions. *Monthly Weather Review*, **110**, 699–706.
- Ogi, M., K. Yamazaki and Y. Tachibana, 2004: The summertime annular mode in the northern hemisphere and its linkage to the winter mode. *Journal of Geophysical Research*, **109**, D20 114, doi:10.1029/2004JD004514.
- Orlowsky, B., O. Bothe, K. Fraedrich, F.-W. Gerstengarbe and X. Zhu, 2009: Yangtze future climates from resampled weather analogues. *Journal of Climate*, submitted.
- Palmer, W. C., 1965: Meteorological drought. Research Paper 45, U. S. Weather Bureau, Washington, D. C. Available from <http://www.ncdc.noaa.gov/climate-monitoring/index.php>.
- Parthasarathy, B., A. A. Munot and D. R. Kothawale, 1994: All-India monthly and seasonal rainfall series: 1871–1993. *Theoretical and Applied Climatology*, **49**, 217–224, doi:10.1007/BF00867461.
- Peings, Y., H. Douville and P. Terray, 2009: Extended winter Pacific North America oscillation as a precursor of the Indian summer monsoon rainfall. *Geophysical Research Letters*, **36**, doi:10.1029/2009GL038453.
- Plumb, R. A., 1985: On the three-dimensional propagation of stationary waves. *Journal of the Atmospheric Sciences*, **42**, 217–229.
- Prescott, J. A. and J. A. Collins, 1951: The lag of temperature behind solar radiation. *Quarterly Journal of the Royal Meteorological Society*, **77**, 121–126, doi:10.1002/qj.49707733112.
- Press, W. H., S. A. Teukolsky, B. P. Flannery and W. T. Vetterling, 1992: *Numerical Recipes in FORTRAN: The Art of Scientific Computing*. 2d ed., Cambridge University Press, New York, NY, USA.
- Qian, W., Q. Hu, Y. Zhu and D.-K. Lee, 2003: Centennial-scale dry-wet variations in east Asia. *Climate Dynamics*, **21**, 77–89, doi:10.1007/s00382-003-0319-3.
- Qian, W., X. Lin, Y. Zhu, Y. Xu and J. Fu, 2007: Climatic regime shift and decadal anomalous events in China. *Climatic Change*, **84**, 167–189, doi:10.1007/s10584-006-9234-z.
- Quadrelli, R. and J. M. Wallace, 2004a: A simplified linear framework for interpreting patterns of northern hemisphere wintertime climate variability. *Journal of Climate*, **17**, 3728–3744.
- Quadrelli, R. and J. M. Wallace, 2004b: Varied expressions of the hemispheric circulation ob-

- served in association with contrasting polarities of prescribed patterns of variability. *Journal of Climate*, **17**, 4245–4253.
- R Development Core Team, 2005: R: A language and environment for statistical computing. <http://www.r-project.org>.
- Raghavan, K., 1973: Tibetan anticyclone and tropical easterly jet. *Pure and Applied Geophysics*, **110**, 2130–2142.
- Rajeevan, M., D. S. Pai, R. A. Kumar and B. Lai, 2007: New statistical models for long-range forecasting of southwest monsoon rainfall over India. *Climate Dynamics*, **28**, doi:10.1007/s00382-006-0197-6.
- Rasmusson, E. M. and P. A. Arkin, 1993: A global view of large-scale precipitation variability. *Journal of Climate*, **6**, 1495–1522.
- Rimbu, N., M. Dima, G. Lohmann and I. Musat, 2005: Seasonal prediction of Danube flow variability based on stable teleconnection with sea surface temperature. *Geophysical Research Letters*, **32**, L21 704, doi:10.1029/2005GL024241.
- Rodell, M., I. Velicogna and J. S. Famiglietti, 2009: Satellite-based estimates of groundwater depletion in India. *Nature*, **460**, 999–1002, doi:10.1038/nature08238.
- Rodwell, M. J. and B. Hoskins, 1996: Monsoons and the dynamics of deserts. *Quarterly Journal of the Royal Meteorological Society*, **122**, 1385–1404.
- Rodwell, M. J. and B. Hoskins, 2001: Subtropical anticyclones and summer monsoons. *Journal of Climate*, **14**, 3192–3211.
- Roeckner, E., G. Bäuml, L. Bonaventura, R. Brokopf, M. Esch, M. Giorgetta, S. Hagemann, I. Kirchner, L. K. E. Manzini, A. Rhodin, U. Schlese, U. Schulzweida and A. Tompkins, 2003: The atmospheric general circulation model ECHAM5, Part I: Model description. MPI-report 349, Max-Planck-Institut für Meteorologie, Hamburg.
- Roeckner, E., R. Brokopf, M. Esch, M. Giorgetta, S. Hagemann, L. Kornblueh, E. Manzini, U. Schlese and U. Schulzweida, 2006: Sensitivity of simulated climate to horizontal and vertical resolution in the ECHAM5 atmosphere model. *Journal of Climate*, **19**, 3771–3791, doi:10.1175/JCLI3824.1.
- Saji, N. H., B. N. Goswami, P. N. Vinayachandran and T. Yamagata, 1999: A dipole mode in the tropical Indian Ocean. *Nature*, **401**, 361–363.
- Sampe, T. and S.-P. Xie, 2009: Large-scale dynamics of the Meiyu-Baiu rain band: Environmental forcing by the westerly jet. *Journal of Climate*, doi:10.1175/2009JCLI3128.1, in press.
- Sato, N. and M. Takahashi, 2006: Dynamical processes related to the appearance of quasi-stationary waves on the subtropical jet in the midsummer northern hemisphere. *Journal of Climate*, **19**, 1531–1544, doi:10.1175/JCLI3697.1.
- Sato, T., 2005: The TianShan rain-shadow influence on the arid climate formation in northwestern China. *SOLA*, **1**, 13–16.
- Sato, T. and F. Kimura, 2007: How does the Tibetan plateau affect the transition of Indian monsoon rainfall? *Monthly Weather Review*, **135**, 2006–2015, doi:10.1175/MWR3386.1.
- Sato, T., M. Tsujimura, T. Yamanaka, H. Iwasaki, A. Sugimoto, M. Sugita, F. Kimura, G. Davaa and D. Oyunbaatar, 2007: Water sources in semiarid northeast Asia as revealed by field

Bibliography

- observations and isotope transport model. *Journal of Geophysical Research*, **112**, D17112, doi:10.1029/2006JD008321.
- Schiemann, R., D. Lüthi and C. Schär, 2009: Seasonality and interannual variability of the westerly jet in the Tibetan-Plateau region. *Journal of Climate*, **22**, 2940–2957, doi:10.1175/2008JCLI2625.1.
- Schiemann, R., D. Lüthi, P. L. Vidale and C. Schär, 2008: The precipitation climate of central Asia—intercomparison of observational and numerical data sources in a remote semiarid region. *International Journal of Climatology*, **28**, 295–314, doi:10.1002/joc.1532.
- Schütte, K., 1967: Cross-correlations of rainfall and water temperature at the equatorial Pacific. *Bonner Meteorologische Abhandlungen*, **7**, 53–74.
- Shaman, J. and E. Tziperman, 2005: The effect of ENSO on Tibetan plateau snow depth: A stationary wave teleconnection mechanism and implications for the South Asian monsoons. *Journal of Climate*, **18**, 2067–2079.
- Sielmann, F., 2007: plumb.f. personal communication, plumb.doc.
- Sielmann, F., 2008: mulregress4.f. personal communication.
- Sienz, F., I. Bordi, K. Fraedrich and A. Schneidereit, 2007: Extreme dry and wet events in Iceland: observations, simulations and scenarios. *Meteorologische Zeitschrift*, **16**, 9–16.
- Sienz, F.-O., 2009: personal communication.
- Simmonds, I., D. Bi. and P. Hope, 1999: Atmospheric water vapor flux and its association with rainfall in China in summer. *Journal of Climate*, **12**, 1353–1367.
- Simmons, A. J., J. M. Wallace and G. W. Branstator, 1983: Barotropic wave propagation and instability, and atmospheric teleconnection patterns. *Journal of the Atmospheric Sciences*, **40**, 1363–1392.
- Singh, P. and L. Bengtsson, 2005: Impact of warmer climate on melt and evaporation for the rainfed, snowfed and glacierfed basins in the Himalayan region. *Journal of Hydrology*, **300**, 140–154, doi:10.1016/j.jhydrol.2004.06.005.
- Small, E. E., F. Giorgi and L. C. Sloan, 1999: Regional climate model simulation of precipitation in central Asia: Mean and interannual variability. *Journal of Geophysical Research*, **104(D6)**, 6563–6582.
- Sun, J., H. Wang and W. Yuan, 2009a: A possible mechanism for the co-variability of the boreal spring Antarctic oscillation and the Yangtze river valley summer rainfall. *International Journal of Climatology*, **29**, 1276–1284, doi:10.1002/joc.1773.
- Sun, J., H. Wang and W. Yuan, 2009b: Role of the tropical Atlantic sea surface temperature in the decadal change of the summer North Atlantic Oscillation. *Journal of Geophysical Research*, **114**, D20110, doi:10.1029/2009JD012395.
- Svoboda, M., D. LeComte, M. Hayes, R. Heim, K. Gleason, J. Angel, B. Rippey, R. Tinker, M. Palecki, D. Stooksbury, D. Miskus and S. Stephens, 2002: The drought monitor. *Bulletin of the American Meteorological Society*, **83**, 1183–1190.
- Tang, M. and E. R. Reiter, 1984: Plateau monsoons of the northern hemisphere: A comparison between north America and Tibet. *Monthly Weather Review*, **112**, 617–637.

- Terao, T., 1998: Barotropic disturbances on intraseasonal time scales observed in the midlatitudes over the Eurasian continent during the northern summer. *Journal of the Meteorological Society of Japan. Ser. II*, **76**, 419–436.
- Tiwari, V. M., J. Wahr and S. Swenson, 2009: Dwindling groundwater resources in northern India, from satellite gravity observations. *Geophysical Research Letters*, **36**, L18401, doi:10.1029/2009GL039401.
- Trenberth, K. E., 1983: What are the seasons? *Bulletin of the American Meteorological Society*, **64**, 1276–1282.
- Trenberth, K. E., 1991: Climate diagnostics from global analyses: Conservation of mass in ECMWF analyses. *Journal of Climate*, **4**, 707–722.
- Trenberth, K. E., D. P. Stepaniak and J. M. Caron, 2000: The global monsoon as seen through the divergent atmospheric circulation. *Journal of Climate*, **13**, 3969–3993.
- U., W., 1884: The winter of 1879–80 in Europe. *Science*, **3 (63)**, 485–486, doi:10.1126/science.ns-3.63.485.
- Ueda, H., H. Kamahori and N. Yamasaki, 2003: Seasonal contrasting features of heat and moisture budgets between the eastern and western Tibetan plateau during the GAME IOP. *Journal of Climate*, **16**, 2309–2324.
- Uno, I., K. Eguchi, K. Yumimoto, T. Takemura, A. Shimizu, M. Uematsu, Z. Liu, Z. Wang, Y. Hara and N. Sugimoto, 2009: Asian dust transported one full circuit around the globe. *Nature Geoscience*, **2**, 557–560, doi:10.1038/ngeo583.
- Uppala, S. M., P. W. Kållberg, A. J. Simmons, U. Andraw, V. da Costa Bechtold, M. Fiorino, J. K. Gibson, J. Haerler, A. Hernandez, G. A. Kelly, X. Li, K. Onogi, S. Saarinen, N. Sokka, R. P. Allan, E. Andersson, K. Arpe, F. Chevallier, A. Dethof, M. Dragosavac, M. Fisher, M. Fuentes, S. Hagemann, E. Hólm, B. J. Hoskins, L. Isaksen, P. A. E. M. Janssen, R. Jenne, A. P. McNally, J.-F. Mahfouf, J.-J. Morcrette, N. A. Rayner, R. W. Saunders, P. Simon, A. Sterl, K. E. Trenberth, A. Untch, D. Vasiljevic, P. Viterbo and J. Woollen, 2005: The ERA-40 re-analysis. *Quarterly Journal of the Royal Meteorological Society*, **131**, 2961–3012, doi:10.1256/qj.04.176.
- Vallis, G. K., 2006: *Atmospheric and Oceanic Fluid Dynamics*. Cambridge University Press, Cambridge, U.K., 745 pp.
- Vallis, G. K. and E. P. Gerber, 2008: Local and hemispheric dynamics of the North Atlantic Oscillation, annular patterns and the zonal index. *Dynamics of Atmospheres and Oceans*, **44**, 184–212, doi:10.1016/j.dynatmoce.2007.04.003.
- van Loon, H. and J. C. Rogers, 1978: The seesaw in winter temperatures between Greenland and northern Europe. Part I: General description. *Monthly Weather Review*, **106**, 296–310.
- van Oldenborgh, G. J., S. Y. Philip and M. Collins, 2005: El Niño in a changing climate: a multi-model study. *Ocean Science*, **1**, 81–95.
- VanMarcke, E., 1983: *Random Fields: Analysis and Synthesis*. The MIT Press, Cambridge MA, 382 pp., Web Edition by Rare Book Services, Princeton University, Princeton NJ, 1998.
- von Storch, H. and F. W. Zwiers, 1999: *Statistical Analysis in Climate Research*. Cambridge University Press, Cambridge, U.K., 494 pp.
- Wakabayashi, S. and R. Kawamura, 2004: Extraction of major teleconnection patterns possibly

Bibliography

- associated with the anomalous summer climate in Japan. *Journal of the Meteorological Society of Japan. Ser. II*, **82**, 1577–1588.
- Walker, G., 1925: Correlation in seasonal variations of weather—further study of world weather. *Monthly Weather Review*, **53**, 252–254.
- Wallace, J. M. and D. S. Gutzler, 1981: Teleconnections in the geopotential height field during the northern hemisphere winter. *Monthly Weather Review*, **109**, 784–812.
- Walter, K. and H.-F. Graf, 2002: On the changing nature of the regional connection between the North Atlantic Oscillation and sea surface temperature. *Journal of Geophysical Research*, **107(D17)**, 4338, doi:10.1029/2001JD000850.
- Walter, K., U. Luksch and K. Fraedrich, 2001: A response climatology of idealized midlatitude thermal forcing experiments with and without a storm track. *Journal of Climate*, **14**, 467–484.
- Wang, B., 2006: *The Asian Monsoon*. Springer, Berlin, Praxis UK, XLIX, 787 pp.
- Wang, B., Q. Bao, B. Hoskins, G. Wu and Y. Liu, 2008a: Tibetan Plateau warming and precipitation changes in east Asia. *Geophysical Research Letters*, **35**, L14702, doi:10.1029/2008GL034330.
- Wang, B. and Q. Ding, 2006: Changes in global monsoon precipitation over the past 56 years. *Geophysical Research Letters*, **33**, L06711, doi:10.1029/2005GL025347.
- Wang, B. and Z. Fan, 1999: Choice of south Asian summer monsoon indices. *Bulletin of the American Meteorological Society*, **80**, 629–638.
- Wang, B. and L. Ho, 2002: Rainy season of the Asian–Pacific summer monsoon. *Journal of Climate*, **15**, 386–398.
- Wang, B., R. Wu and K. M. Lau, 2001: Interannual variability of the Asian summer monsoon: Contrasts between the Indian and the western north Pacific–east Asian monsoons. *Journal of Climate*, **14**, 4073–4090.
- Wang, B., Z. Wu, J. Li, J. Liu, C. P. Chang, Y. Ding and G. Wu, 2008b: How to measure the strength of the east Asian summer monsoon. *Journal of Climate*, **21**, 4449–4463, doi:10.1175/2008JCLI2183.1.
- Wang, B., J. Yang, T. Zhou and B. Wang, 2008c: Interdecadal changes in the major modes of Asian–Australian monsoon variability: Strengthening relationship with ENSO since the late 1970s. *Journal of Climate*, **21**, 1771–1789, doi:10.1175/2007JCLI1981.1.
- Wang, X., Q.-B. Zhang, K. Ma and S. Xiao, 2008d: A tree-ring record of 500-year dry-wet changes in northern Tibet, China. *The Holocene*, **18**, 579–588, doi:10.1177/0959683608089212.
- Wang, Y., 1992: Effects of blocking anticyclones in Eurasia in the rainy season (Meiyu/Baiu season). *Journal of the Meteorological Society of Japan. Ser. II*, **70**, 929–951.
- Wang, Y., S. Li and D. Luo, 2009: Seasonal response of Asian monsoonal climate to the Atlantic Multidecadal Oscillation. *Journal of Geophysical Research*, **114**, D02112, doi:10.1029/2008JD010929.
- Watanabe, M., 2004: Asian jet waveguide and a downstream extension of the North Atlantic Oscillation. *Journal of Climate*, **17**, 4674–4691, doi:10.1175/JCLI-3228.1.
- Webster, P. J. and S. Yang, 1992: Monsoon and ENSO: Selectively interactive systems. *Quarterly Journal of the Royal Meteorological Society*, **118**, 877–926.

- Werner, P. C., F.-W. Gerstengarbe, K. Fraedrich and H. Oesterle, 2000: Recent climate change in the North Atlantic/European sector. *International Journal of Climatology*, **20**, 463–471.
- Wiese, W., 1924: Polareis und atmosphärische Schwankungen. *Geografiska Annaler*, **6**, 273–299, available online at <http://www.jstor.org/stable/519626>.
- Wu, G. and Y. Zhang, 1998: Tibetan plateau forcing and the timing of the monsoon onset over south Asia and the South China Sea. *Monthly Weather Review*, **126**, 913–927.
- Wu, H., M. J. Hayes, D. A. Wilhite and M. D. Svoboda, 2005: The effect of the length of record on the standardized precipitation index calculation. *International Journal of Climatology*, **25**, 505–520, doi:10.1002/joc.1142.
- Wu, H., M. D. Svoboda, M. J. Hayes, D. A. Wilhite and F. Wen, 2007: Appropriate application of the standardized precipitation index in arid locations and dry seasons. *International Journal of Climatology*, **27**, 65–79, doi:10.1002/joc.1371.
- Wu, Z., J. Li, J. He and Z. Jiang, 2006: Occurrence of droughts and floods during the normal summer monsoons in the mid- and lower reaches of the Yangtze river. *Geophysical Research Letters*, **33**, L05 813, doi:10.1029/2005GL024487.
- Wu, Z., J. Li, B. Wang and X. Liu, 2009: Can the southern hemisphere annular mode affect China winter monsoon? *Journal of Geophysical Research*, **114**, D111 007, doi:10.1029/2008JD011501.
- Wunsch, C., 1999: The interpretation of short climate records, with comments on the North Atlantic and Southern Oscillations. *Bulletin of the American Meteorological Society*, **80**, 245–255.
- Xie, P. and P. A. Arkin, 1997: Global precipitation: a 17-year monthly analysis based on gauge observations, satellite estimates, and numerical model outputs. *Bulletin of the American Meteorological Society*, **78**, 2539–2558.
- Xu, K., C. Brown, H.-H. Kwon, U. Lall, J. Zhang, S. Hayashi and Z. Chen, 2007: Climate teleconnections to Yangtze river seasonal streamflow at the Three Gorges Dam, China. *International Journal of Climatology*, **27**, 771–780, doi:10.1002/joc.1437.
- Xu, X., C. Lu, X. Shi and S. Gao, 2008: World water tower: An atmospheric perspective. *Geophysical Research Letters*, **35**, L20 815, doi:10.1029/2008GL035867.
- Xue, F., D. B. Jiang, X. M. Lang and H. J. Wang, 2003: Influence of Mascarene high and Australian high on the summer monsoon in east Asia: Ensemble simulation. *Advances in Atmospheric Sciences*, **20**, 799–809.
- Yadav, R. R., W.-K. Park, J. Singh and B. Dubey, 2004: Do the western Himalayas defy global warming? *Geophysical Research Letters*, **31**, L17 201, doi:10.1029/2004GL020201.
- Yanai, M. and C. Li, 1994: Mechanism of heating and the boundary layer over the Tibetan plateau. *Monthly Weather Review*, **122**, 305–323.
- Yang, J., Q. Liu, Z. Liu, L. Wu and F. Huang, 2009: Basin mode of Indian ocean sea surface temperature and northern hemisphere circumglobal teleconnection. *Geophysical Research Letters*, **36**, L19 705, doi:10.1029/2009GL039559.
- Yatagai, A., O. Arakawa, K. Kamiguchi, H. Kawamoto, M. I. Nodzu and A. Hamada, 2009: A 44-year daily gridded precipitation dataset for Asia based on a dense network of rain gauges. *SOLA*, **5**, 137–140, doi:10.2151/sola.2009-035.
- Yatagai, A. and T. Yasunari, 1995: Interannual variations of summer precipitation in the

Bibliography

- arid/semi-arid regions in China and Mongolia: Their regionality and relation to the Asian summer monsoon. *Journal of the Meteorological Society of Japan. Ser. II*, **73** (5), 909–923.
- Yatagai, A. and T. Yasunari, 1998: Variation of summer water vapor transport related to precipitation over and around the arid region in the interior of the Eurasian continent. *Journal of the Meteorological Society of Japan. Ser. II*, **76** (5), 799–815.
- Ye, D.-Z. and G.-X. Wu, 1998: The role of the heat source of the Tibetan plateau in the general circulation. *Meteorology and Atmospheric Physics*, **67**, 181–198.
- Ye, H., 2000: Decadal variability of Russian winter snow accumulation and its associations with Atlantic sea surface temperature anomalies. *International Journal of Climatology*, **20**, 1709–1728.
- Young, G. J. and K. Hewitt, 1990: Hydrology research in the upper Indus basin. *Hydrology of Mountainous Areas, Proceedings of the Štrbské Pleso Workshop, Czechoslovakia, June 1988. IAHS Publication 190*, 139–152.
- Yun, K.-S., K.-H. Seo and K.-J. Ha, 2008: Relationship between ENSO and northward propagating intraseasonal oscillation in the east Asian summer monsoon system. *Journal of Geophysical Research*, **113**, D14 120, doi:10.1029/2008JD009901.
- Zhang, Q., M. Gemmer and J. Chen, 2008: Climate changes and flood/drought risk in the Yangtze delta, China, during the past millennium. *Quaternary International*, **176-177**, 62–69, doi:10.1016/j.quaint.2006.11.004.
- Zhang, Q., T. Jiang, M. Gemmer and S. Becker, 2005: Precipitation, temperature and runoff analysis from 1950 to 2002 in the Yangtze basin, China. *Hydrological Sciences Journal*, **50**, 65–80, doi:10.1623/hysj.50.1.65.56338.
- Zhang, Q., G. Wu and Y. Qian, 2002: The bimodality of the 100 hPa south Asia high and its relationship to the climate anomaly over east Asia in summer. *Journal of the Meteorological Society of Japan. Ser. II*, **80**, 733–744.
- Zhang, R. and T. L. Delworth, 2006: Impact of Atlantic multidecadal oscillations on India/Sahel rainfall and Atlantic hurricanes. *Geophysical Research Letters*, **33**, L17 712, doi:10.1029/2006GL026267.
- Zhang, R. and T. L. Delworth, 2007: Impact of the Atlantic Multidecadal Oscillation on north Pacific climate variability. *Geophysical Research Letters*, **34**, L23 708, doi:10.1029/2007GL031601.
- Zhang, Y., T. Li and B. Wang, 2004: Decadal change of the spring snow depth over the Tibetan plateau: The associated circulation and influence on the east Asian monsoon. *Journal of Climate*, **14**, 2780–2793.
- Zhou, Y., S. Gao and S. S. P. Shen, 2004: A diagnostic study of formation and structure of the Meiyu front system over east Asia. *Journal of the Meteorological Society of Japan. Ser. II*, **82**, 1565–1576.
- Ziv, B., H. Saaroni and P. Alpert, 2004: The factors governing the summer regime of the eastern Mediterranean. *International Journal Of Climatology*, **24**, 1859–1871, doi:10.1002/joc.1113.

List of Figures

| | | |
|------|---|----|
| 1.1 | Annual sum of precipitation in mm per year (CMAP) | 12 |
| 1.2 | Annual cycles of precipitation, global, various data sets | 14 |
| 1.3 | Annual cycle of vertically integrated moisture fluxes | 15 |
| 1.4 | Regional annual cycles of area averaged precipitation (Vasclimo) | 17 |
| 1.5 | Annual cycles of precipitation for Europe and Asia (Vasclimo and ECHAM5) | 18 |
| 1.6 | Illustration of the transformation of precipitation to SPI adopted from Sienz et al. (2007) | 19 |
| 1.7 | Teleconnectivity map for summer 500hPa geopotential anomalies | 22 |
| 1.8 | Teleconnection map for northern hemispheric precipitation in terms of the SPI | 22 |
| 1.9 | Correlations for summer SPI and the zonal and meridional wind components | 23 |
| | | |
| 2.1 | Regional setting | 31 |
| 2.2 | Teleconnectivity map for northern hemispheric precipitation in terms of the SPI | 37 |
| 2.3 | Regional SPI correlation maps | 38 |
| 2.4 | Correlation maps for SPI with various indices | 40 |
| 2.5 | Summer SPI-3 time series for area averaged precipitation | 42 |
| 2.6 | Summer mean monsoon and SST-index time series | 43 |
| 2.7 | Summer mean atmospheric indices (Pacific sector) | 43 |
| 2.8 | Summer mean atmospheric indices (Atlantic sector) | 44 |
| 2.9 | Indus basin summer SPI covariability 1951 to 2000 | 46 |
| 2.10 | Tibetan Plateau summer SPI covariability 1951 to 2000 | 48 |
| 2.11 | Upper Yangtze reaches summer SPI covariability 1951 to 2000 | 50 |
| 2.12 | Lower Yangtze reaches summer SPI covariability 1951 to 2000 | 52 |
| | | |
| 3.1 | Visualisation of regional subdivisions | 60 |
| 3.2 | Visualisation of regional subdivisions | 60 |
| 3.3 | Climatologies of monthly precipitation relative to the annual maximum | 61 |
| 3.4 | Climatologies of monthly precipitation relative to the annual maximum | 61 |
| 3.5 | Annual cycle for the zonally averaged monthly mean zonal wind | 63 |
| 3.6 | Annual cycle of monthly mean vertically integrated moisture fluxes | 64 |
| 3.7 | Annual cycle of the vertically integrated water vapor content | 65 |
| 3.8 | Annual cycle of ratio of monthly mean to eddy monthly mean moisture fluxes | 65 |
| 3.9 | Variance explained by the PC loadings in each month. | 67 |
| 3.10 | Zonal wind section composite differences relative to PC1 | 68 |
| 3.11 | Zonal wind section composite differences relative to PC2 | 69 |
| 3.12 | Zonal wind section composite differences relative to PC3 | 71 |
| 3.13 | Zonal wind section composite differences relative to PC4 | 72 |
| 3.14 | Calendar monthly composite differences for the monthly mean moisture fluxes | 75 |
| 3.15 | Calendar monthly composite differences for the eddy monthly mean moisture fluxes | 77 |
| 3.16 | Calendar monthly composite differences for the zonal wind on 200hPa | 81 |
| 3.17 | Calendar monthly composite differences for the zonal wind on 600hPa | 82 |
| 3.18 | Calendar monthly composite differences for the meridional temperature difference | 84 |
| 3.19 | Composite differences for the zonally asymmetric 500hPa geopotential | 85 |

List of Figures

| | | |
|------|--|-----|
| 3.20 | Spatial correlations with $U'T'$ | 86 |
| 3.21 | Spatial correlations with $V'T'$ | 88 |
| 4.1 | Schematic plot of the moisture paths to the Tibetan Plateau | 96 |
| 4.2 | Climatological setting of the Tibetan Plateau | 99 |
| 4.3 | Tibetan Plateau averaged annual cycle of precipitation | 100 |
| 4.4 | SPI class frequencies for considered ECHAM5/MPI-OM runs | 101 |
| 4.5 | Linear regression analysis for the Tibetan Plateau SPI | 102 |
| 4.6 | Tibetan Plateau dry case composites for ERA-40 data | 104 |
| 4.7 | Tibetan Plateau wet case composites for ERA-40 data | 106 |
| 4.8 | Longitude-time sections of zonally asymmetric geopotential for summer 1984 | 108 |
| 4.9 | Composited anomalies (ERA-40 data) for months preceding wet and dry episodes | 109 |
| 4.10 | Tibetan Plateau dry case composites for ECHAM5 control-run data | 112 |
| 4.11 | Tibetan Plateau wet case composites for ECHAM5 control-run data | 113 |
| 4.12 | Composite comparison between ECHAM5/MPI-OM and ERA-40 | 114 |
| 4.13 | Control-run longitude time lag diagrams for 300hPa meridional wind correlations | 115 |
| 4.14 | Control-run lag correlations for 300hPa meridional wind | 116 |
| 4.15 | Control-run lag correlations for Tibetan Plateau pluvial episodes | 117 |
| 4.16 | Control-run lag correlations for Tibetan Plateau pluvial episodes | 117 |
| 4.17 | Control-run composites for the months before dry and wet events | 118 |
| 4.18 | Schematic diagram of the dynamics related to Tibetan Plateau drought and wetness | 119 |
| A.1 | Bootstrap estimate for quantiles of correlation coefficients | 131 |
| B.1 | Moving window means for regional SPI series and teleconnection indices | 138 |
| B.2 | Moving window variances for regional SPI series and teleconnection indices | 138 |
| B.3 | Whole Yangtze basin summer SPI covariability 1951 to 2000 | 139 |
| B.4 | Change assessment for area averaged summer SPI series | 140 |
| B.5 | Change assessment for summer monsoon and teleconnection indices | 141 |
| C.1 | Annual cycle for the monthly mean zonal wind on 200hPa | 143 |
| C.2 | Annual cycle of eddy monthly mean vertically integrated moisture fluxes | 144 |
| C.3 | First loadings of the monthly PC-analyses. | 145 |
| C.4 | Second loadings of the monthly PC-analyses. | 145 |
| C.5 | Third loadings of the monthly PC-analyses. | 145 |
| C.6 | Fourth loadings of the monthly PC-analyses. | 145 |
| D.1 | One point correlation maps for short time scale fluctuations | 147 |
| D.2 | One point correlation maps for intermediate time scale fluctuations | 148 |
| D.3 | One point correlation maps for long time scale fluctuations | 148 |

List of Tables

| | | |
|-----|---|-----|
| 1.1 | Standardised Precipitation Index (SPI) classification and event-probability | 19 |
| 3.1 | Correlation coefficients of PC time series with regional SPI series | 70 |
| 3.2 | Additional correlations | 73 |
| 4.1 | Standardised Precipitation Index classification and event-probability | 97 |
| B.1 | Correlation coefficients for the regional summer SPI-3 | 137 |
| C.1 | Variance explained by the first seven PC loadings by month. | 144 |
| C.2 | Correlation coefficients of PC time series with teleconnection indices | 146 |

Acknowledgement

Am Ende schreibst Du
irgendetwas zusammen.

Anonymous, 2009

Prior to everything the financial funding has to be acknowledged, which was obtained through the Deutsche Forschungsgemeinschaft in the project 'The importance of teleconnections for precipitation-patterns in the People's Republic of China' (FR 450/7-1, FR 450/14-2) and the Sonderforschungsbereich 512 'Cyclones and the north Atlantic climate system'. The opportunity to do the research presented here is owed to the administration of the working group 'Theoretical Meteorology' at the Meteorological Institute of the University of Hamburg. This work bases on data-sources maintained by the Model & Data group at the Max Planck Institute for Meteorology, the Climate Prediction Center at the National Oceanic and Atmospheric Administration (NOAA), the CISL Research Data Archive (RDA) at the National Center for Atmospheric Research in Boulder, Colorado, the International Pacific Research Center at the University of Hawaii, the Frontier Research Center for Global Change (FRCGC) at the Japan Agency For Marine-Earth Science And Technology (JAMSTEC) and the Deutscher Wetterdienst (DWD).

Thank you to: my mother, my father (R.I.P.), my companion, my uncle Professor Dr. Friedrich von der Haar.

